BULGARIAN CHEMICAL COMMUNICATIONS

Journal of the Chemical Institutes
of the Bulgarian Academy of Sciences
and of the Union of Chemists in Bulgaria

Materials used for organic light-emitting diodes – organic electroactive compounds

P. Petrova*, R. Tomova

Acad. J. Malinowski Central Laboratory of Photoprocesses, Bulgarian Academy of Sciences,
Acad. G. Bonchev St., Block 109, 1113 Sofia, Bulgaria

This paper introduces the readers into the great variety organic electroactive compounds suitable for the preparation of organic light-emitting diodes (OLED). Some of our results on successful usage of new Zn complexes as light-emitting layers in OLED are presented.

Key words: organic light-emitting diodes (OLEDs), electroluminescence, organic electroactive materials, thin films, organometallic compounds, conducting polymers.

INTRODUCTION

In the past decades, an enormous amount of research work as well as commercial interest has focused on the new field of conjugated organic electronics materials. This interest, which has recently received a new impulse thanks to the Nobel Prize in chemistry of Shirakawa, MacDiarmid and Heeger for year 2000, is due to the fact that these materials combine a number of interesting properties, which give rise to a broad variety of new applications. Probably the most important feature of conjugated organic electronics materials is their ability to transport charges, i.e. they can be conductors or semiconductors. On the other hand, these materials are organic molecules or polymers and thus offer the possibility they to be designed in such a way as to fit perfectly the desired requirements.

The search for polymers and small organic molecules as the active layer in light emitting diodes has made rapid advance. Organic light-emitting diodes (OLEDs) are energy converting devices (electricity-to-light) based on electroluminescence (EL) of organic compounds and are considered as next generation full-colour flat panel display.

Even though the display market is still dominated by Cathode-Ray-Tubes (CRT) and Liquid-Crystal-Displays (LCD) the impact of organic light emitting diodes (OLEDs) is getting stronger, so that the first mass products are hitting the market.

In this paper, an overview of the different organic compounds used as electroluminescent materials in the organic light emitting devices is presented. Besides some of our results on

developing of OLED on the basis of Zn complexes will be discussed.

TYPICAL OLED STRUCTURE

OLED devices contain the substrate materials, electrodes and functional organic substances. Two types of electrodes are used. A layer of indium - tin oxide (extremely thin, because it has to be optically transparent), is used as anode. Low work-function metals such as Mg, Ca, Al, Li and their alloys with Ag are commonly used as cathodes. Several types of organic materials are used as the functional layers: polymers or small molecules transporting the injected charges to the recombination zone, fluorescent or more efficient phosphorescent materials emitting the light.
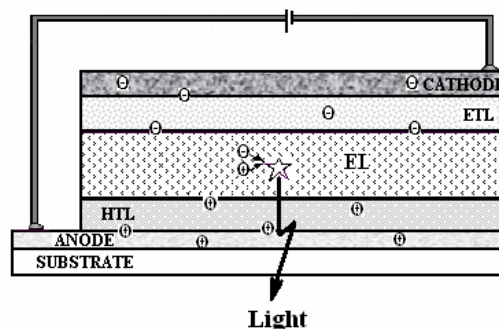

Fig. 1. Scheme of a typical multi-layer OLED with electron transporting layer (ETL), emitting layer (EL), and hole transporting layer (HTL).

When an electric field is applied, electrons are injected from the cathode and holes from the anode into the organic layers. The electron moves through the layers by a hopping process from one molecule to another until it meets an "electronical hole" (a defect formed by the abstraction of an electron at the anode). This abstraction leads to a radical cation,

---

which is neutralized again by receiving an electron from a neighbour molecule, thus drifting in the direction of the cathode. In this way, charges can combine, forming excited molecular species, e.g. excitons, some of which decay to their ground state emitting the light (Fig. 1).

"Small molecular" organic compounds and conjugated oligomers or polymers with precise chain length, and defined electrical and optical qualities are used as organic light-emitting materials. Dendrimers is the newest class investigated materials.

The light emission colour of the polymers strongly depends on their chemical composition. By chemical modification of the polymer structure, a range of soluble light-emitting polymers emitting in the range from 400 nm to 800 nm is made available. This means that any colour in the visible spectrum can be obtained. Important for the emission colour of the light-emitting polymers are the type of polymer and the nature of the side-groups (which are also important for the solubility of the polymer). Well-known examples of light-emitting polymers are poly(*p*-phenylenevinylene), and poly(fluorene) (Fig. 2).

The use of emissive additives (known also as dyes) is an interesting option for influencing the emission colour of light-emitting polymers. By adding a small amount of a suitable dye to a polymer, energy can be transferred from the polymer to the dye and the light will only be emitted from the dye. The colour from the device can be tuned using different dyes. For example, a green dye in a blue polymer will give green light, while a red dye in a blue polymer will give red light.

INDUSTRIAL CHALLENGES

The industrial methods for deposition of organic materials depend on the type of the device produced. Four industrial methods for deposition of organic materials are known:

Thermal vacuum evaporation – used for manufacture of "Small Molecular" Organic Light-Emitting Device (OLED). The small molecules are deposited by vapour deposition.

Spin-coating – used for deposition of soluble polymers. Monochrome displays (PLED) are produced by this method. Conjugated polymers can be applied to a surface either through dip-coating or spin-coating. The thickness of the layers is dependent on the composition of the polymer and the concentration of the polymer solution.

Ink-jet printing – used for manufacture of full-colour display (PLED). Patterning of pixels could be done through *ink-jet printing*, but the pixel pitch at 28 μm obtained by this method is considered too large for microdisplays.

Laser induced thermal image – used for manufacture of high resolution full-colour display (OLED & PLED).

The materials can be deposited in many separate layers or mixed into one or several layers.

Also, an extremely uniform thickness of each layer is necessary for device fabrication. Non uniformities may lead to localized surges of electric current, localized overheating, and gradual destruction of the device. The complexity makes the fabrication of OLEDs difficult and slows down testing of new materials.

Polymeric OLEDs have the advantage that the active layers can be deposited from solution, thus allowing large-area devices preparation, while in "small molecular" OLEDs, the active layers are typically deposited by vapor deposition technique. Vacuum deposition is limited to vaporizable low molecular weight materials and can only be applied to compounds, which endure thermal stress without decomposition. On the other hand, by vacuum technique the complicated multilayer device architecture can be constructed without any serious problems. This technology is relatively expensive and can only be applied for smaller devices with high quality.

However, multi-layer preparation from solution is far from trivial. It is of crucial importance that previously deposited layers are absolutely resistant against the solvent used for deposition of the subsequent layer(s). Yet the most elegant strategy is the application of precursors containing polymerizable groups, which are converted into an insoluble network by an additional crosslinking step.
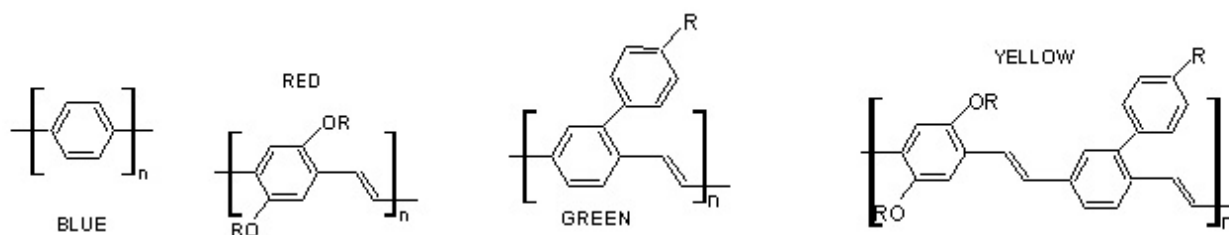

Fig. 2. Light-emitting polymers based on poly(*p*-phenylene) and poly(*p*-phenylenevinylene).

Requirements to the materials used in OLED

The materials need to have a good thermal stability because of the heat generated in the device, low turn-on voltages, high conductivity and high electroluminescence efficiency. The conducting polymers have to be soluble, with good mechanical properties, high resistance to acids and bases and high conductivity.

The *glass transition temperature T*g, of the polymer materials is also an important issue in the choice of the material for the device. In OLEDs the conjugated polymers have a very high *T*g approximately 90–95°C that results in a hard glasslike structure in usage at room temperature. At temperatures over *T*g the display does not obtain a proper functionality and the lifetime is reduced. The upper limit of the temperature range can be improved finding the polymer materials with a higher *T*g [1].

The study of the variety of organic materials as active components is determined by the necessity to optimize the characteristics of the devices.

ELECTRO-CONDUCTING AND/OR LUMINESCENT ORGANIC MATERIALS

"Small molecular" organic compounds

Low-molecular weight materials such as metal chelates (organometallic compounds), simple oxadiazole compounds, triarylamines, po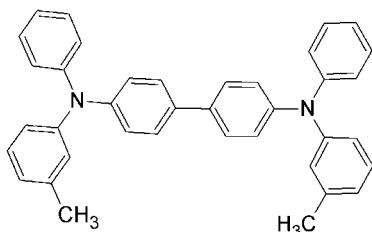rphines, and phthalocyanines are used for OLED [2]. Organometallic compounds are successfully applied in OLEDs as the emitters or electron transporters.

The substituted "small" molecules with aromatic amines are used for hole transport (Fig. 3a), while a variety of polynuclear aromatic complexes with high electron affinity and the oxadiazoles (Fig. 3b) are used for electron transport. The porphines and the phthalocyanines [3, 4] are used as dopant emitters (dyes) and photo-conducting materials. In some cases, the charge transporting "small" molecules (or polymers) themselves assume the role of emitters.

One of the most widely used materials because of its excellent luminescent, electron transporting, and film-forming properties is tris(8-quinolinolato) aluminium, commonly referred to as Alq$_3$ (Fig. 4) [5–9]. The compound Alq$_3$ is one of the typical examples for amorphous films that can be prepared by vacuum vapour deposition. Two geometric isomers can be formulated for Alq$_3$, the meridianal (mer) and the facial (fac) form [10, 11], which may even be interconverted into each other at high temperatures. The 4-methyl-8-quinolinolato ligand also could be used successfully [12].

The efforts with small organometallic compounds (SOC) are directed to design and prepare various electrolumophores (chromophores that are electroluminescent). This is very important area of research, because of the main use of electrolumophores in the fabrication of Organic Light-Emitting Diodes (OLEDs) for full-colour displays.

Fig. 3a. N,N'-diphenyl-N,N'-bis(3-methylphenyl)(1,1'-biphenyl)-4,4'-diamine (TPD) is preferred as a hole transporting material.

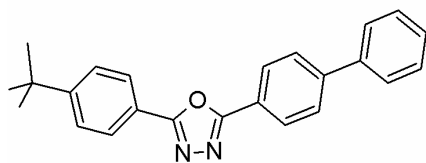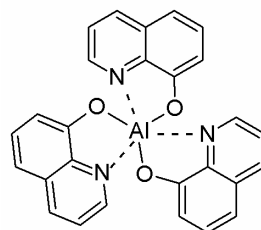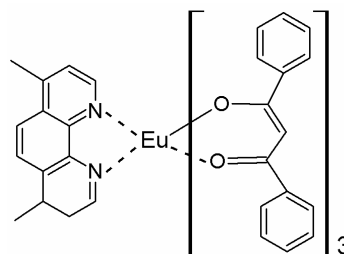Aluminum(III) tris(8-hydroxyquinoline) Alq$_3$ Green Emitter.

Fig. 3b. 2-(4-Biphenylyl)-5-(*p-tert*-butylphenyl)-1,3,4-oxadiazole (PBD) is used as an electron transporting layer.

Europium (III) 4,7-Dimethylphenanthroline-tris(1,3-diphenyl-1,3-propadione) Red Emitter-Dopant.
Fig. 4. Organometallic compounds.

A broad range of metal ions have been used for the complexation of functional ligands, including beryllium [13], zinc, boron [14], transition metals [15] such as iridium [16–19], and the lanthanide metals introduced by Kido [20], especially europium [21] and terbium. Common ligands are phenanthroline (phen) (Fig. 4), bathophenanthroline (bath), 2-phenylpyridine (ppy), acetylacetonate (acac), dibenzoylmethanate (dbm), anthracene [22] and thenoyltrifluoroacetonate (TTFA). A frequently used complex is the volatile Eu(TTFA)$_3$(phen) [23]. In general, these complexes tend to crystallize and require the use of a stabilizing matrix. By incorporating larger ligands, the glass forming tendency is increased.

Electroactive polymers

The electroactive polymers fulfil multiple functions: both electron and hole transport and light emission, even though dopant emitters can be used to tune the colour.

Conjugated polymers. Conjugated polymers (CPs) are organic semiconductors with delocalized π-molecular orbitals along the polymeric chain.

Conjugated polymers have a framework of alternating single and double carbon–carbon (sometimes carbon–nitrogen) bonds. Single bonds are referred to as σ-bonds, and double bonds contain a σ-bond and a π-bond. All conjugated polymers have a σ-bond backbone of overlapping sp^2 hybrid orbitals.

The remaining out-of-plane p$_z$ orbitals on the carbon (or nitrogen) atoms overlap with neighbouring p$_z$ orbitals to give π-bonds. Electron movement within delocalized π-molecular orbitals is the source of conductivity. In CPs (Fig. 5), conductivity within one polymer chain is based on the conjugated nature of the polymer molecules and the resulting mobility of p-electrons.

With the discovery of electrical conductivity of electroactive polymers began a period of intense theoretical and experimental research into the physical and chemical properties of these materials. Polyacetylene (PA) was the first organic conducting polymer, synthesized in 1971 by a co-worker of Shirakawa, who accidentally used an excess of Ziegler-Natta catalyst [24]. This was followed in 1977 by the discovery of Heeger, MacDiarmid and Shirakawa that polyacetylene doped with iodide demonstrated a much higher conductivity than with other dopants, with conductivities reaching as high as 10^6 S·cm^{-1} under appropriate conditions [25, 26]. Following these discoveries, research in the field of conducting polymers began in earnest.

Different types of conjugated polymers such as polyacetylene (PA), poly(*p*-phenylene) (PPP), poly(*p*-phenylenevinylene) (PPV), poly(phenylene ethynylene) (PPE), polyfluorene (PF), polyaniline (PAni), polypyrrole (PPy), polythiophene (PT), poly(3,4-ethylenedioxythiophene) (PEDOT) have been developed and intensively investigated.
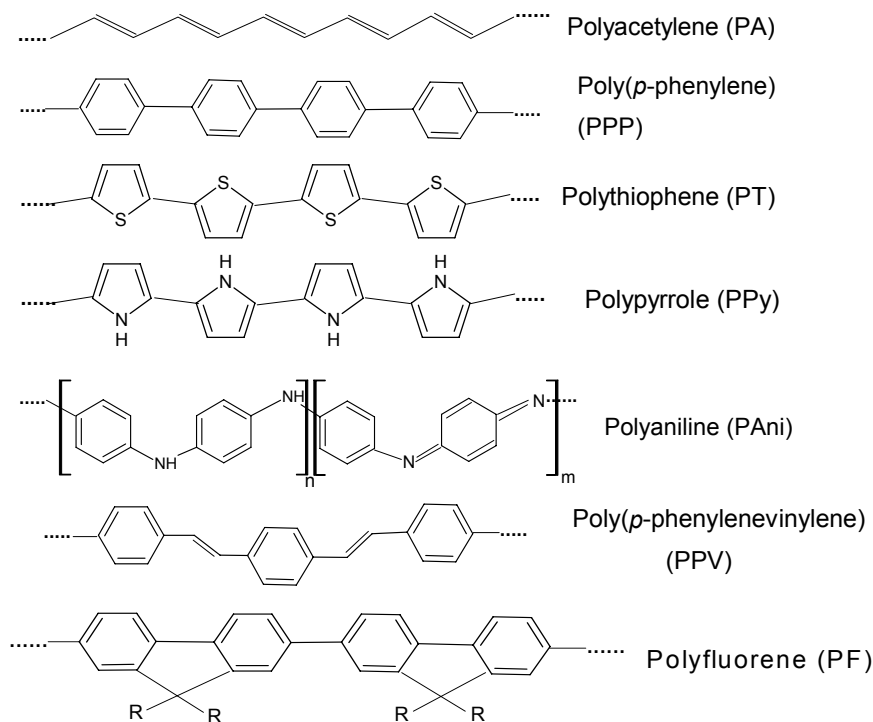

Fig. 5. Basic structures of common conducting polymers.

214

Linear π-conjugated polymers are not only known as electrically conductive materials but also have recently been found to function as electrochromic [27, 28], photovoltaic [29, 30], and organic EL device materials [31, 32].

Most conjugated polymers have semiconductor band gaps of 1.5–3 eV, which means that they are ideal for optoelectronic devices that emit visible light. They can also be chemically modified in a variety of ways, and a lot of efforts have been put into finding materials that can be processed easily from solution – either as directly soluble polymers, or as "precursor" polymers that are first processed in solution and then converted *in situ* to form the semiconducting structure.

Fine tuning of polymers chemical structures is achieved via copolymerization variation of different conjugated units into the polymer backbone. Thus high purity, ease of processability, control of the band-gap and the emission colour of the polymer are achieved [33, 34].

The varieties, excellent optical and electronic properties, and high thermal and chemical stability of polyfluorenes (PFs) make them an attractive class of materials for polymer light-emitting diodes (PLEDs) [35–39]. The polyfluorene copolymers are of high molecular weight, highly photoluminescent, and their emissive colours can be qualitatively correlated to the extent of delocalization in the co-monomers. For example, the thiophene copolymer emits bluish-green light, the cyanostilbene copolymer emits green light, and the bithiophene copolymer emits yellow light [40]. Thus, the choice of co-monomer in the fluorene-based polymer family has served as an excellent synthetic tool for designing polymers with well-balanced hole- and electron-transport properties and fine colour control [41, 42]. No other polymer class offers the full range of colours with high efficiency, low operating voltage, and high lifetime when applied in a device configuration. Thus, the polyfluorene-based molecules are the most viable LEPs for comercialization.

Oligomers. Main chain conjugated polymers inevitably contain random dispersed defects leading to a statistical distribution of lumophore lengths [43, 46]. In contrast, well-defined conjugated oligomers allow strict control of the effective conjugation length. Initially, they have been synthesized as model compounds in order to gain more insight into the structural and electronic peculiarities of the corresponding polymers [44, 45]. However, on account of their controllable and rigorously defined structure, conjugated oligomers have also been used as novel materials and potential alternative in electrooptical applications.

Like the corresponding polymers, the conjugated oligomers can be deposited from solution or, since they are molecular materials, by sublimation. The method of choice depends mainly on molecular weight and solubility of the material.

Solution processing demands sufficient solubility which is typically ensured by introduction of solubilizing side chains. Pursuing this concept, a wide range of oligo(*p*-phenylenevinylene)s with alkyl [47–50] (Fig. 6a) or alkoxy [51–56] (Fig. 6b) substituents have been synthesized. Oligo(*p*-phenylene)s have been used as blue emitters [57–64] (Fig. 7) in electroluminescent devices. They exhibit high-fluorescence quantum yields. Oligothiophenes [65–68] (Fig. 8) with various number of thiophene rings in the molecular chain [69] and end-capping group have been synthesized. Oligothiophenes are intrinsically electron-rich compounds exhibiting low electron affinity. Oligomers have been incorporated into OLEDs as spincast films [50, 70] and in polymeric blends [51, 54].

a

b

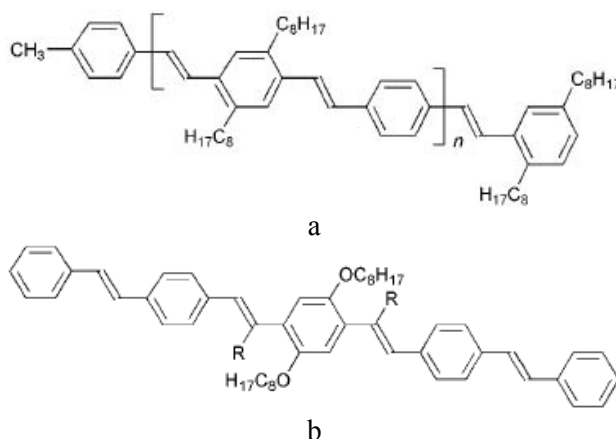Fig. 6. Substituted oligo(*p*-phenylenevinylene)s.

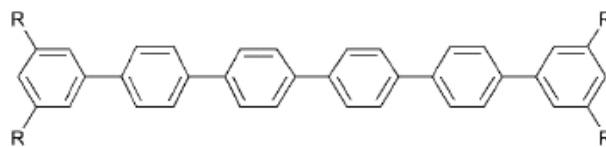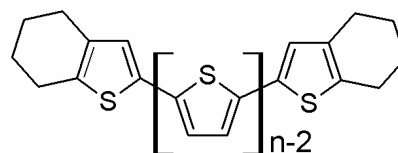

Fig. 7. Oligo(*p*-phenylene).

Fig. 8. End-capped oligothiophenes, n = 5, 6, 7.

Oligomers are very often used as side chain in non-conjugated polymers with pendant π-electron systems. For example, series of non-conjugated vinyl and methacrylate polymers containing pendant

unsubstituted and substituted oligothiophenes have been synthesized [71].

Substituted conjugated polymers. The variety of polymer materials synthesized with the aim to be used for the production of OLED is enormous. One of the main trends is the modification of conjugated polymers.

The most widely used polymer is poly(phenylene vinylene) or "PPV", which has a band gap of about 2.5 eV and emits yellow-green light. PPV is insoluble in common solvents, and as such requires special processing steps to produce a conjugated thin film necessary for EL device application. The researchers often modify PPV by attaching alkyls side-chains to the phenylene rings. The introduction of substituents into the PPV skeleton on one hand allows the modification of the electronic properties (e.g. band gap, electron affinity, and ionization potential) and on the other hand it enables the generation of PPVs that are soluble in organic solvents.

In 1991, Heeger and Braun reported a red-orange emitting OLED based on the asymmetrically substituted soluble PPV derivative poly[2-methoxy-5-(2-ethylhexyloxy)-*p*-phenylenevinylene] (MEH-PPV has an energy gap of about 2.2 eV) (Fig. 9) in a simple single-layer device configuration (ITO/MEH-PPV/Ca) with an external quantum yield of 1% [72].
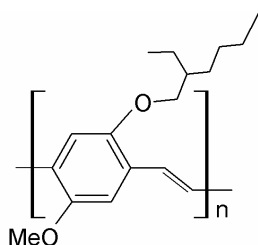

Fig. 9. Poly[2-methoxy-5-(2-ethylhexyloxy)-*p*-phenylenevinylene] (MEH-PPV).

A variety of PPV derivatives containing long alkyl [73–75] and alkoxy [73, 74, 76–81] side chains, and oligoethenyloxy [82–84] substituents have been synthesized by polycondensation. PPV derivatives with at least one long solubilizing alkoxy side chain are soluble in organic solvents such as chloroform or THF providing sufficient processability with respect to electrooptical applications [85]. Furthermore, long side chains separate the polymeric chains from each other and hence impede the formation of non-emissive relaxation sites. This effect seems to be advantageous with regard to the fluorescence and electroluminescence efficiencies of the corresponding polymers.

The introduction of silyl substituents, as realized

for PPV derivative, (see Fig. 10), gave an increase in solubility and a widening of the band gap with respect to PPV, enabling the emission of green light [82, 86–90].
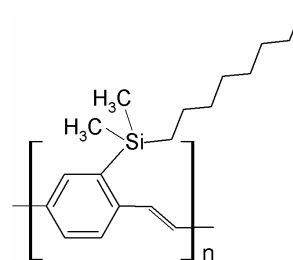

Fig. 10. Silyl substituted poly(*p*-phenylenevinylene).

An orange colour became accessible using copolymers with unsubstituted phenylene and statistically distributed alkoxy-substituted phenylene segments [91, 92].

1

2
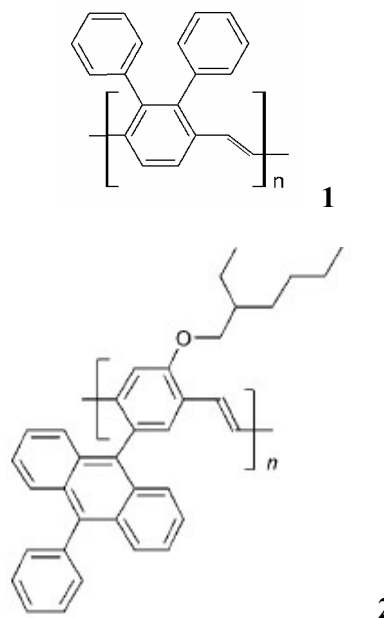
Fig. 11. Aryl substituted poly(*p*-phenylenevinylene)s.

Other successful approaches to tune the band gap were the introduction of oligo(*p*-phenylene) moieties [93, 94] as well as the incorporation of m-phenylene segments [95–97].

The most important example, poly(2,3-diphenyl-*p*-phenylenevinylene) Compound **1** (Fig. 11), [98, 99] exhibits EL in a single-layer configuration (ITO/Comp.1/Al) with an external quantum efficiency of 0.04% [98, 100] similar to the values obtained for simple PPV-diodes [101].

Pendent phenylanthryl substituents have proven to increase the EL efficiency of single-layer devices based on polymer Comp. **2** (Fig. 11) by a factor of 10 in comparison to LEDs based on PPV [102, 103]. This improvement was interpreted based on both increased interchain distance and an intrachain

electronic energy transfer between the main chain and the pendants. The latter effect was expected to slow down the decay of the excited state.

Organic compounds in general, and conjugated polymers in particular, tend to have low electron affinities rendering electron injection more difficult than hole injection. One strategy to overcome this problem is the use of metals with lower work functions for the cathodes. The more perspective strategy is to improve the electron affinity of the inserted polymer. This concept was first used by Friend, Holmes *et al.* in 1993 [104]. They attached electron-withdrawing cyano groups to the vinylene bonds of a dihexyloxy-substituted PPV (Fig. 12), which was synthesized by a Knoevenagel condensation polymerization of suitable monomers. A bright red fluorescent material was obtained (CN-PPV, Fig. 12, Comp. **3**). Internal efficiencies of 0.2% were reported for a single-layer configuration Al/CN-PPV/metal, independent of the type of cathode material (Al or Ca).
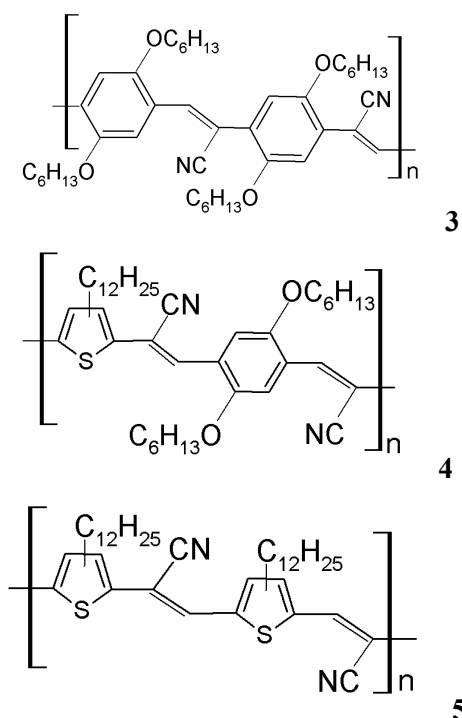

3

4

5

Fig. 12. Polymers with electron-withdrawing substituents.

Following this initial report, a series of other CN-PPV derivatives [105, 106], and thiophene analogues Comp. **4** and Comp. **5** (Fig. 12) [105] have been synthesized by Knoevenagel method. The PLEDs with blue, red and near-IR emission have been fabricated with these polymers.

Polymer OLEDs emitting in the blue region are therefore an attractive target for research. Blue emission from the active luminescent material requires a HOMO-LUMO energy gap of approxi-

mately 2.7–3.0 eV [107]. In 1992, Leising *et al.* for the first time reported on blue electroluminescence from OLEDs containing poly(*p*-phenylene) (PPP) [108]. They observed external quantum efficiencies for simple single-layer devices (ITO/PPP/Al) of 0.05%. Like PPV, PPP is also insoluble and infusible and has to be incorporated into an electrooptical device via a soluble precursor polymer [109].

In an effort to improve processability, PPP derivatives bearing solubilizing alkyl, aryl, alkoxy, or perfluoralkyl side chains have been synthesized by transition metal-catalyzed polymerization of appropriate monomers and have been utilized as active organic materials in OLEDs [110–117].

On account of their good solubility and chemical stability poly(3-alkylthiophene)s (PATs) have attracted considerable interest. The properties of polythiophene derivatives (PTs) in general can easily be altered by structural modification, which allows the control of the torsion of the main chain and thus the adjustment of the effective conjugation length. PATs and other PT derivatives are attractive electroluminescent materials due to their ease of tunability [118–125]. Although simple PATs [126, 127] usually exhibit red emission, all other colours from blue to near infrared have been realized in OLED applications. Although PTs tend to exhibit fluorescence intensities smaller than PPVs and PPP derivatives they have frequently been used as active layers in electrooptical applications [118–123, 128].

Non-conjugated polymers containing pendant π-electron system. Non-conjugated polymers containing pendant π-electron systems are of interest for the following reasons: the variety of possible pendant molecules, chemical stability, ease of processability, possibility to form morphologically stable system, photoconductivity of pendant π-electron systems, and invariance of the standard redox potential with the degree of doping.

The concept of attaching chromophoric groups to or as the side chain of a non-conjugated polymer was found to be of great advantage for the transformation of crystalline electroluminescent materials to amorphous derivatives. Thus, blue electroluminescence from perylene-containing poly(methylacrylamide) was reported Comp. **6** (Fig. 13) [129].

Side group polymers with laterally fixed charge transport units have proven to provide a homogeneous, amorphous morphology essential for device stability. The oxadiazole moieties, including the PBD, were introduced as pendant groups in many non-conjugated polymers in order to reduce the electron-injection barrier and improve the EL efficiency of the device. To avoid phase separation

217

and molecular PBD crystallization several groups introduced the PBD moieties as pendant groups in polymetacrylate [130–132] and polyethylene [133] chains. Polymers (Comp. **7–9,** Fig. 14) have been studied as materials for PLEDs [130, 131], both in a single-layer devices and in combination with PPV hole transporting layer. The authors mention that the device instability is a great problem for these systems, and creating a more robust polymer backbone would be necessary. Later, Register *et al.* [134] synthesized and studied related polymers (Comp. **10** and Comp. **11)** based on polystyrene backbone. Observing the immiscibility of oxadiazole polymer (Comp. **10)** with PVK, the authors designed the co-polymer Comp. **11** containing both electron- and hole-transporting units. The device ITO/Comp. **11**/Mg:Al showed improved external quantum efficiency of 0.3%, although the turn-on voltage was still high (16 V). Doping the polymer with different molecular dyes, the emission colour was tuned from blue to orange [134].
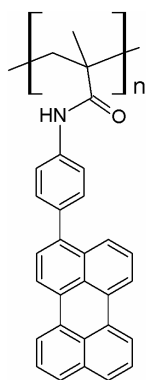
6

Fig. 13.

Polystyrenes with quaterphenylene segments in the side chain (Fig. 15a) were utilized as electron transporting material [135]. Polyacrylate with pendant triphenylene segments (Fig. 15b) was used as an efficient hole transporting material in a two-layer configuration with Alq$_3$ (ITO/ polyacrylate/ Alq$_3$/Al) [136].

A high hole mobility and excellent photoconductive properties of carbazole-containing polymers, such as poly(N-vinylcarbazole) (PVK) (Fig. 15c) [3] and poly(N-epoxyprolylcarbazole) (PEPK, Fig. 15d) rate them among the most studied polymers for optoelectronic application. Generally, the electroluminescent properties of non-conjugated carbazoles are quite poor. On the other hand, being an excellent hole-transporting material, PVK has been extensively used as a HTL [137–144] or as a hole-transporting material in blends with other conjugated EL materials in PLEDs [145–149], and host material in host / guest systems [150].

In an effort to simplify device fabrication and restrict all functions to a single layer, a series of copolymers containing both charge transport and emissive chromophores on pendant side chains has been synthesized [151–154].

High-efficiency red, green and blue phosphorescent polymer light-emitting devices based on phosphorescent polymers involving carbazole units and iridium-complex units (Fig. 16) have been reported by Tokito *et al.* [155]. Many other compounds may be associated with this polymer groups.

Dendrimers

Light-emitting dendrimers generally consist of a light-emitting core, to which one or more branched dendrones are attached. Surface groups are attached to the distal end of the dendrons to provide the solubility necessary for solution processing. The dendritic structure allows independent modification of the core (light emission), branching groups (charge transport) and surface groups (processing properties).

| 7 | 8 | 9 | 10 | 11 |
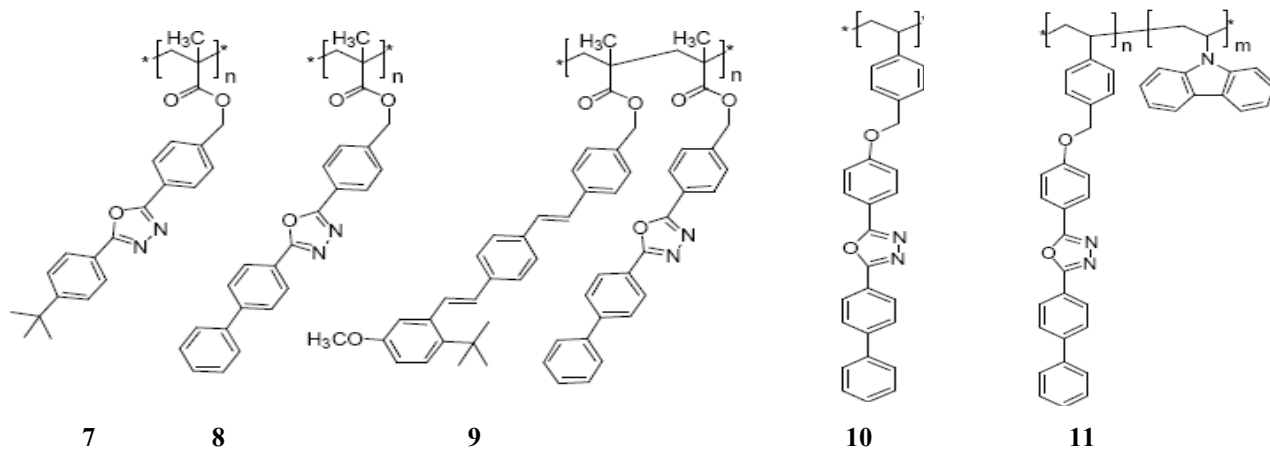
Fig. 14. Non-conjugated polymers containing pendant oxadiazoles as π-electron system.

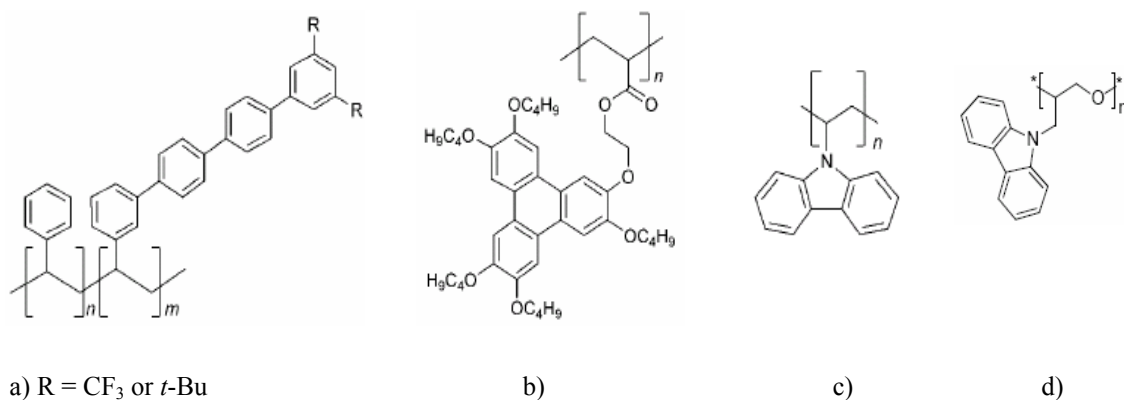a) R = CF$_3$ or *t*-Bu   b)   c)   d)

Fig. 15. Non-conjugated polymers containing pendant phenylene segments or carbazole units as π-electron system.
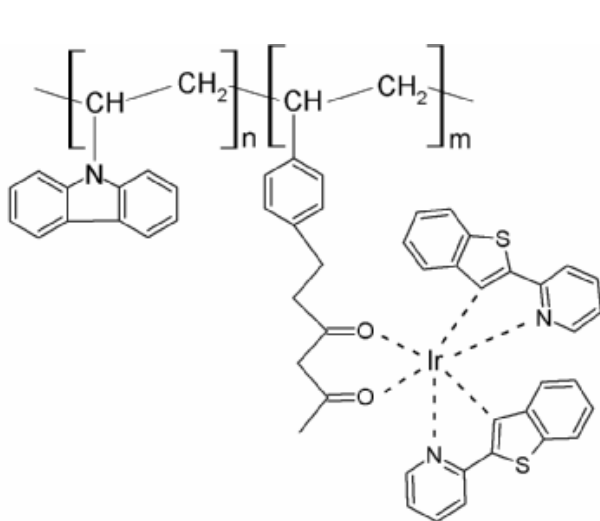

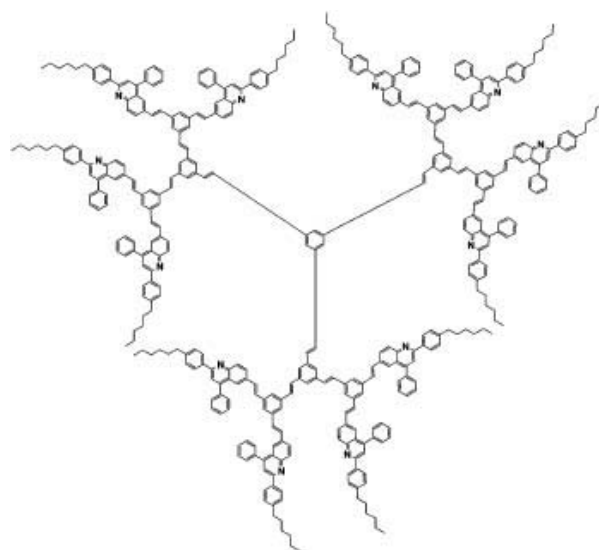Fig. 16. Synthesized molecular structures of red phosphorescent polymers (RPP)

Fig. 17. n-Type conjugated dendrimer [G2–12Q].

Dendrimers possess a number of potential advantages over the conjugated polymers and small molecule light-emitting materials. First, their key electronic properties, such as light emission, can be finely tuned by picking out among a wide range of luminescent chromophores, including phosphorescent groups. Second, solubility of the molecules can be adjusted by selecting the appropriate surface groups to optimize the materials to meet different processing and application requirements. Finally, the level of intermolecular interaction of the electroactive chromophores can be controlled by the type and generation of the dendrons employed, a vital element in the performance of OLEDs. This makes it possible to adapt dendrimers to various processing systems without compromising the quality of light emission.

These design principles have been illustrated in the development of green-light-emitting phosphorescent dendrimers that contained *fac*-tris(2-phenylpyridyl)iridium(III) cores, biphenyl based dendrons and 2-ethylhexyloxy surface groups. The solution

processable green phosphorescent dendrimers have been used to fabricate highly efficient single layer [156, 157] devices, as well as bi-layer OLEDs giving efficiencies of up to 16% and 40 lm·W^{-1} at 400 cd·m^{-2} [158]. Anthopoulos *et al*. [159] reported two new solution processable red phosphorescent dendrimers for use in OLEDs. Kwon *et al*. [160] reported three new electron-acceptor and light-emitting conjugated dendrimers, based on a benzene core, poly(phenylenevinylene) dendrons, and diphenylquinoline peripheral groups (Fig. 17). As the emissive materials in light-emitting diodes, these dendrimers showed yellow electroluminescence, the brightness and efficiency of which increased with generation and number of electron-acceptor peripheral groups.

OLEDS WITH Zn COMPLEXES

It was one of our aims to test the new Zn organometallic compounds bis(2-methyl-8-hydroxyquinoline)zinc (Znq$_2$), bis(2-(2-hydroxyphenyl)

219

benzothiazole)zinc (Zn(BTz)$_2$), and bis(2-(2-hydroxynaphthyl)benzothiazole)zinc (Zn(NBTz)$_2$) as light-emitting materials (Fig. 18). The presented Zn complexes were investigated in electroluminescent devices with conventional structure: ITO/HTL/EL/M, where ITO is a transparent anode of In$_2$O$_3$:SnO$_2$, HTL – a hole-transporting layer, EL – an emitting layer, and M – a metallic cathode of Al. We demonstrated earlier, that the composite film of N,N'-bis(3-methylphenyl)-N,N'-diphenylbenzidine (TPD) incorporated in poly(N-vinylcarbazole) (PVK) matrix [161] was a promising HTL for OLED. More details about device preparation and measurements are published in our previous paper [162].

The electrical and optical properties of the OLED are complicated linked to molecular organization of layers, such as morphology, and chain arrangement in polymer. The surface morphology of the composite film PVK:TPD, spin coated on PET substrate covered with ITO, is shown in Fig. 19a. SEM micrographs of the vacuum deposited Znq$_2$ and Zn(BTz)$_2$ in the case of both investigated OLED structures ITO/PVK:TPD/Zn complex are presented in Figs. 19b, c. The images show very smooth and homogeneous surfaces of the deposited films. It is a substantial prerequisite for developing of OLED with good characteristics.

The present metal complexes showed bright emission as emitting layers. Fig. 20 represents the current/voltage (*I–V*) (a) and luminance/voltage (*L–V*) (b) characteristics of the three type identical devices with different EL at two concentrations ($x = 10$ and 20 wt.%) of TPD in PVK:TPD$_x$ composite HT film. All devices emit from yellow-green for Znq$_2$ to pure green for Zn(BTz)$_2$ and Zn(NBTz)$_2$ spectrum of visible light.

The current densities (*I*) of the all devices are similar, while the luminances (*L*) at the same current densities (*I*) are quite different. It was established that the luminance of the devices with Zn(BTz)$_2$ is 2.5 times higher than those with Znq$_2$ and 3 times higher than those with Zn(NBTz)$_2$ (at 15 V DC). Besides Zn(BTz)$_2$ shows the lowest "turn-on voltage" and the best electroluminescent efficiency – 2 times higher than that of Znq$_2$ and 6x higher than that of Zn(NBTz)$_2$ at luminance of 250 cd/m^2 (Fig. 21).

The current density and the luminance of the devices with Znq$_2$ increase with the concentration (*x*) of TPD in composite PVK:TPD$_x$ while the "turn-on voltage" becomes lower. Just the opposite are the results in the cases of Zn(BTz)$_2$ and Zn(NBTz)$_2$.

| Znq$_2$ | Zn(BTz)$_2$ | Zn(NBTz)$_2$ |
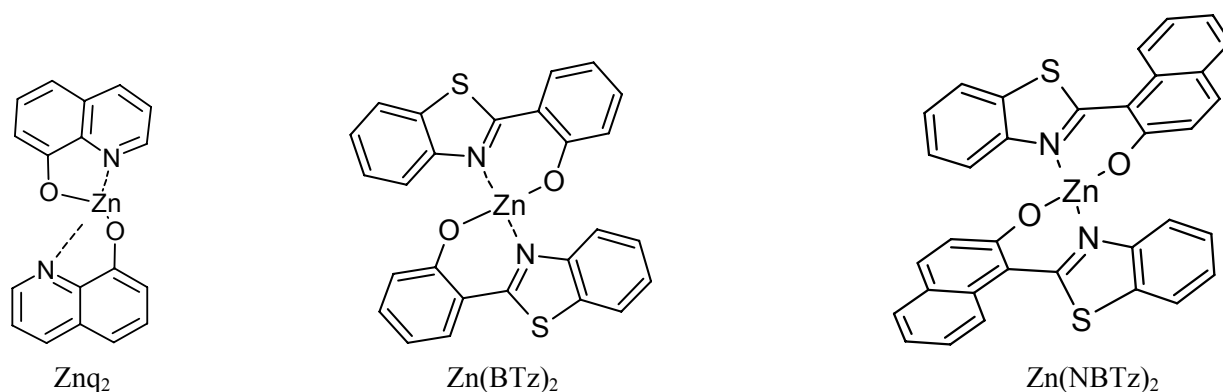
Fig. 18. Chemical structures of the investigated Zn complexes.

a) PET/ITO/ PVK:TPD   b) PET/ITO/ PVK:TPD/ Znq$_2$ c) PET/ITO/ PVK:TPD/ Zn(BTz)$_2$

Fig. 19. SEM micrographs of PET/ITO/PVK:TPD, PET/ITO/PVK:TPD/Znq$_2$, and PET/ITO/PVK:TPD/ Zn(BTz)$_2$ surfaces.
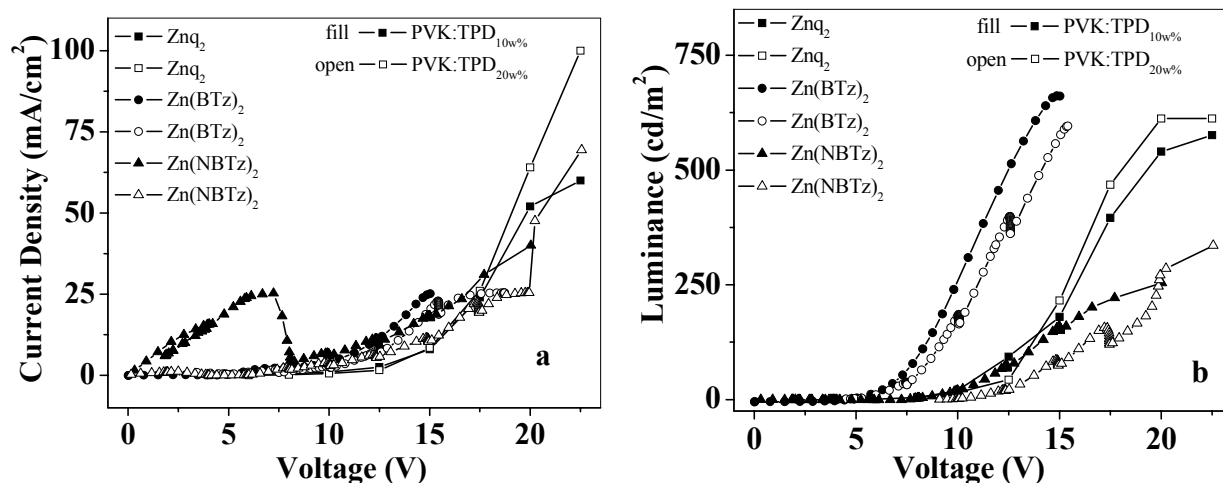
Fig. 20. Current/voltage (I-V) (a) and luminance/voltage (L-V) (b) characteristics of the three types of identical devices with different EL at two concentrations (x = 10 and 20wt.%) of TPD in PVK:TPD$_x$ composite HT film.
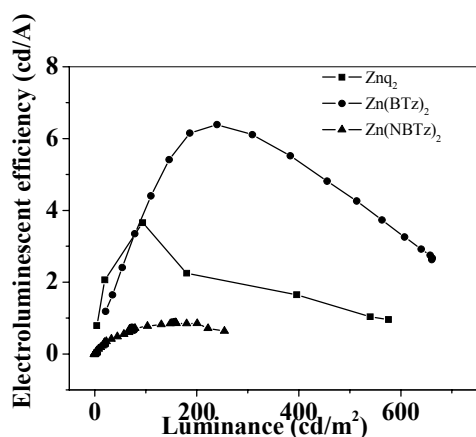

Fig. 21. Electroluminescent efficiency of devices with HTL of PVK:TPD$_{10wt.\%}$ and different EL.

The results presented in this paper show that the studied Zn complexes can be successfully used as emitters and electron transporting layers for OLED. The best characteristics are shown by the devices on the basis of Zn(BTz)$_2$ (Fig. 22). It could be emphasized that the efficiency of the devices with Zn(BTz)$_2$ is 6.3 cd/A at luminance 250 cd/m^2 and 4.1 cd/A at luminance 100 cd/m^2. It is one of the best reported up to now in the literature for the devices with similar structure. Sano [163] reported efficiency 1.39 cd/A at luminance 100 cd/m^2 for ITO/TPD/Zn(BTz)$_2$/Mg:In device. Maximum quantum efficiency of 0.3% was found for ITO/PVK/Zn(BTz)$_2$/Al device by Wu [164]. Zheng *et al*. [165] showed maximum quantum efficiency 0.63% and the corresponding luminance efficiency 4.05 cd/A and luminance 4048 cd/m^2 for the white device on the basis of Zn(BTz)$_2$ doped with rubrene.

Studying the molecular structure of Zn(BTz)$_2$ Wu *et al*. [164] showed that as disturbed by Zn^{2+}, the complex molecular rigidity and planar structure

were strengthened and enlarged greatly. Moreover, augmented conjugative effect of π electron made the transition π --- π * more easily, which results in high fluorescence of Zn(BTz)$_2$, eventually. Probably it is a reason for the best characteristics of the devices on the basis of Zn(BTz)$_2$.

Fig. 22. Picture of our luminous OLED device with structure ITO/(PVK:TPD$_{20}$)/Zn(BTz)$_2$/Al at 15 V DC.

It was established that Zn complexes synthesized by T. Deligeorgiev [166] are useful for the development of OLED and further improvement of their characteristics is in progress. Besides some other Zn and Al organometallic complexes are under investigations.

CONCLUSION

Although this review is not exhaustive, it does illustrate some recent developments of organic materials used in OLED.

The use of π-conjugated materials is not limited to their application in OLEDs. Organic chemistry offers an endless variety of structures, and therefore, the choices of charge transporters, emitters and other dopants are virtually unlimited.

For highly stable and efficient materials of such applications semi-conducting materials with smart

221

designed and optimized properties are greatly desired. The toolbox of organic chemistry hereby opens a broad variety of suitable reactions and easily accessible target compounds. The optimization of the target structures results therefore in smart materials with finely-tuned optical and electronic properties.

The advantages of polymeric materials compared with other "classic" materials like glass, ceramic or metal are the low specific weight, high corrosion stability and good process ability. The addition of additives opens furthermore the option of fine-tuning of properties.

REFERENCES

1. T. P. Nguyen, P. Molinie, P. Destruel, in: Organic and Polymer-Based Light Emitting Diodes. Handbook of Advanced Electronic and Photonic Materials and Devices, H. Sing Nalwa (ed), vol. 10, Academic Press, San Diego, 2001, p. 3.
2. T. Fuhrmann, J. Salbeck in: Funnctional Molecular Glasses: Building Blocks for Future Optoelectronics. Advances in Photochemistry, D. C. Neckers, G. von Bünau, W. S. Jenks (eds), vol. 27, John Wiley & Sons Inc. 2002, p. 83.
3. S. K. Kim, T. G. Chung, D. H. Chung, H. S. Lee, M. J. Song, J. W. Park, J. U. Lee, T. W. Kim, *Opt. Mater.,* **21**, 159 (2002).
4. P.-C. Kao, S.-Y. Chu, Z. X. You, S. J. Liou, C.-A. Chuang, *Thin Solid Films*, **498,** 249 (2006).
5. H. Tang, H. Liao, K. Xu, Z. Zhou, L. Zhu, *J. Lumin.*, **118**, 39 (2006).
6. J.-S. Kim, H. Kajii, Y. Ohmori, *Thin Solid Films*, **499**, 343 (2006).
7. Y. Iwama, T, Itoh, T. Mori, T. Mizutani, *Thin Solid Films*, **499**, 364 (2006).
8. C. Y.Kwong, A. B. Djurišić, W. C. H. Choy, D. Li, M. H. Xie, W. K. Chan, K. W. Cheah, P. T. Lai, P. C. Chui, *Mater. Sci. Eng. B,* **116**, 75 (2005).
9. C.-Y Yang, Y. S. Tsai, F.-S. Juang, Y.-K. Su, D. Lin, C.-H. Chu, Y.-T. Chiu, *Jpn. J. Appl. Phys.*, **44**, (4B), 2833 (2005).
10. C. H. Chen, J. Shi, J. Coord, *Chem. Rev.*, **171**, 161 (1998).
11. M. Brinkmann, G. Gadret, M. Muccini, C. Taliani, N. Masciocchi, A. Sironi, *J. Am. Chem. Soc.*, **122**, 5147 (2000).
12. J. Kido, Y. Iizumi, *Appl. Phys. Lett.*, **73**, 2721 (1998).
13. Y. Hamada, H. Kanno, T. Sano, H. Fujii, Y. Nishio, H. Takahashi, T. Usuki, K. Shibata, *Chem. Lett.*, 905 (1993).
14. T.-R. Chen, R.-H. Chien, M.-S. Jan, A. Yeh, J.-D. Chen, *J. Organomet. Chem.*, **691**, 799 (2006).
15. J. Yang, K. C. Gordon, Y. Zidon, Y. Shapira, *J. Appl. Phys.*, **94**, 6391 (2003).
16. M. A. Baldo, S. Lamansky, P. E. Burrows, M. E. Thompson, S. R. Forrest, *Appl. Phys. Lett.*, **75**, 4 (1999).
17. M.-L. Xu, T.-L. Li, W.-L. Li, Z.-R. Hong, Z. -W. An, Q. Zhou, *Thin Solid Films*, **497**, 239 (2006).
18. K.-H. Fang, L.-L. Wu, Y.-T. Huang, C.-H. Yang, I.-W. Sun, *Inorg. Chim. Acta*, **359**, 441 (2006).
19. J. H. Kim, E. J. Nam, S. Y. Hong, B. O. Kim, S. M. Kim, S. S. Yoon, J. H. Suh, Y. Ha, Y. K. Kim, *Mater. Sci. Eng. C,* **24**, 167 (2004).
20. J. Kido, H. Hayase, K. Hongawa, K. Nagai, K. Okuyama, *Appl. Phys. Lett.*, **65**, 2124 (1994).
21. H. Xin, F. Y. Li, M. Guan, C. H. Huang, M. Sun, K. Z. Wang, Y. A. Zhang, L. P. Jin, *J. Appl. Phys.*, **94**, 4729 (2003).
22. K.-Y. Lai, T.-M. Chu, F. C.-N. Hong, A. Elangovan, K.-M. Kao, S.-W. Yang, T.-I. Ho, *Surf. Coat. Technol.*, **200**, 3283 (2006).
23. T. Sano, M. Fujita, T. Fujii, Y. Hamada, K. Shibata, K. Kuroki, *Jpn. J. Appl. Phys.*, **34**, 1883 (1995).
24. H. Shirakawa, E. J. Louis, A. G. MacDiarmid, C. K. Chiang, A. J. Heeger, *J. Chem. Soc., Chem. Commun.*, 578 (1977).
25. C. K. Chiang, C. R. Fincher, Y. W. Park, A. J. Heeger, H. Shirakawa, E. J. Louis, S. C. Gau, A. G. MacDiarmid, *Phys. Rev. Lett.,* **39**, 1098 (1977).
26. T. Schimmel, M. Schwoerer, H. Naarmann, *Synth. Met.,* **1,** 1 (1990).
27. S. A. Sapp, G. A. Sotzing, J. R. Reynolds, *Chem. Mater.*, **10**, 2101 (1998).
28. F. Garnier, G. Tourillon, M. Gazard, J. C. Dubois, *J. Electrochem. Anal. Chem.*, **148**, 299 (1983).
29. G. Yu, A. J. Heeger, *J. Appl. Phys.*, **78**, 4510 (1995).
30. G. Yu, J. Gao, J. C. Hummelen, F. Wudl, A. J. Heeger, *Science*, **270**, 1789 (1995).
31. A. Kraft, A. C. Grimsdale, A. B. Holmes, *Angew. Chem., Intern. Ed.*, **37**, 402 (1998).
32. R. H. Friend, R. W. Gymer, A. B. Holmes, J. H. Burroughes, R. N. Marks, C. Taliani, D. D. C. Bradley, D. A. Dos Santos, J. L. Brédas, M. Lögdlung, W. R. Salaneck, *Nature*, **397**, 121 (1999).
33. Y. Zou, S. Tan, Z. Yuan, Z. Yu, *J. Mater. Sci.* **40**, 3561 (2005).
34. Y. -H. Niu, Q. Hou, Y. Cao, *Appl. Phys. Lett.*, **82**, 2163 (2003).
35. D. Fujishima, T. Mori, T. Mizutani, T. Yamamoto, N. Kitamura, *Jpn. J. Appl. Phys.*, **44**, 546 (2005).
36. M. Bernius, M. Inbasekaran, E. Woo, W. Wu, L. Wujkòwski, *J. Mater. Sci.: Mater. Electron.*, **11**, 111 (2000).
37. M. T. Bernius, M. Inbasekaran, J. O'Brien, W. Wu, *Adv. Mater.*, **12**, 1737 (2000).
38. M. Leclerc, *J. Polym. Sci. Part A: Polym. Chem.* **39**, 2867 (2001).
39. D. Y. Kim, H. N. Cho, C. Y. Kim, *Prog. Polym. Sci.*, **25,** 1089, (2000).
40. M. T. Bernius, M. Inbasekaran, J. O'Brien, W. Wu, *Adv. Mater.*, **12**, 1737 (2000).
41. J. H. Kim, P. Herguth, M.-S. Kang, A. K.-Y. Jen, Y.-H. Tseng, C.-F. Shu, *Appl. Phys. Lett.*, **85**, 1116

(2004).

42. D.-H. Hwang, M.-J. Park, J.-H. Lee, *Mater. Sci. Eng. C*, **24,** 201 (2004).
43. J. Roncali, *Chem. Rev.*, **97**, 173 (1997).
44. W. J. Feast, J. Tsibouklis, K. L. Pouwer, L. Groenendaal, E. W. Meijer, *Polymer*, **37**, 5017 (1996).
45. H. S. O. Chan, S. C. Ng, *Prog. Polym. Sci.*, **23**, 1167 (1998).
46. L. Pu, *Acta Polym.*, **48**, 116 (1997).
47. D. Oelkrug, A. Tompert, H.-J. Egelhaaf, M. Hanack, E. Steinhuber, M. Hohloch, H. Meier, U. Stalmach, *Synth. Met.*, **83**, 231 (1996).
48. E. Thorn-Csányi, P. Kraxner, *Macromol. Chem. Phys.*, **198**, 3827 (1997).
49. R. E. Gill, A. Meetsma, G. Hadziioannou, *Adv. Mater.*, **8**, 212 (1996).
50. M. Halim, J. N. G. Pillow, I. D. W. Samual, P. L. Burn, *Adv. Mater.*, **11**, 371 (1999).
51. V. Gebhardt, A. Bacher, M. Thelakkat, U. Stalmach, H. Meier, H.-W. Schmidt, D. Haarer, *Adv. Mater.*, **11**, 119 (1999).
52. V. Gebhardt, A. Bacher, M. Thelakkat, U. Stalmach, H. Meier, H. -W. Schmidt, D. Haarer, *Synth. Met.*, **90**, 123 (1997).
53. J. L. Segura, N. Martin, M. Hanack, *Eur. J. Org. Chem.*, 643 (1999).
54. P. Frederiksen, T. Bjornholm, H. G. Madsen, K. Bechgaard, *J. Mater. Chem.*, **4**, 675 (1994).
55. M. Era, J. -I. Koganemaru, T. Tsutsui, A. Watakabe, T. Kunitake, *Synth. Met.*, **91**, 83 (1997).
56. S. Pfeiffer, H.-H. Hörhold, H. Boerner, H. Nikol, W. Busselt, *Proc. SPIE Intern. Soc. Opt. Eng.*, **3476**, 258 (1998).
57. G. Leising, E. J. W. List, S. Tasch, C. Brandstätter, W. Graupner, P. Markart, F. Meghdadi, G. Kranzelbinder, A. Niko, R. Resel, E. Zojer, P. Schlichting, U. Rohr, Y. Geerts, U. Scherf, K. Müllen, R. Smith, D. Gin, *Proc. SPIE Intern. Soc. Opt. Eng.*, **3476**, 76 (1998).
58. G. Leising, S. Tasch, F. Meghdadi, L. Athouel, G. Froyer, U. Scherf, *Synth. Met.*, **81**, 185 (1996).
59. N. Koch, A. Pogantsch, E. J. W. List, G. Leising, R. I. R. Blyth, M. G. Ramsey, F. P. Netzer, *Appl. Phys. Lett.*, **74**, 2909 (1999).
60. F. Meghdadi, S. Tasch, B. Winkler, W. Fischer, F. Stelzer, G. Leising, *Synth. Met.*, **85**, 1441 (1997).
61. B. Winkler, F. Meghdadi, S. Tasch, R. Müllner, R. Resel, R. Saf, G. Leising, F. Stelzer, *Opt. Mater.*, **9**, 159 (1998).
62. J. Salbeck, N. Yu, J. Bauer, F. Weissörtel, H. Bestgen, *Synth. Met.*, **91**, 209 (1997).
63. K. -H. Weinfurtner, F. Weissörtel, G. Harmgarth, J. Salbeck, *Proc. SPIE Intern. Soc. Opt. Eng.*, **3476**, 40 (1998).
64. N. Johansson, J. Salbeck, J. Bauer, F. Weissörtel, P. Bröms, A. Andersson, W. R. Salaneck, *Adv. Mater.*, **10**, 1136 (1998).
65. F. Geiger, M. Stoldt, H. Schweizer, P. Bäuerle, E. Umbach, *Adv. Mater.*, **5**, 922 (1993).

66. H. Neureiter, W. Gebauer, C. Väterlein, M. Sokolowski, P. Bäuerle, E. Umbach, *Synth. Met.*, **67**, 173 (1994).
67. C. Väterlein, H. Neureiter, W. Gebauer, B. Ziegler, M. Sokolowski, P. Bäuerle, E. Umbach, *J. Appl. Phys.*, **82**, 3003 (1997).
68. P. Bäuerle, U. Mitschke, E. Mena-Osteritz, M. Sokolowski, D. Müller, M. Groβ, K. Meerholz, *Proc. SPIE Intern. Soc. Opt. Eng.*, **3476**, 32 (1998).
69. G. Gigli, O. Inganäs, M. Anni, M. De Vittorio, R. Cingolani, G. Barbarella, L. Favaretto, *Appl. Phys. Lett.*, **78**, 1493 (2001).
70. T. Goodson III, W. Li, A. Gharavi, L. Yu, *Adv. Mater.*, **9**, 639 (1997).
71. Y. Shirota, *J. Mater. Chem.*, **10**, 1 (2000).
72. D. Braun, A. J. Heeger, *Appl. Phys. Lett.*, **58**, 1982 (1991).
73. M. R. Andersson, G. Yu, A. J. Heeger, *Synth. Met.*, **85**, 1275 (1997).
74. B. J. Schwartz, F. Hide, M. R. Andersson, A. J. Heeger, *Chem. Phys. Lett.*, **265**, 327 (1997).
75. E. G. J. Staring, R. C. J. E. Demandt, D. Braun, G. L. J. Rikken, Y. A. R. R. Kessener, T. H. J. Venhuizen, H. Wynberg, W. T. Hoeve, K. J. Spoelstra, *Adv. Mater.*, **6**, 934 (1994).
76. J. Salbeck, *Ber. Bunsenges. Phys. Chem.*, **100**, 1666 (1996).
77. H. F. M. Schoo, R. C. J. E. Demandt, J. J. M. Vleggaar, C. T. H. Liedenbaum, *Macromol. Symp.*, **125**, 165 (1997).
78. M. Hamaguchi, K. Yoshino, *Jpn. J. Appl. Phys.*, **34**, L712 (1995).
79. K. L. Brandon, P. G. Bentley, D. D. C. Bradley, D. A. Dunmur, *Synth. Met.*, **91**, 305 (1997).
80. C. T. Wong, W. K. Chan, *Adv. Mater.*, **11**, 455 (1999).
81. M. S. Jang, S. Y. Song, J.-I. Lee, H.-K. Shim, T. Zyung, *Macromol. Chem. Phys.*, **200**, 1101 (1999).
82. B. S. Chuah, D. -H. Hwang, S. T. Kim, S. C. Moratti, A. B. Holmes, J. C. de Mello, R. H. Friend, *Synth. Met.*, **91**, 279 (1997).
83. B. Winkler, L. Dai, A. W.-H. Mau, *Chem. Mater.*, **11**, 704 (1999).
84. R. O. Garay, B. Mayer, F. E. Karasz, R. W. Lenz, *J. Polym. Sci., Part A: Polym. Chem.*, **33**, 525 (1995).
85. A. Kraft, A. C. Grimsdale, A. B. Holmes, *Angew. Chem., Intern. Ed.*, **37**, 402 (1998).
86. D.-H. Hwang, I.-N. Kang, M.-S. Jang, H.-K. Shim, T. Zyung, *Polym. Bull.*, **36**, 383 (1996).
87. D.-H. Hwang, S. T. Kim, H.-K. Shim, A. B. Holmes, S. C. Moratti, R. H. Friend, *Synth. Met.*, **84**, 615 (1997).
88. S. Höger, J. J. McNamara, S. Schricker, F. Wudl, *Chem. Mater.*, **6**, 171 (1994).
89. Z.-K.Chen, L.-H. Wang, E.-T. Kang, Y.-H. Lai, W. Huang, *Bull. Chem. Soc. Jpn.*, **72**, 1941 (1999).
90. Z.-K. Chen, L.-H. Wang, E.-T. Kang, W. Huang, *Phys. Chem. Chem. Phys.*, **1**, 3789 (1999).
91. E. G. J. Staring, R. C. J. E. Demandt, D. Braun, G. L. J. Rikken, Y. A. R. R. Kessener, A. H. J. Venhuizen,

M. M. F. van Knippenberg, M. Bouwmans, *Synth. Met.*, **71**, 2179 (1995).

92. E. Z. Faraggi, H. Chayet, G. Cohen, R. Neumann, Y. Avny, D. Davidov, *Adv. Mater.*, **7**, 742 (1995).

93. M. Remmers, D. Neher, J. Grüner, R. H. Friend, G. H. Gelinck, J. M. Warmann, C. Quattrocchi, D. A. Dos Santos, J. L. Brédas, *Macromolecules*, **29**, 7432 (1996).

94. Y. Liu, M. S. Liu, X.-C. Li, A. K.-Y. Jen. *Chem. Mater.*, **10**, 3301 (1998).

95. D. D. C. Bradley, M. Grell, A. Grice, A. R. Tajbakhsh, D. F. O'Brien, A. Bleyer, *Opt. Mater.*, **9**, 1 (1998).

96. M. Baumgarten, T. Yüksel, *Phys. Chem. Chem. Phys.*, **1**, 1699 (1999).

97. T. Ahn, M. S. Jang, H.-K. Shim, D.-H. Hwang, T. Zyung, *Macromolecules*, **32**, 3279 (1999).

98. H. Antoniadis, D. Roitman, B. Hsieh, W. A. Feld, *Polym. Adv. Technol.*, **8**, 392 (1997).

99. B. R. Hsieh, W. C. Wan, Y. Yu, Y. Gao, T. E. Goodwin, S. A. Gonzalez, W. A. Feld, *Macromolecules*, **31**, 631 (1998).

100. W. C. Wan, H. Antoniadis, V. E. Choong, H. Razafitrimo, Y. Gao, W. A. Feld, B. R. Hsieh, *Macromolecules*, **30**, 6567 (1997).

101. J. H. Burroughes, D. D. C. Bradley, A. R. Brown, R. N. Marks, K. Mackay, R. H. Friend, P. L. Burns, A. B. Holmes, *Nature*, **347**, 539 (1990).

102. S.-J. Chung, J.-I. Jin, C.-H. Lee, C.-E. Lee, *Adv. Mater.*, **10**, 684 (1998).

103. J.-I. Jin, S.-J. Chung, S.-H. Yu, *Macromol. Symp.*, **128**, 79 (1998).

104. N. C. Greenham, S. C. Moratti, D. D. C. Bradley, R. H. Friend, A. B. Holmes, *Nature*, **365**, 628 (1993).

105. S. C. Moratti, R. Cervini, A. B. Holmes, D. R. Baigent, R. H. Friend, N. C. Greenham, J. Grüner, P. J. Hamer, *Synth. Met.*, **71**, 2117 (1995).

106. Y. Liu, G. Yu, Q. Li, D. Zhu, *Synth. Met.*, **122**, 401 (2001).

107. J. L. Segura, *Acta Polym.*, **49**, 319 (1998).

108. G. Grem, G. Leditzky, B. Ullrich, G. Leising, *Adv. Mater.*, **4**, 36 (1992).

109. U. Mitschke, P, Bäuerle, *J. Mater. Chem.*, **10**, 1471 (2000).

110. M. Grell, D. D. C. Bradley, *Adv. Mater.*, **11**, 895 (1999).

111. G. LuÈssem, J. H. Wendorff, *Polym. Adv. Technol.*, **9**, 443 (1998).

112. R. H. Friend, R. W. Gymer, A. B. Holmes, J. H. Burroughes, R. N. Marks, C. Taliani, D. D. C. Bradley, D. A. Dos Santos, J. L. Breädas, M. LoÈgdlund, W. R. Salaneck, *Nature*, **397**, 121 (1999).

113. J. L. Segura, *Acta Polym.*, **49**, 319 (1998).

114. J. Kido, *Phys. World*, **12**, 27 (1999).

115. H. S. O. Chan, S. C. Ng, *Prog. Polym. Sci.*, **23**, 1167 (1998).

116. Y. Liu, M. S. Liu, X.-C. Li, A. K.-Y. Jen, *Chem. Mater.*, **10**, 3301 (1998).

117. J. W. Baur, S. Kim, P. B. Balanda, J. R. Reynolds,

M. F. Rubner, *Adv. Mater.*, **10**, 1452 (1998).

118. M. Pomerantz, Y. Cheng, R. K. Kasim, R. L. Elsenbaumer, *J. Mater. Chem.*, **9**, 2155 (1999).

119. S.-D. Jung, D.-H. Hwang, T. Zyung, W. H. Kim, K. G. Chittibabu, S. K. Tripathy, *Synth. Met.*, 98, 107 (1998).

120. S.-D. Jung, T. Zyung, W. H. Kim, C. J. Lee, S. K. Tripathy, *Synth. Met.*, **100**, 223. (1999).

121. M. R. Andersson, O. Thomas, W. Mammo, M. Svensson, M. Theander, O. Inganäs, *J. Mater. Chem.*, **9**, 1933 1999.

122. P. Barta, J. Sanetra, M. Zagórska, *Synth. Met.*, 94, 119 (1998).

123. P. Barta, F. Cacialli, R. H. Friend, M. Zagórska, *J. Appl. Phys.*, **84**, 6279 (1998).

124. A. Bolognesi, C. Botta, L. Cecchinato, *Synth. Met.*, **111–112**, 187 (2000).

125. S.-H. Ahn, M.-Z. Czae, E.-R. Kim, H. Lee, S.-H. Han, J. Noh, M. Hara, *Macromolecules*, **34**, 2522, (2001).

126. H. Spreitzer, H. Becker, E. Kluge, W. Kreuder, H. Schenk, R. Demandt, H. Schoo, *Adv. Mater.*, **10**, 1340 (1998).

127. P. K. H. Ho, M. Granstroèm, R. H. Friend, N. C. Greenham, *Adv. Mater.*, **10**, 769, (1998).

128. S. H. Jin, B, U. Yoo, S. Y. Kang, Y. S. Gal, D. K. Moon, *Opt. Mater.*, **21**, 153 (2003).

129. C. H. Lee, S. H. Ryu, S. Y. Oh, *J. Polym. Sci. B, Polym. Phys.* **41**, 2733 (2003).

130. F. Cacialli, X. -C. Li, R. H. Friend, S. C. Moratti, A. B. Holmes, *Synth. Met.,* **75**, 161, (1995).

131. X. -C. Li, F. Cacialli, M. Giles, J. Grüner, R. H. Friend, A. B. Holmes, S. C. Moratti, T. M. Yong, *Adv. Mater.* **7**, 898 (1995).

132. M. Strukelj, T. M. Miller, F. Papadimitrakopoulos, S. Son, *J. Am. Chem. Soc.* **117**, 11976, (1995).

133. S. Dailey, W. J. Feast, R. J. Peace, I. C. Sage, S. Till, E. L. Wood, *J. Mater. Chem.* **11**, 2238 (2001).

134. X. Jiang, R. A. Register, K. A. Killeen, M. E. Thompson, F. Pschenitzka, J. C. Sturm, *Chem. Mater.,* **12**, 2542 (2000).

135. J. Pommerehne, A. Selz, K. Book, F. Koch, U. Zimmermann, C. Unterlechner, J. H. Wendorff, W. Heitz, H. Bässler, *Macromolecules*, **30**, 8270 (1997).

136. A. Bacher, I. Bleyl, C. H. Erdelen, D. Haarer, W. Paulus, H. -W. Schmidt, *Adv. Mater.*, **9**, 1031 (1997).

137. T. Ahn, S. Ko, J. Lee, H. Shim, *Macromolecules*, **35**, 3495 (2002).

138. M. R. Robinson, S. Wang, A .J. Heeger, G. C .Bazan, *Adv. Funct. Mater.*, **11**, 413 (2001).

139. J. Pei, W.-L. Yu, W. Huang, A. J. Heeger, *J. Chem. Soc. Chem. Commun.*, **33,** 1631 (2000).

140. B. Liu, W.-L. Yu, Y.-H. Lai, W. Huang, *Macromolecules*, **33**, 8945 (2000).

141. J. Pei, W. L. Yu, J. Ni, Y. H. Lai, W. Huang, A. J. Heeger, *Macromolecules*, **34**, 7241 (2001).

142. X. Chen, M. Liu, Z. Xu, Y. Hou, F. Teng, X. Xu, *J. Phys. D: Appl. Phys.*, **37,** 1007 (2004).

143. A. P. Kulkarni, A. P. Gifford, C. J. Tonzola, S. A. Jenekhe, *Appl. Phys. Lett.*, **86**, 061106 (2005).

144. M. Jin, Y. J. Liang, R. Lu, X. H. Chuai, Z. H. Yi, Y. Y. Zhao, H. J. Zhang, *Synth. Met.*, **140,** 37 (2004).

145. X. Zhan, S. Wang, Y. Liu, X. Wu, D. Zhu, *Chem. Mater.*, **15**, 1963 (2003).

146. S. Destri, U. Giovanella, A. Fazio, W. Porzio, B. Gabriele, G. Zotti, *Org. Electron.*, **3**, 149 (2002).

147. G. Gigli, M. Ani, G. Barbarella, L. Favaretto, F. Cacialli, R. Cingolani, *Phys. E*, **7**, 612 (2000).

148. J. Yang, K. C. Cordon, A. J. McQuillan, Y. Zidon, Y. Shapira, *Phys. Rev. B*, **71**, 155209 (2005).

149. X. Chen, Z. Xu, Y. Hou, S. Liu, F. Teng, X. Xu, *J. Phys. D: Appl. Phys.*, **36**, 2054 (2003).

150. K. M. Vaeth, C. W. Tang, *J. Appl. Phys.,* **92**, 3447 (2002).

151. F. Cacialli, X.-C. Li, R. H. Friend, S. C. Moratti, A. B. Holmes, *Synth. Met.*, **75**, 161 (1995).

152. X.-C. Li, F. Cacialli, M. Giles, J. Grüner, R. H. Friend, A. B. Holmes, S. C. Moratti, T. M. Yong, *Adv. Mater.*, **7**, 898 (1995).

153. Y. Heischkel, H.-W. Schmidt, *Macromol. Chem. Phys.*, **199**, 869 (1998).

154. X.-C. Li, T.-M. Yong, J. Grüner, A. B. Holmes, S. C. Moratti, F. Cacialli, R. H. Friend, *Synth. Met.*, **84**, 437 (1997).

155. S. Tokito, M. Suzuki, F. Sato, M. Kamachi, K. Shirane, *Org. Electron.,* **4**, 105 (2003).

156. J. P. J. Markham., S. -C. Lo, S. W. Magennis, P. L. Burn, I. D. W. Samuel, *Appl. Phys. Lett.*, **80**, 2645 (2002).

157. T. D. Anthopoulos, J. P. J. Markham, E. B. Namdas, I. D. W. Samuel, S.-C. Lo, P. L. Burn, *Appl. Phys. Lett.*, **82**, 4824 (2003).

158. S.-C. Lo, N. A. H. Male, J. P. J. Markham, S. W. Magennis, P. L. Burn, O. V. Salata, I. D. W. Samuel, *Adv. Mater.*, **14**, 975 (2002).

159. T. D. Anthopoulos, M. J. Frampton, E. B. Namdas, P. L. Burn, I. D. W. Samuel, *Adv. Mater.*, **16**, 557 (2004).

160. T. W. Kwon, M. M. Alam, S. A. Jenekhe, *Chem. Mater.*, **16**, 4657 (2004).

161. R. Tomova, P. Petrova, A. Buroff, R. Stoycheva-Topalova, *J. Chem. Soc. Chem. Commun.*, **39**, 247 (2007).

162. R. Tomova, P. Petrova, R. Stoycheva-Topalova, A. Buroff, A. Vassilev, T. Deligeorgiev, *J. Nanosci. Nanotechnol.,* in press.

163. T. Sano,Y. Nishio, Y. Hamada, H. Takahashi, T. Usuki, K. Shibata, *J. Mater. Chem.*, **10**, 157, (2000).

164. X. Wu, Y. Hua, Z. Wang, J. Zheng, X. Feng, Y. Sun, *Chin. Phys. Lett.*, **22**, 1797, (2005).

165. J. Zheng, Y. Hua, S. Yin, X. Feng, X. Wu, Y. Sun, Y. Li, Ch. Yang, Z. Shuai, *Chin. Sci. Bull.*, **50**, 509, (2005).

166. T. Deligeorgiev, http://www.chem.unisofia.bg/ UNIDYES/oled.html.

МАТЕРИАЛИ ИЗПОЛЗВАНИ ЗА ОРГАНИЧНИ СВЕТОИЗЛЪЧВАЩИ ДИОДИ – ОРГАНИЧНИ ЕЛЕКТРОАКТИВНИ СЪЕДИНЕНИЯ

П. К. Петрова*, Р. Л. Томова

Централна лаборатория по фотопроцеси „Акад. Й. Малиновски“, Българска академия на науките, ул. „Акад. Г. Бончев“, Блок 109, 1113 София

(Резюме)

Тази статия въвежда читателя в голямото разнообразие от органични електроактивни съединения подходящи за направата на органични светоизлъчващи диоди (OLED). Представени са наши резултати за успешно използване на нови Zn органометални съединения като електролуминесцентни слоеве в OLED.

Base-catalyzed synthesis of 2-thioxo-2,3-dihydrothieno[2,3-d]pyrimidin-4(1H)-ones and isolation of intermediates using microwave irradiation

A. Davoodnia*, M. Bakavoli, N. Zareei, N. Tavakoli-Hoseini

*Department of Chemistry, School of Sciences, Islamic Azad University,
Mashhad Branch, Mashhad 91735-413, Iran*

A simple and fast method for the synthesis of some 3-substituted-5,6-dimethyl-2-thioxo-2,3-dihydrothieno[2,3-d]pyrimidin-4(1H)-ones has been developed *via* base-catalyzed cyclocondensation of ethyl 2-amino-4,5-dimethyl-thiophene-3-carboxylate with isothiocyanates. The uncyclized intermediates, ethyl 4,5-dimethyl-2-[(substituted carbamothioyl)amino]thiophene-3-carboxylates, were isolated when the reactions were carried out under microwave irradiation. These intermediates subsequently underwent cyclization in t-butanol in the presence of potassium *t*-butoxide on heating under reflux to give the desired bicyclic products.

Key words: ethyl 2-amino-4,5-dimethylthiophene-3-carboxylate, isothiocyanates, 2-thioxo-2,3-dihydrothieno[2,3-d]pyrimidin-4(1H)-ones, microwave irradiation.

INTRODUCTION

Our interest in thieno[2,3-d]pyrimidine synthesis emerges from the numerous reports on their diverse biological activities [1–10]. Various methods have already been proposed for the synthesis of these compounds and the most general ones involve cyclocondensation of suitably functionalized thiophenes with different electrophiles such as chloroformamidine [11], α-substituted acetonitriles [12], formic acid [13], phosgene [14], ethyl chloroformate [14] and guanidine [15]. To the best of our knowledge, base-catalyzed cyclocondensation of ethyl 2-amino-4,5-dimethylthiophene-3-carboxylate (**1**) with isothiocyanates for the synthesis of 3-substituted-5,6-dimethyl-2-thioxo-2,3-dihydrothieno[2,3-d]pyrimidin-4(1H)-ones (**3a–e**) and the utilization of microwave irradiation for isolation of the intermediates (**2a–e**) has not been reported in the literature.

Prompted by these findings and due to our interest in the synthesis of heterocyclic compounds [16–25] and in continuation of our previous works on the synthesis of thieno[2,3-d]pyrimidine derivatives [26–28], we report here a simple and fast method for the synthesis of 3-substituted-5,6-dimethyl-2-thioxo-2,3-dihydrothieno[2,3-d]pyrimidin-4(1H)-ones (**3a–e**) through cyclocondensation of ethyl 2-amino-4,5-dimethylthiophene-3-carboxylate (**1**) with isothiocyanates under basic conditions.

RESULTS AND DISCUSSION

The starting material (**1**) was prepared according to the literature method [29]. Cyclocondensation of this compound with isothiocyanates in the presence of potassium *t*-butoxide in *t*-butanol under reflux gave products identified as 3-substituted-5,6-dimethyl-2-thioxo-2,3-dihydrothieno[2,3-d]pyrimidin-4(1H)-ones (**3a–e**). Under this conditions, attempts to isolate the reaction intermediates (**2a–e**) failed when we monitored the course of the reactions carefully (Scheme 1).

Due to our interest in the utilization of microwave irradiation for the synthesis of heterocyclic compounds [30–33], we tried to extend this nonconventional synthetic method for the synthesis of compounds **3a–e**. Therefore, ethyl 2-amino-4,5-dimethylthiophene-3-carboxylate (**1**) was allowed to interact with isothiocyanates under microwave irradiation under solvent-free conditions at 800 W. During monitoring of the reaction mixture by TLC (CHCl$_3$:MeOH = 95:5), surprisingly, we observed that unexpected products, with R$_f$-values different from those expected for compounds **3a–e**, were being formed. During work up and identification, it was established that a condensation and not a cyclocondensation reaction had occurred and the intermediates ethyl 4,5-dimethyl-2-[(substituted carbamothioyl)amino]thiophene-3-carboxylates (**2a–e**) were isolated. The reaction did not proceed to form cyclic products even after prolonged irradiation, but when the latter compounds were heated under reflux for 3 hours in the presence of potassium *t*-butoxide

---

in *t*-butanol, cyclization reaction occurred and the cyclic products **3a–e** were obtained (Scheme 1).

The structure of the synthesized compounds was deduced from their spectral and microanalytical data. For example, the ^{1}H NMR spectrum of **2a** did not show the NH_2 signal of the precursor 1 at δ 5.61 ppm, but instead of it showed two broad signals at δ 9.62 and 11.80 ppm belonging to the NH groups indicating the formation of compound **2a**. The IR spectrum showed the absorption bands at 1651, 3215 and 3299 cm^{-1} for carbonyl and two NH groups respectively. The MS of **2a** showed a molecular ion peak at m/z 286 (M$^+$) corresponding to the molecular formula $C_{12}H_{18}N_2O_2S_2$. This compound gave also satisfactory elemental analysis data (See Experimental).

a: R = Et
b: R = Ph
c: R = 3-MeC$_6$H$_4$
d: R = 4-MeC$_6$H$_4$
e: R = 4-O$_2$NC$_6$H$_4$
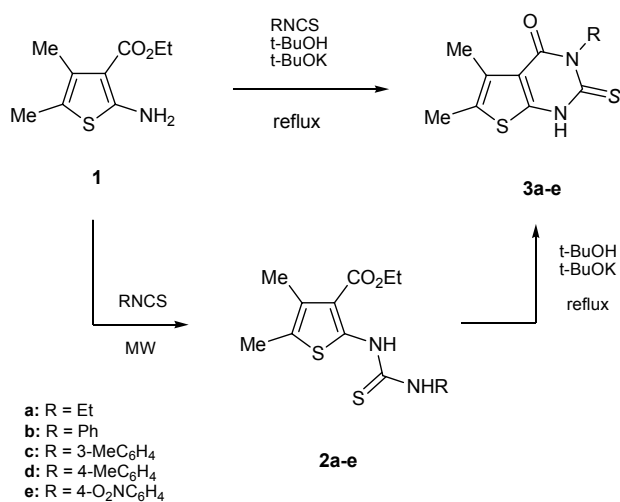
Scheme 1.

In conclusion, we have developed a facile method for the synthesis of 3-substituted-5,6-dimethyl-2-thioxo-2,3-dihydrothieno[2,3-d]pyrimidin-4(1H)-ones (**3a–e**) through cyclocondensation of ethyl 2-amino-4,5-dimethylthiophene-3-carboxylate (**1**) with isothiocyanates in *t*-butanol containing potassium *t*-butoxide as a base catalyst. Using microwave irradiation, the uncyclized intermediates **2a–e** were isolated.

EXPERIMENTAL

Melting points were measured on a Stuart Model SMP3 melting point apparatus. The IR spectra were obtained on a 4300 Shimadzu spectrophotometer as KBr disks. The ^{1}H NMR (100 MHz) spectra were recorded on a Bruker AC 100 spectrometer. The mass spectra were determined on a Shimadzu GCMS 17A instrument. Elemental analysis was performed on a Thermo Finnigan Flash EA micro-analyzer. Reactions were performed in a domestic microwave oven Model LG MS-543XD.

Preparation of 3-substituted-5,6-dimethyl-2-thioxo-2,3-dihydrothieno[2,3-d]pyrimidin-4(1H)-ones (**3a–e**). *General Procedure .Method A*. To a solution of the ethyl 2-amino-4,5-dimethyl-thiophene-3-carboxylate (**1**) (5 mmol) and potas-sium *t*-butoxide (2 mmol) in *t*-butanol (20 ml), the appropriate isothiocyanate (6 mmol) was added. The reaction mixture was heated under reflux for 6 hours. After the completion of the reaction (monitored by TLC, CHCl$_3$:MeOH = 93:7), the solvent was evaporated in vacuum, the residue was dissolved in water (15 ml) and subsequently neutralized by 1 N HCl. The crude product was collected and recrystallized from ethanol to give compounds **3a–e** in 75, 77, 68, 86 and 74% yields, respectively.

Method B. A mixture of ethyl 4,5-dimethyl-2-[(substituted carbamothioyl)amino]thiophene-3-car-boxylates (**2a–e**) (3 mmol) and potassium *t*-butoxide (1 mmol) in *t*-butanol (15 ml) was heated under reflux for 3 hours. After the completion of the reaction (monitored by TLC, CHCl$_3$:MeOH = 93:7), the solvent was evaporated in vacuum, the residue was dissolved in water (15 ml) and subsequently neutralized by 1 N HCl. The crude product was collected and recrystallized from ethanol to give compounds **3a–e** in 79, 78, 73, 91 and 75% yields, respectively.

3-Ethyl-5,6-dimethyl-2-thioxo-2,3-dihydrothieno-[2,3-d]pyrimidin-4(1H)-one (**3a**). M.p. 257–259°C; ^{1}H NMR (DMSO-*d*$_6$, δ ppm): 1.17 (t, 3H, J = 7 Hz, CH$_3$), 2.24 (s, 6H, 2CH$_3$), 4.36 (q, 2H, J = 7 Hz, CH$_2$), 13.45 (br, 1H, NH); IRS (KBr disc): ν 1684 (C=O), 3137 cm^{-1} (NH); MS, m/z: 240 (M$^+$); Analytically calculated for $C_{10}H_{12}N_2OS_2$: C 49.97; H 5.03; N 11.66; S 26.68. Found: C 50.24; H 5.21; N 11.35; S 26.91.

5,6-Dimethyl-3-phenyl-2-thioxo-2,3-dihydrothi-eno[2,3-d]pyrimidin-4(1H)-one (**3b**). M.p. 325–327°C; ^{1}H NMR (DMSO-*d*$_6$, δ ppm): 2.24 (s, 6H, 2CH$_3$), 7.0–7.6 (m, 5H, phenyl), 13.65 (s br, 1H, NH); IRS (KBr disc): ν 1703 (C=O), 3152 cm^{-1} (NH); MS, m/z: 288 (M$^+$); Analytically calculated for $C_{14}H_{12}N_2OS_2$: C 58.31; H 4.19; N 9.71; S 22.24. Found: C 58.67; H 3.98; N 9.50; S 22.45.

5,6-Dimethyl-3-(3-methylphenyl)-2-thioxo-2,3-dihydrothieno[2,3-d]pyrimidin-4(1H)-one (**3c**). M.p. 295–297°C; ^{1}H NMR (DMSO-d$_6$, δ ppm): 2.25 (s, 3H, CH$_3$), 2.29 (s, 6H, 2CH$_3$), 6.85–7.45 (m, 4H, arom-H), 13.61 (br, 1H, NH); IRS (KBr disc): ν 1709 (C=O), 3163 cm^{-1} (NH); MS, m/z: 302 (M$^+$); Analytically calculated for $C_{15}H_{14}N_2OS_2$: C 59.57; H 4.67; N 9.26; S 21.21. Found: C 59.28; H 4.89; N 9.51; S 20.97.

5,6-Dimethyl-3-(4-methylphenyl)-2-thioxo-2,3-dihydrothieno[2,3-d]pyrimidin-4(1H)-one (**3d**). M.p.

270°C (dec); ^{1}H NMR (DMSO-d_6, δ ppm): 2.24 (s, 3H, CH$_3$), 2.28 (s, 3H, CH$_3$), 2.34 (s, 3H, CH$_3$), 6.90–7.25 (overlapped doublets, 4H, arom-H), 13.60 (br, 1H, NH); IRS (KBr disc): ν 1703 (C=O), 3155 cm^{-1} (NH); MS, m/z: 302 (M$^+$); Analytically calculated for C$_{15}$H$_{14}$N$_2$OS$_2$: C 59.57; H 4.67; N 9.26; S 21.21. Found: C 59.34; H 4.46; N 9.48; S 21.43.

5,6-Dimethyl-3-(4-nitrophenyl)-2-thioxo-2,3-di-hydrothieno[2,3-d]pyrimidin-4(1H)-one (**3e**). M.p. 340–342°C; ^{1}H NMR (DMSO-d_6, δ ppm): 2.25 (s, 3H, CH$_3$), 2.32 (s, 3H, CH$_3$), 7.40–8.45 (overlapped doublets, 4H, arom-H), 13.68 (s br, 1H, NH); IRS (KBr disc): ν 1707 (C=O), 3170 cm^{-1} (NH); MS, m/z: 333 (M$^+$); Analytically calculated for C$_{14}$H$_{11}$N$_3$O$_3$S$_2$: C 50.44; H 3.33; N 12.60; S 19.24. Found: C 50.71; H 3.62; N 12.73; S 19.01.

Preparation of ethyl 4,5-dimethyl-2-[(substituted carbamothioyl)amino]thiophene-3-carboxylates (**2a**–**e**). *General Procedure*. A mixture of ethyl 2-amino-4,5-dimethylthiophene-3-carboxylate (**1**) (3 mmol) and the appropriate isothiocyanate (4 mmol) was subjected to microwave irradiation at 800 W for 2–3 min (4–5 times). After the completion of the reaction (monitored by TLC, CHCl$_3$:MeOH = 95:5) the crude product was recrystallized from ethanol to give compounds **2a**–**e** in high yields.

Ethyl 2-[(ethylcarbamothioyl)amino]-4,5-dime-thylthiophene-3-carboxylate (**2a**). Time 5×2 min; Yield 75%; m.p. 165–167°C; ^{1}H NMR (DMSO-d_6, δ ppm): 1.44 (t, 3H, J = 6.5 Hz, CH$_3$), 1.58 (t, 3H, J = 7 Hz, CH$_3$), 2.32 (s, 6H, 2CH$_3$), 4.41 (q, 2H, J = 6.5 Hz, CH$_2$), 4.52 (q, 2H, J = 7 Hz, CH$_2$), 9.62 (br, 1H, NH), 11.80 (br, 1H, NH); IRS (KBr disc): ν 1651 (C=O), 3215, 3299 cm^{-1} (two NH); MS, m/z: 286 (M$^+$); Analytically calculated for C$_{12}$H$_{18}$N$_2$O$_2$S$_2$: C 50.32; H 6.33; N 9.78; S 22.39. Found: C 50.05; H 6.11; N 10.06; S 22.21.

Ethyl 4,5-dimethyl 2-[(phenylcarbamothioyl)-amino]thiophene-3-carboxylate (**2b**). Time 4×3 min; Yield 90%; m.p. 170–172°C; ^{1}H NMR (DMSO-d_6, δ ppm): 1.22 (t, 3H, J = 7 Hz, CH$_3$), 2.17 (s, 6H, 2CH$_3$), 4.20 (q, 2H, J = 7 Hz, CH$_2$), 7.0–7.6 (m, 5H, phenyl), 10.91 (s, 1H, NH), 11.79 (s, 1H, NH); IRS (KBr disc): ν 1664 (C=O), 3175, 3282 cm^{-1} (two NH); MS, m/z: 334 (M$^+$); Analytically calculated for C$_{16}$H$_{18}$N$_2$O$_2$S$_2$: C 57.46; H 5.42; N 8.38; S 19.17. Found: C 57.78; H 5.19; N 8.64; S 18.98.

Ethyl 4,5-dimethyl-2-{[(3-methylphenyl)carb-amothioyl]amino}thiophene-3-carboxylate (**2c**). Time 5×3 min; Yield 84%; m.p. 168–169°C; ^{1}H NMR (DMSO-d_6, δ ppm): 1.48 (t, 3H, J = 7.5 Hz, CH$_3$), 2.30 (s, 6H, 2CH$_3$), 2.47 (s, 3H, CH$_3$), 4.37 (q, 2H, J = 7.5 Hz, CH$_2$), 7.1–7.6 (m, 4H, arom-H),

228

11.12 (s, 1H, NH), 12.10 (s, 1H, NH); IRS (KBr disc): ν 1659 (C=O), 3165, 3180 cm^{-1} (two NH); MS, m/z: 348 (M$^+$); Analytically calculated for C$_{17}$H$_{20}$N$_2$O$_2$S$_2$: C 58.59; H 5.78; N 8.04; S 18.40. Found: C 58.94; H 6.01; N 7.81; S 18.59.

Ethyl 4,5-dimethyl 2-{[(4-methylphenyl)-carba-mothioyl]amino}thiophene-3-carboxylate (**2d**). Time 4×3 min; Yield 89%; m.p. 165–167°C; ^{1}H NMR (DMSO-d_6, δ ppm): 1.25 (t, 3H, J = 7 Hz, CH$_3$), 2.18 (s, 6H, 2CH$_3$), 2.29 (s, 3H, CH$_3$), 4.11 (q, 2H, J = 7 Hz, CH$_2$), 7.1–7.5 (overlapped doublets, 4H, arom-H), 10.89 (s, 1H, NH), 11.78 (s, 1H, NH); IRS (KBr disc): ν 1658 (C=O), 3178, 3200 cm^{-1} (two NH); MS, m/z: 348 (M$^+$); Analytically calculated for C$_{17}$H$_{20}$N$_2$O$_2$S$_2$: C 58.59; H 5.78; N 8.04; S 18.40. Found: C 58.81; H 5.54; N 7.87; S 18.73.

Ethyl 4,5-dimethyl 2-{[(4-nitrophenyl)carba-mothioyl]amino}thiophene-3-carboxylate (**2e**). Time 5×3 min; Yield 78%; m.p. 213–215°C; ^{1}H NMR (DMSO-d_6, δ ppm): 1.26 (t, 3H, J = 7 Hz, CH$_3$), 2.22 (s, 6H, 2CH$_3$), 4.30 (q, 2H, J = 7 Hz, CH$_2$), 7.7–8.4 (overlapped doublets, 4H, arom-H), 11.61 (s, 1H, NH), 12.08 (s, 1H, NH); IRS (KBr disc): ν 1654 (C=O), 3184, 3205 cm^{-1} (two NH); MS, m/z: 379 (M$^+$); Analytically calculated for C$_{16}$H$_{17}$N$_3$O$_4$S$_2$: C 50.64; H 4.52; N 11.07; S 16.90. Found: C 50.35; H 4.77; N 10.79; S 16.62.

REFERENCES

1. U. S. Pathak, S. Singh, J. Padh, *Indian J. Chem. Sec. B.*, **30B**, 618 (1991).
2. I. S. Rathod, A. S. Pillai, V. S. Shirsath, *Indian J. Heterocycl. Chem.*, **10**, 93 (2000).
3. CA **95**, 115592y (1981).
4. I. A. Kharizomenova, A. N. Grinev, N. V. Samsonova, E. K. Panisheva, N. V. Kaplina, I. S. Nikolaeva, T. V. Pushkina, G. N. Pershin, *Khim.-Farm. Zh.,* **15**, 40 (1981).
5. M. Perrissin, M. Favre, C. Luu-Duc, F. Bakri-Logeais, F. Huguet, G. Narcisse, *Eur. J. Med. Chem.-Chim. Ther.*, **19**, 420 (1984).
6. A. K. El-Ansary, A. H. Omar, *Bull. Fac. Pharm.*, **39**, 17 (2001).
7. U. S. Pathak, N. V. Gandhi, S. Singh, R. P. Warde, K. S. Jain, *Indian J. Chem. Sec. B.*, **31B**, 223 (1992).
8. CA **80**, 108567f (1974).
9. CA **80**, 70825y (1974).
10. CA **115**, 256224y (1991).
11. I. O. Donkor, H. Li, S. F. Queener, *Eur. J. Med. Chem.*, **38**, 605 (2003).
12. C. J. Shishoo, M. B. Devani, U. S. Pathak, S. Ananthan, V. S. Bhadti, G. V. Ullas, K. S. Jain, I. S. Rathod, D. S. Talati, N. H. Doshi, *J. Heterocycl. Chem.*, **21**, 375 (1984).
13. Z. Csuros, R. Soos, J. Palinkas, I. Bitter, *Acta Chim. (Budapest)*, **68**, 397 (1971).
14. F. Sauter, *Monatsh. Chem.*, **101**, 535 (1970).

15. H. Link, *Helv. Chim. Acta*, **73**, 797 (1990).
16. M. Bakavoli, A. Davoodnia, M. Rahimizadeh, M. M. Heravi, M. Ghassemzadeh, *J. Chem. Res. Synop.*, 178 (2002).
17. M. Bakavoli, A. Davoodnia, M. Rahimizadeh, M. M. Heravi, *Phosphorus, Sulfur, Silicon*, **177**, 2303 (2002).
18. M. Roshani, A. Davoodnia, M. Sh. Hedayat, M. Bakavoli, *Phosphorus, Sulfur, Silicon*, **179**, 1153 (2004).
19. A. Davoodnia, M. Bakavoli, A. Vahedinia, M. Rahimizadeh, M. Roshani, *Heterocycles*, **68**, 801 (2006).
20. A. Davoodnia, R. Zhiani, M. Roshani, M. Bakavoli, M. Bashash, *Phosphorus, Sulfur, Silicon*, **182**, 1219 (2007).
21. A. Davoodnia, M. Momen-Heravi, E. Golshani, M. Bakavoli, L. Dehabadi, *J. Chem. Res.*, 257 (2007).
22. A. Davoodnia, M. Bakavoli, M. Bashash, M. Roshani, R. Zhiani, *Turk. J. Chem.*, **31**, 599 (2007).
23. A. Davoodnia, M. Bakavoli, N. Pooryaghoobi, M. Roshani, *Heterocycl. Commun.*, **13**, 323 (2007).
24. A. Davoodnia, M. Bakavoli, Sh. Mohseni, N. Tavakoli-Hoseini, *Monatsh. Chem.*, **139**, 963 (2008).
25. A. Davoodnia, R. Zhiani, N. Tavakoli-Hoseini, *Monatsh. Chem.*, in press.
26. A. Davoodnia, M. Bakavoli, Gh. Barakouhi, N. Tavakoli-Hoseini, *Chin. Chem. Lett.*, **18**, 1483 (2007).
27. A. Davoodnia, H. Behmadi, A. Zare-Bidaki, M. Bakavoli, N. Tavakoli-Hoseini, *Chin. Chem. Lett.*, **18**, 1163 (2007).
28. A. Davoodnia, H. Eshghi, A. Salavaty, N. Tavakoli-Hoseini, *J. Chem. Res.*, 1 (2008).
29. K. Gewald, *Chem. Ber.*, **98**, 3571 (1965).
30. A. Davoodnia, M. Bakavoli, F. Khorramdelan, M. Roshani, *Indian J. Heterocycl. Chem.*, **16,** 147 (2006).
31. A. Davoodnia, M. Rahimizadeh, Sh. Rivadeh, M. Bakavoli, M. Roshani, *Indian J. Heterocycl. Chem.*, **16**, 151 (2006).
32. A. Davoodnia, M. Roshani, E. Saleh Nadim, M. Bakavoli, N. Tavakoli-Hoseini, *Chin. Chem. Lett.*, **18**, 1327 (2007).
33. A. Davoodnia, M. Roshani, S. H. Malaeke, M. Bakavoli, *Chin. Chem. Lett.*, **19**, 525 (2008).

СИНТЕЗА НА 2-ТИОКСО-2,3-ДИХИДРОТИЕНО[2,3-d]ПИРИМИДИН-4(1Н)-ОНИ ЧРЕЗ БАЗИЧНА КАТАЛИЗА И ИЗОЛИРАНЕ НА МЕЖДИННИ СЪЕДИНЕНИЯ С ИЗПОЛЗВАНЕ НА МИКРОВЪЛНОВО ОБЛЪЧВАНЕ

А. Давудниа*, М. Бакаволи, Н. Зариеи, Н. Таваколи-Хосейни

Департамент по химия, Училище по науки, Ислямски университе Азад, Отдел Машхад, Машхад 91735-413, Иран

(Резюме)

Предложен е прост и бърз метод за синтезата на 3-заместени-5,6-диметил-2-тиоксо-2,3-дихидротиено[2,3-d]пиримидин-4(1Н)-они чрез циклокондензация на 2-амино-4,5-диметилтиофен-3-карбоксиетилат с изотиоцианати чрез базична катализа. Нециклизиралите междинни продукти 4,5-диметил-2-[(заместени карбаматотиоил)амино]тиофен-3-карбоксилати са изолирани когато реакциите се провеждат при микровълново облъчване. Тези междинни продукти впоследствие циклизират в *t*-бутанол в присъствие на калиев *t*-бутоксид при нагряване с обратен хладник до получаване на желаните бициклични продукти.

Simultaneous determination of trace amounts of thorium and zirconium using spectrophotometric partial least-squares calibration method

H. R. Pouretedal[1,*], B. Shafiee[2], M. H. Keshavarz[1]

[1] *Chemistry Department, Malek-ashtar University of Technology, Shahin-shahr, I. R. Iran*
[2] *Islamic Azad University, Shahreza Branch, I. R. Iran*

A new, attractive and applicable method, based on spectrophotometic partial least-squares procedure, was proposed for simultaneous determination of thorium and zirconium using SPADNS as a colour reagent. Absorbance measurements were made in the interval of 541–620 nm with 1.0 nm steps in buffered solutions at pH 3.5. The linear dependences were obtained in the ranges of 0.5–11.5 and 1.5–14.5 $\mu g \cdot ml^{-1}$ for Th^{4+} and Zr^{4+} ions, respectively. The limits of detection were determined 0.4 and 1.2 $\mu g \cdot ml^{-1}$ for thorium and zirconium, respectively. The standard deviation (n = 3) and recovery percentage of 10 samples in the prediction set were obtained in the range 0.22–0.38 $\mu g \cdot ml^{-1}$ and 91.3–109.2, respectively. The proposed method was used for simultaneous determination of mentioned ions in spiked real water samples and wastewater of AENTC. The satisfactory results showed that the method was applicable to the analysis of samples with similar matrix.

Key words: thorium, zirconium, spectrophotometic determination, SPADNS.

INTRODUCTION

For a number of reasons, spectral measurement is one of the powerful methods in quantitative analysis of chemical mixtures. It is relatively easy to generate good data in short time by proper using of spectroscopy. However, getting useful results from a set of spectral data is not always straightforward. Determining the amounts of the components of a mixture can often be problematic without a prior separation steps because of the overlap of spectral response. For this reason, the analysts have increasingly turned to chemometrics in dealing with spectral data [1].

Quantitative spectrophotometry has been greatly improved by the use of variety of multivariate statistical methods such as classical least square (CLS), inverse least squares (ILS), principal component regression (PCR), and partial least squares (PLS). Multivariate calibrations are effective in spectrophotometric analysis because the simultaneous inclusion of multiple spectral intensities can greatly improve the precision and applicability. The widespread use of these methods is due to the proliferation of commercial software for laboratory computers and detectors, capable of recording full spectra very rapidly [2–4].

Partial least-squares modelling is a powerful multivariate analysis of spectroscopic data. PLS is capable of being a full spectrum method such as principal component regression and classical least squares. It has also characteristics and the advantages of inverse least-squares method, which is limited in the number of spectral frequencies that can be included in the analysis. The use of PLS method in chemical analysis was pioneered by Wold and co-workers [5]. A particularly detailed study of multivariate calibration by PLS was carried out for spectrophotometric determination of metals [6–11].

Heavy metal ions represent a major environmental problem and their detection and monitoring in waste water outlets, rivers, reservoirs or sources of drinking water is necessary [12]. Thorium is a naturally occurring element that has a number of industrial and medical applications. It is present in very small quantities in virtually all rocks, soils, waters, plants and animals. Where high concentrations occur in rock, thorium can be mined and refined, producing waste products such as mill tailings. If not properly controlled, wind and water can introduce the tailings into the wide environment [13]. Zirconium is used in a wide range of applications including nuclear caps, catalytic converters, surgical appliances, metallurgical furnaces, superconductors, ceramics, lamp filaments, anti-corrosive alloys and photographical purposes. Hence, nanogram level determinations of zirconium are critically important [14, 15].

However, there are few reports on the determination of zirconium and thorium simultaneously. Although strong claims are made for the specificity

---

* To whom all correspondence should be sent:
E-mail: HR_POURETEDAL@mut-es.ac.ir

and sensitivity of NAA, ICP-AES and ICP-MS, some interference causes a problem using this method [16]. Therefore, spectrophotometric methods for thorium and rare earth continue to be of interest [17–20].

UV-Vis spectrophotometric techniques, due to both the simplicity and rapidness of the method, are the most widely used analytical methods in multi-component analysis [21–24]. However, the simultaneous determination of thorium and zirconium ions by the use the traditional spectrophotometry technique is difficult because, the absorption region and the superimposed curves are not suitable for quantitative evaluation. There is a serious problem in most complex samples spectral overlap because the information for each component obtained from the overlapping spectra is very limited and the condition number of the absorbance coefficient matrix is too large to give satisfactory results. In most cases of analysis of complex samples, physical separation and non-standard instrumentation are required. Spectrophotometric techniques as well as chemometrics methods have been recently used to solve these problems [9, 10, 25–27].

In this work, a spectrophotometric method based on using partial least-squares multivariate calibration is proposed for simultaneous determination of Th(IV) and Zr(IV) ions in synthetic and real samples. The method is based on the reaction between these ions with SPADNS as chromogenic reagent at pH 3.5.

EXPERIMENTAL

Reagent

All of the chemicals used were analytical reagent grade of purity. Doubly distilled water was used throughout. Standard solutions of Th(IV) and Zr(IV) ($1000 \ \mu g \cdot ml^{-1}$) were made using $Th(NO_3)_4 \cdot 6H_2O$ in 0.1 M HNO_3 and $ZrOCl_2 \cdot 8H_2O$ in 2.0 M HCl, respectively (Merck Co.). The diluted Th(IV) and Zr(IV) solutions were prepared with dilution of stock solutions. A 1.5×10^{-3} M solution of SPADNS as sodium salt was prepared and used daily. Adjusting the pH values of the working solution was carried out using acetic acid and sodium acetate solutions. The foreign ions were introduced using their suitable salts having analytical grade of purity.

Apparatus

A portable 100 UV-Vis scanning spectrophotometer was used to record the absorbance spectra of Th–SPADNS and Zr–SPADNS complexes with a 1.0 cm path length quartz cell. The cell temperature

is controlled by circulating water around the cell by thermostat. The slit width was set at 2 nm and a fast scan speed at 600 nm /min was used. The spectra were recorded between 400 and 700 nm at 1 nm scanning intervals. A Metrohm 691 pH meter equipped with combined glass electrode was used for measurement of the pH. The computations were performed on a Pentium IV computer. All the programs in the computing process were written in MATLAB® for Windows.

Procedure

Individual calibration. In order to obtain the calibration curve for each element as an analyte, 1.0 ml of 1.5×10^{-3} M SPADNS as reagent, 2.0 ml of buffer with pH 3.5 and appropriate amounts of the metal ion solution were added to 10 ml volumetric flask and made up to the mark with doubly distilled water. The concentrations of Th(IV) and Zr(IV) ions were 0.50–11.50 and 1.50–14.50 $\mu g \cdot ml^{-1}$, respectively, that means the proposed method is a valuable method for simultaneous determination of Th^{4+} and Zr^{4+} in a sample. The absorbances were measured at 580 nm, against a reagent blank for thorium and zirconium ions, respectively.

PLS calibration. To a series of 10 ml volumetric flasks, 1.0 ml of 1.5×10^{-3} M SPADNS as reagent and 2.0 ml of buffer with pH 3.5 were added. The appropriate amounts of each metal ion containing 5.0–115.0 μg of Th(IV) and 15.0–145.0 μg of Zr(IV) were also added and the solutions were made up to the mark with distilled water. These solutions were used for preparation of data sets of calibration and prediction in PLS multivariate calibration method. Excess concentration of SPADNS has been applied to ensure quantitative formation of the complexes in the whole range of calibration. The absorbance of the solutions was measured in the range of 561–640 nm with 1.0 nm steps and therefore 80 experimental points (λ) per spectrum were obtained.

RESULTS AND DISCUSSION

SPADNS or (4,5-dihydroxy-3-(*p*-sulphophenyl-azo)-2,7-naphthalene disulphonic acid, trisodium salt) can be used as an indicator for determination of zirconium and thorium [28]. The complexes stoichiometry of Th(IV)–SPADNS and Zr(IV)–SPADNS is 1:1 and 2:1, respectively. Both normal absorption spectra of Th–SPADNS and Zr–SPADNS complexes show maximum absorption (λ_{max}) value at 580 nm; whereas the free ligand has λ_{max} at 510 nm (Fig. 1).
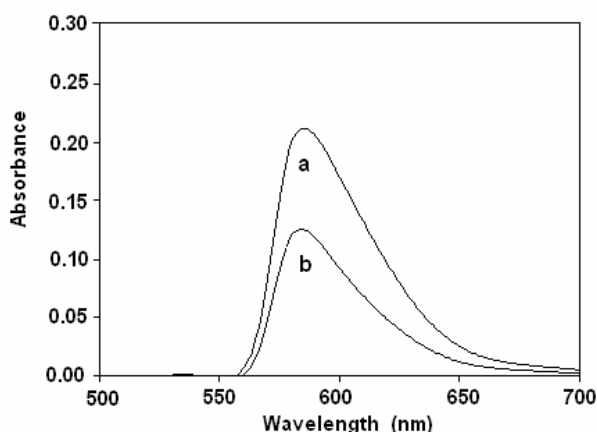
Fig. 1. Absorbance spectra of (a) Th–SPADNS and (b) Zr–SPADNS against reagent blank. Conditions: C_{SPADNS} 1.5×10^{-4} M, C_M 2 µg·ml^{-1}, pH 3.5 and t 25°C.

Therefore, a calibration curve was obtained with absorbance measurement of standard solutions of metal complex versus concentration of each metal ion. As it is seen in Fig. 1, since there is overlapping of obtained spectra in the amplitude 560–640 nm, the presence of each metal ion is interfered in measurement of the other ion. Thus, multivariate calibration such as partial-least squares method can be used to determine two analytes in a mixture sample.

Assay conditions, such as pH of the solutions, were investigated for optimization. The effect of pH on the spectrum of each complex was studied separately in the pH range of 2.0–5.0. The absorbance of each complex solution at a constant concentration of metal ion was measured at its λ_{max} and as a function of pH. In the case of both formed complexes, the absorbance of solutions increased up to pH 3.5, then diminished in the pH above 3.5 for Th–SPADNS, whereas, the absorbance of Zr–SPADNS decreased in the pH above 4.5. Therefore, the pH value of 3.5 of acetate buffer was selected as an optimum pH for simultaneous determination of Th^{4+} and Zr^{4+} ions. This pH was achieved via addition of 2.0 ml of buffer solution (pH 3.5) per 10 ml of final solution. Excess concentration of SPADNS (1.5×10^{-4} M) has been applied to ensure quantitative formation of the complexes in the whole range of calibration.

Single component calibration. In order to find the linear range of concentration of each metal ion, single component calibration was performed for each analyte. In a 10 ml volumetric flask, 1.0-ml SPADNS 1.5×10^{-3} M, 2.0 ml acetate buffer 3.5 and different volumes of 100 µg·ml^{-1} solution of thorium(IV) ion were added and diluted to the mark with distilled water. The absorbance of the thorium(IV) ion standard solutions was measured at

λ_{max} of Th–SPADNS complex (580 nm). The same procedure was followed for zirconium and the absorbance of the solutions was monitored at 580 nm. The linear dependences were obtained in the ranges of 0.50–11.50 and 1.50–14.50 µg·ml^{-1} for Th^{4+} and Zr^{4+} ions, respectively. The R^2 values for thorium and zirconium calibration curves were obtained to be 0.9987 and 0.9981, respectively. The limits of detection were also determined 0.4 and 1.2 µg·ml^{-1} for thorium and zirconium, respectively.

Two components calibration. The calibration set contains 30 standard solutions. The compositions of the calibration mixtures were selected, randomly, in the amplitude of calibration curve of each analyte. For preparation of each solution, different volumes of two analyte solutions (25 µg·ml^{-1}) were added to 1.0 ml of SPADNS 1.5×10^{-3} M and 2.0 ml of acetate buffer 3.5 in a 10 ml volumetric flasks. The concentration of each cation was in the linear range of the cation in single component calibration. The calibration matrix used for the analysis is presented in Table 1. After 5 min, the absorption spectra of the prepared solutions were recorded.

Table 1. Concentration of the components (µg·ml^{-1}) in the calibration set.

No.	Th(IV)	Zr(IV)	No.	Th(IV)	Zr(IV)	No.	Th(IV)	Zr(IV)
1	0.50	1.50	11	10.50	4.00	21	5.50	5.50
2	1.50	3.00	12	11.50	6.00	22	7.50	7.50
3	2.50	4.50	13	1.00	12.00	23	9.50	9.50
4	3.50	6.00	14	3.00	10.00	24	11.50	11.50
5	4.50	7.50	15	5.00	8.00	25	11.50	14.50
6	5.50	9.00	16	7.00	6.00	26	8.50	10.00
7	6.50	10.50	17	9.00	4.00	27	6.50	8.00
8	7.50	12.00	18	11.00	2.00	28	4.50	6.00
9	8.50	13.50	19	1.50	1.50	29	2.50	4.00
10	9.50	2.00	20	3.50	3.50	30	1.50	2.00

Selection of the number of factors. The selection of the number of the factors in the PLS algorithm is very important to achieve the best prediction. The number of factors was estimated in the PLS1 by cross-section validation method, leaving out one sample at a time and plotting the prediction residual sum of squares (PRESS) versus the number of factors for each individual component [29–31]. Predictive residual error sum of squares (PRESS) was computed using the following equation:

$$PRESS = \sum (C_{true,i} - C_{pred,i})^2$$

Where, $C_{true,i}$ is the known concentration for ith sample and $C_{pred,i}$ represents the concentration predicted by the model. The PLS calibrations were performed based on the 29 spectra out of 30 calibration spectra. The components in the sample left out during calibration were predicted using this

calibration. This process was repeated 30 times and in each step of calibration, one sample was left out. The prediction residual sum of squares was calculated by comparing the predicted concentration of components in each sample with known concentration of components in standard solutions. To optimize the number of factors, the F-statistic with F-ratio probability of 0.75 was used. The optimum number of factors was selected for the first PRESS values the F-ratio probability, which drops down below 0.75. The Fig. 2 shows, the PRESS obtained by optimizing the calibration matrix of the absorbance data with PLS. The optimal number of factors for thorium and zirconium was obtained to be 5 and 6, respectively.

Statistical parameters. To evaluate prediction ability of a multivariate calibration model, the root mean square error of prediction (*RMSEP*), the square of the correlation coefficient (R^2) and relative standard error of prediction (*RSEP*) can be used.

$$RMSEP = \sqrt{\sum_{i=1}^{n}(C_{pred} - C_{true})^2 / n}$$

$$R^2 = \sum_{i=1}^{n}(C_{pred} - \overline{C}_{true})^2 / \sum_{i=1}^{n}(C_{true} - \overline{C}_{true})^2$$

$$RSEP(\%) = 100 \times \sqrt{\sum_{i=1}^{n}(C_{pred} - C_{true})^2 / \sum(C_{true})^2}$$

where C_{pred} is the predicted concentration in the sample, C_{true} is the true value of the concentration in the sample, $\overline{C}_{true}$ is the mean true value of the concentration in the sample and n is the number of samples in the prediction test.
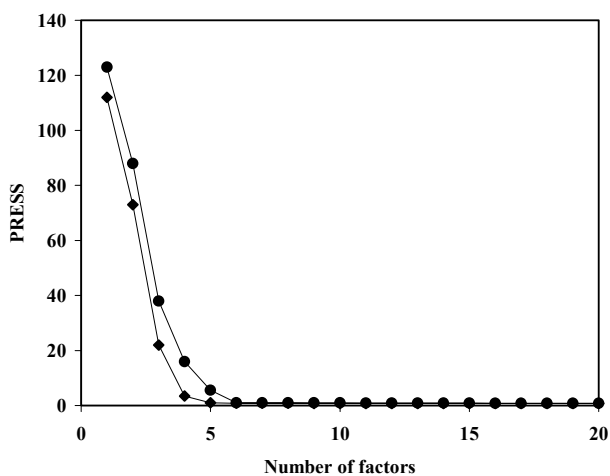
Simultaneous determination of thorium and zirconium was made on the 10 synthetic test samples by the proposed method. Figs. 3 and 4 show plots of predicted concentrations *versus* true concentrations using the optimized model. Predicted results and their recovery percentage are given in Table 2.

Table 2. Concentration of the components ($\mu g \cdot ml^{-1}$) in the prediction set, predicted values and recovery percent.

No	True value		Predicted value[a]		Recovery, %	
	Th(IV)	Zr(IV)	Th(IV)	Zr(IV)	Th(IV)	Zr(IV)
1	0.50	1.50	0.52 ± 0.25	1.37 ± 0.25	104.0	91.3
2	1.50	3.00	1.53 ± 0.27	2.96 ± 0.24	102.0	98.7
3	1.50	10.00	1.60 ± 0.22	10.92 ± 0.28	107.0	109.2
4	4.00	3.00	3.86 ± 0.28	3.06 ± 0.31	96.5	102.0
5	4.00	12.00	4.16 ± 0.25	11.96 ± 0.25	104.0	99.7
6	10.00	2.50	10.28 ± 0.38	2.33 ± 0.27	102.8	93.2
7	10.00	10.00	9.78 ± 0.25	10.10 ± 0.25	97.8	101.0
8	5.00	1.50	5.36 ± 0.26	1.60 ± 0.30	107.2	106.7
9	5.00	8.00	5.42 ± 0.33	7.77 ± 0.28	108.4	97.1
10	11.50	14.50	11.28 ± 0.25	14.24 ± 0.35	98.00	98.2

[a] Mean ± S.D. (n = 3)

y = 0.986x + 0.1531
R^2 = 0.9967

Fig. 3. Plots of predicted concentration *versus* true concentration for Th(IV) ion in the prediction set.

y = 1.0078x - 0.0206
R^2 = 0.9953

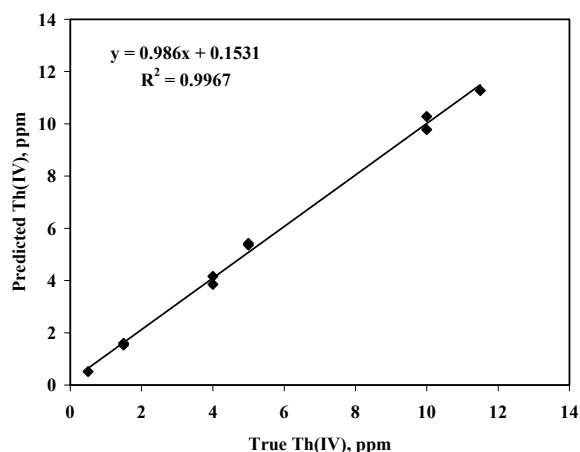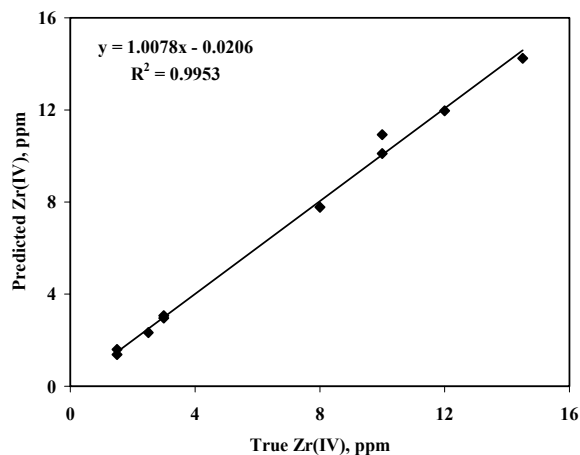Fig. 4. Plots of predicted concentration *versus* true concentration for Zr(IV) ion in the prediction set.

Fig. 2. Plot of PRESS *versus* number of factors: (♦) Th(IV) and (●) Zr(IV).

Table 3. Statistical parameters of the test matrix.

Analyte	No. of factors	RMSEP	R^2	RSEP, %
Th(IV)	5	0.0448	0.9967	2.18
Zr(IV)	6	0.0535	0.9953	1.18

Table 4. Tolerance limits for the diverse ions in the determination of Th(IV) and Zr(IV) ions.

Interfere ion	Tolerance limit (w_{Ion}/w_M)
Li^+, Ag^+, K^+, NH_4^+, Mg^{2+}, Sr^{2+}, Ba^{2+}, Ca^{2+}, HCO_3^-, I^-, Br^-, Cl^-, F^-, NO_3^-, NO_2^-, $S_2O_8^{2-}$, SO_4^{2-}, SCN^-, $S_2O_3^{2-}$, IO_3^-, ClO_3^-	1000
Hg^{2+}, Ti(IV), Mo(VI), Cr(VI), Mn(VII)	500
Cr^{3+}, Sn^{4+}, Sn^{2+}, Ti(III), V(IV), V(V)	100
Mn^{2+}, Co^{2+}, Ni^{2+}, Zn^{2+}, Cu^{2+}, Cd^{2+}, Pb^{2+}, Bi^{3+}, HPO_4^{2-}, $H_2PO_4^-$	50
Fe^{2+}, PO_4^{3-}	10
F^-, Fe^{3+}, Al^{3+}	1

Table 5. Analysis of real samples.

Sample	Spiked, μg/ml [a]		Found, μg/ml [b]		Recovery, %	
	Th(IV)	Zr(IV)	Th(IV)	Zr(IV)	Th(IV)	Zr(IV)
Tap water	5.0	5.0	5.2 ± 0.2 (5.1± 0.2)[c]	4.8 ± 0.3 (4.7 ± 0.1)	104.0	96.0
River water	5.0	5.0	4.9 ± 0.3 (4.9 ± 0.2)	5.3 ± 0.1 (4.9 ± 0.3)	98.0	106.0
Spring water	5.0	5.0	4.8 ± 0.3 (4.9 ± 0.2)	4.6 ± 0.2 (4.7 ± 0.3)	96.0	92.0
Waste water of AENTC[d]			240 ± 6 (245 ± 5)	195 ± 4 (198 ± 4)		

[a] Thorium and zirconium were not detected prior to spiking samples using AAS method; [b] Proposed method and mean ± S.D. (n = 3); [c] AAS; [d] The actual amounts of Th and Zr are 250 and 200 μg/ml, respectively.

The standard deviation and recovery percentage of 10 samples in the prediction set were obtained in the range 0.22–0.38 μg·ml^{-1} and 91.3–109.2, respectively. Also, the values of *RMSEP*, R^2, *RSEP* (%) and number of factors according to the obtained results for prediction test are summarized in Table 3.

Effect of foreign ions. The interference by several cations and anions on the determination of two components (5 μg·ml^{-1}) has been investigated by multivariate calibration method. The tolerance limit for each foreign ion is obtained when its presence at tested weight ratio produced a variation in concentration of analytes lower than 5%. The results (Table 4) indicate that the most of the cations and anions did not show any significant spectral interference at weight ratio greater than 1000. The most interfering ions are F^-, Fe^{3+} and Al^{3+} ions.

Application of the method. The proposed method was successfully applied to determination of thorium and zirconium in several real water spiked samples and wastewater of AENTC after dilution (Table 5). Thorium and zirconium were not detected prior to spiking samples using AAS (atomic absorption spectroscopy) method. As it is seen from Table 5, good recovery and low standard deviation was obtained by the PLS method using absorbance data. Therefore, this proposed method can be used for the analysis of samples of similar matrix, effectively.

CONCLUSION

Thorium(IV) and zirconium(IV) have chemical properties which can interfere with each other in their determination. For example, in spectrophotometric methods using colour reagents for complex formation with these elements, a high spectral overlapping can be observed between the absorption spectra of these components. Thus, there are reliable

234

methods for simultaneously determination of these elements in the real samples. However, the partial least-squares (PLS) method shows two advantages in this work: (i) it is applicable to analysis of two analyte in a sample; (ii) there is not need of pretreatment in complex samples.

REFERENCES

1. K. S. Booksh, B. R. Kowalski, *Anal. Chem,.* **66**, 782 A (1994).
2. B. Kuswandi, A. Vaughan, R. Narayanaswamy, *Anal. Sci.,* **17**, 181 (2001).
3. Y. Ni, *Anal. Chim. Acta,* **284**, 199 (1993).
4. E. Marengo, M. C. Gennaro, D. Giacosa, C. Abrigo, G. Saini, M. T. Avignone, *Anal. Chim. Acta*, **317**, 53 (1995).
5. S. Wold, M. Sjostrom, L. Eriksson, *Chemom. Intell. Lab. Syst.,* **58**, 109 (2001).
6. A. Abdollahi, M. Shariat Panahi, M. R. Khoshayand, *Iranian J. Pharm. Res.,* 207 (2007).
7. A. Lorber, L. Wangen, B. R. Kiwalski, *J. Chemom.,* **1**, 19 (1986).
8. D. M. Haaland, E. V. Thomas, *Anal. Chem.,* **60**, 1193 (1988).
9. J. Ghasemi, Sh. Ahmadi, K. Torkestani, *Anal. Chim. Acta,* **487**, 181 (2003).
10. A. Safavi, H. Abdollahi, M. Mirzajani, *Spectrochim. Acta A,* **63**, 196 (2006).
11. G. Absalane, M. Nekoeinia, *Anal. Chim. Acta,* **531**, 293 (2005).
12. S. Dhara, N. L. Misra, K. D. S. Mudher, S. K. Aggarwal, *Spectrochim. Acta B,* **62**, 82 (2007).
13. A. Safavi , M. Sadeghi, *Anal. Chim. Acta,* **567**, 184 (2006).
14. A. Abbaspour, L. Baramakeh, *Spectrochim. Acta A,* **64**, 477 (2006).
15. M. B. Gholivand, A. Babakhanian, M. Joshaghani, *Anal. Chim. Acta,* **584**, 302 (2007).
16. C. J. Kantipuly, A. D. Westland, *Talanta,* **35**, 1 (1988).

17. S. Ishimaru, R. Kuroda, *Anal. Sci.,* **6**, 613 (1990).
18. S. Ku, N. Obarski, Z. Marczenko, *Anal. Sci,.* **8**, 213 (1992).
19. L. Silverman, D. W. Hawley, *Anal. Chem.,* **28**, 806 (1956).
20. A. S. Amin, T. Y. Mohammed, *Talanta,* **54**, 611 (2001).
21. H. R. Pouretedal, M. Rafat, *Chinese J. Chem. Soc.,* **54**, 157 (2007).
22. H. R. Pouretedal, M. H. Keshavarz, *Chinese J. Chem.,* **24**, 557 (2006).
23. J. H. Kalivaz, *Anal. Chim. Acta,* **428**, 31 (2001).
24. J. Gasemi, R. Amini, A. Niazi, *Anal. Lett.,* **35**, 533 (2002).
25. H. Martens, T. Naes, Multivariate Calibration, Wiley, Chichester, 1989.
26. K. R. Beebe, A. R. Kowalski, *Anal. Chem.,* **59**, 1007A (1987).
27. A. Safavi, M. Mirzaee, A. Abdollahi, *Anal. Lett.,* **36**, 699 (2003).
28. G. Banerjee, *Fresenius' J. Anal. Chem.,* **146**, 417 (1955).
29. M. E. Diaz Garcia, A. Sanz Medel, *Talanta,* **33**, 255 (1986).
30. G. Jin, W. Zhu, W. Jiang, B. Xie, B. Cheng, *Analyst,* **122**, 263 (1997).
31. D. M. Halaand, E. V. Thomas, *Anal. Chem.,* **60**, 1193 (1988).

ЕДНОВРЕМЕННО СПЕКТРОФОТОМЕТРИЧНО ОПРЕДЕЛЯНЕ НА СЛЕДИ ОТ ТОРИЙ И ЦИРКОНИЙ ЧРЕЗ ЧАСТИЧЕН МЕТОД НА НАЙ-МАЛКИТЕ КВАДРАТИ

Х. Р. Пуретедал[1,*], В. Шафии[2], М. Х. Кешаварз[1]

[1] *Департамент по химия, Технологичен уверситет Малек-аштар, Шахин-шахр, Ислямска република Иран*
[2] *Ислямски университет Азад, Отдел Шахреза, Ислямска република Иран*

(Резюме)

Предложен е нов спектрофотометричен метод, основаващ се на процедурата на най-малките квадрати, за едновременно определяне на торий и цирконий с реагент SPADNS. Абсорбционните измервания са проведени в интервала 541–620 nm при стъпка 1.0 nm в буферен разтвор с pH 3.5. Получени са линейни зависимости в областите 0.5–11.5 и 1.5–14.5 $\mu g \cdot ml^{-1}$ съответно за Th^{4+} и Zr^{4+}. Границите на откриване са 0.4 и 1.2 $\mu g \cdot ml^{-1}$, стандартното отклонение (n = 3) е 0.22–0.38 $\mu g \cdot ml^{-1}$ и процентният добив от 10 образци е 91.3–109.2% съответно за торий и цирконий. Предлаганият метод е използван за едновременно определяне на посочените йони в дотирани реални проби от вода, както и в отпадни води. Задоволителните резултати показват, че методът е приложим за анализ на образци с подобен състав.

An efficient one-pot synthesis of α-aminophosphonic acid esters from Schiff bases using sodium ethoxide as a catalyst (Pudovik reaction) and their bio-activity

Ch. Mohan[1], C. N. Raju[1]*, A. J. Rao[1], R. U. N. Lakshmi[2]

[1] Department of Chemistry, Sri Venkateswara University, Tirupati, India
[2] Department of Botany, Sri Venkateswara University, Tirupati, India

Synthesis of novel α-aminophosphonic acid esters was achieved through a one-pot two-step reaction process (Pudovik reaction). In the first step tryptophan methyl ester is reacted with substituted aromatic aldehydes in absolute ethanol to form Schiff bases. In the second step, these are treated with dialkyl/diaryl phosphites *in situ* using sodium ethoxide as a catalyst at refluxing temperature. The structures of these compounds were established by elemental analyses IRS, ^{1}H, ^{13}C, ^{31}P NMR and mass spectral data. All the title compounds exhibited moderate antimicrobial activity.

Key words: α-aminophosphonic acid esters, dialkyl/diaryl phosphites, aldehydes, tryptophan methyl ester, sodium ethoxide, antimicrobial activity.

INTRODUCTION

α-Aminophosphonic acid esters are an important class of compounds since they are structural analogues of the corresponding α-aminoacids [1]. Recently they have been receiving considerable attention due to their wide applications in the synthesis of phosphanopeptides [2]. The utilization of α-aminophosphonic acid esters as peptide mimics [3], haptens of catalytic antibodies [4], enzyme inhibitors [5], antibiotics and pharmacological agents [6] is also well established. Even though few synthetic approaches are available [7] for α-aminophosphonic acid esters, nucleophilic addition of dialkyl/diaryl phosphites to imines (Pudovik reaction) [8] is one of the most convenient methods. This method has been successfully used for the synthesis of title compounds.

Tryptophan itself is an important bio-active aminoacid [9], which undergoes enzymatic decarboxylation to tryptamine. It plays an important role in nerve functioning. Its hydroxy derivative is a well known antimigraine drug. Tryphtophan is phosphorylated in the present investigation to increase its bioactivity [10, 11].

RESULTS AND DISCUSSION

The synthesis of the title compounds (**5a–l**) was accomplished by the conversion of tryptophan methyl ester to the corresponding Schiff's base (**3**) by the reaction with the respective aldehydes. Compound **3** upon treatment with diphenyl/diethyl/dimethyl phosphite in the presence of catalytic amount of sodium ethoxide in absolute ethanol at reflux temperature for 4–5 hours afforded α-aminophosphonic acid esters (**5a–l**) in 72–82% yield. Thin layer chromatography was employed to monitor the reaction progress and to determine the purity of the products. All the title compounds (**5a–l**) were readily soluble in polar solvents and melted in the temperature range of 90–302ºC.

Absorption bands were present in the regions 3354–3413, 1200–1250, 951–957, 1175–1191, 737–748 and 1039–1094 cm^{-1} for –NH, P=O, P–O, O–C, P–C$_{(aliphatic)}$ and P–O–C$_{(aliphatic)}$ respectively [12], in compound **5a–l** (Table 1).

The ^{1}H NMR spectral data of compound **5a–l** are given in Table 2. The aromatic protons [13] of α-aminophosphonic acid esters showed a complex multiplet at δ 6.67–8.85. The P–C–H protons resonated as a multiplet [14] at δ 3.58–3.74 due to coupling with phosphorus and N–H. The N–H proton signals appeared at δ 2.94–3.75 (J = 6.5–8.8 Hz) as doublets and aromatic NH appeared at δ 10.73–10.90 as a singlet. These signals are confirmed by D$_2$O exchange spectral recording. The –CH$_2$ protons showed a doublet at δ 2.93–3.61 (J = 7.1–8.7 Hz) and –CH proton appeared at δ 3.55–3.64 as a multiplet and –COO–CH$_3$ as a singlet at δ 2.30–2.85. The proton signal of P–OCH$_2$–CH$_3$ appeared as a multiplet and P–OCH$_2$–CH$_3$ gave a triplet at δ 3.61–3.68 and 1.08–1.20 (J = 6.9–7.0 Hz) respect-ively. The P–OCH$_3$ appeared as a singlet at δ 2.31–2.50.

Table 1. Physical, analytical, infrared and ^{31}P NMR spectral data of **5a–l**.

Comp.	m. p., °C	Yield [a], %	Molecular formula	Elemental Analysis Found (Calc.), %			IRS λ_{max}, cm^{-1}						^{31}P NMR[b]
				C	H	N	–NH	P=O	P–O–C$_{aryl}$		P–C$_{(aliphatic)}$	P–O–C$_{(aliphatic)}$	
									P–O	O–C			
5a	249–251	72	C$_{21}$H$_{24}$N$_2$O$_5$PCl	55.89 (55.96)	5.26 (5.30)	6.15 (6.20)	3413	1203	-	-	745	1078	2.44
5b	278–280	76	C$_{23}$H$_{28}$N$_2$O$_5$PCl	57.60 (57.68)	5.81 (5.89)	5.78 (5.84)	3404	1230	-	-	746	1094	1.62
5c	300–302	74	C$_{31}$H$_{28}$N$_2$O$_5$PCl	64.65 (64.71)	4.87 (4.90)	4.77 (4.82)	3412	1227	951	1180	-	-	5.14
5d	115–117	80	C$_{21}$H$_{24}$N$_3$O$_7$P	54.58 (54.61)	5.18 (5.24)	9.07 (9.10)	3408	1201	-	-	747	1054	2.79
5e	120–122	82	C$_{23}$H$_{28}$N$_3$O$_7$P	56.37 (56.42)	5.70 (5.76)	8.47 (8.53)	3413	1208	-	-	737	1079	2.31
5f	109–111	79	C$_{31}$H$_{28}$N$_3$O$_7$P	63.47 (63.51)	4.76 (4.82)	7.12 (7.17)	3410	1203	957	1175	-	-	5.19
5g	117–119	79	C$_{21}$H$_{25}$N$_2$O$_6$P	58.25 (58.30)	5.77 (5.82)	6.40 (6.47)	3389	1211	-	-	746	1054	2.30
5h	114–116	80	C$_{23}$H$_{29}$N$_2$O$_6$P	59.91 (59.99)	6.25 (6.34)	6.01 (6.08)	3354	1250	-	-	747	1039	2.96
5i	120–122	78	C$_{31}$H$_{29}$N$_2$O$_6$P	66.86 (66.90)	5.19 (5.25)	4.97 (5.03)	3351	1249	955	1182	-	-	5.14
5j	95–97	78	C$_{23}$H$_{28}$N$_2$O$_5$P	62.22 (62.29)	6.29 (6.36)	6.25 (6.31)	3401	1220	-	-	743	1077	2.96
5k	90–92	77	C$_{25}$H$_{32}$N$_2$O$_5$P	63.55 (63.60)	6.78 (6.83)	5.83 (5.90)	3395	1200	-	-	746	1075	2.43
5l	91–93	76	C$_{33}$H$_{32}$N$_2$O$_5$P	69.75 (69.83)	5.60 (5.68)	4.87 (4.93)	3392	1219	954	1191	-	-	5.17

a - After one crystallization;   b - Recorded in DMSO-d_6.

Sheme 1.
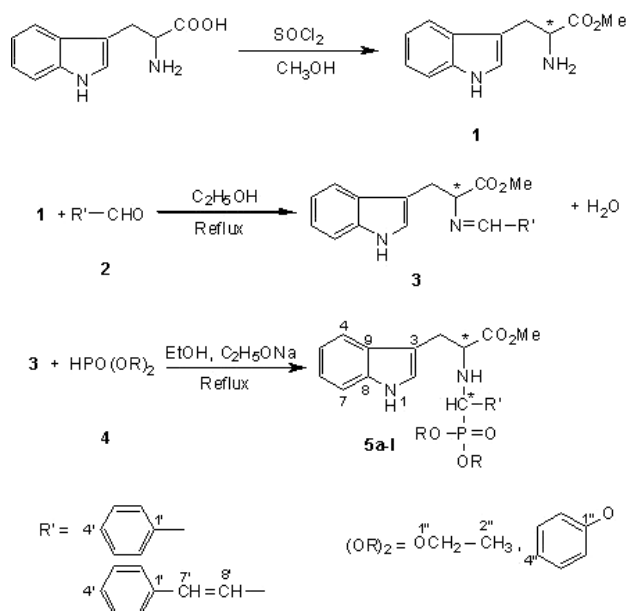
Comp.	R'	(OR)$_2$	Comp.	R'	(OR)$_2$
5a	4-Cl–C$_6$H$_4$	CH$_3$	**5g**	2-OH–C$_6$H$_4$	CH$_3$
5b	4-Cl–C$_6$H$_4$	C$_2$H$_5$	**5h**	2-OH–C$_6$H$_4$	C$_2$H$_5$
5c	4-Cl–C$_6$H$_4$	C$_6$H$_5$	**5i**	2-OH–C$_6$H$_4$	C$_6$H$_5$
5d	3-NO$_2$–C$_6$H$_4$	CH$_3$	**5j**	C$_6$H$_5$–CH=CH	CH$_3$
5e	3-NO$_2$–C$_6$H$_4$	C$_2$H$_5$	**5k**	C$_6$H$_5$–CH=CH	C$_2$H$_5$
5f	3-NO$_2$–C$_6$H$_4$	C$_6$H$_5$	**5l**	C$_6$H$_5$–CH=CH	C$_6$H$_5$

There is corresponding doubling of signals of the ethoxy group in ^{13}C NMR spectra (Table 3).

In fact, P–O–CH$_2$–C$\underline{H_3}$ group resonated [15] as a doublet at δ 13.2–13.5 ($^3J_{P-O-C-C}$ = 8.2–9.1 Hz) and at δ 14.2–15.6 ($^3J_{P-O-C-C}$ = 8.2–9.2 Hz), the P–O–C$\underline{H_2}$–CH$_3$ group gave two doublets one at δ 62.3–63.1 ($^2J_{P-O-C}$ = 6.9–7.0 Hz) and the other one at δ 63.1–64.2 ($^2J_{P-O-C}$ = 7.0–7.1 Hz) and –COO–C$\underline{H_3}$ resonated at δ 50.2–50.9. The chiral carbon of tryptophan methyl ester (–C$\underline{H}$–CO$_2$CH$_3$) resonated in the region δ 60.5–63.4. The chiral carbon of P–C–H gave a doublet in the range of δ 39.5–49.2 (d, J_{P-C} = 143–147 Hz). The methoxy carbon (P–OC$\underline{H_3}$) resonated as a doublet due to coupling with phosphorus at δ 51.8 (d, $^2J_{P-O-C}$ = 16.9 Hz). These values are in agreement with the literature data [16, 17].

^{31}P NMR chemical shifts [14, 18] (Table 1) of these compounds (**5a–l**) appeared in the down field region 1.62–5.19 ppm.

In the FAB mass spectra [19] (Table 4), compounds **5a, 5d, 5e, 5g** and **5i** exhibited their respective molecular ions at m/z 450 (**7**), 461 (**11**), 489 (**7**), 432 (**10**) and 528 (**10**).

ANTIBACTERIAL ACTIVITY

Compounds **5a–l** were screened in regard to their antibacterial activity against gram positive bacteria,

Staphylococcus aureus, Bacillus faecalis and gram negative bacteria, *Escherichia coli, Klebsiella pneumoniae* by the disc diffusion method [20, 21], in luria bertani nutrient agar medium at various concentrations (75, 100 μg/ml) in DMSO. These solutions containing 10^6 cells/ml were added to each Whatmann No.1 (made in UK) filter paper disc (6 mm diameter) and DMSO was used as the control. The freshly prepared agar medium containing the bacteria species was loaded on the discs by using micropipette. The plates were incubated at 35ºC and examined for zone of inhibition around each disc after 24 h. The results were compared with the activity of the standard antibiotic *Penicillin* (75 μg/ml).

EXPERIMENTAL

Solvents were used after purifying them by the established procedure. The progress of the reaction and purity of the compounds were monitored by thin layer chromatography (TLC) using *n*-hexane and ethylacetate (2:1, by volume) as eluating system on silica gel and iodine as visualizing agent. Melting points were determined in open capillary tubes on Mel-temp apparatus and were uncorrected. Microanalysis was performed at Indian Institute of Science, Bangalore, India.

IR spectra were recorded using KBr pellets on Nicolet 380 double beam spectrophotometer ($\bar{v}$ in cm^{-1}) in Environmental Engineering Lab, Sri Venkateswara University, Tirupati. ^{1}H and ^{13}C NMR spectra were recorded on a Bruker AMX 400 MHz spectrometer operating at 400 MHz for ^{1}H and 100 MHz for ^{13}C, 161.9 MHz for ^{31}P NMR as solutions in DMSO-d$_6$. The ^{1}H and ^{13}C chemical shifts were referenced with respect to tetramethyl silane, and ^{31}P chemical shifts to 85% H$_3$PO$_4$ (*ortho*-phosphoric acid). The techniques of double heteronuclear resonance were used while recording ^{1}H NMR spectra. ^{1}H, ^{13}C and ^{31}P NMR spectral data were obtained by Indian Institute of Science, Bangalore, India. Mass spectra were recorded on a Jeol SX 102 DA/600 mass spectrometer using Argon/Xenon (6 kV, 10 mA) as the fast atom bombardment (FAB) gas and also a Shimadzu QP-2000 GC-MS (gas chromatography-mass spectroscopy) instrument.

Table 2. ^{1}H NMR chemical shifts [a,b] of **5a–l**.

Comp.	Ar–H	–CH₂ (d, 2H)	–CH (m, 1H)	P–C–H (m, 1H)	N–H (d, 1H)	–COO–CH₃ (s, 3H)	P–OCH₂–CH₃ (m, 2H)	P–OCH₂–CH₃/OCH₃ (3H)	Ar–NH (s, 1H)	Other H's
5a	7.85–6.91 (m, 9H)	2.93 (J = 7.1)	3.61–3.58	3.70–3.68	3.01 (J = 6.5)	2.32	-	2.31 (s)	10.80	-
5b	7.83–6.95 (m, 9H)	2.94 (J = 7.0)	3.60–3.57	3.69–3.67	2.94 (J = 8.3)	2.32	3.65–3.61	1.08 (t, J = 6.9)	10.87	-
5c	8.52–6.87 (m, 19H)	2.94 (J = 6.8)	3.58–3.55	3.74–3.70	2.98 (J = 6.8)	2.30	-	-	10.90	-
5d	7.86–6.90 (m, 9H)	3.12 (J = 8.1)	3.60–3.58	3.72–3.68	3.13 (J = 8.4)	2.31	-	2.30 (s)	10.90	-
5e	7.84–6.95 (m, 9H)	3.06 (J = 8.2)	3.60–3.57	3.71-3.69	3.12 (J = 8.5)	2.31	3.67–3.64	1.09 (t, J = 7.0)	10.87	-
5f	8.85–7.22 (m, 19H)	3.36 (J = 8.3)	3.59–3.55	3.62–3.59	3.35 (J = 8.1)	2.50	-	-	10.88	-
5g	7.44–6.68 (m, 9H)	3.03 (J = 7.9)	3.61–3.58	3.64–3.63	3.71 (J = 8.3)	2.85	-	2.49 (s)	10.74	10.42 (s, 1H, OH)
5h	7.43-6.67 (m, 9H)	3.30 (J = 7.9)	3.60–3.58	3.63–3.61	3.72 (J = 8.4)	2.49	3.68–3.64	1.18 (J = 6.9)	10.75	10.41 (s, 1H, OH)
5i	8.13–6.76 (m, 19H)	3.28 (J = 8.2)	3.60–3.59	3.61–3.58	3.75 (J = 8.2)	2.51	-	-	10.73	10.40 (s, 1H, OH)
5j	7.87–6.95 (m, 10H)	3.60 (J = 8.6)	3.62–3.59	3.70–3.67	3.33 (J = 8.8)	2.61	-	2.50 (s)	10.81	7.45 (–CH=CH₂, t, J = 11.4 Hz, 1H), 6.65 (–CH=CH₂, d, J = 13.3 Hz, 1H)
5k	7.85–6.93 (m, 10H)	3.60 (J = 8.5)	3.61–3.57	3.71–3.68	3.34 (J = 8.6)	2.49	3.67–3.62	1.20 (t, J = 7.0)	10.80	7.44 (–CH=CH₂, t, J = 11.2, 1H), 6.64 (–CH=CH₂, d, J = 13.1, 1H)
5l	8.15–6.73 (m, 19H)	3.61 (J = 8.7)	3.64–3.60	3.71–3.67	3.35 (J = 8.2)	2.71	-	-	10.82	7.46 (–CH=CH₂, t, J = 11.5 Hz, 1H), 6.60 (–CH=CH₂, d, J = 13.5, 1H)

- No such type of protons present;   a - Chemical shifts in ppm from TMS and coupling constants *J* in Hz in parenthesis;   b - Recorded in DMSO-d₆.

Table 3. ^{13}C NMR spectral data[a,b] of compounds **5b**, **5e**, **5g** and **5l**.

Comp.	Chemical shifts in ppm
5b	128.6 (C-2). 115.8 (C-3), 127.5 (C-4), 128.4 (C-5), 119.7 (C-6), 111.0 (C-7), 136.4 (C-8), 131.9 (C-9), 30.9 (–$\underline{CH_2}$–CHCOOCH$_3$), 64.3 (–CH$_2$–$\underline{CH}$COOCH$_3$), 171.2 (–CH$_2$–CH$\underline{COO}$CH$_3$), 50.3 (–CH$_2$–CHCOO$\underline{CH_3}$), 48.9 (d, J_{P-C} = 143 Hz, 1C, P–C–$\underline{H}$), 136.1 (C-1′), 129.5 (C-2′&C-6′), 128.7 (C-3′&C-5′), 132.4 (C-4′), 62.3 (d, $^2J_{P-O-C}$ = 6.9 Hz, IC, –$\underline{OCH_2}$–CH$_3$), 14.5 (d, $^3J_{P-O-C-C}$ = 8.2 Hz, IC, –OCH$_2$–$\underline{CH_3}$), 63.1 (d, $^2J_{P-O-C}$ = 7.0 Hz, IC, –$\underline{OCH_2}$–CH$_3$), 15.6 (d, $^3J_{P-O-C-C}$ = 8.2 Hz, IC, –OCH$_2$–$\underline{CH_3}$).
5e	128.9 (C-2). 115.9 (C-3), 127.8 (C-4), 128.5 (C-5), 119.7 (C-6), 111.0 (C-7), 136.7 (C-8), 132.1 (C-9), 31.3 (–$\underline{CH_2}$–CHCOOCH$_3$), 63.4 (–CH$_2$$\underline{CH}$COOCH$_3$), 172.3 (–CH$_2CH\underline{COO}CH_3$), 50.5 (–CH$_2$CHCOO$\underline{CH_3}$), 42.3 (d, J_{P-C} = 145 Hz, 1C, P–C–$\underline{H}$), 138.2 (C-1′), 123.3 (C-2′), 148.3 (C-3′), 121.9 (C-4′), 129.2 (C-5′), 134.2 (C-6′), 63.1 (d, $^2J_{P-O-C}$ = 7.0 Hz, IC, –$\underline{OCH_2}$–CH$_3$), 13.2 (d, $^3J_{P-O-C-C}$ = 9.1 Hz, IC, –OCH$_2$–$\underline{CH_3}$), 64.2 (d, $^2J_{P-O-C}$ = 7.1 Hz, IC, –$\underline{OCH_2}$–CH$_3$), 14.2 (d, $^3J_{P-O-C-C}$ = 9.2 Hz, IC, –OCH$_2$–$\underline{CH_3}$).
5g	128.7 (C-2). 115.7 (C-3), 127.4 (C-4), 128.4 (C-5), 118.4 (C-6), 111.2 (C-7), 136.2 (C-8), 133.4 (C-9), 28.9 (–$\underline{CH_2}$–CHCOOCH$_3$), 60.5 (–CH$_2$$\underline{CH}$COOCH$_3$), 172.8 (–CH$_2CH\underline{CO}OCH_3$), 50.5 (–CH$_2$CHCOO$\underline{CH_3}$), 39.5 (d, J_{P-C} = 147 Hz, 1C, P–C–H), 120.8 (C-1′), 156.4 (C-2′), 117.5 (C-3′), 129.1 (C-4′), 126.5 (C-5′), 129.4 (C-6′), 51.8 (d, $^2J_{P-O-C}$ = 16.9 Hz, IC, –O–$\underline{CH_3}$).
5l	128.5 (C-2). 116.0 (C-3), 127.9 (C-4), 128.6 (C-5), 119.6 (C-6), 111.0 (C-7), 136.5 (C-8), 131.7 (C-9), 31.5 (–$\underline{CH_2}$–CHCOOCH$_3$), 63.4 (–CH$_2$$\underline{CH}$COOCH$_3$), 172.3 (–CH$_2CH\underline{CO}OCH_3$), 50.2 (–CH$_2$CHCOO$\underline{CH_3}$), 49.2 (d, J_{P-C} = 147 Hz, 1C, P–C–H), 135 (C-1′), 126.3 (C-2′&C-6′), 128.3 (C-3′&C-5′), 127.3 (C-4′), 127.4 (C-7′), 123.3 (C-8′), 157.3 (C-1″), 115.8 (C-2″ & C-6″), 129.2 (C-3″ & C-5″), 121.2 (C-4″) .

a - Chemical shift in ppm from TMS and coupling constants J (Hz) in parenthesis; b - Recorded in DMSO-d_6.

Table 4. FAB Mass spectral data of compounds **5a**, **5d**, **5e**, **5g** and **5i**.

Comp.	m/z (%)
5a	450 (7.1, M$^{+•}$) 417 (81.2), 335 (100), 193 (19.2), 146 (18.2), 118 (20.3), 64 (14.2).
5d	461 (10.7 M$^{+•}$), 428 (17.8), 339 (100), 215 (7.5), 118 (10.8), 64 (7.1).
5e	489 (7.3, M$^{+•}$) 431 (5.2), 399 (10.7), 359 (14.2), 327 (71.4), 255 (78.5), 118 (100), 64 (71.4).
5g	432 (10.0, M$^{+•}$), 390 (14.2), 309 (25.7), 249 (100), 231 (17.1), 203 (11.4), 188 (77.1).
5i	528 (9.8, M$^{+•}$), 492 (7.8), 419 (17.1), 235 (65.2), 118 (100), 64 (31.2).

Table 5. Antibacterial activity[a] of some new α-amino-phosphonic acid esters (**5a–l**).

Comp.	*Staphylococcus aureus*		*Bacillus faecalis*		*Escherichia coli*		*Klebsiella pneumoniae*	
	75 µg/ml	100 µg/ml	75 µg/ml	100 µg/ml	75 µg/ml	100 µg/ml	75 µg/ml	100 µg/ml
5a	-	-	8	9	-	-	7	8
5b	6	8	-	-	10	12	10	12
5c	-	-	10	11	9	12	-`	-
5d	-	-	9	10	-	-	6	8
5e	7	9	-	-	8	10	9	10
5f	13	16	12	14	16	18	10	12
5g	8	10	-	-	10	11	12	15
5h	12	13	-	-	11	12	10	11
5i	8	11	-	-	8	10	-	-
5j	-	-	6	8	8	10	-	-
5k	7	8	10	12	8	9	6	9
5l	8	11	14	15	6	10	-	-
Penicillin[b]	9		8		7		11	

a - Concentration in ppm;   b - Standard antibacterial compound.

Synthesis of 2-{[hydroxy-phenyl-methyl-2-di-methoxy-phosphoryl)-methyl]amino}-3-(1H-indol-3-yl)-propionic acid methyl ester (**5g**). Tryptophan-methyl ester was prepared using the reported procedure [22].

Tryptophan methyl ester (1.09 g, 0.005 mol) and *o*-hydroxybenzaldehyde (**2**) (0.52 g, 0.005 mol) in dry ethanol (20 ml) were refluxed upon stirring for 2 hours to form the imine (**3**). A solution of dimethyl-phosphite (**4**) (0.53 ml, 0.005 mol) was added slowly at room temperature, in the presence of catalytic amount of sodium ethoxide without iso-lating the imine. The reaction temperature was raised to reflux value and maintained for 4 h. Completion of the reaction was monitored by TLC analysis. After completion of the reaction, solvent was removed in a rotary evaporator. The residue was purified by column chromatography using silica gel (60–120 mesh) as adsorbent and hexane and ethyl-acetate (2:1) as an eluent to afford pure α-amino-phosphonic acid ester (5 g) as a solid phase, yield 1.16 g (79%), m. p. 117–119°C.

The results indicate that the compounds **5b**, **5e**, **5f** and **5h** exhibited promising antibacterial activity. The compound 5a showed the same activity against gram positive bacteria *Bacillus faecalis* when com-pared to that of the standard. The compound **5l** exhibited more activity against gram positive bacteria *Bacillus faecalis* when compared to that of *Penicillin*. It is gratifying to note that the nitro compound **5f** exhibited very high activity against both gram positive and negative bacteria, since it contains nitro-group.

CONCLUSION

In conclusion, synthesis of α-aminophosphonic acid esters is achieved in good yields in a two-step reaction process in the presence of sodium ethoxide as a catalyst. The advantages are smaller reaction time intervals, low cost of the reactant chemicals, simple experimental procedure.

REFERENCES

1. (a) S. C. Fields, *Tetrahedron* **55**, 12237 (1999). (b) D. Redmore, *J. Org. Chem.,* **43**, 992 (1978).
2. B. Kaboudin, R. Nazari, *Tetrahedron Lett.,* **42**, 8211 (2001).
3. P. Kafarski, B. Lejczak, *Phosphorus, Sulfur, Silicon Relat. Elem.*, **63**, 193 (1991).
4. R. Hirschmann, A. B. Smith III, C. M. Taylor, P. A. Venkovic, S. D. Taylor, K. M. Yager, P. A. Sprengler, S. J. Venkovic, *Science,* **265**, 234 (1994).
5. (a) M. C. Allen, W. Fuhrer, B. Tuck, R. Wade, J. M. Wood, *J. Med. Chem.,* **32**, 1652 (1989); (b) P. P. Giannousis, P. A. Bartlet, *Ibid.* **30**, 1603 (1987).
6. (a) F. R. Atherton, C. H. Hassal, R. W. Lambert, *J. Med. Chem.,* **29**, 29 (1986); (b) C. H. Hassal, in: Antibiotics, F. E. Halm (ed), vol. 6, Springer-Verlag, Berlin, 1983, p. 1.
7. (a) D. Redmore, in: Topics in Phosphorus Chemistry, E. J. Griffith, M. Grayson (eds), vol. 8, John Wiley & Sons, New York, 1976, p. 515; (b) V. P. Kukhar, V. A. Solodenko, *Russ. Chem. Rev.,* **56**, 859 (1987).
8. A. A. Sobanov, A. V. Zolotukhim, V. I. Galkin, R. A. Cherkasov, A. N. Pudovik, *Russ. J. Chem.*, **72**, 1967 (2002).
9. R. A. Cherkasov, V. I. Galkin, *Usp. Khim.,* **67,** 940 (1998).
10. G. Syamprasad, J. Radhakrishna, M. Manjunath, O. V. Reddy, M. Kasthuraiah, C. S. Reddy, V. G. Puranik, *Arkivoc*, **13**, 133 (2007).
11. P. Haranath, V. S. Kumar, C. S. Reddy, C. N. Raju, C. D. Reddy, *J. Heterocyc. Chem.,* **44**, 369 (2007).
12. L. C. Thomas, Interpretation of the Infrared Spectra of Organophosphorus Compounds, Heydon and Sons Ltd., London, 1974.
13. J. S. Yadav, B. V. S. Reddy, K. Saritha Raj, K. B. Reddy, A. R. Prasad, *Synthesis,* **15**, 2277 (2001).
14. J. Xu, N. Fu, *J. Chem. Soc. Perkin Trans. I*, 1223 (2001).
15. D. Hall, C. R. Ardrey, R. Dyer, G. Paul, *J. Chem. Soc. Perkin. Trans. II*, 1232 (1977).
16. (a) E. D. Matveeva, T. A. Podrugina, E. V. Tishkovskaya, L. G. Tomilova, N. S. Zefirov, *Synlett.,* **15**, 2321 (2003). (b) E. Van Meonen, K. Moonen, D. Ake, V. C. Stevens, *Arkivoc,* **1**, 31, (2006).
17. (a) W. A. Fadel, N. Tesson, *Eur. J. Org. Chem.,* 2153 (2000). (b) H. Firouzabadi, N. Iranpour, S. Sobhani, *Synthesis,* **16**, 2692 (2004).
18. L. D. Quin, J. G. Verkade (eds), Phosphorus ^{31}P NMR Spectral Properties in Compound Characterization and Structural Analysis, VCH Publ., New York, 1994.
19. H. Keck, W. Kuchem, H. F. Mahler, *Org. Mass Spectrom*, **15**, 591 (1980**)**.
20. K. R. Cruickshan, Medical Microbiology, A Guide to Diagnosis and Control of Infection, II ed. E. S. Livingston Ltd, Edinburgh and London, 1968.
21. A. W. Beuer, M. M. Kirby, J. C. Sherries, A. Truck, *Am. J. Clin. Pathol.,* **45,** 493, (1969).
22. R. G. Webb, *J. Org. Chem.,* **34**, 576 (1969).

ЕФИКАСНА СИНТЕЗА В ЕДИН СЪД НА ЕСТЕРИ НА α-АМИНОФОСФОРНАТА КИСЕЛИНА С ШИФОВИ БАЗИ С ИЗПОЛЗВАНЕ НА НАТРИЕВ ЕТОКСИД КАТО КАТАЛИЗАТОР (РЕАКЦИЯ НА ПУДОВИК) И ТЯХНАТА БИОЛОГИЧНА АКТИВНОСТ

Ч. Мохан[1], С. Н. Раджу[1]*, А. Дж. Рао[1], Р. Ю. Н. Лакшми[2]

[1] *Департамент по химия, Университет „Сри Венкатесуара", Тирупати, Индия*
[2] *Департамент по ботаника, Университет „Сри Венкатесуара", Тирупати, Индия*

(Резюме)

Осъществена е синтеза на нови естери на α-аминофосфорната киселина чрез двустадийна реакция в един съд (Реакция на Пудовик). В първия стадий метилов естер на триптофан реагира със заместени ароматни алдехиди в абсолютен етанол до образуване на Шифови бази. Във втория стадий те взаимодействат *in situ* с диалкил/диарилфосфит с използване на натриев етоксид като катализатор и при нагряване с обратен хладник. Структурата на тези съединения е определена с елементен анализ, ИЧС, ^{1}H, ^{13}C, [31]P ЯМР и масспектрометрия. Всички споменати съединения показаха умерена антимикробна активност.

Simple and convenient procedures for the synthesis of novel heterocyclic compounds containing 1-phenyl-3-pyridylpyrazole moiety

H. F. Rizk*

Chemistry Department, Faculty of Science, Tanta University, Tanta, Egypt

New 1-phenyl-3-pyridin-3-yl-1*H*-thieno[2,3-*c*]pyrazole-5-carboxylic acid ethyl ester has been obtained by the reaction of 5-chloro-1-phenyl-3-pyridin-3-yl-1*H*-pyrazole-4-carbaldehyde with ethyl bromoacetate and sodium sulphide. Alkaline hydrolysis of the ester gave the corresponding acid, while reaction of the same ester with hydrazine hydrate gave the corresponding hydrazide. Reactions of the hydrazide with potassium isocyanate and ammonium isothiocyanate gave the corresponding triazole and thiadiazole, respectively. The treatment of 5-chloro-1-phenyl-3-pyridin-3-yl-1*H*-pyrazole-4-carbaldehyde with hydroxylamine hydrochloride gave 4-cyanopyrazole-5-one. Reaction of the latter with POCl$_3$ afforded 5-chloro-4-cyanopyrazole, which cyclized by hydrazines to give pyrazolo[3,4-*c*]pyrazol-3-yl-amine derivatives. The reaction of 4-nitrosopyrazol-3-ol with *o*-aminophenol and *o*-phenylenediamine afforded the corresponding dipyrazolyl derivative, benzoxiazine and quinoxaline, respectively. The reduction of 4-nitrosopyrazol-3-ol with Zn/AcOH afford 4-(5-hydroxy-1-phenyl-3-pyridin-3-yl-1*H*-pyrazol-4-ylimino)2-phenyl-5-pyridin-3-yl-2,4-dihydropyrazol-3-one, which was also obtained from reaction of 2-phenyl-5-pyridine-3-yl-2*H*-pyrazole-3,4-dione with benzylamine. Finally, the reaction of 4-nitrosopyrazol-3-ol with 5-chloro-1-phenyl-3-pyridin-3-yl-1*H*-pyrazole-4-carbaldehyde gave 3,5-diphenyl-7-pyridin-3-yl-1-pyridin-4-yl-3,5-dihydro-4-oxa-2,3,5,6,8-pentaazocyclopenta [*f*]azulene.

Keywords: pyridyl pyrazolone, thieno[2,3-*c*]pyrazole, 4-nitrosopyrazole, Vilsmeier-Haack reaction.

INTRODUCTION

5-Pyrazolones are very important class of heterocyclic compounds due to their biological and pharmacological activities [1, 2] such as anti-inflammatory [3], herbicidal [4], fungicidal [5], bactericidal [5], plant growth regulation [4], antipyretic properties [6] and protein kinase inhibiting effect [7]. They are also used as key starting materials for the synthesis of commercial arylazopyrazolone dyes [8, 9]. In conjunction with our interest in preparing pyrazolone derivatives, we tried to prepare sulphur heterocyclic moieties fused to pyrazole ring, which might have some interesting bioactive properties. We report herein the results of the reactions of 5-chloro-1-phenyl-3-pyridin-3-yl-1*H*-pyrazole-4-carbaldehyde and 4-nitroso-2-phenyl-5-pyridin-3-yl-2*H*-pyrazol-3-ol with different readily available reagents.

RESULTS AND DISCUSSION

Firstly, the Vilsmeier-Haack reaction of 2-phenyl-5-pyridin-3-yl-2,4-dihydro-pyrazol-3-one (**1**) gave 5-chloro-1-phenyl-3-pyridin-3-yl-1*H*-pyrazole-4-carbaldehyde (**2**) in 55% yield. Treatment of (**2**) with ethyl bromoacetate and sodium sulphide in ethanol produced 1-phenyl-3-pyridin-3-yl-1*H*-thieno [2,3-*c*]pyrazole-5-carboxylic acid ethyl ester (3) in

70% yield.

Alkaline hydrolysis of (**3**) gave 1-phenyl-3-pyridine-3-yl-1*H*-thieno[2,3-*c*]pyrazole-5-carboxylic acid (**4**) in 85% yield. The reaction of (**3**) with hydrazine hydrate afforded 1-phenyl-3-pyridine-3-yl-1*H*-thieno[2,3-*c*]pyrazole-5-carboxylic acid hydrazide (**5**) in 65% yield. When compound (**5**) reacted with potassium cyanate in 50% acetic acid cyclization took place to give 5-(1-phenyl-3-pyridin-3-yl-1*H*-thieno[2,3-*c*]pyrazol-5-yl)-4*H*[1,2,4]-triazol-3-ol (**6**) in 50% yield. Similarly, treatment of (**5**) with ammonium thiocyanate in ethanol in presence of concentrated HCl gave (1-phenyl-3-py-ridin-3-yl-1*H*-thieno[2,3-*c*]pyrazol-5-yl)-[1,3,4]thia-diazol-2-yl-amine (**7**) in 45% yield (Scheme 1). This result is consistent with the one that was reported by Balagh *et al.* [10].

The reaction of 5-chloropyrazole-4-carbaldehyde (**2**) with hydroxylamine hydrochloride in ethanol gave directly 5-oxo-1-phenyl-3-pyridin-3-yl-4,5-dihydro-1*H*-pyrazole-4-carbonitrile (**10**) in 85% yield through the removal of HCl from the nonisolable oxime (**8**). The chlorination of compound (**10**) with POCl$_3$ gave 5-chloro-1-phenyl-3-pyridin-3-yl-1*H*-pyrazole-4-carbonitrile (**11**) in 90% yield. Condensation of compound (**11**) with hydrazine hydrate and phenyl hydrazine afforded the corresponding 6-phenyl-4-pyridin-3-yl-1,6-dihydro-pyrazolo[3,4-*c*] pyrazol-3-yl amine (**12a**) and 1,6-diphenyl-4-pyri-

---

* To whom all correspondence should be sent:
E-mail: dr_hala_fawzy@yahoo.com

din-3-yl-1,6-dihydro-pyrazolo[3,4-*c*]pyrazol-3-yl amine (**12b**). The mechanism supposed by us for the reaction is outlined in Scheme 2. This mechanism is in accordance with that proposed by El-Sayed *et al*. [11].

The intermediate products were characterised by spectroscopic methods including IRS, NMR, mass spectra and microanalysis (Tables 1, 2).
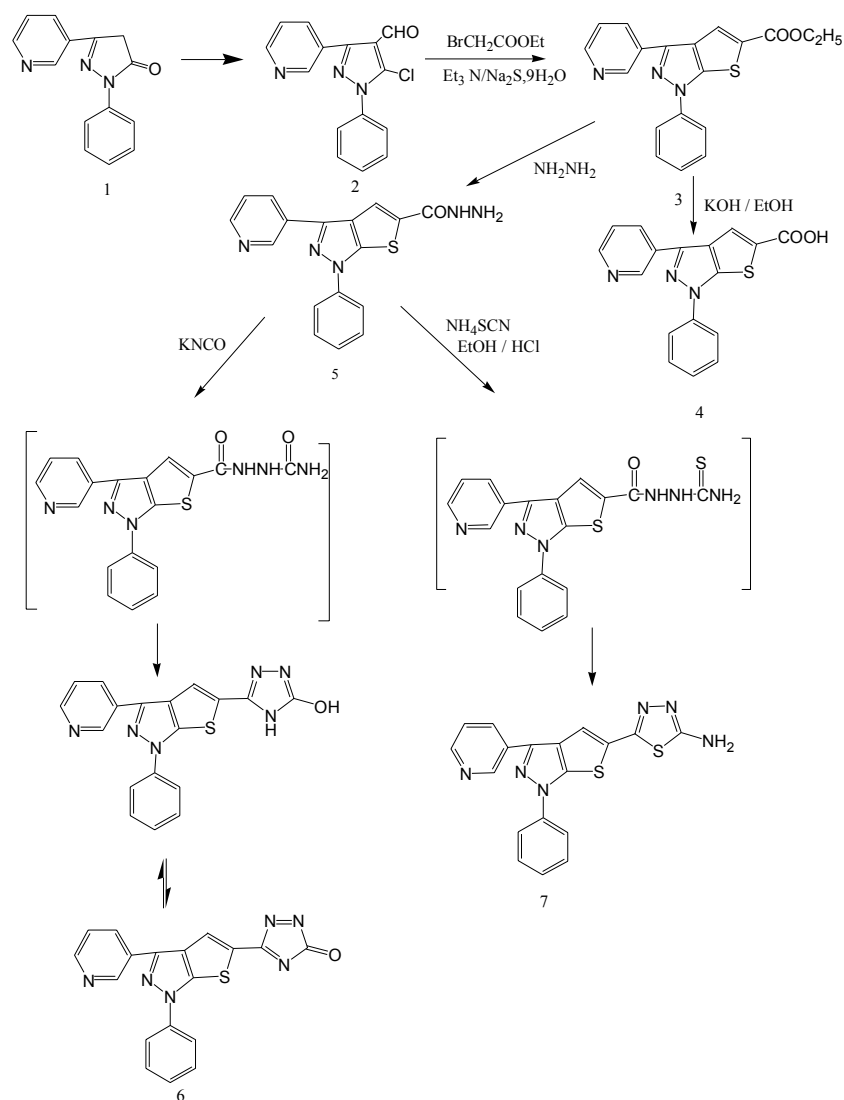
Scheme 1.
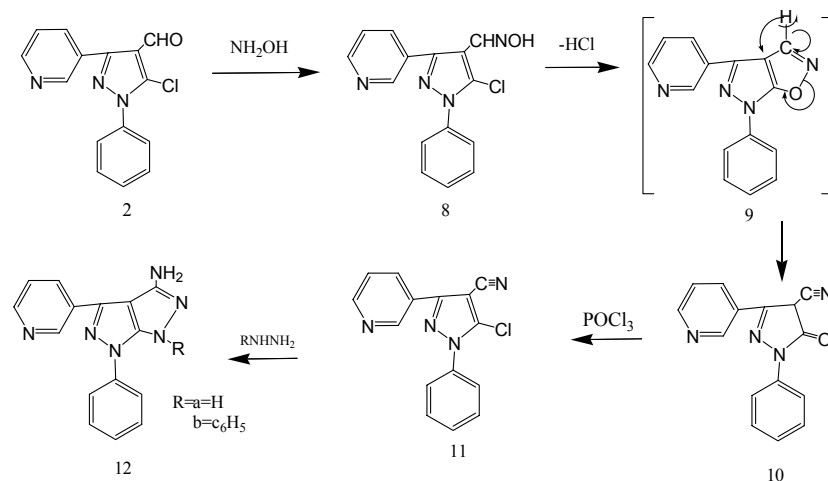
Scheme 2.

Table 1. Physical data of compounds **2–25**.

Com-pound	m.p., °C	Yield %, (colour)	Molecular formula, mass	Analysis, % Calculated/Found				
				C	H	N	Cl	S
2	110–112	55 (pale yellow)	$C_{15}H_{10}N_3OCl$ 283.71	63.50 63.23	3.55 3.34	14.81 14.75	12.50 12.32	-
3	160–161	70 (white)	$C_{19}H_{15}N_3O_2S$ 349.41	65.31 65.20	4.33 4-28	12.03 11.84	-	9.18 9.00
4	> 300	85 (white)	$C_{17}H_{11}N_3O_2S$ 321.06	63.54 63.45	3.45 3.35	13.08 12.93	-	9.98 9.87
5	258–259	65 (pale yellow)	$C_{17}H_{13}N_5OS$ 335.38	60.88 60.52	3.91 3.85	20.88 20.78	-	9.56 9.40
6	243–245	50 (pale yellow)	$C_{18}H_{12}N_6OS$ 360.39	59.99 59.88	3.36 3.25	23.23 22.98	-	8.90 8.75
7	275–277	45 (yellow)	$C_{18}H_{12}N_6S_2$ 376.46	57.43 57.21	3.21 3.00	22.32 22.10	-	17.04 16.85
10	160–162	85 (pale yellow)	$C_{15}H_{10}N_4O$ 262.27	68.69 68.44	3.84 3.64	21.36 21.14	-	-
11	150–152	90 (yellow)	$C_{15}H_9N_4Cl$ 280.71	64.18 63.98	3.23 3.12	19.96 19.88	12.63 12.22	-
12a	210–212	88 (yellow)	$C_{15}H_{12}N_6$ 276.30	62.21 61.88	4.38 4.23	30.42 30.22	-	-
12b	165–168	30 (dark orange)	$C_{21}H_{16}N_6$ 352.39	71.58 71.20	4.58 4.33	23.85 23.61	-	-
13	245-248	80 (orange)	$C_{14}H_{10}N_4O_2$ 266.25	63.15 62.89	3.79 3.55	21.04 20.80	-	-
17	190–192	50 (buff)	$C_{28}H_{20}N_6O_2$ 472.16	71.17 70.86	4.27 4.02	17.79 17.43	-	-
18a	125–127	60 (dark brown)	$C_{20}H_{14}N_4O$ 326.35	73.61 73.23	4.32 4.12	17.17 16.94	-	-
18b	184–185	75 (yellow)	$C_{20}H_{15}N_5$ 325.37	73.83 73.44	4.65 4.33	21.52 21.31	-	-
19	122–124	60 (yellow)	$C_{14}H_9N_3O_2$ 251.24	66.93 66.63	3.61 3.33	16.73 16.55	-	-
23	270–272	70 (red violet)	$C_{28}H_{19}N_7O_2$ 485.50	69.27 69.02	3.94 3.74	20.20 19.98	-	-
25	250–252	75 (brown)	$C_{29}H_{19}N_7O$ 481.51	72.34 72.13	3.98 3.77	20.36 20.11	-	-

The nitrosation of 2-phenyl-5-pyridin-3-yl-2,4-dihydro-pyrazol-3-one (**1**) gave 4-nitroso-2-phenyl-5-pyridin-3-yl-2*H*-pyrazol-3-ol (**13**) in 80% yield (Scheme 3). When compound (**13**) was heated with 2-aminophenol and 2-phenylenediamine at 140°C with ammonium acetate afforded the dimer (**17**), pyrazolo[3,4-*b*]benzoxazine (**18a**) and pyrazolo[3,4-*b*]quinoxaline (**18b**). This result could be explained by the nucleophilic attack of both amino groups of 2-phenylenediamine or hydroxyl and amino groups of *o*-aminophenol on the C_4 and C_5 of nitroso compound (**13**) to give intermediate (**15**) followed by simultaneous elimination of both water and hydroxylamino molecules yielding the pyrazolo[3,4-b]benzoxiazine (**18a**) and pyrazolo[3,4-b]quinoxaline (**18b**) (Scheme 3). However, dipyrazolyl compound (**17**) could be formed from pyrazole radical (**16**), which would be obtained from the intermediate (**15**) *via* elimination of an amine molecule and nitric oxide (Scheme 3). Analogous results were previously reported by El-Rady [12].

The acidic hydrolysis of 4-nitrosopyrazole (**13**)

with concentrated HCl at 0°C gave the expected dione (**19**) in 60% yield (Scheme 4). Compound (**23**) could be obtained by two routes: (a) by the reaction of compound (**19**) with benzylamine in alcoholic medium, which produced the imine intermediates (**20**) and (**21**) followed by air oxidation of amino compound (**22**) to afford (**23**). The route (b) involved the air oxidation of intermediate (**24**). Finally, compound (**25**) was obtained in 75% yield by the reaction of (**2**) with the amino intermediate (**24**), which could be obtained by reduction of nitroso compound (**13**).

EXPERIMENTAL

All melting points were measured on a Gallen-Kamp melting point apparatus and are uncorrected. The IR spectra were measured on Perkin-Elmer-1430 spectrophotometer using KBr tablets technique. ^{1}H and ^{13}C NMR spectra were recorded on a Bruker AV400 spectrometer operating at 400 MHz for ^{1}H and 100 MHz for ^{13}C measurements at Chemistry Department, University of Wales Swansea, UK.
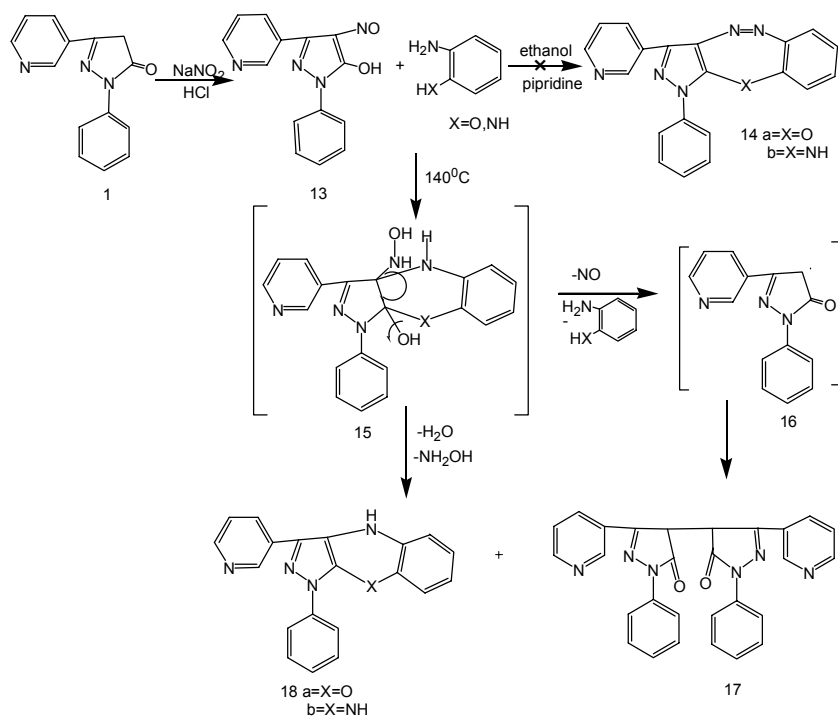
Scheme 3.
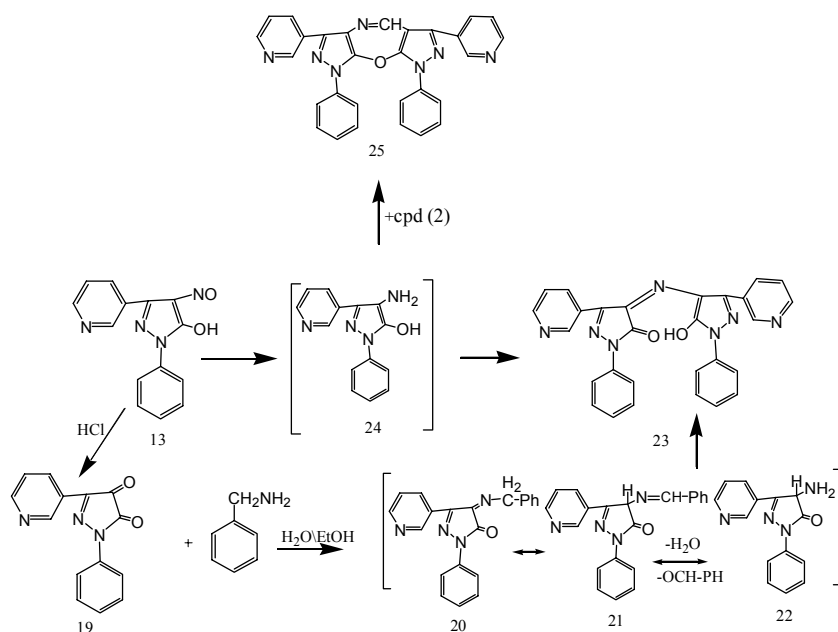
Scheme 4.

Low-resolution mass spectra were recorded on a VG 12.253 spectrometer, electron impact (EI) at 70 eV. Microanalyses were performed by the Micro-analysis Laboratory at Cairo University. Progress of reaction was monitored by thin-layer chromato-graphy (TLC) using benzene/acetone (3:1) mixture as an eluent.

5-Chloro-1-phenyl-3-pyridin-3-yl-1H-pyrazole-4-carbaldehyde (**2**). The pyrazolone (**1**) [13] (1.3 g, 0.0057 mol) was added to a cold Vilsmeier reagent prepared by the addition of POCl3 (2.75 ml, 0.0285 mol) to DMF (5 ml, 0.068 mol) at 0°C, and the reaction mixture was heated for 8 h at 80°C. The reaction mixture was poured onto ice-cold water (10 ml) and basified with K_2CO_3 solution to reach pH = 9. The pale yellow solid phase thus separated was filtered and recrystallized from benzene.

1-Phenyl-3-pyridin-3-yl-1H-thieno[2,3-c]pyrazo-le-5-carboxylic acid ethyl ester (**3**). A solution of (**2**) (22.98 g, 0.081 mol) in ethanol (50 ml) was added to a solution of sodium sulphide nonahydrate (19.41 g 0.081 mol) in ethanol (500 ml) at 40°C. The reaction mixture was refluxed for 2 h, and then ethyl bromoacetate (9.0 ml, 0.0081mol) was added in a

dropwise manner. The reaction temperature was kept constant at 50°C and triethylamine (11 ml) was added and the reaction mixture was allowed to stay overnight at room temperature. The precipitate, which was formed, was then filtered and recrystallized from ethanol.

1-Phenyl-3-pyridin-3-yl-1H-thieno[2,3-c]pyrazole-5-carboxylic acid (**4**). A solution of (**3**) (3.5 g, 0.01 mol) in a mixture of ethanol (62.5 ml) and water (15 ml) was treated with aqueous 85% potassium hydroxide (0.95 g, 0.017 mol). The reaction mixture was refluxed for 2 h. The reaction mixture was left to cool down and water was added to dissolve the salt obtained. Concentrated hydrochloride acid was added in a dropwise manner until the solution became acidic. The formed solid phase was filtered, washed with water and recrystallized from water/ethanol solvent.

1-Phenyl-3-pyridin-3-yl-1H-thieno[2,3-c]pyrazole-5-carboxylic acid hydrazide (**5**). A mixture of (**3**) (3.5 g, 0.01 mol), 98% hydrazine hydrate (7.5 g, 0.15 mol) and ethanol (100 ml) was heated under reflux on a steam bath for 2 h. A colourless solid was formed, filtered and recrystallized from ethanol.

5-(1-Phenyl-3-pyridin-3-yl-1H-thieno[2,3-c]pyrazol-5-yl)-4H-[1,2,4]-3-ol (**6**). A solution of potassium cyanate (1.7 g, 0.022 mol) in (10 ml) water was added dropwise to a cold (0°C) solution of (**5**) (6.7 g, 0.02 mol) a mixture of acetic acid (40 ml) and water (40 ml). The reaction mixture was left for

one hour at 0°C upon stirring and then heated under reflux for 4 h. A pale yellow solid was formed after 3 h. The formed solid phase was filtered, washed with water, dried and recrystallized from ethanol.

5-(1-Phenyl-3-pyridin-3-yl-1H-thieno[2,3-c]pyrazol-5-yl)-4H-[1,3,4]thiodiazol-2-ylamine (**7**). A mixture of (**5**) (3.35 g, 0.01 mol), ammonium thiocyanate (2.3 g, 0.03 mol) and concentrated HCl (9 M, 4 ml) in ethanol (200 ml) was heated under reflux for 15 h. The solvent was removed by distillation and water (500 ml) was added. The formed solid phase was dried and recrystallized from ethanol.

5-Oxo-1-phenyl-3-pyridin-3-yl-4,5-dihydro-1H-pyrazole-4-carbonitrile (**10**). Hydroxylamine hydrochloride (2.0 g, 0.29 mol) in water (5 ml) was treated with NaOH solution (4 M) to reach pH = 8. A solution of (2) (2.83 g, 0.01 mol) in ethanol (40 ml) was added and the reaction mixture was heated under reflux for 2 h. The mixture was left to cool down, poured into ice-cold water (100 ml) and acidified with 20% aqueous HCl (4 M). The formed solid phase was filtered, washed with water, dried and recrystallized from ethanol.

5-Chloro-1-phenyl-3-pyridin-3-yl-4,5-dihydro-1H-pyrazole-4-carbonitrile (**11**). Compound (**10**) (2.6 g, 0.01 mol) was heated under reflux with POCl₃ (15 ml) for 1 h. The reaction mixture was left to cool down, poured into ice-cold water. The formed solid phase was filtered and recrystallized from ethanol.

Table 2. Spectroscopic data of compounds **2–25**.

Comp	IR spectra (ν_{max} in cm^{-1})	^{1}H NMR (δ in ppm), ^{13}C NMR (δ in ppm), Mass spectra
2	1680 (C=O), 1580 (C=N)	δ 7.3–9.3 (m, 9H, Ar–H), δ 10.0 (s, 1H,CHO), M.S: 283 (100%).
3	1605 (C=N), 1599 (C=O)	δ 1.35 (t, 3H, CH₃CH₂O), δ 4.35 (q, 2H, CH₃CH₂O), δ 7.4–9.3 (m, 9H, Ar–H), δ 7.5 (s, 1H, H₄), M.S: 349 (75%).
4	3050 (OH), 1581(C=N)	δ 7.4–9.3 (m, 9H, Ar–H), δ 7.5 (s, 1H, H₄), δ 11 (s, 1H, OH), M.S : 321 (100%).
5	1660 (C=O), 1620 (NH₂), 1605 (C=N), 1570 (C–N–H amide)	δ 4.6 (s, 2H, exch., NH₂,), δ 7.4–9.2 (m, 9H, Ar–H), δ 7.5 (s, 1H, H₄), δ 9.9 (s, exch., 1H, NH), 107 (C₂c), 124.64 (C₃c), 138.10 (C₄), 142.29 (C₃), 143.09 (C₅), 118.02, 126.8, 130.44, 138.86 (C_phenyl), 128.86, 133.51, 134.20, 147.35, 150.17 (C_pyridyl), 161.86 (C=O), M.S: 335 (35%).
6	3450 (OH), 3100 (NH), 1650 (C=N)	δ 6.2 (s, exch., 1H, OH), δ 7.4–9.3 (m, 9H, Ar–H), δ 7.5 (s, 1H, H₄), δ 10.4 (s, exch., 1H, NH); M.S: 360 (80%).
7	3390 (NH₂), 1605 (C=N)	δ 6 (s, exch., 2H, NH₂), δ 7.4–9.3 (m, 9H, Ar–H), δ 7.5 (s, 1H, H₄), M.S: 376 (65%)
10	2220 (C≡N), 1660 (C=O), 1610 (C=N)	δ 3.4 (s, 1H, H₄), δ 7.4–9.2 (m, 9H, Ar–H), M.S: 263 (100%).
11	2230 (C≡N), 1612 (C=N)	δ 7.4–9.2 (m, 9H, Ar–H); M.S : 280 (90%).
12a	3450 (NH₂), 3100 (NH), 1605 (C=N)	δ 4.2 (s, exch., 2H, NH₂), δ 7.4–9.2 (m, 9H, Ar–H), δ 13.3 (s, exch., 1H, NH); M.S: 276 (80%).
12b	3300 (NH₂), 1612 (C=N)	δ 4 (s, exch., 2H, NH₂), δ 7.4–9.2 (m, 14H, Ar–H), M.S: 352 (75%).
13	3380 (OH), 1604 (NO)	δ 4.8 (s, 1H, OH), δ 7.3–9.1 (m, 9H, Ar–H), 118.51 (C₄), 128.68 (C₃), 139.37 (C₅), 118.87, 123.86, 129.05, 135.05 (C_phenyl), 124.28, 135.78, 146.89, 149.13, 149.91 (C_pyridyl); M.S: 266 (100%).
17	1700 (C=O), 1612 (C=N)	δ 3.1 (s, 2H, H₄, H₄'), δ 7.2–9.3 (m, 18H, Ar–H); M.S: 472 (34%).
18a	3150 (NH), 1615 (C=N), 1320 (C-O)	δ 6 (s, exch., 1H, NH), δ 7.0–9.3 (m, 13H, Ar–H; M.S: 326 (56%).
18b	3150 (NH), 1620 (C=N)	δ 6.2 (s, exch., 2H, NH), δ 7.3–9.1 (m, 13H, Ar–H; M.S: 325 (34%)
19	1670(C=O), 1625(C=N)	δ 7.3–9.1 (m, 9H, Ar–H), 153.65 (C₅), 187.73 (C₄), 160 (C₃), 120.42, 124.16, 128.73, 138.31 (C_phenyl), 123.70, 126.3, 136.25, 150.30, 152.1 (C_pyridyl); M.S: 251 (100%).
23	3030 (OH), 1760 (=N), 1690 (C=N)	δ 5.4 (s, 1H, OH), δ 7.3–9.3 (m, 18H, Ar–H); M.S : 485 (98%).
25	1670(C=N), 1612 (CH=N), 1312 (C-O)	δ 7.3-9.2(m, 18H, Ar–H), δ 9.7 (s, 1H, CH=N); M.S : 481 (100%).

245

6-Phenyl-4-pyridine-3-yl-1,6-dihydro-pyrazolo [3,4-c]pyrazol-3-ylamine (**12a**) and *1,6-diphenyl-4-pyridin-3-yl-1,6-dihydro-pyrazolo[3,4-c]pyrazol-3-yl amine* (**12b**). Compound (**11**) (2.8 g, 0.01 mol) was heated with hydrazine derivatives (0.51 mol) for 6 h in ethanol (30 ml). The reaction mixture was left to cool down and poured into water. The formed solid phase was filtered and recrystallized from ethanol.

4-Nitroso-2-phenyl-5-pyridin-3-yl-2H-pyrazol-3-ol (13). A solution of 2-phenyl-5-pyridin-3-yl-2,4-dihydro-pyrazol-3-one (**1**) (2.37 m, 0.01 mol) in acetic acid (40 ml) was added in a dropwise manner to a solution of sodium nitrite (0.075 g, 0.01 mol) in water (2 ml). The mixture was left for 15 min upon stirring. An orange solid phase was formed, filtered and washed with petroleum ether.

2,2′-Dipenyl-5,5′-di-pyridin-3-yl-2,4,2′,4′-tetra-hydro-[4,4′]bipyrazolyl-3,3′-dione (**17**). A mixture of (**13**) (0.8 g, 0.003 mol), ammonium acetate (1 g, 0.013 mol), *o*-aminophenol and/or *o*-phenylene-diamine (0.003 mol) and ammonium acetate (1 g, 0.013 mol) was heated at 140°C for 30 min then diluted with methanol. A buff crystal was precipitated, washed with hot methanol and filtered.

1-Phenyl-3-pyridin-4-yl-4-hydro-1H-pyrazolo [3,4-b]benzoxiazine (**18a**) and *1-phenyl-3-pyridin-4-yl-4,9-dihydro-1H-pyrazolo[3,4-b]quinoxaline* (**18b**). A mixture of (**13**) (0.8 g, 0.003 mol), ammonium acetate (1 g, 0.013 mol), *o*-aminophenol and/or *o*-phenylenediamine (0.003 mol) and ammonium acetate (1 g, 0.013 mol) was heated at 140°C for 30 min, diluted with methanol, the formed precipitate was filtered. The filtrate was concentrated and the coloured precipitate was filtered off and recrystallized from ethanol.

2-Phenyl-5-pyridin-3-yl-2H-pyrazole-3,4-dione (**19**). To a stirred solution of (**13**) (2.66 g, 0.01 mol) in ether (100 ml), 10% H_2SO_4 (100 ml) was added dropwise at 0°C. The mixture was stirred for 30 min at room temperature. The organic layer was separated and ammonium sulphate (5 g) was added, the aqueous layer was extracted with ethyl acetate (100 ml). The combined organic layers were dried over anhydrous $MgSO_4$ and the solvent was removed under reduced pressure. The formed solid phase was collected, washed with cold ethanol and recrystallized from ethanol.

4-(5-Hydroxy-1-phenyl-3-pyridin-3-yl-1H-pyrazol-4-ylimino)-2-phenyl-5-pyridin-3-yl-2,4-dihydro-pyrazol-3-one (**23**). *Method (a)*: A mixture of (**19**)

(2.5 g, 0.01 mol) and benzyl amine (1.072 g, 0.01 mol) in a mixture of water (20 ml) and ethanol (10 ml) was heated under reflux for 30 min. The mixture was concentrated and the precipitate obtained on cooling was isolated under vacuum and recrystallized from ethanol. *Method (b)*: To a cold (0°C) solution of (**13**) (1.3 g, 0.005 mol) in acetic acid (10 ml) Zn powder (2.0 g, 0.03 mol) was added upon stirring for 1 h. The Zn powder was removed by filtration. The filtrate was concentrated. A red violet solid substance formed was filtered, washed with cold ethanol and recrystallized from ethanol.

3,5-Diphenyl-7-pyridin-3-yl-1-pyridin-4-yl-3,5-dihydro-4-oxa-2,3,5,6,8-pentaazacyloazacyclopenta[f]azulene (**25**). To a cold (0°C) solution of (**13**) (1.3 g, 0.005 mol) in acetic acid (10 ml) Zn powder was added (2 g, 0.03 mol) upon stirring. The Zn powder was filtered off and the filtrate was transferred to a flask containing (**2**) (1.8 g, 0.005 mol) in acetic acid (10 ml). The reaction mixture was refluxed for 4 h and left to cool down and the formed solid phase was filtered, washed with water and recrystallized from acetic acid.

REFERENCES

1. S. Scheibye, A. El-Barbary, S. Lawesson, H. Fritz, G. Rihs, *Tetrahedron,* **38**, 3735 (1982).
2. The Chemistry of Heterocyclic Compounds: Pyrazolinones, Pyrazolidones and Derivatives, A. Weissberger, R. Wiley, P. Wiley (eds), John Wiley, New York, 1964**.**
3. S. Hiremith, K. Rudresh, A. Saundan, *Indian J. Chem.* **41B**, 394 (2002).
4. S. Joerg, G. Reinhold, S. Otto, S. Joachim, S. Robert, L. Klaus, Geroffen. 04 Feb 1988: DE 3.625-686 (ClC07D 231/22); CA **108**, 167465 (1988)].
5. P. N. Dhol, T. E. Achary, A. Nayak, *J. Indian Chem. Soc.,* **52**, 1196 (1975).
6. F. R. Souza, V. T. Souaza, V. Ratzalaff, L. P. Borges, M. R Olivera, H. G. Bonacorso, *Eur. J. Pharmacol.,* **45**, 141 (2002).
7. J. Singh, R. Tripathy, *PCT Int. Appl.,* 138 (2001).
8. S. Gupta, A. Sivasubramanian, M. A. Rodrigues, R. Esteves, M. F. Oliveira, *Dyes Pigment*s, **5**, 82 (2007)**.**
9. A. Khalil, M. Hassen, A. El-Sayed, *Dyes Pigment*s, **66**, 241 (2005).
10. M. Balagh, I. Hermecz, Z. Meszaros, E. Pusztay, *J. Heterocycl. Chem.*, **25**, 1737 (1988).
11. O. A. El-Sayed, H. Y. Aboul-Enein, *Arch. Pharm., Pharm. Med. Chem.,* **334**, 117(2001).
12. E. A. El-Rady, *J .Chin. Chem. Soc.*, **51**, 859 (2004).
13. R. George, H. Thomas, *J. Chem. Soc.,* 1739 (1934).

ПРОСТИ И ПОДХОДЯЩИ ПРОЦЕДУРИ ЗА СИНТЕЗАТА НА НОВИ ХЕТЕРОЦИКЛИЧНИ СЪЕДИНЕНИЯ СЪДЪРЖАЩИ 1-ФЕНИЛ-3-ПИРИДИЛАЗОЛОВА ЧАСТ

Х. Ф. Ризк

Химически департамент, Факултет по науки, Университет на Танта, Танта, Египет

(Резюме)

Получен е нов етилов естер на 1-фенил-3-пиридин-3-ил-1*H*-тиено[2,3-*c*]пиразол-5-карбоксилова киселина чрез реакция на 5-хлор-1-фенил-3-пиридин-3-ил-1*H*-пиразол-4-карбалдехид с етилбромацетат и натриев сулфид. При алкалната хидролиза на естера се получава съответната киселина, докато при реакцията на същия естер с хидразинхидрат се получава съответния хидразид. При реакциите на хидразида с калиев изоцианат и амониев изотиоцианат се получават съответния триазол и тиодиазол. При взаимодействието на 5-хлор-1-фенил-3-пиридин-3-ил-1*H*-пиразол-4-карбалдехид с хидроксиламин хидрохлорид се получава 4-цианопиразол-5-он. Реацията на последния с POCl₃ дава 5-хлор-4-цианопиразол, който циклизира с хидразини до пиразоло[3,4-c]пиразол-3-иламинови производни. Реакцията на 4-нитрозопиразол-3-ол с *о*-аминофенол и *о*-фенилендиамин дава съответното дипиразолилово производно, бензоксиазин и хиноксалин. Редукцията на 4-нитрозопиразол-3-ол с Zn/AcOH дава 4-(5-хидрокси-1-фенил-3-пиридин-3-ил-1*H*-пиразол-4-илимино)2-фенил-5-пиридин-3-ил-2,4-дихидропиразол-3-он, който бе получен също при реакция на 2-фенил-5-пиридин-3-ил-2*H*-пиразол-3,4-дион с бензиламин. Накрая, реакцията на 4-нитрозопиразол-3-ол с 5-хлор-1-фенил-3-пиридин-3-ил-1*H*-пиразол-4-карбалдехид дава 3,5-дифенил-7-пиридин-3-ил-1-пиридин-4-ил-3,5-дихидро-4-окса-2,3,5,5,8-пентаазоцикло-пента[*f*]азулен.

Synthesis of phosphorus, nitrogen, oxygen and sulphur macrocycles

M. Kasthuraiah, M. V. N. Reddy, A. U. R. Sankar, B. S. Kumar, C. S. Reddy*

Department of Chemistry, Sri Venkateswara University, Tirupati – 517 502, India

Phosphorus macromolecules containing oxygen, nitrogen and sulphur were synthesised by the addition of phosphoric acid diallyl esters to 1,2-ethandithiol or various amines in dry dichloromethane. All compounds were characterised by IR, NMR (^{1}H, ^{13}C and ^{31}P) and mass spectral studies and elemental analysis. Their antimicrobial activity has also been evaluated.

Key words: allylic alchol, macrocycles, phosphorodichloridates, antimicrobial activity.

INTRODUCTION

Phosphorus-containing macrocycles are interesting molecules with potential application in supramolecular and synthetic organic chemistry [1]. They have been synthesised as phosphine oxides, phosphines, phosphonium salts, phosphates, phosphonates and phosphoranes [2]. The importance of these molecules, as phosphorous analogues of crown ethers, is their potential catalytic activity and ion-carrier properties. The design and synthesis of host molecules capable of binding neutral organic molecules as guests is an area of rapidly expanding interest [3]. Cram [4], Lehn [5], Vogtle [6], Diederich [7] and others have made significant advances in the field of host-guest complexation [8]. Some of our past and present research has led to the construction of large preorganised macrocyclic cavities bearing concave functionalities [9]. They are also expected to function as good 'Hosts' in the 'Host-guest chemistry'. This particular property enables them to carry the drug molecule to the required cite in the living system, thus foreseeing great future for them in pharmaceutical industry. More recently Pietrusiewicz *et al.* have presented the synthesis of macrocyclic systems containing phosphorus and sulphur-based on a double conjugate addition of dithiolates to vinyl phosphane oxides and sulphides as Michael acceptors [10]. Nitrogen and oxygen mixed donor macrocycles can form stable complexes with alkali and transition metal ions. Therefore, mixed donor macrocycles have received much attention as receptors for a range of metal ions and other cations [11−14]. This particular property enables their use as efficient reagents to trap heavy toxic metals in polluted water.

In view of their possible applications and novelty in the chemistry of Host-guest molecular ensembles, it is thought worth to synthesise and study the properties of several phosphorus macro-cycles with nitrogen, oxygen and sulphur as donor atoms.

RESULTS AND DISCUSSION

The synthesis Scheme 1 involves the condensation of allylic alcohol (**2**) with various aryl phosphorodichloridates (**1a–c**) at 0°C under inert, anhydrous conditions in dry dichloromethane to afford the corresponding phosphoric acid diallyl esters (**3a–c**). Their subsequent addition to 1,2-ethanedithiol or various amines in dry dichloromethane at refluxed conditions leads to the final products, which were purified by column chromatography using hexane: ethylacetate step gradient mixtures as eluents.

All the compounds (**4a–c**, **5a–i**) exhibited IR stretching frequencies for P=O, P–O–(C$_{(aromatic)}$), (P)–O–C$_{arom}$ in the region of 1260−1291, 926−939 and 1202−1228 cm^{-1}, respectively [15−21] (Table 1). Their ^{1}H NMR spectra gave signals (Table 2) for all aromatic protons at δ 6.96−7.69 as complex multiplets [22−24]. The methylene groups (H-4 and 13) directly attached to oxygen in **4a–c** resonated as triplets at δ 4.24−4.26 (J = 5.0−6.0 Hz). Another two triplets in the region of 2.82−2.85 ppm and 2.62−2.63 ppm are attributed to H-6 and 11 and H-5 and 9, respectively. Multiplets in the region of 1.93−1.96 ppm are assigned to H-5 and 12. Similarly, the endocyclic six methylene protons of dioxaphosphocin system in **5a–i** exhibited two triplets for H-4 and 10 and multiplets for H-5 and 9 in the expected regions. All carbons in the compounds (**4a–b**, **5a**, **5d**, **5h** and **5i**) exhibited signals at their expected values (Table 3). Carbons 8 and 9 in compounds **4a** and **4b**, exhibited one singlet.

Scheme 1.
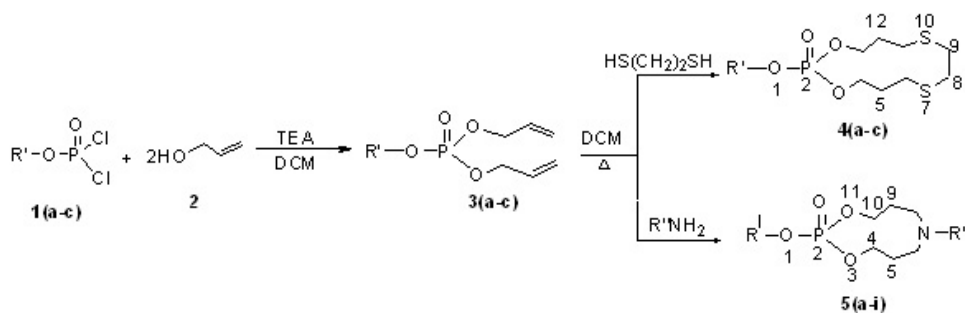
Compound	R'	Compound	R'	R"	Compound	R'	R"	Compound	R'	R"
1a & 4a	C_6H_5	5a	C_6H_5	$CH_2CH_2CH_3$	5d	$2\text{-}CH_3C_6H_4$	$CH_2CH_2CH_3$	5g	$4\text{-}CH_3C_6H_4$	$CH_2CH_2CH_3$
1b & 4b	$2\text{-}CH_3C_6H_5$	5b	C_6H_5	$CH_2(CH_2)_2CH_3$	5e	$2\text{-}CH_3C_6H_4$	$CH_2(CH_2)_2CH_3$	5h	$4\text{-}CH_3C_6H_4$	$CH_2(CH_2)_2CH_3$
1c & 4c	$4\text{-}CH_3C_6H_5$	5c	C_6H_5	$CH_2C_6H_5$	5f	$2\text{-}CH_3C_6H_4$	$CH_2C_6H_5$	5i	$4\text{-}CH_3C_6H_4$	$CH_2C_6H_5$

Table 1. Analytical and spectral data of **4a–c** and **5a–i**.

Compound	M.p., °C	Yield, %	Molecular formula	Elemental analysis, % Calculated (Found)		P–O–C, cm^{-1}			^{31}P NMR (85% H$_3$PO$_4$)
				C	H	P=O	P–O	O–C	
4a	77−79	86	$C_{14}H_{21}O_4S_2P$	48.13 (48.26)	6.01 (6.07)	1270	928	1212	−3.29
4b	99−101	89	$C_{15}H_{23}O_4S_2P$	49.60 (49.71)	6.21 (6.39)	1260	926	1210	−4.73
4c	85−87	87	$C_{15}H_{23}O_4S_2P$	49.56 (49.71)	6.26 (6.39)	1291	939	1202	−2.2
5a	48−50	80	$C_{16}H_{26}O_4NP$	58.58 (58.70)	7.91 (8.00)	1282	930	1216	−2.2
5b	69−71	79	$C_{17}H_{28}O_4NP$	59.70 (59.81)	8.11 (8.26)	1273	931	1228	−4.5
5c	110−111	80	$C_{20}H_{26}O_4NP$	63.79 (63.99)	6.81 (6.98)	1289	929	1213	−3.3
5d	63−65	83	$C_{16}H_{26}O_4NP$	58.60 (58.70)	8.00 (8.005)	1261	931	1221	−3.7
5e	69−71	79	$C_{17}H_{28}O_4NP$	59.70 (59.81)	8.11 (8.26)	1276	928	1228	−4.5
5f	77−78	78	$C_{20}H_{26}O_4NP$	63.80 (63.99)	6.968 (6.979)	1273	931	1215	−4.3
5g	72−74	76	$C_{16}H_{26}O_4NP$	58.58 (58.70)	8.09 (8.01)	1269	936	1219	−3.8
5h	95−96	86	$C_{17}H_{28}O_4NP$	59.75 (59.81)	8.16 (8.26)	1278	924	1227	−3.2
5i	110−112	88	$C_{20}H_{26}O_4NP$	63.79 (63.94)	6.81 (6.98)	1289	929	1213	−3.3

The signals for C-4 and 10, C-6 and 8, and C-5 and 9 in **5a–b** appeared as doublets at their corresponding values. The oxygen bearing C-4 and 13, C-4 and 10 in **4a–b** and **5a**, **5d**, **5h**, **5i** experienced coupling with phosphorous and exhibited doublets. All the compounds except **4a**, **4b** exhibited two ^{31}P NMR chemical shift values because of their presence as two conformers in solution state.

EXPERIMENTAL

Melting points were determined in open capillary tubes on a Mel-Temp. apparatus and were not corrected. IR spectra (ν_{max} in cm^{-1}) were recorded in KBr pellets on a Perkin-Elmer 1000 unit. The ^{1}H, ^{13}C and ^{31}P NMR spectra were recorded on various Gemini 300 and Varian AMX 400 MHz NMR spectrometers operating at 300 or 400 MHz for ^{1}H, 75.46 or 100.57 MHz for ^{13}C and 121.7 MHz for ^{31}P. All the compounds were dissolved in CDCl$_3$ and chemical shifts was referred to those of TMS (^{1}H and ^{13}C) and 85% H$_3$PO$_4$ (^{31}P). Microanalytical data were obtained from the Central Drugs Research Institute, Lucknow, India.

Table 2. ^{1}H NMR spectral data of **4a–c** and **5a–i.**

Com-pound	Chemical shifts, ppm
4a	6.98−7.26 (m, 5H, Ar-H), 4.26 (t, *J* = 5.1 Hz, 4 H, H-4 & 13), 2.85, (t, *J* = 10.8 Hz, H-6 & 11), 2.63 (t, *J* = 10.8 Hz, H-8 & 9), 1.96 (m, 4H, H-5 & 12)
4b	7.07−7.29 (m, 4H, Ar-H), 4.25 (t, *J* = 5.0 Hz, 4H, H-4 & 13), 2.82 (t, *J* = 10.6 Hz, 4H, H-6 & 11), 2.63 (t, *J* = 10.3 Hz, 4H, H-8 & 9), 1.95 (m, 4H, H-5 & 12), 2.31 (s, 3H, H-7')
4c	7.06−7.28 (m, 4H, Ar-H), 4.24 (t, *J* = 6.0 Hz, 4H, H-4 & 13), 2.84 (t, *J* = 10.8 Hz, H-6 & 11), 2.62 (t, *J* = 9.6 Hz, 4H, H-8 & 9), 1.93 (m, 4H, H-5 & 12), 2.30 (s, 3H, H-7')
5a	7.06−7.28 (m, 5H, Ar-H), 4.23 (t, *J* = 5.3 Hz, 4H, H-4 & 10), 2.81−2.86 (t, *J* = 8.9 Hz, 4H, H-6 & 8), 2.69−2.74 (m, 2H, H-1″), 1.68−1.73 (m, 4H, H-5 & 9), 1.26−1.31 (t, 2H, H-2″), 0.88−0.92 (m, 3H, H-3″)
5b	7.03−7.24 (m, 5H, Ar-H), 4.21−4.27 (t, *J* = 5.1 Hz, 4H, H-4 & 10), 2.85−2.92 (t, *J* = 8.8 Hz, 4H, H-6 & 8), 2.66−2.72 (m, 2H, H-1″), 1.70−1.74 (m, 4H, H-5 & 9), 1.42−1.46 (m, 2H, H-2″), 1.25−1.31 (m, 2H, H-3″), 0.87−0.94 (m, 3H, H-4″)
5c	6.96−7.33 (m, 10H, Ar-H), 4.19−4.25 (t, *J* = 4.9 Hz, 4H, H-4 & 10), 3.82 (d, *J* = 16.2 Hz, 2H, H-1″), 2.73−2.76 (t, *J* = 9.2 Hz, 4H, H-6 & 8), 1.76−1.81 (m, 4H, H-5 & 9)
5d	7.11−7.42 (m, 4H, Ar-H), 4.41−4.44 (t, *J* = 5.4 Hz, 4H, H-4 & 10), 2.84−2.90 (t, *J* = 9.1 Hz, 4H, C-6 & 8), 2.65−2.71 (m, 2H, H-1″), 2.3 (s, 3H, Ar-CH₃), 1.77−1.82 (m, 4H, H-5 & 9), 1.36−1.39 (m, 2H, H-2″), 0.81−0.87 (m, 3H, H-3″)
5e	7.09−7.52 (m, 4H, Ar-H), 4.28−4.34 (t, *J* = 4.84 Hz, H, H-4 & 10), 2.82−2.87 (t, *J* = 9.4 Hz, 4H, H-6 & 8), 2.59−2.63 (m, 2H, H-1″), 2.36 (s, 3H, Ar-CH₃), 1.72−1.79 (m, 4H, H-5 & 9), 1.42−1.47 (m, 2H, H-2″), 1.21−1.26 (m, 2H, H-3″), 0.81−0.85 (m, 2H, H-4″)
5f	7.12−7.69 (m, 9H, Ar-H), 4.42−4.49 (t, *J* = 5.1 Hz, 4H, H-4 & 10), 3.74 (d, *J* = 16.7 Hz, 2H, H-1″), 2.71−2.78 (m, 4H, H-6 & 8), 2.29 (s, 3H, Ar-CH₃), 1.69−1.72 (m, 4H, H-5 & 9)
5g	6.92−7.34 (m, 4H, Ar-H), 4.11−4.16 (t, *J* = 5.0 Hz, 4H, H-4 & 10), 2.76−2.81 (m, 4H, H-6 & 8), 2.63−2.68 (m, 2H, H-1″), 2.27 (s, 3H, Ar-CH₃), 1.74−1.79 (m, 4H, H-5 & 9), 1.21−1.26 (m, 2H, H-2″), 0.91−0.96 (m, 3H, H-3″)
5h	6.97−7.28 (m, 4H, Ar-H), 4.21−4.27 (t, *J* = 4.9 Hz, 4H, H-4 & 10), 2.91−2.94 (m, 4H, H-6 & 8), 2.72−2.76 (m, 2H, H-1″), 2.32 (s, 3H, Ar-CH₃), 1.69−1.74 (m, 4H, H-5 & 9), 1.41−1.45 (m, 2H, H-2″), 1.11−1.16 (m, 2H, H-3″), 0.90−0.94 (m, 3H, H-4″)
5i	7.04−7.36 (m, 9H, Ar-H), 4.280−4.33 (t, *J* = 5.1 Hz, 4H, H-4 & 10), 3.76 (d, *J* = 16.9 Hz, 2H, H-1″), 2.67−2.71 (t, *J* = 9.3 Hz, 4H, H-6 & 8), 2.29 (s, 3H, Ar-CH₃), 1.68−1.71 (m, 4H, H-5 & 9)

ᵃ Chemical shifts in ppm from TMS and coupling constants *J* (Hz) given in parenthesis; ᵇ Recorded in deuterochloroform.

Synthesis of 2-o-tolyloxy-1,3-dioxa-7,10-dithio-2-phosphacyclotridecane-2-oxide (**3b**)

A solution of 2-methylphenylphosphorodichloridate (**1b**, 2.25 g, 0.01 mole) dissolved in 20 ml of

dry dichloromethane (DCM) was added over a period of 20 minutes at 0°C to a stirred solution of allyl alcohol (1.24 g, 0.02 mole) and triethylamine (2.02 g, 0.021 mole) in 30 ml of dry DCM. After completion of addition, the temperature of the reaction mixture was raised to 45−50°C and kept for two hours with stirring. Progress of the reaction was monitored by TLC analysis, the precipitated triethyl-amine hydrochloride was separated by filtration and the filtrate was vacuum evaporated. The crude product obtained was dissolved in DCM and 1,2-ethanedithiol (1.4 g, 0.015 mole) in 25 ml of dry DCM was added dropwise with stirring. The mixture was refluxed over a period of two hours to ensure the completion of the reaction. The resulting syrupy liquid was purified by column chromatography (ethyl acetate-hexane 0:100 to 25:75) to afford 1.25 g (89%) of **3b** as a semi-solid. Analogous were prepared by adopting the above procedure.

Table 3. ^{13}C NMR spectral data of **4a-b**, **5a**, **5d**, **5h** and **5i**.

Com-pound	Chemical shifts, ppm
4a	67.9 (d, *J* = 5.2 Hz, 1C, C-4), 66.9 (s, 1C, C-13), 38.6 (s, 1C, C-6), 36.9 (s, 1C, C-11), 31.3 (s, 1C, C-5), 30.8 (s, 1C, C-12), 25.6 (s, 2C, C-8 & 9), 148.4 (s, 1C,C-1'), 120.0 (s, 2C, C-2' & 6'), 132.8 (s, 2C, C-3' & 5'), 123.9 (s, 1C, C-4')
4b	68.66 (d, *J* = 5.1 Hz, 1C, C-4), 66.69 (s, 1C, C-13), 38.2 (s, 1C, C-6), 37.4 (s, 1C, C-11), 31.3 (s, 1C, C-5), 30.1 (s, 1C, C-12), 24.5 (s, 2C, C-8 & 9), 148.9 (s, 1C, C-1'), 129.1 (s, 1C, C-2'), 131.2 (s, 1C, C-3'), 126.9 (s, 1C, C-4'), 127.3 (s, 1C, C-5'), 119.6 (s, 1C, C-6'), 16.3 (s, 1C, C-2', $\underline{C}H_3$)
5a	149.1 (s, 1C, C-1'), 134.3 (s, 1C, C-4'), 132.2 (s, 2C, C-3′ & 5′), 119.5 (d, *J* = 6.0 Hz, 2C, C-2′ & 6′), 66.61 (d, *J* = 5.8 Hz, 2C, C-4 & 10), 46.8 (d, *J* = 4, 2C, C-6 and 8), 46.1 (d, *J* = 21.7 Hz, C-1″), 31.2 (s, 2C, C-5 & 9), 36.8 (s, 1C, C-2″), 13.9 (s, 1C, C-3″)
5d	66.63 (d, *J* = 5.8 Hz, 2C, C-4 & 10), 46.2 (d, *J* = 4.1, Hz 2C, C-6 & 8), 46.1 (d, *J* = 21.5 Hz, C-1″), 37.1 (s, 1C, C-2″), 13.02 (m, 1C, C-3″), 149.8 (s, 1C, C-1′), 133.9 (s, 1C, C-4′), 132.1 (s, 2C, C-3′ & 5′), 118.9 (d, *J* = 6.1 Hz, 2C, C-2′ & 6′), 20.7 (s, 1C, C-2′, $\underline{C}H_3$)
5h	66.72 (d, *J* = 6.1 Hz, 2C, C-4 & 10), 46.1 (d, *J* = 4.1, 2C, C-6 & 8), 32.8 (s, 2C, C-5 & 9), 47.2 (d, *J* = 27.8 Hz, 1C, C-1″), 37.9 (s, 1C, C-2″), 21.2−21.7 (m, 1C, C-3″), 13.6−13.9 (m, 1C, C-4″), 150.9 (d, *J* = 7.3 Hz, 1C, C-1′), 133.8 (s, 1C, C-4′), 131.9 (s, 2C, C-3′ & 5′), 119.7 (d, *J* = 4.6 Hz, 2C, C-2′ & 6′), 22.9 (s, 1C, C-4′)
5i	66.63 (d, *J* = 6.9 Hz, 2C, C-4 & 10), 45.7 (d, *J* = 5.9 Hz, 2C, C-6 & 8), 31.3 (s, 2C, C-5 & 9), 47.2 (d, *J* = 17.8 Hz, 1C, C-1″), 148.7 (s, 1C, C-1′), 143.7 (s, 1C, C-2″), 135.7 (s, 1C, C-4′), 133.1 (s, 1C, C-3′ & 5′), 128.7 (s, 2C, C-4″ & 6″), 126.9 (s, 2C, C-3″ & 7″), 126.1 (s, 1C, C-5″), 22.9 (s, 1C, C-4′, CH₃)

ᵃ Chemical shifts in ppm from TMS and coupling constants *J* (Hz) given in parenthesis; ᵇ Recorded in deuterochloroform.

Table 4. Mass spectral data of **4b**, **5a** and **5i**.

Compound	m/z, %
4b	363[M$^+$1] (24), 267 (31), 186 (24), 162 (19), 150 (26)
5a	313[M$^+$] (30), 289 (60), 270 (56), 188 (24), 141 (20)
5i	375[M$^+$] (60), 285 (32), 281 (40), 236 (80), 190 (28), 186 (29)

ANTIMICROBIAL ACTIVITY

Compounds **4a–c** and **5a–i** were screened for their antimicrobial activity against the growth of bacteria *Staphylococcus aureus* (gram +Ve) and *Escherichia coli* (gram −Ve) and fungi *Aspergillus niger* and *Helminthosporium oryzae* at concentrations [25, 26] 20 µg/disc and 400. µg/disc. They have exhibited moderate antibacterial and moderate antifungal activity when compared to the standard reference compounds (Table 5, 6).

Table 5. Antibacterial activity of **4a–c** and **5a–i**.

Compound	Zone of inhibition, mm			
	Staphylococcus aureus		*Escherichia coli*	
	200 [a] µg/disc	400 [a] µg/disc	200 [a] µg/disc	400 [a] µg/disc
4a	14	19	13	20
4b	13	18	11	15
4c	18	16	15	15
5a	16	14	16	12
5b	17	12	18	14
5c	17	15	17	13
5d	12	18	14	13
5e	13	19	18	12
5f	16	17	16	11
5g	13	18	14	17
5h	15	17	16	18
5i	14	20	17	18
Penicillin [b]	22		21	

[a] Concentration in ppm; [b] Standard reference compound.

Table 6. Antifungal activity of **4a–c** and **5a–i.**

Compound	Zone of inhibition, mm			
	Aspergillus niger		*Helminthosporium oryzae*	
	200 [a] µg/disc	400 [a] µg/disc	200 [a] µg/disc	400 [a] µg/disc
4a	16	22	18	23
4b	14	23	16	22
4c	13	21	14	20
5a	18	24	17	23
5b	17	21	16	20
5c	18	23	17	21
5d	11	19	12	21
5e	13	22	13	21
5f	12	20	11	19
5g	18	23	15	22
5h	17	22	16	24
5i	18	25	16	23
Griseofulvin [b]	28		28	

[a] Concentration in ppm; [b] Standard reference compound.

REFERENCES

1. A. M. Caminade, J. P. Majoral, *Chem. Rev.*, **94**, 1183 (1994).
2. J. P. Dutasta, P. Simon, *Tetrahedron Lett.,* **28,** 3577 (1987).
3. For an excellent review see: F. Diederich, *Angew. Chem. Int. Ed., Eng.*, **27**, 362 (1988).
4. A. J. Tucker, C. B. Knobler, K. N. Trueblood, J. D. Cram, *J. Am. Chem. Soc.,* **111***,* 3688 (1989)**.**
5. F. Fages, J. P. Desvergue, F. Kotzbahibert, J. M. Lehn, P. Marson, A. M. Albrechtgary, H. Bouaslarent, M. Aljoubloeh, *J. Am. Chem. Soc.,* **111**, 8672 (1989).
6. A. Wallar, J. Peter-Katinic, W. M. Werher, F. Vogtle, *Chem. Ber.*, **123**, 375 (1990).
7. E. M. Seward, R. B. Hopkins, W. Sauerer, S. W. Tam, F. Diederich, *J. Am. Chem. Soc.*, **112**, 1783 (1990).
8. R. Brelow, N. Greenspoon, T. Guo, R. Zarzycki, *J. Am. Chem. Soc.*, **111**, 8296 (1989).
9. R. E. Sheridan, H. W. Whitlock,. *J. Am. Chem. Soc.*, **110,** 407 (1988).
10. K. Zygo, W. Wieczorek, K. M. Pietrusiemicz, 14th Int. Conf. Phosphorous Chemistry, Cincinnati, 1998.
11. Y. Inous Gokel, G. W. Cation, Binding by Macrocycles*,* Marcel Dekker, New York, 1991.
12. J. S. Bradshaw, R. M. Lzatt, *Acc. Chem.* Res., **30**, 388 (1997).
13. B. Zhao, F. Q. Wang, L. J. Tian, *J. Heterocycl. Chem.*, **38**, 781(2001).
14. S. Kumar, S.H. Mashnaqui, *Indian J. Chem.*, **36B**, 656 (1997).
15. L. W. Daash, S. C. Smith, *Anal. Chem.,* **23**, 853 (1961).
16. L. C. Thomas, R. A. Chittenden, *Spectrochim. Acta*, **20**, 489 (1964).
17. L. C. Thomas, Interpretation of the Infrared Spectra of Organophosphorous Compounds, Heydon, London, 1974.
18. D. E. C. Corbridge, *Top. Phosphorus Chem.*, **6**, 235 (1969).
19. L. J. Bellamy, L. J. Beecher, *J. Chem. Soc.*, 728. (1953).
20. R. A. Nyquist, *Appl. Spectrosc.*, **11,** 161 (1957).
21. M. M. Crutchfield, C. H. Dungan, J. H. Letcher, V. Mark, J. R. Van Wazer, ^{31}P Nuclear Magnetic Resonance, Interscience Publisher, New York, 1967.
22. R. M. Silverstein, G. C. Bassler, T. C. Morril, Spectrometric Identification of Organic Compounds, John Wiley & Sons, New York, 1991.
23. C. D. Reddy, R. .S. Reddy, C. N. Raju, M. Elmasri, K. D. Berlin, S. Subramanian, *Magn. Reson. Chem.,* **29**, 01 (1991).
24. E. Pretsch, J. Selible, W. Simon, T. Clerc, Tables of Spectral Data of Structure Determination of Organic Compounds, Springer-Verlag, Berlin, 1981.

25. J. C. Vincent, H. W. Vincent, *Proc. Soc. Exp. Biol., Med.*, **55**,162 (1944).

26. H. J. Benson, Microbiological Applications, 5th ed., W. C. Brown Publications, Boston, 1990.

СИНТЕЗА НА МАКРОЦИКЛИ СЪДЪРЖАЩИ ФОСФОР, АЗОТ, КИСЛОРОД И СЯРА

М. Кастурайа, М. В. Н. Реди, А. Ю. Р. Санкар, Б. С. Кумар, С. С. Реди*

Департамент по химия, Университет Сри Венкатесуара, Тирупати 517 502, Индия

(Резюме)

Синтезирани са макромолекули съдържащи фосфор, кислород, азот и сяра чрез реакция на диалилови естери на фосфорна киселина с 1,2-етандитиол или различни амини в сух дихлорометан. Всички съединения са охарактеризирани с ИЧС, ^{1}H, ^{13}C и ^{31}P ЯМР, масспектрални изследвания и елементен анализ. Оценена е също и тяхната антимикробна активност.

Simultaneous growth of high quality $Ca_{1-x}Sr_xF_2$ boules by optimised Bridgman-Stockbarger apparatus. Reliability of light transmission measurement

J. T. Mouchovski[1]*, K. A. Temelkov[2], N. K. Vuchkov[2], N. V. Sabotinov[2]

[1] Acad. Ivan Kostov Central Laboratory of Mineralogy and Crystallography,
Bulgarian Academy of Sciences, Acad. G. Bonchev St., Block 107, 1113 Sofia, Bulgaria
[2] Georgi Nadjakov Institute of Solid State Physics, Bulgarian Academy of Sciences,
72, Tzarigradsko Chaussee Blvd., 1784 Sofia, Bulgaria

Calcium-strontium fluoride boules with different Sr-content were grown simultaneously in crucible with axis-symmetrically disposed nests by utilizing an original Bridgman-Stockbarger (BS) apparatus. Implemented control upon the position of crystallization front (CF) within an unusually broad adiabatic furnace zone (AdZ) minimizes the radial heat exchange that ensures in practical planar CF-shape for proceeding a normal growth. The CF-positions are determined by empirical formulae taking into account various impacts altering the thermal field inside the load and are related to characteristic parameters, representing: 1) the mean value and 2) the alteration of absorption + light-scattering losses per unit of optical path of monochromatic beam transmitted through optical windows prepared from different sections of the boules. The irradiation is induced utilizing either CuBr vapour laser operating with wavelengths in ultraviolet (UV) or visible (Vis) regions as well as SrF_2 vapour laser operating in infrared (IR) region, or high sensitive spectrophotometer operating in UV–near IR. The use of vapour lasers allows the measurement of external transmittance (transmissivity) being carried out rapidly at wavelengths of practical interest under highly sensitive control upon the area and the position of the beam spot. The grown boules represent complete solid solutions of CaF_2 and SrF_2 with uniform compositions and negligible amounts of structural defects. Thus, they appear to be a high-grade optical material for manufacturing various elements with wide applicability in UV–IR optical systems.

Key words: optical mixed fluoride crystals, optimum growth control, structural imperfection, UV-lithography.

INTRODUCTION

The increasing industrial demands for integrated circuits with increasing number of components and increasing integral density in layouts cause a rapid development of semiconductor fabrication technology in direction of improving the efficiency of optical reduction system as key section in the exposure device for any micro-lithographic apparatus. Since the demand for an ever-decreasing minimum size is very high, it becomes increasingly important to enlarge the resolution of micro-lithographic techniques. This can be accomplished by shortening the light-wavelength used in fabrication procedure but retaining at the same time significantly high light-transmittance. An optical material, whose transmissivity is high enough to satisfy the demands of 193- and even of 157-micro-lithography, is calcium fluoride. However, this single fluoride crystal reveals a relatively high degree of intrinsic (spatial-dispersion-induced) birefringence, which is dependent strongly on the direction of light propagation [1]. For this reason the transmissivity

and refraction in CaF_2 elements vary unevenly across a beam incident. The final impact is blurring and/or reduction of image sharpness as well as loss of the light through the optical reduction system.

A generally used approach for eliminating the birefringence effect in any optical system appears to be a relevant combination of catadioptric design to crystal orientations and clocking strategies [2]. Another approach consists in nulling out the birefringence effect at a given wavelength in each optical element by combining CaF_2 with some other crystal materials (SrF_2 and BaF_2) having birefringence values that are opposite to those of CaF_2 [3]. Since the cubic fluorite symmetry of CaF_2, BaF_2, and SrF_2 is preserved when they form solid solutions, the optical properties of $Ca_{1-x}Sr_xF_2$, $Ca_{1-x}Ba_xF_2$, and $Ca_{1-x-y}Ba_xSr_yF_2$ mixed crystals are supposed to be intermediate between those of end members, CaF_2 and SrF_2, as the variations can be thought to be linearly dependent on composition. The techniques for growing mixed fluoride compounds vary from Bridgman-Stockbarger (BS) method [4] or its modifications [5], gradient freeze technique (GFT) [6] to the newly developed single crystal technology (SCT) [7].

---

* To whom all correspondence should be sent:
E-mail: jmouhovski@abv.bg

The external transmittance determining the absorption and light-scattering losses, refractive losses, structural homogeneity, and overall residual stress-induced plus spatial-induced birefringence appear to be key parameters for efficient control of crystal quality so that they have to be correctly determined and interpreted. The absorption + light scattering losses turn out to be especially convenient for linking crystal quality to growth conditions and this manner to provide growth optimum with planar or slightly convex CF-shape for single boules [8] as well as for group of boules with different composition [9].

The methodologies for measurement of birefringence and transmissivity in VUV region (below 193 nm) demand relatively sophisticated devices and apparatuses [10]. Thus, the VUV-external transmittance is being measured precisely using complicated and very expensive highly-sensitive spectrophotometers. At $\lambda \geq 193$ nm either highly sensitive UV-spectrophotometer is used or the method of laser irradiating the samples and measuring the beam attenuation is implemented. The vapour lasers irradiation (VLIr) technique has already been applied by us to measure the transmissivity, t, of optical windows, finished from different sections of calcium fluoride single boules [8] as well as of calcium-strontium fluoride boules with different Sr content, grown simultaneously in multicameral crucible with axis-symmetrical nests [9]. Our originally constructed vapour lasers are two types: 1) CuBr, operating in UV region at 248.6 nm and Vis region at 510.6 nm; 2) SrBr$_2$, operating in middle IR at 6.45 μm [11–13]. The total absorption + light-scattering losses, L_{abs+sc}, are distinguished from twice the reflectivity of the first face of used optical window, $2r$, calculated for operating wavelengths, where $t + L_{abs+sc} + 2r = 1$. We have traced a way for improvement of the control of growing conditions in order to produce boules with stable optical characteristics. The applied approach consists in derivation of empirical relationships between the CF-position inside the furnace unit and two structural parameters, the mean absorption + light-scattering losses per unit of opti-cal path, $L_{abs+sc/lwin}$, and the difference in $L_{abs+sc/lwin}$-values along the height of grown boules. Since the accurate determination of these parameters depends on the reliability of applied t-measurement technique we apprehend the necessity of comparative analysis between spectrophotometrical (SpPh) and VLIr techniques in order to assess their usefulness for specifying the needed empirical relationships. Thus, we hope to ensure much better growing control aimed at obtaining simultaneously several boules of calcium-strontium fluoride crystals with different ratio of alkali earth elements. Boules grown by such technique are unique for research purposes since the crystallization optimum may be reached, in practice, for each one of the boules, independently of alterations of solidus/liquidus temperatures.

The goals of the present study are: *first*, to analyse comparatively the data from *t*-measurements, carried out consecutively by VLIr and SpPh techniques, on optical windows of calcium-strontium fluoride crystals with different composition grown simultaneously by improved BS-technique; *second*, to obtain reliable empirical relationships between quality-determining parameters – absorption + light scattering losses per unit of optical path and its alteration along boule's height, and key growing parameter – the shift in CF-position within the furnace unit; *third*, using the obtained relationships to verify their potential for efficient control of the CF-optimum during simultaneous growth of calcium-strontium fluoride crystals with significant variation in composition.

EXPERIMENTAL

The crystal growth is accomplished in specially designed Bridgman-Stockbarger Growth System (BSGS) [14]. Its key specifications are: 1) the diaphragm, which separates the upper hot zone (Z1) from the lower cold zone (Z2) in the furnace unit, is constructed to be much thicker than usually, in this way differentiating a broad adiabatic zone (AdZ), where the radial temperature non-uniformity is marginal and the vertical temperature gradient remains constantly sufficiently steep; 2) an introduction of additional shielding system of molybdenum devices for control of the ratio of radial to axial thermal heat transfer through the moving load; 3) a precise control of residual atmosphere inside the furnace chamber by quadruple mass-spectrometer, when growing is carried out in vacuum; 4) a device for preliminary deep gas purification (< 1 vpm) when working in argon atmosphere.

The applied multichamber crucibles have central and peripheral sections (nests), the latter provided by 8 axis-symmetrical interior or by up to 9 fixed cylin-drical inserts, all sections being end-tipped conically at angle 90° [14]. Highly concentrated fluorspar ($\geq$ 99.7 wt.%) and a Suprapur® quality of SrF$_2$ (Merck) are used as starting materials for pre-melting mixtures. The optical windows are finished to meet requirements: 3 arc minutes – for parallelism, 40–20 scratch-dig – for surface finishing of both surfaces, 1–2 waves at 632.8 nm for both surfaces – for surface figure, and 80% – for clear

aperture. Two windows were prepared from each boule, the "lower" windows, adjacent to conical boules' section, are located at a mean distance of (2.18 ± 0.50) cm from the "upper" windows. The mean windows' thickness, l_{win}, varies within 0.59 and 0.67 cm interval, while the diameter takes values of (24.3 ± 0.1) mm, (29.1 ± 0.1) mm or (32.3 ± 0.1) mm according to crucible modification. Two series of windows were specified along the boules' height: Ser. 1 – for sequence of the "lower" windows and Ser. 2 – for sequence of the "upper" windows. The windows were used for measuring consecutively transmissivity, t, by VLIr and SpPh techniques. The spectroscopic technique is applied for obtaining the light transmission spectrum within the UV–near IR region (190–900 nm), that is the operating range for the used highly sensitive spectrophotometer, type Varian Cary 100. The t-values at 248.6 nm, 510.6 nm and 900 nm are taken for comparison with t-values measured at 248.6 nm, 510.6 nm, and 6450 nm by VLIr technique. The comparison in the IR region is correct since the optical transmittance is proved to alter insignificantly within this spectral region in case of pure CaF$_2$ crystals [5].

The structural parameters for the studied mixed fluorides crystals are estimated based on the equations:

$$L_{abs+sc/lwin} = [1-t-2(n_{mix}-1)^2/(n_{mix}+1)^2]/l_{win} \qquad (1)$$

$$L_{abs+sc/h2-1} = [1-t-2(n_{mix}-1)^2/(n_{mix}+1)^2]/h_{2-1} \qquad (2)$$

where the reflectivity, r_{mix}, is replaced by its functional expression of refractive index, n_{mix} [15], the dependence of which on the crystal composition is considered linear:

$$n_{mix} = (1-x)n_{CaF2} + xn_{SrF2} \qquad (3)$$

although a polynomial of second order may be a better expression, taking into account the difference between calcium and strontium ionic radii. Nevertheless, the linear approximation seems rather reasonable comparing the very close λ-dependence of the index of refraction for end-members: CaF$_2$ ($x = 0$) and SrF$_2$ ($x = 1$) [9]. The divergence from linearity should be so small that the relative errors upon estimating the quantity $2r_{mix}$ by applying the formulas for calculating errors of complex functions [16] are expected to be insignificant within investigated spectral range (Table 1).

The method of Quenched Interface (QI) determination in a fixed crucible [14] is applied to determine the position along the furnace unit of the CF shift in particular bowels according to the thermal conditions and mixtures' content. The derived formulas for CF-positions are:

$$x_{CR} = x_{CF}(x_1 = 0) - 0.36x_1(z) - [0.6T_1(x_1) + \\ + 0.18T_2(x_1)] + 0.0017[x_1(z) - 80][(T_1(x_1) - T_2(x_1)]$$

$$\text{for } 0 \le x_1(z) \le 110 \text{ mm} \qquad (4a)$$

$$x_{CR} = x_{CF}(x_1 = 110) + 0.23[x_1(z) - 110] - [0.6T_1(x_1) + \\ + 0.18T_2(x_1)] + 0.0017[x_1(z) - 110][T_1(x_1) - T_2(x_1)]$$

$$\text{for } x_1(z) > 110 \text{ mm} \qquad (4b)$$

where $x_1(z)$ is the distance of crucible movement in z-direction beginning from starting position fixed at 22 mm from the upper plane section of Z1, while $T_1(x_1)$ and $T_2(x_1)$ represent the set up rises of temperatures at given x_1-value for Z1 and Z2, respectively.

Table 1. Maximal theoretical relative errors for refractive index, n_{mix}, and twice reflectivity, $2r_{mix}$, of optical windows made of mixed fluoride crystals Ca$_{1-x}$Sr$_x$F$_2$.

Wavelength λ, nm	$(\Delta n_{mix}/n_{mix})_{max}$	$[\Delta(2r_{mix})/2r_{mix}]_{max}$
248.6	0.003602	0.0597
510.6	0.001485	0.0280
900	0.001411	0.0310
6450	0.002772	0.0644

Two growing experimental runs were carried out at different temperature regimes for both furnace zones, manifesting in different dwell levels and rises of T_1 (run 1) and T_2 (run 2). The speed of crucible withdrawal towards Z2 is maintained constant between 2 and 6 mm/h. The mutual configuration of the fixed and moving parts for additionally inserted molybdenum shielding system differs in the number of rings slipped on crucible tail. The mole part of strontium x in final Ca$_{1-x}$Sr$_x$F$_2$ crystals varies within 0.007–0.307 (9 boules for run 1) and 0.383–0.675 (8 boules for run 2). The coefficient of distribution for calcium/strontium in such crystallized solid solutions remains uniform within the experimental error along the boules' height [17]. The phase diagram of Ca$_{1-x}$Sr$_x$F$_2$ compounds is built on the basis of newly obtained data for liquid/solid phase temperature functionalities of calcium strontium solid solutions [18], corrected by estimated quantities based on assumption of linear lowering on calcium content (1–x) in both curves, starting at initial value of 43 K for $x = 0$.

RESULTS AND DISCUSSION

The x-dependence of $L_{abs+sc/lwin}$ shows a similar course within the studied UV–NIR range independently of the technique applied for t-measurement (Fig. 1a–c).

The minimum absorption + light-scattering losses per unit of window's thickness vary for x within 0.5 and 0.6 according to the operating wavelengths. At fixed composition (x = const) $L_{abs+sc/lwin}$ decreases rapidly when the wavelengths become longer as the difference diminishes for x within 0.5–0.6. This is a reflection of the peculiarities in growing conditions for the two runs. At wavelengths within UV and VIS the calculated $L_{abs+sc/lwin}$-values for Ser. 2-windows (Fig. 1a, b), based on t-data using VLIr technique, appear higher than the corresponding $L_{abs+sc/lwin}$-values, obtained by SpPh technique. The found differences diminish around function minima, where the growing conditions are supposed to be optimal to ensure a normal growth of boules with stable optical properties. Such result is grounded on the specificity of VLIr technique itself, where the relatively large size of the beam spot supposes a stronger effect of any structural defects as light-scattering centres. Nevertheless, the sizes of these centres are, evidently, too small to cause a noticeable internal light-scattering within the IR range, so that VLIr technique gives more reliable results especially in the middle IR region (Fig. 1c).

The calculated data for $L_{abs+sc/lwin}$ were used for performing a correlation analysis (Table 2).

Comparing the data, obtained consecutively by the applied techniques, one can see very high R-values throughout the studied spectral range. R is highest (0.9825) in the UV region (248.6 nm) where the relationship becomes, practically, a functional one. With increasing the wavelength, R-values reduce to 0.7287 in NIR–MIR range that is clearly shown in Fig. 2. These results indicate: *first*, both techniques provide a reliable qualitative analysis for recording and explanation of any alterations in absorption and light-scattering losses per unit of optical path, when monochromatic light passes through the studied optical windows, depending on the wavelength, composition of grown boules, and growing conditions; *second*, there are some structurally inhomogeneous areas inside testified samples, revealing themselves upon rising up the scattering probability when λ becomes longer. On the other hand, the spectrophotometrical technique itself leads to R-values varying near to 1 (0.9375–0.9943) for the chosen values of λ within UV–NIR spectral range. Such strong correlations confirm the high reliability for SpPh-technique and the used spectrophotometer.

At the same time, the VLIr technique itself manifests significantly lower R-values in comparison with those obtained by SpPh, as R declines fast, decreasing λ towards IR region due to disor-

dering of data points and increase in their SD. More likely, the reason for such behaviour lies in the relatively large spot of laser beam, different in size for the used vapour lasers, which should promote an increasing effect of any structural inhomogeneity on the total attenuation for passing beam.

a

b

c
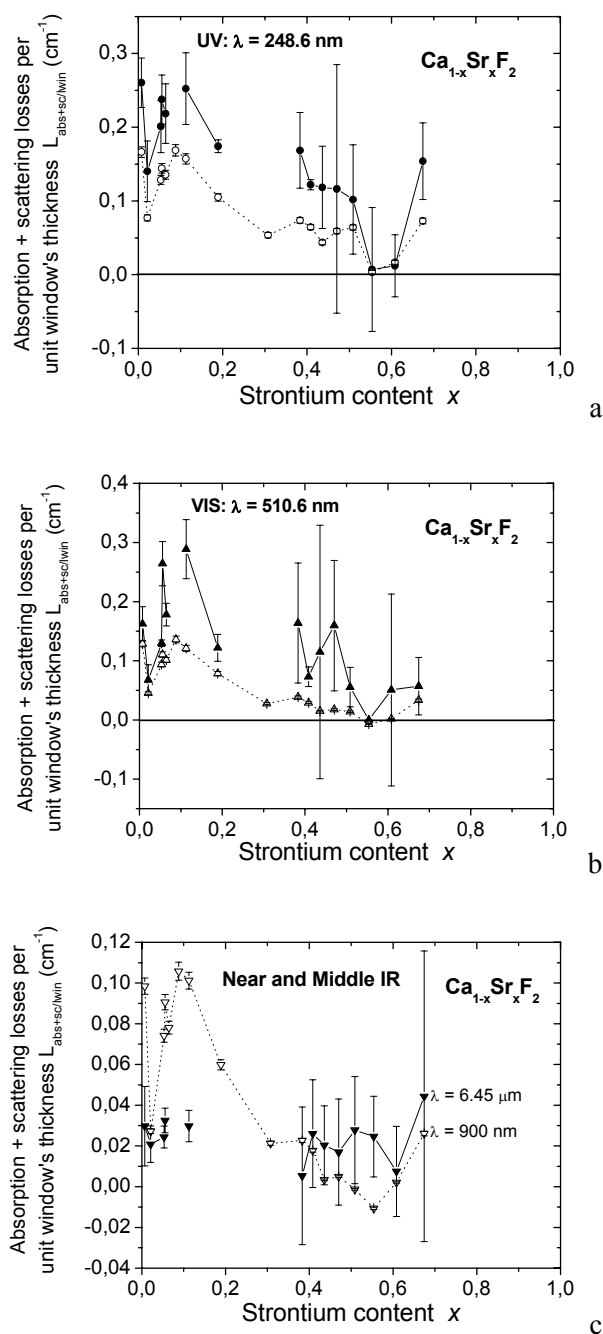
Fig. 1. Absorption plus internal light-scattering losses as part of the total losses for Ser. 2 Ca$_{1-x}$ Sr$_x$F$_2$ optical windows with different strontium contents measured in UV–IR range by using of vapour laser irradiation and spectrophotometric techniques. a) 248.6 nm: (●) - VLIr, (o) - SpPh;   b) 510.6 nm: (▲) - VLIr, (△) – SpPh;   c) NIR (900 nm): (▼) - VLIr and MIR (6.45 μm), (▽) - SpPh.

Table 2. Correlational analysis of absorption plus internal light-scattering losses in $Ca_{1-x}Sr_xF_2$ optical windows obtained from VLIr and SpPh t-measurements.

Statistics		Coefficient of linear correlation R / (SD)					
$L_{ab+sp/lwin}$		Vapor Laser Irradiation			Spectrophotometer		
$L_{ab+sp/lwin}$	λ (nm)	248.6	510.6	6450	248.6	510.6	900
VLIrr	248.6	●	**0.8725** (1.1029)	**0.4359** (1.8789)	**0.9825** (0.4200)	**0.9537** (0.6794)	**0.9440** (0.7446)
	510.6	**0.8725** (1.1029)	●	**0.0932*** (0.0885)	**0.7862*** (0.0514)	**0.7766*** (0.0524)	**0.7783*** (0.0522)
	6450	**0.4359** (1.8789)	**0.0932*** (0.0885)	●	**0.7159** (0.3758)	**0.7246** (0.3709)	**0.7287** (0.3685)
SpPh	248.6	**0.9825** (0.4200)	**0.7862*** (0.0514)	**0.7159** (0.3758)	●	**0.9680** (2.8450)	**0.9375** (3.9446)
	510.6	**0.9537** (0.6794)	**0.7766*** (0.0524)	**0.7246** (0.3709)	**0.9680** (2.8450)	●	**0.9943** (0.0053)
	900	**0.9440** (0.7446)	**0.7783*** (0.0522)	**0.7287** (0.3685)	**0.9375** (3.9446)	**0.9943** (0.0053)	●

* The standard deviation (SD) of the particular point is not taken into consideration.
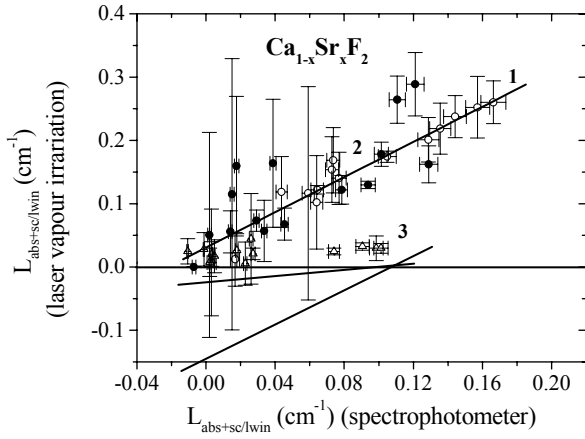
Fig. 2. Linear fit regression for two series of data for absorption + internal light-scattering losses in $Ca_{1-x}Sr_xF_2$ optical windows obtained consecutively by vapour laser irradiation and spectrophotometric techniques at wavelengths within UV–IR range: 1) 248.6 nm (R = 0.9825, SD = 0.42); 2) 510.6 nm (R = 0.7766, SD = 0.0524); 3) 900 nm/6.45 μm (R = 0.7287, SD = 0.3685).

Fig. 3. Difference in absorption plus light-scattering losses, determined at particular wavelength within UV–NIR range, between pairs of optical windows prepared from non-adjacent parallel sections of $Ca_{1-x}Sr_xF_2$ boules as a function of the strontium content x at λ 248.6 nm (o); 510.6 nm (●) and 900 nm/6.45 μm (Δ).

Longitudinal inhomogeneity of the grown boules is assessed following the variations of $L_{abs+sc/h2-1}$ on strontium content x and λ within UV–MIR (Fig. 3). Since the shift of CF also depends on x [9], in this way we found out indirect relationship between structural and growing parameters. A larger absolute divergence from zero is seen for run 1-boules compared to run 2-boules. The differences for run 1 are positive with the exception of the boule with the lowest x (0.0073), whereas they appear negative or near to zero for run 2-boules.

Most of the studied run 1-boules show higher divergences in the Vis region compared to UV and IR regions that is just the opposite of run 2-boules,

the $L_{abs+sc/h2-1}$-values of which approach zero in the Vis region. The established trend for increase in the parameter $L_{abs+sc/h2-1}$ towards the top section of run 1-boules testifies the changing towards worse growing conditions during crystallization. At the same time, the growing conditions during crystallization of run 2-boules turn out either constant (for three of the boules) or change to better (for the remaining five ones) that corresponds to the observed variations of $L_{abs+sc/h2-1}$-values near to or noticeably below zero. For two boules (with $x \approx$ 0.38 and $x \approx$ 0.5) the divergences appear insignificant and close to zero, which reveals high structural homogeneity along boules' height, and suggests

reaching the optimum set of growing conditions. The opposite trend for $L_{\text{abs+sc/h2-1}}$-alteration in the Vis region emphasizes again the importance of growing conditions for ensuring a normal growth with minimum structural defects acting in this case as internal scattering sites rather than colour (absorption) centres for Vis-light.

Optical properties and crystallization front position

The optical quality of grown boules, assessed by involved semi-empirical parameters, is related to growing conditions *via* the shift of CF-positions, x_{CF}, according to formulas (4). The distance from conical tip of crucible's interior (where nucleation starts) to lower plane section of AdZ ($z = 0$) is marked by $x_{\text{con}}(z)$. Then the height of crystallized volume is determined by the difference ($x_{\text{CF}} - x_{\text{con}}$), where for simplicity of analysis the quantities are reduced by division to 24 mm (AdZ thickness) and marked by asterisk. The variable x_1^* represents the distance of crucible withdrawal towards Z2 as a part of total crucible movement during the run. The cross points of $x_{\text{CF}}^*(x_1^*)$ curves with straight line $x_{\text{con}}^*(x_1^*)$ specify a nucleation curve $x_{\text{nucl}}^*(x_1^*)$ that manifests the crystallization start in particular nests.

Several peculiarities may be discussed following the dependences in this study (Fig. 4a, b):

1) The CF-positions shift equidistantly at constant slope towards Z2 during approximately 50% of total crucible movement, remaining within Z1 or AdZ. This determines planar or convex shape for CF that is favourable for normal growth with minimal built in structural defects.

2) The second half of the boules are crystallized under entirely different thermal conditions expressed in gradual decrease of the negative slope of x_{CF}^*-curves (run 1) or in twice changed sign of the curves' slope (run 2), being implemented into AdZ or the adjacent lower section of Z1. This is due to redistribution of thermal exchange between the load and its surroundings causing significant radial heat losses [9]. Under such thermal conditions the CF-shape is expected to vary slightly around planarity, being closer to convex if CF-position turns out to be above the middle cross section of AdZ, which ensures an optimum for growing boules with perfect optical quality. This is a result of the effective removal of plenty of micro-defects (impurities, parasitic nuclei, and others) aside from the thin layer in front of the CF.

3). The starting point for $x_{\text{nucl}}^*(x_1^*)$-curves varies widely between –0.27 (run 1, $x = 0.307$) and +4.41 (run 2, $x = 0.675$) that shows great differences in the initial nucleation conditions at the tip of particular nests for further propagation of normal growth. This way, two of run 1-boules, with the highest x (0.189 and 0.307), turn out under worst conditions in regards to the initial shape of the just nucleated CF, which remains firmly concave within the entire conical section, thus initiating dendroidal crystallization (Fig. 5).
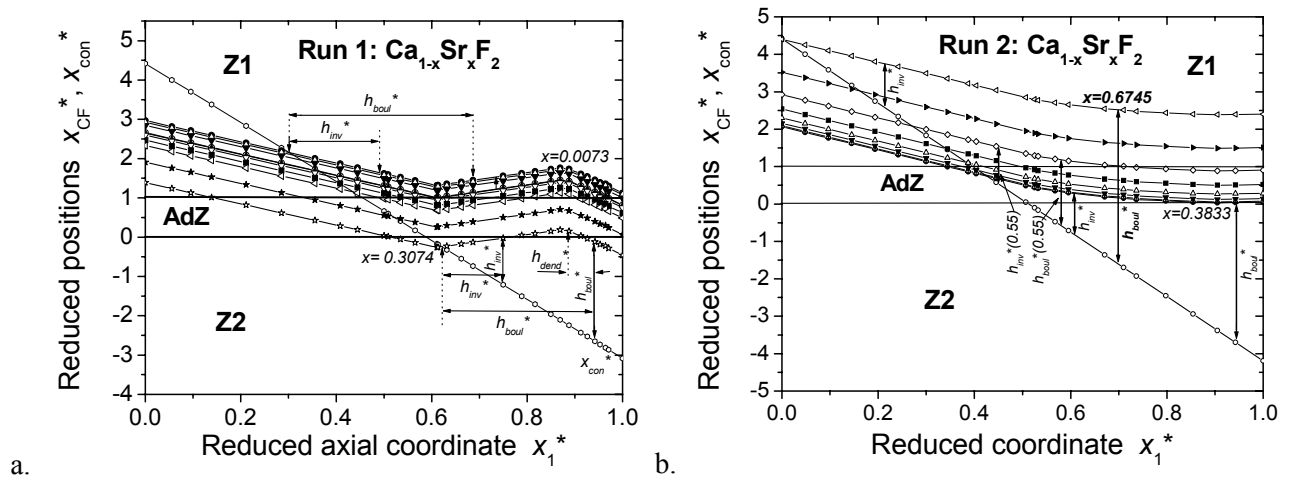
Fig. 4a, b. Reduced positions of the CF and of the conical crucible's tips along the furnace unit during two experimental runs carried out under different thermal conditions into a load, representing a multichamber graphite crucible charged with portions of pre-melted CaF$_2$-SrF$_2$ mixtures for growing of Ca$_{1-x}$Sr$_x$F$_2$ crystals.
a) run 1: (●) – 0.007, (△) – 0.021, (▼) – 0.054, (o) – 0.056, (▽) – 0.065, (■) – 0.088, (◁) – 0.113, (v) – 0.189, (✶) – 0.307, (▲) – Centre-0.213, (¤) – x$_{\text{con}}$*; b) run 2: (●) – 0.383, (△) – 0.408, (▼) – 0.436, (△) – 0.471, (■) – 0.509, (◇) – 0.554, (▶) – 0.608, (◁) – 0.675, (o) – x$_{\text{con}}$*.

4) The higher position of x_{nucl}^* within Z1 suggests larger and more convex curvature of the CF favouring the efficiency of self-purifying mechanism. Here, it has to be taken into consideration that the magnitude of the vertical temperature gradient decreases upwards in the furnace unit approximately up to the middle cross section of Z1 that leads to increase in melt suppercooling within the thin layer in front of the CF, which, in turn, initiates deterioration in the normal growth with rapidly propagating dendroidal crystallization [20]. Besides, stronger radial inhomogeneities will arise into the load [21, 22] as far as CF shifts from AdZ, which would disrupt additionally the normal growth. As a whole, the growing conditions for run 2 seem to be much more favourable to ensure a normal growth at steeper vertical temperature gradient and gradually changing negligible shift for most CF within the AdZ that implies a perfect crystal quality.
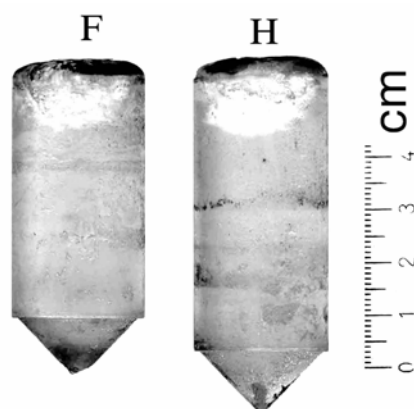
Fig. 5. Boules grown during run 1 with upper section of dendroidal crystallization: F – $x = 0.307$, H – $x = 0.189$.

CONCLUSIONS

Important relationships between structural, technological and characteristic parameters, controlling a simultaneous growth in multichamber crucible and originally modified furnace unit of BS apparatus of calcium–strontium fluoride boules of different composition, are firmly established. The growing conditions are set to be optimal *via* appropriate shift of the CF-position according to the composition of starting mixtures. The optimum is reached when the CF are positioned predominantly in an unusually broad adiabatic zone, while the real crystallization rate remains steady slightly over the set up crucible movement speed. A realistic assessment of the grown boules optical quality is being implemented by measuring the transmissivity t of optical windows, finished from different boules' sections, and separating the actual absorption from refractive losses. The t-measurements are performed by two different techniques using a highly intensive vapour lasers irradiation within DUV–NIR spectral range (VLIr) and a highly sensitive spectrophotometer (SpPh). The advantages of VLIr over SpPh technique lie in the higher efficiency of VLIr since it allows large statistics for a short time at particular wavelengths, high sensitivity and precise control of the area and position of the beam spot. The grown mixed fluoride crystals represent solid solutions with wide range of compositions and possess practically uniform distribution of Ca and Sr atoms inside the lattice and nearly perfect microstructure especially for boules with x between 0.5 and 0.6.

The applied original growing technique and reliable methods for assessing the key optical properties imply production of high-grade optical material with stable unique characteristics ranged from DUV to NIR. This material is favourable for UV-lithography optics being also suitable for optics of newly developed vapour lasers.

The successful reiteration of simultaneously grown calcium-strontium fluoride boules with widely altering composition has acquired also a definite scientific importance supplying the researchers with perfect material for new explorations in non-linear optics as appear to be cleaning of femto-second pulses and precise measurements of short high intensive laser pulses in UV.

REFERENCES

1. J. H. Burnet, Z. H. Levine, E. L. Shirley, *Phys. Rev. B: Condens. Matter. Mater. Phys.,* **64**, 241102-R (2002).
2. http://www.tf.unikiel.de/matwis/amat/elmat_en/kap_6/advanced/t6_6_1.html.
3. D. C. Allan, N. F. Borrelli, C. M. Smith, R. W. Sparrow, *U.S. Patent 6806039*.
4. D. C. Stockbarger, *J. Opt. Soc. Am.*, **39**, 731 (1949).
5. J. T. Mouchovski, *Prog. Cryst. Growth Charact. Mater.*, **53**, 79 (2007).
6. K. Hein, E. Buhrig, H. Gohler, *Cryst. Res. Technol.*, **27**, 351 (2006).
7. K. A. Pandelisev, in: Plate Form Having Superior Properties. (Proc. 2nd Int. Symp. 157 Lithography, Dana Point, CA, USA, 2001).
8. J. T. Mouhovski, K. A. Temelkov, N. K. Vuchkov, N. V. Sabotinov, *J. Phys. D*: *Appl. Phys.*, **40**, 7682 (2007)
9. J. T. Mouhovski, K. A. Temelkov, N. K. Vuchkov, N. V. Sabotinov, *Compt. Rend. Acad. Bulg. Sci.*, **62**, 687 (2009).
10. B. Wang, M. Ward, R. Rockwell, J. List, *Photonic Spectra*, 62 (2002).
11. N. K. Vuchkov, K. A. Temelkov, N. V. Sabotinov, *IEEE J. Quantum Electron.,* **37,** 1538 (2001).
12. N. K. Vuchkov, K. A. Temelkov, N. V. Sabotinov, *IEEE J. Quantum Electron.,* **41**, 62 (2005).

13. K. A. Temelkov, N. K. Vuchkov, B. L. Pan, N. V. Sabotinov, B. Ivanov, L. Lyutov, *J. Phys. D: Appl. Phys.,* **39**, 3769 (2006).
14. J. T. Mouchovski, V. Tz. Penev, R. B. Kuneva, *Cryst. Res. Technol.*, **31**, 727 (1996).
15. Optical Crystals by Optovac, Handbook 82, Optovac Inc., North Brookfield, Massachusetts, 5-3 (1982).
16. G. L. Squires, Practical Physics, McGraw-Hill, London, 1968, p. 246.
17. J. T. Mouchovski, *Bulg. Chem. Commun.* **39**, 3 (2007).
18. D. K. Kimm, M. Rabe, R. Bertram, R. Uecker, L. Parthier, *J. Cryst. Growth*, **310**, 152 (2008).
19. B. Kostova, J. Mouchovski, O. Petrov, L. Dimitrov, L. Konstantinov, *Mater. Chem. Phys.*, **113**, 260 (2009).
20. V. A. Arhangelskaya, V. M. Reiterov, I. L. Smolyanskii, *Neorg. Mater.*, **12**, 1560 (1976) (in Russian).
21. R. J. Naumann, *J. Cryst. Growth*, **58**, 554 (1982).
22. T. Jasinski, A. F. Witt, *J. Cryst. Growth,* **71**, 295 (1985).

ЕДНОВРЕМЕНЕН РАСТЕЖ НА КРИСТАЛНИ БУЛИ ОТ Ca$_{1-X}$Sr$_X$F$_2$ С РАЗЛИЧНО СЪДЪРЖАНИЕ НА Sr ЧРЕЗ ПОДОБРЕНА АПАРАТУРА НА БРИДМАН-СТОКБАРГЕР. НАДЕЖДНОСТ НА ТЕХНИКИТЕ ИЗПОЛЗВАНИ ЗА ИЗМЕРВАНЕ НА СВЕТОПРОПУСКЛИВОСТТА

Й. Т. Муховски[1]*, К. А. Темелков[2], Н. К. Вучков[2], Н. В. Съботинов[2]

[1] *Централна лаборатория по минералогия и кристалография „Акад. Иван Костов",*
Българска академия на науките, ул. „Акад. Г. Бончев", Блок. 107, 1113 София
[2] *Институт по физика на твърдото тяло „Георги Наджаков",*
Българска академия на науките, бул. „Цариградско шосе" № 72, 1784 София

(Резюме)

Осъществено е едновременно израстване на кристални були от калциево-стронциев флуорид с различен количествен състав в симетрични спрямо аксиалната ос отделения на тигел като е използвана оригинална Бридман-Стокбаргер апаратура. Контрол върху положението на кристализационния фронт (КФ) в границите на необичайно широка адиабатна зона (АдЗ) на пещта, минимизира радиалния топлообмен, което осигурява практически равнинна форма на КФ за нормален растеж на отделните були. Положението на КФ е определено чрез емпирични формули, които отчитат различните фактори, влияещи върху термично поле в товара. Позицията на КФ е свързана с характеристични параметри, представляващи: 1) средната стойност и 2) измене-нието на сумата от абсорбционните загуби и тези от светоразсейване за единица оптичен път на моно-хроматичен светлинен лъч, пропускан през оптически прозорци, изготвени от различни сектори на булите. Излъчването е предизвикано или чрез използване на CuBr лазер с метални пари, работещ при дължина на вълната в ултравиолетовия (УВ) и видимия (Вид) диапазони, както и SrF$_2$ лазер с метални пари, работещ в инфрачервения (ИЧ) диапазон, или чрез високочувствителен спектрофотометър, работещ в УВ–близкия ИЧ диапазон. Използването на лазери с метални пари позволява измерването на външното светопропускане да бъде осъществено бързо за фиксирани дължини на вълната с интерес за практиката при високочувствителен контрол върху площта и положението на петното на лъча. Израслите були представляват еднородни твърди разтвори на CaF$_2$ и SrF$_2$ с незначително присъствие на структурни дефекти. Така получени, те са висококачествен оптически материал за изработване на разнообразни елементи с широка приложимост в УВ–ИЧ оптически системи.

One new carboxylato-bridged dimeric network of Co(II):
Synthesis and structural aspects

A. Datta[1], W.-S. Hwang[1], N. Revaprasadu[2]*

[1] *Department of Chemistry, National Dong-Hwa University, 1, Sec. 2, Da-Hsueh Rd., Shoufeng, Hualien – 974, Taiwan, Republic of China*
[2] *Department of Chemistry, University of Zululand, Private Bag X1001, 3880 KwaDlangezwa, Republic of South Africa*

A new carboxylato-bridged Co(II) dimeric complex, formulated as $\{Co(H_2O)_5[Co(2,6\text{-}pdc)_2].2H_2O\}$ (H_2PDC = Pyridine-2,6-dicarboxylic acid), was synthesized in solid state under mild conditions, solved by single crystal X-ray diffraction techniques and characterized by elemental analysis, IR and electronic spectra, thermogravimetric analysis and variable temperature magnetic moments. The structural investigation shows that the crystal system of the new complex is monoclinic, having space group $P2(1)/c$, $a = 8.3545(5)$, $b = 27.1474(16)$, $c = 9.5882(6)$ Å, $\beta = 99.089(1)°$, and $Z = 4$. The neighbouring Co atoms are bridged by carboxylate group of one pdc ligand and the dihedral angle defined by the mean planes of two pdc ligands is 88.6°, showing that they fall almost perpendicular. The effective magnetic moment μ_{eff} value of the new complex is close to 5.31 μ_B at 302 K, and much larger than the spin-only value of 3.87 μ_B for high-spin Co(II). The complex is extended into a three-dimensional hydrogen bonding network.

Key words: Crystal structure, cobalt(II), carboxylato-bridge, H_2-PDC, spectral studies, TGA analysis.

INTRODUCTION

The compounds containing carboxylate group are an important class of ligands in inorganic and bioinorganic chemistry. Metal complexes containing monocarboxylic acids are well known regarding the versatility of the carboxylate group as an inner-sphere ligand [1]. Rigid dicarboxylates are particularly attractive because the metal carboxylate bonding is also rigid and the use of appropriate spacers can lead to predetermined network structures [2–5].

Previously it was found out that the reaction of simple transition metal salts with functionalized carboxylic and dicarboxylic acids leads to the isolation of soluble materials, which were structurally elucidated [6–8]. H_2PDC (pyridine-2,6-dicarboxylic acid) is an efficient ligand, which is usually used as a tridentate ligand, as well as a bridging linker in the chemical design of metal-organic molecular assemblies [9–13]. H_2PDC forms chelates with simple metal ions and oxo-metal cations and it can display widely varying coordination behaviour, functioning as a multidentate ligand. Other isomeric pyridine-dicarboxylic acids, e.g. pyridine-2,3-, 2,4- and 2,5-dicarboxylic acids, behave like picolinic acid and act as bidentate (chelating) N,O donors. A very important characteristic of these ligands is their diverse biological activity. Pyridine-2,3-dicarboxylic acid is an intermediate in the tryptophan degradation pathway and it is precursor for NAD [14]. However, reports for H_2PDC's coordination complexes having 3D open framework structures are rarely seen [15, 16].

In this regard, Ghosh *et al.* [17] reported the complex, [Co(pdc)(4,4'-bpy)].1/2MeOH, where pyridine-2,6-dicarboxylic acid has been used as a ligand for binding more than one metal ion through carboxylate bridging to form 1-D coordination polymeric chains.

On the basis of the aforementioned considerations, herein, we describe the crystal structure, spectroscopic study, thermogravimetric analysis and low-temperature magnetic properties of a new carboxylato-bridged cobalt(II) complex (**1**), using pyridine-2,6-dicarboxylic acid, in which the Co(2) atom possesses a distorted octahedral geometry.

EXPERIMENTAL

All the chemicals used for the synthesis were of reagent purity grade. Cobalt(II) nitrate and pyridine-2,6-dicarboxylic acid (Aldrich) were used as received.

C, H, and N analyses were carried out using a Perkin-Elmer 240C elemental analyzer. Infrared spectra were recorded on a Perkin-Elmer 883 infrared spectrophotometer in the range 4000–200 cm⁻¹

* To whom all correspondence should be sent:
E-mail: nrevapra@pan.uzulu.ac.za

as KBr pellets. Electronic spectra were measured on a Hitachi U-3400 (UV-Vis-NIR) spectrophotometer in methanol. The thermal investigation was carried out on a Shimadzu TGA-50 thermal analyser in a dynamic nitrogen environment. Magnetic susceptibility measurements were carried out on a Quantum Design SQUID MPMS-XL susceptometer apparatus working in the range 2–302 K.

Synthesis of {Co(H$_2$O)5[Co(2,6-pdc)2].2H$_2$O} (1)

To a 10 ml methanolic solution of cobalt(II) nitrate (2 mmol, 0.582 g), 10 ml of aqueous solution of pyridine-2,6-dicarboxylic acid (2 mmol, 0.334 g) were added upon stirring and reaction mixture was kept at room temperature. Several days later good quality green square-shaped crystals of **1** were separated. They were filtered, washed with methanol-water mixture (1:1) and dried. Yield: 73%. Anal. Calcd. for $C_{14}H_{20}Co_2N_2O_{15}$: C 29.25, H 3.51, N 4.87%; Found: C 29.19, H 3.46, N 4.82%.

Crystallography

The details concerning crystal data, data collection characteristics and structure refinement are summarized in Table 1. Diffraction data were measured at 100(2) K on a Bruker AXS P4 four-circle diffractometer fitted with graphite-monochromated CuKα radiation, $\lambda = 0.71073$ Å and the $\omega : 2\theta$ scan technique for data collection within a θ range of 1.50–28.33°.

Table 1. Crystal data and refinement parameters for complex **1**.

Chemical formula	$C_{14}H_{20}Co_2N_2O_{15}$
Molecular weight	574.18
Space group	P2(1)/c
Wavelength	0.71073 Å
Crystal system	Monoclinic
a (Å)	8.3545(5)
b (Å)	27.1474(16)
c (Å)	9.5882(6)
α (°)	90
β (°)	99.089(1)
γ (°)	90
T (K)	100(2)
V (Å^3)	2153.0(2)
Z	4
D (mg/m^3)	1.771
Absorptin coefficient (mm^{-1})	1.620
θ for data collection (°)	1.50–28.33
Reflections collected	16028
Independent reflections	5354
Goodness-of-fit on F^2	1.044
Final R indices [$I > 2\sigma(I)$]	$R1 = 0.0310$, $wR2 = 0.0740$
R indices (all data)	$R1 = 0.0378$, $wR2 = 0.0764$
Largest diff. Peak and hole	0.469 and –0.339 $e{\cdot}Å^{-3}$

The structure was solved by direct methods using the SHELXTL PLUS [18] system and refined by

full-matrix least-squares methods based on F^2 using SHELXL93 [19]. In this case, non-hydrogen atoms were calculated employing anisotropic displacement parameters and the hydrogen atom positions were calculated with fixed isotropic displacement parameters.

RESULTS AND DISCUSSION

Crystal structure section

The ORTEP representation of **1** is shown in Fig. 1 with selected bond lengths and angles summarized in Table 2.
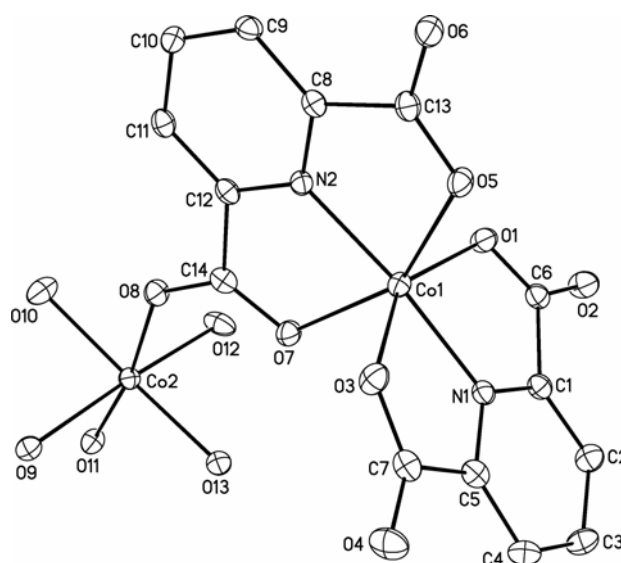
Fig. 1. An ORTEP plot of complex **1** drawn with 40% probability level. Hydrogen atoms have been omitted for simplicity.

Complex **1** crystallizes in monoclinic system with space group *P2(1)/c*. It consists of elongated octahedral molecules, where the Co(1) centre exhibits a coordination surrounding O$_4$+N$_2$, of the type 4+2. The six donor atoms are the one N-pyridine and two O-carboxylate donors of each tridentate pdc ligand. They define well a mean plane (deviations < 0.032 Å), which virtually contains the metal atom (deviation of 0.019 Å). The *trans*-angles, O(1)–Co(1)–O(3) and O(5)–Co(1)–O(7), have a significantly low value. Both O–Co–O *trans*-angles of **1** reveal the rather rigid structures of such tridentate ligands, which are approximately planar (within 0.019 Å). In contrast, the *trans*-angle N–Co–N [N(1)–Co(1)–N(2)] is quite close to ~ 180° and the dihedral angle defined by the mean planes of two pdc ligands is 88.6°, showing that they fall almost perpendicular.

The Co(1) and Co(2) atoms are held together by single *μ*-carboxylate oxygen of the pdc ligand. The Co(2) atom is chelated by one oxygen atom of

bridging-carboxylate from the pdc ligand and it coordinates five oxygen atoms from five water molecules. Thus, the Co(2) atom exhibits a distorted octahedral coordination geometry. Among the six coordination sites, the four sites are almost in an equatorial plane (the deviation from a regular square-planar structure is 9.47°) and these are occupied by four oxygen atoms from four water molecules, the two sites in the axial position are occupied by one oxygen atom from bridging-carboxylate and one oxygen atom from one water molecule. The deviation from the octahedral geometry is also indicated by the bond angles between the atoms in the *cis* positions, which vary from 79.83(5) to 99.25(5)° as well as the angles involving the *trans* positions that vary to a large extent from 168.78(5) to 176.58(5)°. The Co(2) sites are located on a crystal inversion centre.

Table 2. Selected bond lengths (in Å) and interbond angles 9in °) for complex **1**.

Co(1)–N(1)	2.0157(16)
Co(1)–N(2)	2.0241(15)
Co(1)–O(1)	2.1708(13)
Co(1)–O(5)	2.1802(12)
Co(1)–O(3)	2.113(13)
Co(1)–O(7)	2.2148(12)
Co(2)–O(8)	2.0868(12)
Co(2)–O(9)	2.1681(13)
Co(2)–O(10)	2.0525(14)
Co(2)–O(11)	2.0877(13)
Co(2)–O(12)	2.0516(14)
Co(2)–O(13)	2.0832(13)
N(1)–Co(1)–N(2)	171.83(6)
O(1)–Co(1)–O(3)	149.90(5)
O(5)–Co(1)–O(7)	151.48(5)
O(1)–Co(1)–O(7)	96.82(5)
O(3)–Co(1)–O(5)	85.36(5)
O(8)–Co(2)–O(10)	79.83(5)
O(10)–Co(2)–O(9)	86.09(5)
O(9)–Co(2)–O(11)	85.65(5)
O(11)–Co(2)–O(13)	99.25(5)
O(13)–Co(2)–O(12)	88.31(6)
O(12)–Co(2)–O(8)	87.29(5)
O(8)–Co(2)–O(11)	170.37(5)
O(10)–Co(2)–O(13)	168.78(5)
O(9)–Co(2)–O(12)	176.58(5)

Extensive intermolecular hydrogen bonds are formed in the crystal by means of the five coordinated water molecules O9, O10, O11, O12 and O13 and the two lattice water molecules O14 and O15, the two coordinated carboxylic oxygen atoms O1 and O5, and three uncoordinated carboxylic oxygen atoms O2, O4 and O6, respectively. Thus, the complex is extended into a three-dimensional network by means of hydrogen bonds (Fig. 2). The data on hydrogen bonds for **1** is summarized in Table 3.
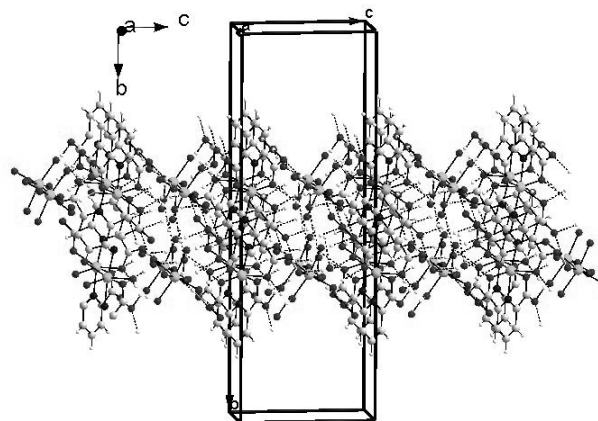
Fig. 2. The crystallographic packing diagram of complex **1** along the *a* axis.

Spectral data section

The infrared spectrum of **1** is very consistent with the structural data presented in this paper. It shows characteristic absorption of the coordinated carboxyl groups. The strong bands at 1646 and 1400 cm^{-1} for Co(1) centre and 1680 cm^{-1} and 1395 cm^{-1} for Co(2) centre were assigned as v_{as} (COO$^-$) and v_{sym} (COO$^-$) stretching vibrations, respectively. In the low energy region, a series of absorption peaks is also observed, such as v_{O-C-O} at 1670 cm^{-1}, v_{OH} at 925 cm^{-1}, v_{C-H} at 1370 cm^{-1} [20]. There are also three absorption peaks at 3385, 3345 and 3047 cm^{-1}, due to v_{O-H} vibration modes for water molecules. The absorption bands in the 1400–1600 cm^{-1} region arise from the skeletal vibrations of the aromatic rings of the ligand.

The UV-visible absorption peaks correspond to the absorptions for octahedral Co(II), which has features between 19600 and 21600 cm^{-1} assigned to the $^4T_{1g}(F) \rightarrow {}^4A_{2g}(F)$ and $^4T_{1g}(F) \rightarrow {}^4T_{1g}(P)$ transitions, respectively [21].

Table 3. Data on hydrogen bonds for **1**.

Bond	Distances, Å	Bond	Distances, Å
O11$_{cw}$…O14$_{lw}$	2.655	O11$_{cw}$…O5	2.767
O10$_{cw}$…O15$_{lw}$	2.986	O10$_{cw}$…O6	2.636
O12$_{cw}$…O15$_{lw}$	2.821	O12$_{cw}$…O4	2.723
O9$_{cw}$…O1	2.799	O9$_{cw}$…O6	2.684
O13$_{cw}$…O2	2.710	O15$_{lw}$…O9$_{cw}$	2.938
O14$_{lw}$…O4	2.769	O14$_{lw}$…O2	2.781

cw = coordinated water; lw = lattice water.

Thermogravimetric study

Thermogravimetric analysis was carried out in N$_2$ atmosphere with a heating range of 10°C·min^{-1}. The TGA curve indicates that complex **1** experienced three steps of weight loss. It began to lose lattice water slowly at 115°C and this ended at about 140°C. The loss of an aqua ligand began at 160°C

rapidly and ended at 190°C. This could occur because the latter has much higher bond energy than the former and higher lattice energy. Pyridine-2,6-dicarboxylate rapidly decomposes at 270°C and the process ends at 295°C.

Magnetic moment measurements

The effective magnetic moment, μ_{eff} value of **1** is close to 5.31 μ_B at 302 K, and much larger than the spin-only value of 3.87 μ_B for high-spin Co(II). Upon cooling down, the μ_{eff} value decreases gradually to 3.96 μ_B at 18 K. The magnetic behaviour should be due to a larger orbital contribution arising from the $^4T_{1g}$ ground state of Co(II). It is very close and comparable with the μ_{eff} value on cooling 3.94 μ_B, derived by Liao *et al.* [22]. The magnetic calculation has been done with the susceptibility equation based on $H = -2J(S_1S_2 + S_2S_1)$.

$$(\chi_M = (Ng2\beta^2/4kT)[1 + \exp(-2J/kT) + 10\exp(J/kT)]/[1 + \exp(-2J/kT) + 2\exp(J/kT)] + N\alpha \qquad (1)$$

Where $\chi = \lambda/kT$, χ_M denotes the susceptibility per dinuclear complex, λ is the spin-orbital coupling constant and $N\alpha$ is the temperature independent paramagnetism. Magnetic data were well fitted to Eqn. (1) in the temperature range of 18–302 K with $\lambda = -130.6$ cm^{-1} and $g = 2.31$.

Very recently, Ribas and coworkers [17] derived the magneto-structural relationship for carboxylate-bridged 1-D coordination polymeric chain of Co(II) complexes, $J = -5.35$ cm^{-1}. Obviously, here the calculated J value may be affected by the spin-orbital coupling and should be regarded only as the highest possible value for the antiferromagnetic coupling. In our present complex (1), an agreement factor has been defined as $\Sigma = (\chi^{calcd} - \chi^{obsd})^2/\Sigma(\chi^{obsd})$ and its value was 2.73×10^{-5}.

CONCLUSION

One new carboxylato-bridged Co(II) complex, has been reported in which two different Co centres possess distorted octahedral geometry. Electronic spectra of the complex support its geometry as established based on X-ray analysis. Magnetic studies indicate that upon cooling down, the μ_{eff} value decreases gradually to 3.96 μ_B at 18 K. We are presently probing the capability of different modes of pyridine-dicarboxylic acids, like pyridine-2,3-, 2,4- or 2,5-dicarboxylic acids, to form metal-organic frameworks structures acting as bidentate (chelating) N,O donors on the Co(II) and other transition metal systems.

Supplementary material

Crystallographic data have been submitted to the Cambridge Crystallographic Data Center with deposition number 273379. Copies of the information may be obtained free of charge from the Director, CCDC, 12 Union Road, Cambridge, CB2 1EZ, UK (fax: +44-1233-336033; E-mail: deposit@ccdc.cam.ac.uk; http://www.ccdc.cam.ac.uk).

REFERENCES

1. R. C. Mehrotra, R. Bohra, Metal Carboxylates, Academic Press, London, 1983.
2. M. Eddaoudi, H., Li, O. M. Yaghi, *J. Am. Chem. Soc.*, **123**, 1391 (2000).
3. J.-C. Dai, X.-T. Wu, Z.-Y. Fu, S.-M. Hu, W.-X. Du, C.-P. Cui, L.-M. Wu, H.-H. Zhang, R.-Q. Sun, *Chem. Commun.*, 12 (2000).
4. (a) D. Sun, R. Cao, Y Liang,. Q. Shi, W. Su, M. Hong, *J. Chem. Soc., Dalton Trans.*, 2335 (2001) (b) C. S. Hong, S. K. Son, Y. S. Lee, M. J. Jun, Y. Do, *Inorg. Chem.*, **38**, 5602 (1999).
5. S. Subramaniam, M. J. Zaworotko, *Angew. Chem., Int. Ed.*, **34**, 2127 (1995).
6. M. McCann, M. T. Casey, M. Devereux, M. Curran, V. McKee, *Polyhedron,* **15**, 2321 (1996).
7. M. McCann, M. T. Casey, M. Devereux, M. Curran, C. Cardin, A. Todd, *Polyhedron,* **15**, 2117 (1996).
8. S. McCann, M. McCann, M. T. Casey, M. Devereux, V. McKee, P. McMichael, J. McCrea, *Polyhedron,* **16**, 4247 (1997).
9. M. G. B. Drew, *Coord. Chem. Rev.*, **24**, 179 (1977).
10. B. Zhao, P. Cheng, Y. Dai, C. Cheng, D. Z. Liao, S. P. Yan, Z. H. Jiang, G. L. Wang, *Angew. Chem., Int. Ed.*, **42**, 934 (2003).
11. C. Brouca-Cabarrecq, A. Fernandes, J. Jaud, J. P. Costes, *Inorg. Chim. Acta,* **332**, 54 (2002).
12. W. Z. Wang, X. Liu, D. Z. Liao, Z. H. Jiang, S. P. Yan, G. L. Wang, *Inorg. Chem. Commun.*, **4**, 327 (2001).
13. K. Y. Choi, H. Ryu, Y. M. Lim, N. D. Sung, U. S. Shin, M. Suh, *Inorg. Chem. Commun.*, **6**, 412 (2003).
14. D. C. Crans, L. Yang, T. Jakusch, T. Kiss, *Inorg. Chem.*, **39**, 4409 (2000).
15. G. Nardin, L. Randaccio, R. P. Bonomo, E. Rizzarelli, *J. Chem. Soc., Dalton Trans.*, **3**, 369 (1980).
16. N. Bresciani-Pahor, G Nardin, R. P. Bonomo, E. Rizzarelli, *J. Chem. Soc.*, *Dalton Trans.*, **12**, 2625 (1984).
17. S. K. Ghosh, J. Ribas, P. K. Bharadwaj, *Cryst. Growth Des.,* **5**, 623 (2005).

18. G. M. Sheldrick, *SHELXL-PLUS*, Siemens X-ray Analytical Instruments Inc., Madison, USA, 1990.
19. G. M. Sheldrick, *SHELXL 93*: Program for Crystal Structure Refinement, Univ. Gottingen, Germany, 1993.
20. K. Nakamoto, Infrared and Raman Spectra of Inorganic and Coordination Compounds*, 4th Ed.,

Wiley & Sons Interscience Publ., New York, 1986.
21. A. B. P. Lever, Inorganic Electronic Spectroscopy, 2nd Ed., Elsevier Science, New York, 1984.
22. L.-N. Zhu, M. Liang, Q.-L. Wang, W.-Z. Wang, D.-Z. Liao, Z.-H. Jiang, S.-P. Yan, P. Cheng, *J. Mol. Struct.*, **657**, 157 (2003).

НОВА ДВУМЕРНА МРЕЖА ОТ КОМПЛЕКС НА Co(II) С КАРБОКСИЛАТНИ МОСТОВЕ: СИНТЕЗ И СТРУКТУРНИ АСПЕКТИ

А. Датта[1], У.-С. Хуанг[1], Н. Revaпрасаду[2,]*

Департамент по химия, Национален университет Донг-Хуа, „Да-Хсюе" роуд, № 1, сек. 2, Шуфенг, Хюалиен – 974, Тайван, Китайска република
Департамент по химия, Университет на Зулуленд, ПК Х1001, Ква Длангезуа, Южноафриканска република

(Резюме)

Синтезиран е в меки условия нов димерен комплекс на Co(II) в твърдо състояние, определен като {Co(H$_2$O)$_5$[Co(2,6-pdc)$_2$].2H$_2$O} (H$_2$PDC = пиридин-2,6-дикарбонова киселина) чрез рентгенова дифракция от монокристал и е охарактеризиран с елементен анализ, ИЧС, електронни спектри, термогравиметричен анализ и магнитен момент при различни температури. Структурните изследвания показват че кристалната система на новия комплекс е моноклинна, пространствена група *P2(1)/c*, *a* = 8.3545(5), *b* = 27.1474(16), *c* = 9.5882(6) Å, *β* = 99.089(1)°, и *Z* = 4. Съседните Co атоми са свързани с мостове от карбоксилатни групи от един PDC лиганд и пространственият ъгъл, определен от равнините на два PDC лиганда е 88.6°, показвайки, че те са почти перпендикулярни. Стойността на ефективния магнитен момент μ$_{eff}$ на новия комплекс е близо до 5.31 μ$_B$ при 302 K, много по-голям от спиновата стойност от 3.87 μ$_B$ за високоспинов Co(II). Комплексът се разраства в триизмерна мрежа чрез водородни връзки.

Investigation of Zn sorption by natural clinoptilolite and mordenite

N. Lihareva*, L. Dimova, O. Petrov, Y. Tzvetanova

Central Laboratory of Mineralogy and Crystallography, Bulgarian Academy of Sciences,
Acad. G. Bonchev St., Block 107, 1113 Sofia, Bulgaria

Sorption and desorption of zinc on two natural zeolites – clinoptilolite and mordenite was studied using batch technique. The sorbed Zn quantity was studied as a function of its concentration in solutions. The equilibrium sorption data were analyzed using Langmuir's and Freundlich's models. It was found that for the sorption on clinoptilolite both Langmuir's and Freundlich's isotherm expressions gave a good fit to the experimental data. For mordenite, at low added concentrations the sorption followed well both models, but at higher concentrations the shape is different for the two applied models. The amount of zinc, sorbed by clinoptilolite, is greater than that sorbed by mordenite. The modeling of the release of sorbed zinc is carried out by extraction with ethylenediamine tetraacetic acid (EDTA). The percentage of extracted to sorbed zinc varies from 94.2% to 74.6% and from 95.5% to 67.9% for clinoptilolite and mordenite, respectively, with the increase in Zn concentration of the initial treatment. The results of this study show that both zeolites possess a high potential for zinc sorption and slow rate of desorption.

Key words: clinoptilolite, mordenite, zinc sorption.

INTRODUCTION

Natural zeolites clinoptilolite and mordenite are potential adsorbent agents for metal cations because of their porous structure, high specific surface area and cation exchange capacity [1, 2].

Their application as sorbents is important for purification of wastewaters or for metal immobilization in the processes of removal of heavy metals from polluted soils. The agricultural application of natural zeolites includes also their use as fertilizers, when metals, adsorbed on zeolites are released under control in order to compensate for nutrient deficiency in microelements of some soils or as soil-additives to modify its water regime, physical properties, pH, *etc*.

Zinc plays a substantial role as a microelement in the formation of proteins in the body and thus it assists the general growth and maintenance of human and animal bodies, in healing skin lesions and blood formation. This metal is component in a large number of enzymes, participating in the metabolic processes. The main way to obtain enough zinc in our body is eating a variety of foods that contain an appropriate amount of Zn. That is why the soil content of zinc and its mobile form, accessible to plants, is very important for nutrition. The average content of zinc in soils is 50 mg·kg^{-1} and depends on the soil composition. When the amount of extractable forms of zinc is low, the metal is imported artificially into soils either directly (as $ZnSO_4$) or as an incidental component in other fertilizers [3, 4]. The direct addition of zinc is not preferable due to the risk of eventual exceeding of limit levels that results in contamination of soil. Therefore, in order to preserve environment at present the introduction of zinc as well as some other components in the soil is realized through slow-release zeolite-bound zinc fertilizers, which are considered as natural carriers for trace elements.

The effective utilization of such fertilizers needs the design of chemical models that describe the processes of equilibrium. The investigations on sorption and desorption of zinc on zeolites constantly increase with the time, which proves the importance of this metal for such purposes [5–7]. Chemical models, describing the processes of equilibrium between sorption and desorption of Zn are studied by Langella [8], Roman [9] and Top [10]. On the other hand several investigators have reported that clinoptilolite shows low selectivity towards the Zn^{2+} ion [8, 11–13]. The exchange reaction of Zn^{2+} on zeolite is reversible and Zn^{2+} can be released by appropriate extractants.

This study represents the applicability of two Bulgarian natural zeolites, namely clinoptilolite and mordenite, for sorption of zinc, considering utilization of ion-exchanged forms as soil fertilizer. The effect of addition of these zeolites to soil and the mobility of sorbed zinc, were evaluated by a modelling leaching procedure.

* To whom all correspondence should be sent:
E-mail: nlihareva@abv.bg

EXPERIMENTAL

Materials and Methods

Two naturally occurring zeolites in Eastern Rhodopes, Bulgaria, were studied – namely clinoptilolite and mordenite. The clinoptilolite sample is a clinoptilolite rich tuff from Beli Plast layer deposit. The sample of mordenite is mordenite tuff from Lyaskovets deposit.

The samples were ground in an agate mortar and sieved through a 0.16 mm sieve. The sieve fractions of 0.016–0.032 mm for clinoptilolite and 0.016–0.064 mm for mordenite were obtained by sedimentation technique. The purity of the separated material was checked by powder XRD phase analysis.

Then the two samples were further enriched in zeolite phase by separation with heavy liquid (ethanol and bromoform mixture with specific gravity of 2.2).

The chemical composition of the two samples was determined by AAS and inductively coupled plasma atomic emission spectrometry ICP-AES after dissolution in a mixture of HF-HNO_3-$HClO_4$. The silicon was determined gravimetrically. The data are shown in Table 1.

Table 1. Chemical composition of the studied zeolites.

Component	Clinoptilolite	Mordenite
SiO_2	68.05	60.32
Al_2O_3	12.63	12.72
Fe_2O_3	0.83	1.25
K_2O	3.02	4.89
Na_2O	0.51	4.03
CaO	3.53	8.80
MgO	0.18	0.10
TiO_2	0.08	0.06
MnO	0.02	0.01
H_2O	11.24	8.4
Sum	100.09	100.58
Zn*	36.8	34.3
Si/Al	5.39	4.74

* in µg/g.

Powder XRD analysis was used to determine the mineral composition of the initial zeolite samples (Table 2).

Table 2. Quantitative phase analysis of clinoptilolite and mordenite samples (wt.%).

Sample	Clinop-tilolite	Morde-nite	Feldspar	Quartz	Opal
Clinoptilolite	80	–	2	3	15
Mordenite	–	75	25	–	–

The XRD powder patterns were obtained by DRON 3M diffractometer using CoKα radiation (40 kV, 25 mA) with a Fe filter. The step scan was performed in the 2θ range from 8 to 60° at a step of 0.050° with 3 s intensity measurement in each step.

The ion-exchange experiments were carried out by a bath technique. To 1 g of samples, taken in double portions, 20 ml of solutions of zinc were added, with concentrations of 0.0, 5.0, 25.0, 50.0, 100.0, 250.0 and 500.0 mg·l^{-1}, prepared from $ZnSO_4.7H_2O$ [5]. The pH value of all used solutions of Zn was adjusted to 5.80, so the influence of different pH on the sorption was eliminated. No pH adjustment was made during the experiments. Precipitation of oxides, hydroxides or carbonates, especially at certain higher pH cannot occur in this case, because the solubility product, depending on the pH and Zn concentration, cannot be reached. The samples were agitated in a shaker (amplitude 20 mm and 150 oscillation·min^{-1}) until equilibrium was reached. Preliminary experiments were carried out in order to determine the time interval, necessary to reach ion equilibrium. The samples were shaken for 8 hours and an aliquot was taken at 2 hours intervals. The Zn^{2+} concentration in the solution after each period was measured by AAS. It was found that the ion-exchange equilibrium was completely achieved in about 4 hours. The suspension was centrifuged for 15 min at 3000 rpm. The supernatant liquid was removed and the zinc concentration was measured by AAS. The amount of sorbed Zn was determined as the difference between added zinc and the amount in the equilibrium solution

The equations of Langmuir and Freundlich were applied to describe the sorption equilibrium of the studied zeolites. The Langmuir's model used is:

$$q_{eq} = b.S_{max}C_{eq}/(1 + bC_{eq}),$$

where C_{eq} (mmol/l) and q_{eq} (mmol/g) are the equilibrium Zn concentration in the aqueous phase and in the solid phase, respectively, and the Langmuir's parameters S_{max} (mmol/kg), representing maximum sorption capacity and b (l/mol) – the site energy factor.

The Freundlich's model used is:

$$q_{eq} = K_F C_{eq}^{N},$$

where K_F (mmol/g)/(mmol/l) and N (dimensionless) are Freundlich's parameters.

The biologically accessible amount of sorbed zinc is the water-soluble one and the zinc fractions dissolved during biological processes. A large number of single extractants have been studied for prediction and assessment of mobility of trace elements available for the plants [14]. Among the various organic and inorganic reagents that are used for modeling of the above processes EDTA and DTPA are mostly preferred [5, 15, 16]. In our study we used EDTA according to the method proposed

by Ure *et al*. [14], which, at present, is a harmonized procedure of BCR of the European Commission. Moreover, Haq and Miller [17] have found that the correlation coefficients between the content of zinc in plants and the extractable zinc in soil estimated by extraction with EDTA and DTPA are respectively 0.607 and 0.602. These findings suggest that both extractants are applicable. As it was suggested by Ure *et al*. [14] EDTA is preferable because it extracts greater amounts and is simpler to prepare and use.

RESULTS AND DISCUSSION

The studies of the sorption isotherms were conducted in order to evaluate the sorption efficiency of clinoptilolite and mordenite. The sorption isotherms of zinc with the studied samples are shown in Figure 1 and 2.
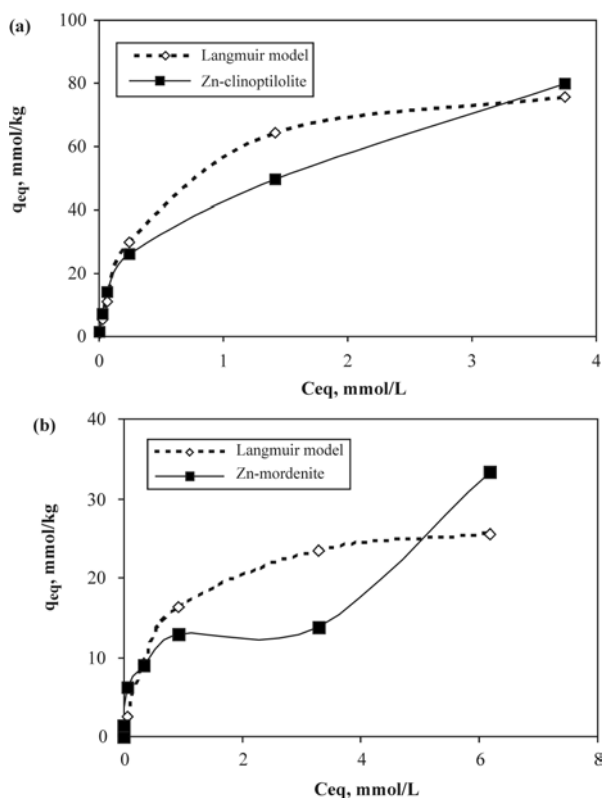
Fig. 1. Sorption isotherms of Zn on: a) clinoptilolite and b) mordenite. Solid and dashed lines represent experimental data and the Langmuir's model fitting, respectively.

The shapes of the two isotherms are similar at the low initial concentrations and are characterized with relatively steep slope. At higher concentrations the slope is more uniform and the shapes are different – for clinoptilolite the sorbed amount of Zn increases, whereas for mordenite there is a defined

plateau before the next increase. These results are in conformity with the results, presented by Langella [8]. The data of our experiments show that the exchange levels of zinc at different initial concentrations are between 98% and 81% and 100% and 47.3% for clinoptilolite and mordenite, respectively.

Both Langmuir's and Freundlich's isotherms are displayed for the two zeolites in order to determine the model with better mathematical fit to the experimental data. The equation of the Zn sorption isotherms for the Langmuir's model is:

$$C_{eq}/q_{eq} = C_{eq}/S_{max} + 1/b.S_{max}.$$

The linear Freundlich's model used to fit the Zn sorption data is:

$$\log q_{eq} = \log K_F + N.\log C_{eq}.$$

The Langmuir,s parameters (b and S_{max}) for Zn sorption were calculated from the best fitting equation, describing the C_{eq}/q_{eq} and C_{eq} dependence (Table 3). The calculated data for maximum adsorption (S_{max}) show that clinoptilolite adsorbs more zinc than mordenite. The site binding energy values are of the same order: clinoptilolite > mordenite, although the difference is not significant.
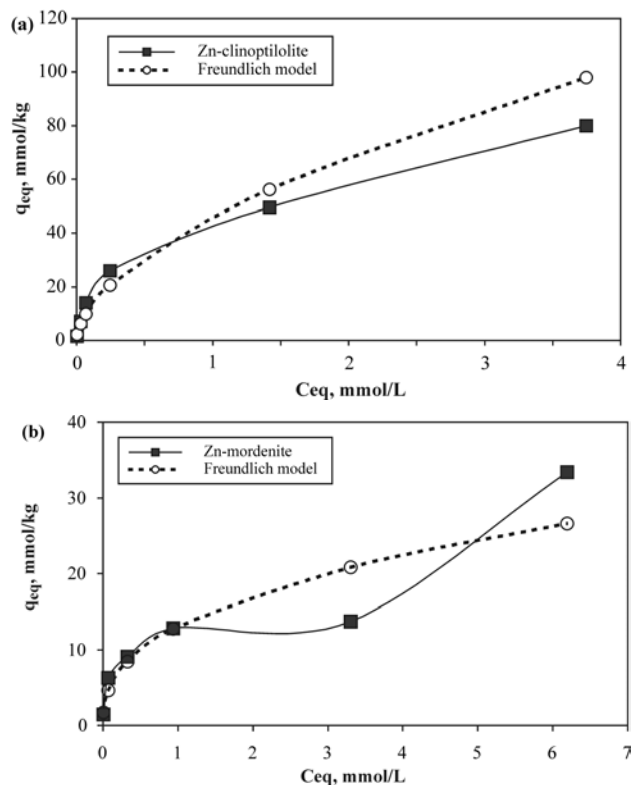
Fig. 2. Sorption isotherms of Zn on a) clinoptilolite and b) mordenite. Solid and dashed lines represent experimental data and Freundlich's model fitting, respectively.

Table 3. Langmuir's model parameters for sorption of Zn on clinoptilolite and mordenite.

Sample	Langmuir's equation	R^2	S_{max}, mmol/kg	b, l/mmol
Clinoptilolite	$Y = 0.0118x + 0.0054$	0.9617	84.74	2.2263
Mordenite	$Y = 0.0351x + 0.0244$	0.7349	28.49	1.4385

Table 4. Freundlich's model parameters for sorption of Zn on clinoptilolite and mordenite.

Sample	Freundlich's equation	R^2	K_F $[(mmol/kg)/(mmol/l)]^N$	N
Clinoptilolite	$Y = 0.5719x + 1.6629$	0.9611	48.02	0.5719
Mordenite	$Y = 0.3893x + 1.1167$	0.9346	13.08	0.389

The sorption isotherms of Freundlich's model and the calculated parameters according to Freundlich's adsorption equation are presented in Figure 2 and Table 4, respectively. The sorption isotherms are highly nonlinear as indicated by the N-values of Freundlich's model (0.389−0.572). They are characterized by an almost complete sorption at low concentrations of added zinc and decrease at the higher concentrations.

It is not clearly evident from the calculated isotherms which model describes the experimental data better. As the regression coefficient for clinoptilolite is the same for the two models it can be supposed that Langmuir's model gives better description because the calculated values for S_{max} are close to the experimental data. Experimental results with a good fit for Zn sorption with both Langmuire's and Freundlich's isotherms have been presented also by Ören [18]. El Kamash [19] has found based on the obtained results for Zn sorp-tion good fitting using Freundlich's and Dubinin-Radushkevitch (D-R) isotherm models. According to Purna *et al.* [20] the sorption of zinc follows Freundlich's sorption model, while Sheta [5] finds better fitting for experimental results with Langmuir's model. Panalitova *et al.* (21), studying the Zn sorption by Bulgarian zeolite, also reported a best description of uptake by Langmuir's isotherm. In case of mordenite the two models give difference in the isotherm shape at higher concentrations.

In order to evaluate the sorption behavior of natural zeolites it is necessary to establish the mechanism of fixation of zinc to the zeolite structure (as well as the sorption capacity of different zeolites.)

The sorption behavior of zinc ions depends on the differences in the structure of zeolite species, the surface characteristics, the amount of other cations and their ionic radii and hydrating energy.

As it is given in Table 1 the contents of sodium, potassium, and calcium are higher in mordenite than in clinoptilolite sample. The content of magnesium is low and it is similar in both zeolites. In the clinoptilolite structure, potassium is located in M(3)

site, which has the highest coordination number among all the cation sites in the unit cell [22]. In this site K^+ is coordinated by six framework oxygen atoms and three water molecules and therefore it is strongly bonded. This may be effective reason for its lower exchange ability [23].

On the other hand, the cations in the solutions interact with water molecules to form hydrated complexes. In general, the radius of these hydrates is inversely proportional to the cation radius. Thus, the smaller alkaline-earth cations Ca^{2+} and Mg^{2+}, have a bigger hydration radius than the monovalent cations like K^+ and Na^+ [24, 25] and cannot be removed easily out of the channels. This fact can also explain the lower sorption ability of mordenite for zinc than clinoptilolite. As the contents of sodium, potassium and calcium in mordenite are higher than those in clinoptilolite the zinc selectivity in case of mordenite is lower (Fig. 3).
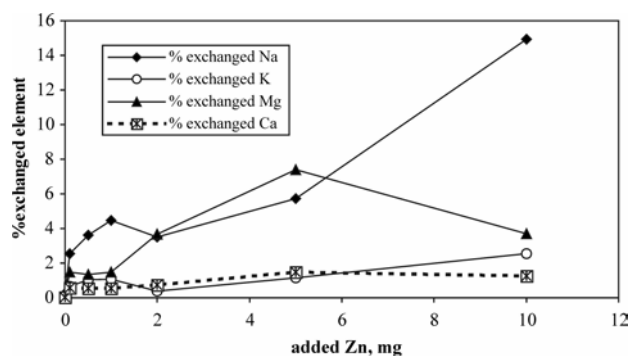
Fig. 3. Percentage of exchanged elements in the solution with respect to their content in mordenite during Zn sorption.

The low amounts of Ca, K in the solution that are registered after reaching equilibrium (Fig. 3) during Zn sorption on mordenite demonstrate that zinc cations are exchanged mainly on the sites of Na and Mg in the mordenite structure.

The results of studying the extraction of sorbed zinc are represented in Table 5. The data reveal, that the sum of the extracted amounts of zinc during four successive extractions is greater for clinoptilolite than that for mordenite.

Table 5. Amount of sorbed zinc and EDTA extracted zinc.

Zn added, mkg/g	Zn sorbed, mkg/g	Sum of EDTA extracted Zn, mkg/g	Extracted/Sorbed Zn, %	Extracted Zn in first extraction, %
		Clinoptilolite		
0	0	0.31	-	-
100	85.6	81	94.2	95
500	462	365	78.6	60.3
1000	919	796	86.7	66.4
2000	1704	1402	82.3	34/54
5000	3237	2409	74.4	56.8
10000	5222	3896	74.6	52.4
		Mordenite		
0	0	0.21	-	-
100	93.5	89	95.5	100
500	413	352	85.2	100
1000	593	493	83.0	92
2000	837	681	81.4	96
5000	896	503	56.1	70.3
10000	2183	1483	67.9	81

For both zeolites, the percentage of the total amount extracted to the sorbed zinc decreases with increasing the initial amount of Zn added. Up to 2000 mg/kg added zinc, the difference between these percentages remains small. After that, the percentage becomes lower for the amounts extracted from mordenite. The lowest percentage of desorbed zinc is about 60%.

The extracted amount of Zn during the fourth extraction from clinoptilolite is 140 mg/kg for the sample treated with 500 mg/l Zn. Under the same conditions, the extraction of sorbed zinc from mordenite leads to a release of 70 mkg/g. These results indicate that both zeolites have a capacity for slow releasing of zinc allowing to use them as fertilizers.

CONCLUSION

The studied natural zeolites display difference in their sorption behavior in respect to zinc cations as well as difference during extraction of zinc with EDTA. It can be accepted that the cation exchange and sorption properties of the two zeolites are dependent on the initial content and distribution of cations in the structure, which determines the different accessibility of the cationic sites for cationic exchange. Clinoptilolite has a higher sorption ability for zinc, which can be explained by more favorable cationic complex. Also the greater the zeolite content in the rock sample the higher is its sorption capacity.

Further on, in order to model the mobility of the sorbed zinc and to evaluate its accessibility and assimilation by plants we used EDTA extraction applying the method proposed by BCR.

The cation exchange and sorption properties of these two Bulgarian natural zeolites showed a good selectivity for zinc that is promising for different practical applications.

REFERENCES

1. D. W. Breck, Zeolite Molecular Sieves: Structure, Chemistry and Use, John Wiley and Sons, New York, 1974.
2. S. K. Ouki, M. Kavannagh, *Water Sci. Tech*., **39**, 667 (1999).
3. E. C. Varsa, J. D. Hernandez, S. A. Ebelhar, T. D. Wyciskalla, in: Illinois Fertilizer Conf. Proc., 2005, Report No 10.
4. G. Nzigulheba, E. Smolders, *Sci. Total. Environ*., **390**, 53 (2008).
5. A. S. Sheta, A. M. Falatah, M. S. Al-Sewailem, E. M. Khaled, A. S. H. Salam, *Micropor. Mesopor. Mater*., **61**, 127 (2003).
6. A. Bujnová, J. Lesný, *Hung. Electron. J. Sci.* (ISSN 1418-7108), Manuscript no.: ENV-061123-A.
7. M. Rehàková, S. Čuvanová, M. Dzivák, J. Rimár, Z Gaval'ová, *Curr. Opin. Solid State Mater. Sci*., **8**, 397 (2004).
8. A. Langella, M. Pansini, P. Cappalleti, B. De Gennaro, M. de Gennaro, C. Colella, *Micropor. Mesopor. Mater*., **37**, 337 (2000).
9. P. Roman, J. Warchol, *Micropor. Mesopor. Mater*., **61**, 137 (2003).
10. A. Top, S. Ulku, *Appl. Clay Sci*., **27**, 13 (2004).
11. M. J. Semmens, M. Seyfarth, in: Natural zeolites: Occurrence, Properties, Use, L. B. Sand, F. A. Mumpton (eds.), Pergamon Press, Oxford, 1978, p. 517.
12. Š. Cerjan-Stefanović, L. Ćurcović, in: Natural zeolites − Sofia' 95, G. Kirov, L. Filizova, O. Petrov (eds.), Pensoft, Sofia, 1997, p. 121.
13. M. J. Zamazow, J. E. Murphy, *Sep. Sci. Technol*., **27**, 1969 (1992).
14. A. M. Ure, Ph. Quevauviller, H. Mintau, B. Griepink,

Int. J. Environ. Anal. Chem., **51**, 135 (1993).
15. W. L. Lindsay, W. A. Norwell, *Soil Sci. Soc. Am. J.*, **42**, 421 (1978).
16. J. F. Trierweiller, W. L. Lindsay, *Soil Sci. Soc. Am. Proc.*, **33**, 49 (1969).
17. A. U. Haq, M. H. Miller, *Agron. J.*, **64**, 779 (1972).
18. A. H. Oren, A. Kaya, *J. Hazard. Mater.*, **B131**, 59 (2006).
19. A. M. El-Kamash, A. A. Zaki, M. A. El Geleel, *J. Hazard. Mater.*, **127**, 211 (2005).
20. Ch. R. G. Purna, S. Satyaveny, A. Ramesh, K. Seshaiah, K. Samurthy, N. V. Choudry, *J. Environ. Manag.*, **81**, 265 (2006).

21. M. Panajotova, V. Panajotov, Ts. Mitrov, Proc. 19th Balkan Mineral Processing Congr., G. Őnal, S. Atak, A. Güney, M. S. Çelik, A. E. Yüce (eds.), Istanbul, 2001, p. 617.
22. K. Koyama, Y. Tackeushi, *Zeits. Krist.*, **145**, 216 (1977).
23. M. A. Jama, H. Yucel, *Sep. Sci. Technol.*, **24**, 1393 (1989).
24. J. L. Palmer, M. E. Gunter, *Am. Mineral.*, **86**, 431 (2001).
25. E. Czaran, J. Papp, A. Meszaaros-Kis, E. Domokos, *Acta Chim. Hung.*, **126**, 673 (1989).

ИЗСЛЕДВАНЕ НА СОРБЦИЯТА НА Zn^{2+} ОТ ПРИРОДНИ КЛИНОПТИЛОЛИТ И МОРДЕНИТ

Н. Лихарева*, Л. Димова, О. Петров, Я. Цветанова

Централна лаборатория по минералогия и кристалография, Българска академия на науките, ул. „Акад. Г. Бончев“, бл. 107, 1113 София

(Резюме)

Изследвана е сорбцията и десорбцията на цинк от два природни зеолита - клиноптилолит и морденит като експериментите са извършени в статични условия. Изследвана е зависимостта на сорбираното количество цинк от неговата концентрация в разтвора и времето на сорбция. Данните за равновесието при различни начални концентрации са анализирани, използувайки моделите на Лангмюир и Фройндлих. Намерено е, че сорбцията върху клиноптилолит се описва еднакво добре и с двата модела. При морденита и двата модела описват добре сорбцията при ниски концентрации, но при по-големи концентрации формата се различава и за двата модела. Количествата на цинка, сорбирани от клиноптилолит са по-големи от тези, сорбирани от морденит при същите условия. Изследвана е десорбцията на цинка чрез екстракция с етилендиамин тетраоцетна киселина (EDTA). Процентът на екстрахирания цинк спрямо сорбирания се изменя от 94.2 % до 74.6% и от 95.5% до 67.6%, респективно за клиноптилолит и морденит за проби, в които нараства началната концентрация на третиране с цинк. Резултатите от тези изследвания показват, че двата зеолита притежават висок потенциал като сорбенти на цинк и бавна десорция.

Reversed phase extraction chromatographic separation of palladium(II) using liquid anion exchanger

S. J. Kokate, H. R. Aher, S. R. Kuchekar*

*P. G. Department of Analytical Chemistry, Padmashri Vikhe Patil College, Pravaranagar,
At/Po – Loni (Kd), Tal. Rahata, Dist. Ahmednagar, 413713, India*

A selective, sensitive, less expensive and more precise method has been developed for separation of palladium(II) with N-*n*-octylaniline, coated on silica gel as a stationary phase. Quantitative extraction of palladium(II) is observed in the acidic medium within the range 0.8–1.2 M nitric acid with 1.5% N-*n*-octylaniline at a flow rate of 0.5 ml /min. The extracted metal ion is striped with 7.0 M ammonia and determined by spectrophotometric method. The extraction behaviour of palladium(II) has been studied as a function of different parameters such as concentration of mineral acids, reagent, eluation time and diverse ions. The method is free from large number of cations and anions. It is applied for separation of palladium(II) from synthetic mixtures corresponding to alloys. A scheme for mutual separation of platinum(IV), palladium(II) and iridium(III) has been developed. Log-log plot of N-*n*-octylaniline concentration versus distribution ratio indicates that probable extracted species is $[RR'NH_2^+Pd(NO_3^-)_3]_{org}$.

Key words: extraction chromatography, palladium(II), separation alloys.

INTRODUCTION

Abundance of palladium in Earth's crust is 8.5×10^{-13}%. It is used as a catalyst for various organic reactions as well as multi-layer ceramic capacitor (MLCC), photography and jewelry. Palladium alloys have wide range of applications in industry. It is used as low current electrical contact, preliminary telephone equipment and integrated circuit, *etc*. [1], in view of its wide range of applications, the separation of palladium has analytical importance.

Palladium(II) has been extracted using LIX 841 [2], but extraction quality is poor and it requires higher concentration of hydrochloric acid for stripping. Palladium(II) was extracted and separated with aliquot-336 [3], in hydrochloric acid media. Cyanex 471X [tri-isobutyl phosphine sulphide) [4], has been used for separation of palladium(II) by extraction chromatography in nitric acid media using thiourea as a stripping agent. Palladium(II) and platinum(IV) were preconcentrated on Amberlite XAD-7 resin, coated with dimethylglyoxal bis (4-phenyl-3-thiosemicarbazone) [5], using acidic solution in the presence of iodide and it was eluated with dimethylformamide. Palladium(II) has been extracted with various ketones [6], from nitric acid media, which requires 3.0 M ligand concentration above 2.0 M acidity. Silica gel, impregnated with prime JMT, is used for separation of palladium(II)

in sulphuric acid media and eluated using sulphate phases [7]. Palladium(II) was extracted from hydrobromic acid media by hexadecylpyridinium bromide [8], which gives metal recovery 99%. 1-(2-pyridylazo)-2-naphthol [9], has been used for solvent extraction of palladium(II) but in the method, nonferrous alloys affect the determination of palladium.

In our laboratory *n*-octylaniline has been used for solvent extraction of gallium(III), indium(III), thallium(III), [10], zinc(II), cadmium(II), mercury(II) [11], lead(II) [12]. *n*-Octylaniline and N-*n*-octylaniline has also been used for extraction column chromatography of gallium(III), indium(III), thallium(III) [13], and reversed phase paper chromatographic separation of zinc(II), cadmium(II), and mercury(II) [14]. The N-*n*-octylaniline has also been used for reversed phase paper chromatographic study of cooper(II), silver(I), gold(III) [15], gallium(III), indium(III), thallium(III) [16].

In the present communication selective, sensitive, less expensive and more precise method has been developed for extraction chromatographic separation of palladium (II) is achieved at 1.5% N-*n*-octylanilne in 1.0 M nitric acid and the metal ion was stripped with 7.0 M ammonia. Various parameters are studied such as acid concentration, reagent concentration, effect of flow rate and different ions. The method is extended for separation of palladium(II) from synthetic mixture corresponding to alloys and mutual separation of palladium(II), platinum(IV) and iridium(III) has been achieved.

---

* To whom all correspondence should be sent:
E-mail: shashi17@gmail.com

EXPERIMENTAL

Apparatus. An Elico spectrophotometer model SL-159 with 10 mm path length quartz cell has been used for absorbance measurements. Control dynamic pH meter is used for pH measurements.

Reagent and chemicals. A stock standard solution of palladium(II) is prepared by dissolving 1.0 g palladium chloride ($PdCl_2$) (Loba. Chem.) in 1.0 M hydrochloric acid and diluted to 250 ml with distilled water. It is standardized by gravimetric method [17]. A working solution of palladium(II), 25 μg/ml has been made by diluting the stock standard solution with distilled water. Other standard solutions of different metal ions are prepared by dissolving the respective salt in distilled water and diluted hydrochloric acid. N-*n*-octylaniline has been prepared using method reported by Gardlund [18]. The stock solution of N-*n*-octylaniline is prepared in chloroform. All other chemical used were of an analytical reagent purity grade.

Preparation of anion exchange material. Silica gel (60–120 mesh), obtained from BDH, has been dried at 120°C for 2–3 h and stored in desiccators. It is packed in U tube, through which a stream of nitrogen that has been bubbled though a small Durand bottle, containing about 20.0 ml of dimethyldichlorosilane (DMCS) (Across organic). The passage of DMCS vapour continued for 4 h. The silica gel is then washed with anhydrous methanol and dried. A portion of 5.0 g of this silaned silica gel has been soaked with 1.5% (v/v) N-*n*-octylaniline, previously equilibrated with nitric acid (1.0 M) for 10 min. The solvent has been evaporated to get nearly dried gel. The slurry of N-*n*-octylaniline coated silica gel has been prepared by centrifugation at 2000 rpm and coated silica gel is packed into chromatographic column to give a bed height of 6.0 cm. The bed has been covered with glass wool plug.

General procedure. An aliquot of a solution containing 25.0 μg of Pd (II), made up to 25.0 mL by adjusting concentration of nitric acid 1.0 M, is passed through the column containing silica coated with 1.5% N-*n*-octylaniline at a flow rate of 0.5 ml/min. After extraction, the metal ion is stripped with 25.0 mL aqueous ammonia, evaporated to dryness and determined spectrophotometrically [19].

RESULTS AND DISCUSSION

Effect of acid concentration on extraction. The extraction of palladium(II) has been studied in hydrochloric (0.2 to 2.0 M), hydrobromic (0.2 to 2.0 M), sulphuric (0.015 to 0.96 M), perchloric (0.5 to 2.5 M) and nitric (0.2 to 1.2 M) acid media with 1.5% (v/v) N-*n*-octylaniline. A maximum extraction of palladium(II) is in hydrochloric 74.35%, in hydrobromic 91.82%, in sulphuric 82.22%, in perchloric 22.02% and in nitric acid 99.65% (Fig. 1).
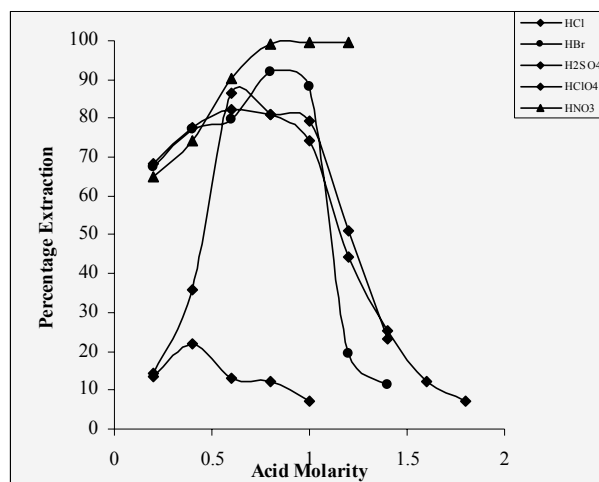
Fig. 1. Extraction behaviour of palladium(II) as a function of acid concentration.

Effect of flow rate. The effect of flow rate on percentage extraction for palladium(II) has been studied from flow rate 0.5 ml/min up to 3.0 ml/min. It is observed that percentage extraction decreases with increase in flow rate. Therefore normal flow rate is kept at 0.5 ml/min for further extraction studies.

Effect of N-n-octylaniline concentration. The concentration of N-*n*-octylaniline in chloroform is varied from 0.1% up to 2 .5% (v/v) over nitric acid range 0.2 to 1.2 M for palladium(II). It is extracted quantitatively with 1.5% (v/v) N-*n*-octylaniline in 1.0 M nitric acid media. The increase in N-*n*-octylaniline concentration increases the percentage extraction. Log-log plot of N-*n*-octylaniline concentration versus distribution ratio at 0.4 M and 0.6 M nitric acid gives slope 1.0 indicating that the probable extracted species is $[RR'NH_2^+ Pd(NO_3^-)_3]_{org}$ (Fig. 2).
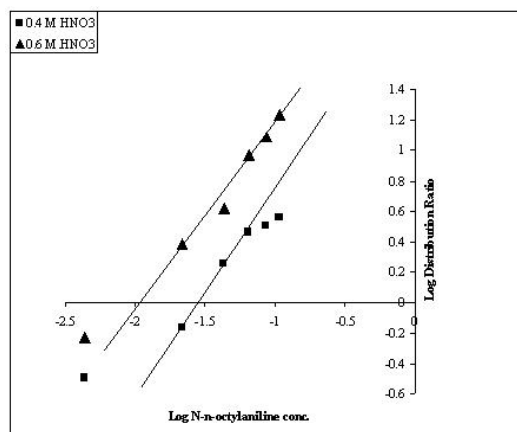
Fig. 2. Log-log plot N-*n*-octylaniline concentration *versus* distribution ratio.

Effect of diverse ions. The extraction of palladium(II) in presence of cations and anions has been carried out according to recommended procedure to examine their interferences. The tolerance limit is set at the amount required to cause ± 2% error in recovery of palladium(II). For 25 µg of palladium(II) there is no interference from 400 µg chromium(VI); 200 µg of tin(II) and molybdenum(VI); 100 µg of mercury(II), cobalt(II), bismuth(III), nickel(II), uranium(VI), iron(II), cadmium(II), cerium(IV) and vanadium(V); 75 µg of titanium(IV); 50 µg of magnesium(II), copper(II), rhodium(III), gold(III), ruthenium(III), osmium(VIII), silver(I), manga-nese(II), strontium(II), platinum(IV), lead(II), iron(III), selenium(IV) and iridium(III); 25 µg of gallium(III), indium(III), thallium(III) and aluminium(III). 500 µg of citrate and tartrate; 300 µg of oxalate and acetate; 250 µg of thiourea; 200 µg of thiosulphate, fluoride, EDTA and malonate (Table 1).

Analysis of synthetic mixture corresponding to alloy. Validity of the method is confirmed by applying method for separation of palladium(II) from synthetic mixtures corresponding to alloy. The composition of alloy has been prepared for 'Golden-coloured silver alloy resistance to tarnishing, iridium alloy, oaky alloy, solder alloy, jewelry alloy, stibio palladinite mineral, jewelry alloy (Pd-Au

alloy), Pd-Ag alloy and Pd-Cu alloy' in laboratory and the proposed method was applied for separation of palladium(II). The results are reported in Table. 2.

Table 1. Effect of various ions on the extraction of palladium(II). Pd(II) 25µg, Organic phase N-*n*-octylanilin 1.5% in chloroform, Eluent 7.0 M ammonia.

Foreign ion	Tolerance limit, µg	Foreign ion	Tolerance limit, µg
Co(II)	100	Mo(VI)	200
U(VI)	100	Cr(VI)	400
Ni(II)	100	Pb(II)	50
Bi(III)	100	W(IV)	150
Hg(II)	100	Ti(IV)	75
Pt(IV)	50	Ir(III)	50
Ga(III)	25	In(III)	25
Tl(III)	25	Al(III)	25
Fe(II)	100	Mg(II)	50
Cu(II)	50	Rh(III)	50
Sn(II)	200	Ru(III)	50
Cd(II)	100	V(V)	100
Fe(III)	50	Ag(I)	50
Se(IV)	50	Sr(II)	50
Ce(IV)	100	Mn(II)	50
Os(VIII)	50	Au(III)	50
Oxalate	300	H_2O_2	0.5 ml
Acetate	300	Citrate	500
Tartrate	500	Fluoride	200
Thiourea	250	Malonate	200
Thiosulphate	200	E.D.T.A.	200

Table 2. Analysis of synthetic mixture corresponding to alloy Pd(II) 25 µg, organic phase N-*n*-octylaniline1.5% in chloroform, eluent 7.0 M ammonia.

Sample alloy, % composition	Sample solution taken equivalent to Pd(II) µg	Pd(II) found, µg	Mean µg	Average recovery, %	Relative errors, %
Low melting dental alloy (Pd 34.0, Au 10.0, Co 22.0, Ni 34.0)	50	49.4, 49.9, 49.6	49.6	99.1	0.9
Golden colored silver alloy (Pd 25.5, In 21.0, Cu 18.0, Ag 35.0)	25	24.8, 24.8, 24.7	24.8	99.2	0.8
Iridium alloy (Pd 3.5, Cu 8.01, Pt 55.51, Fe 3.51, Rh 7.01, Ir 28.01)	25	24.7, 24.9, 24.8	24.8	99.2	0.8
Oaky alloy (Pd 18.2, Pt 18.2, Ni 54.2, V 9.1)	50	49.6, 49.7, 49.6	49.6	99.1	0.9
Solder alloy (Pd 30.0, Pt 10.0, Au 60.0)	50	49.4, 49.9, 49.6	49.6	99.1	0.9
Jewelry alloy (Pd 95.0, Ru 4.0, Rh1.0)	100	99.2, 99.0, 99.1	99.1	99.1	0.9
Stibio palladinite mineral (Pd 75.0, Sb 25.0)	100	99.3, 99.0, 99.0	99.1	99.1	0.9
Jewelry alloy (Pd-Au alloy) (Pd 50.0, Au 50.0)	100	99.8, 99.0, 99.4	99.4	99.4	0.6
Pd-Ag alloy (Pd 60.0, Ag 40.0)	100	99.4, 99.6, 99.2	99.4	99.4	0.6
Pd-Cu alloy (Pd 60.0, Cu 40.0)	100	99.6, 99.6, 99.1	99.4	99.4	0.6

In 25 ml. vol. flask add 25 µg Pd(II) + 50 µg Pt(IV) + 50 µg Ir(III) + HNO₃ to make 1.0 M solution and transfer it in a column containing silica coated with 1.5% N-*n*-octylaniline.

↓

Organic phase (in column) Pd(II) Eluted with 7.0 M ammonia and determined by the spectrophotometric method

Aqueous phase Pt(IV) and Ir(III) evaporate the aqueous phase up to dryness, add water to it, add to the solution ascorbic acid equivalent to make 25.0 ml solution 0.015 M at pH 1.0. Transfer this solution to a column containing silica coated with 1.5% N-*n*-octylaniline.

↓

Organic phase Pt(IV) Eluate distilled water. determined by spectrophotometric method [20].

Aqueous phase Ir(III) Evaporate to dryness and add distilled water to it, determine by spectrophotometric method [20].

Scheme. 1. Mutual separation scheme for palladium(II), platinum(IV) and iridium(III).

Mutual separation of palladium(II), platinum(IV) and iridium(III). In 25.0 mL volumetric flask 25 µg palladium(II), 50 µg platinum(IV), 50 µg iridium(III) were transferred, nitric acid has been added to make total solution 1.0 M with respect to nitric acid and this solution was transferred to column containing silica coated with N-*n*-octylaniline. Palladium (II) is extracted in column, which is stripped with 7.0 M ammonia and determined by spectrophotometric method [20]. Platinum(IV) and iridium(III) are eluated in aqueous solution. Aqueous solution was evaporated to dryness, after addition of distilled water and ascorbic acid to make 25.0 ml solution, 0.015 M at pH 1.0. It is transferred to a column containing silica coated with 1.5% N-*n*-octylaniline equilibrated with 0.015 M ascorbic acid at pH 1.0. Iridium(III) was not extracted and it was eluated in aqueous phase, which is evaporated to dryness and is estimated by spectrophotometric method [20]. Column containing platinum(IV) is eluated with distilled water and determined by spectrophotometric method [20] (Scheme 1, Table 3).

Table 3. Mutual separation of palladium(II), platinum(IV) and iridium(III). N-n-octylaniline 1.5%.

Metal ion	Amount taken, µg	Amount found,* µg	Recovery, %	RSD, %
Pd(II)	25	24.85	99.43	0.47
Pt(IV)	50	49.53	99.06	0.40
Ir(III)	50	49.50	99.00	0.66

* - Average of three determinations.

CONCLUSION

Literature survey revealed that some of the existing methods have drawbacks as:

- Palladium(II) was quantitatively extracted with very high concentration of hydrochloric acid (11.5 M) as a chloro-complex in the presence of tin(II) chloride by tri-*n*-octylamine (TOA) [21].

- Palladium(II) was extracted with 1.0 M *n*-octylaniline in chloroform from 3 M hydrochloric acid but the method requires multiple extractions for quantitative recovery of metal ion [22].

- Effectiveness of *n*-octylaniline in this extraction depends on its method of preparation [23].

- Extraction of palladium using hexaacetato calix(6) arene but the methods have major interferences from copper and chromium [24].

- Extraction of palladium(II) and other VIII group metals using 2-hydroxy-4-*sec*-octanoyl diphenylketoxime [26], but for its quantitative recovery high hydrochloric acid concentrations were used.

The proposed extraction chromatographic separation of palladium(II) has advantages over other reported method.

- The method is simple, rapid, reproducible and reliable.

- Extraction of palladium(II) requires low concentration of N-*n*-octylaniline.

- It permits mutual separation of palladium(II), platinum(IV) and iridium(III).

- The method is free from large number of foreign ions.

- The method gives separation of palladium(II) from alloys.

- Silica gel is used as good solid support because of the higher stability towards stationary phase.

REFERENCES

1. http:// www. education.jlab.org.
2. M. V. Rane, V. Venugopal, *Hydrometallurgy*, **84**, 54 (2006).
3. K. K. Dutta, U. S. Roy, *Chem. Environ. Res*., **12**, 113 (2003).
4. A. Dakshinamoorthy, T. Kumar, K. K. Nandy, R. H. Iyer, J. N. Mathur, S. B. Manohar, *J. Radioanal. Nucl. Chem*., **245**, 595 (2000).
5. H. Suwaru, H. Koki, S. Mamiko, S. Yasutoshi, S. Kazuharu, U. Masayuki, A. Kunihiko, *Talanta*, **44**, 571 (1997).
6. H. N. Trong, W. Masayuki, K. Takaumi, *Solvent. Extr. Ion Exch.*, **25**, 407 (2007).
7. S. Tsuneo, K. Mayumi, T. Yoshimi, *J. Planar. Chromatogr.-Modern TLC*, **8**, 152 (1995)
8. N. Alizadeh, S. Salimi, A. Jabbari, *Anal. Sci.,* **18**, 307 (2002).
9. T. V. Popova, V. L. Tolmachev, S. V. Alansari, N. V. Shcheglova, *J. Anal .Chem.*, **56**, 364 (2001).
10. S. R. Kuchekar, M. B. Chavan, *Talanta,* **35**, 357 (1988).
11. S. R. Kuchekar, H. R. Aher, M. B. Chavan, *Ind. J. Chem.*, **42**, 1674 (2003).
12. H. R. Aher, P. S. Gunjal, S. R. Kuchekar, M. B. Chavan, *Asian J. Chem.,* **10**, 43 (1998).
13. H. R. Aher, S. R. Kuchekar, *Ind. J. Chem. Technol.,* **15**, 403 (2008).
14. H. R. Aher, S. R. Kuchekar*, Asian. J. Chem.,* **16**, 695 (2004).
15. H. R. Aher, S. R. Kuchekar, *Int. J. Chem.,* **4**, 157 (2006).
16. H. R. Aher, S. R. Kuchekar, *Chem. Environ. Res.,* **15**, 161(2006).
17. N. H. Furman, Standard Method of Chemical Analysis, 6th ed, Malabar, Florida, 1962.
18. Z. G. Gardlund, R. J. Curtis, G. W. Smith, *Liq. Cryst. Ordered Fluids,* **2**, 541(1973).
19. F. Snell, C. Hilton, Encyclopedia of Industrial Chemical Analysis, vol. 17, Inter Science Publishers, New York, 1973, p. 265.
20. E. B. Sandell, Colorimetric Determination of Traces of Metals, Interscience Publishers, INC, New York, 1965.
21. M. A. Khattak, R. J. Magee, *Anal. Chim. Acta*., **35**, (1966) 17.
22. C. Pohlandt, Natl. Inst. Metall. Rep. South Africa, Project No. 03276, 28 March 1977.
23. R. N. Gedye, J. Bozic, P. M. Durbano, B. Williamson, *Talanta*, **36**, 1055 (1989).
24. V. J. Mathew, S. M. Khopkar, *Talana,* **44**, 1699 (1995).
25. Y. F. Shen, W. Y. Xue, *Sep. Purif. Technol*., **56**, 278 (2007).

РАЗДЕЛЯНЕ НА ПАЛАДИЙ(II) ЧРЕЗ ХРОМАТОГРАФСКА ЕКСТРАКЦИЯ С ОБЪРНАТА ФАЗА С ИЗПОЛЗВАНЕ НА ТЕЧЕН АНИОНООБМЕННИК

С. Дж. Кокате, Х. Р. Ахер, С. Р. Кучекар*

Департамент по аналитична химия, Колеж „Падмашри Викхе Патил“, Праваранагар, Рахата, Р-н Ахмеднагар 413713, Индия

(Резюме)

Разработен е селективен, чувствителен, евтин и точен метод за разделяне на паладий(II) с N-*n*-октиланилин, нанесен на силикагел като постоянна фаза. Наблюдава се количествена екстракция на паладий(II) в кисела среда (0.8–1.2 М азотна киселина) с 1.5% N-*n*-октиланилин при скорост на потока 0.5 ml/min. Екстрахираният метален йон се реекстрахира с 7.0 М амоняк и се определя спектрофотометрично. Изследвана е екстракцията на паладий(II) като функция на различни параметри като концентрация на минералната киселина, реагенти, време на елуиране и различни йони. Методът не се влияе от голям брой катиони и аниони. Приложен е за разделяне на паладий(II) от изкуствени смеси, съответстващи на сплави. Разработена е схема за разделяне на платина(IV), паладий(II), и иридий(III) един от друг. Логаритмичната зависимост на концентрацията на N-*n*- октиланилин от коефициента на разпределение показва, че вероятната екстрахирана форма е $[RR'NH_2^+Pd(NO_3^-)_3]_{org}$.

Redox activity of gold-molybdena catalysts: influence of the preparation methods

P. Petrova, L. Ilieva, D. H. Andreeva*

Institute of Catalysis, Bulgarian Academy of Sciences, Acad. G. Bonchev St., Block 11, 1113 Sofia, Bulgaria

The redox activity of gold-molybdena catalysts, supported on ceria-alumina, prepared by two different methods, was studied. The oxidation activity was measured in complete benzene oxidation reaction. The reduction activity was evaluated by TPR measurements of fresh catalysts and after reoxidation. The influence of the preparation methods is discussed. It was established that two factors were of great importance for the higher redox activity: oxygen mobility and the enhanced electron transfer involving the participation of gold. Both factors depend on the oxygen vacancies formation after adding gold and alumina to ceria as well as on the average size of gold and ceria particles.

Key words: gold-molybdena catalysts, ceria-alumina supports, preparation method, redox activity.

INTRODUCTION

Supported molybdenum oxide catalysts are widely used as catalysts for redox reactions such as propene metathesis [1, 2], ethanol oxidative dehydrogenation [1], propene oxidation [3] methanol oxidation [4, 5], selective partial oxidation of methane [6], *etc*. Recently it was established in our laboratory that $Au-V_2O_5$ and $Au-MoO_x$ catalysts, supported on titania, zirconia, ceria and ceria-alumina were very active at low temperatures in complete benzene oxidation (CBO) [7−10]. It could be assumed that the main factors responsible for the higher activity in CBO are as follows: structure and dispersity of the surface vanadium, resp. molybdenum phase, strength of the V(Mo)=O bond and ease of reduction of the supported $VO_x(MoO_x)$ catalysts. Wachs and co-authors [11, 12] have revealed that the V–O–support bridging bond appears to be controlling the reactivity and reducibility of supported vanadium oxide catalysts. Mestl *et al*. [5] studying MoO_x supported catalysts have suggested that the degree of reduction, and, hence, the presence of reduced surface metal centres, strongly affects the adsorption properties for hydrocarbons, related directly to the reactivity of these catalysts. It was also observed by some of the present authors [13] that a good correlation exists between reducibility and activity of vanadia and molybdena supported catalysts on ceria and titania. Quite recently, it was shown in our laboratory that gold catalysts based on ceria-alumina exhibited a high and stable CBO activity [10]. The addition of alumina to ceria increases the oxygen vacancies concentration and

oxygen mobility, which is reflected on the redox activity of this type of catalysts.

The accent in this study is on the relationship between the reducibility and CBO activity of gold-molybdena catalysts supported on ceria-alumina. The influence of the preparation methods on the redox activity is discussed.

EXPERIMENTAL

Catalysts preparation

Two different methods were applied for the preparation of modified ceria support – co-precipitation (CP) and mechano-chemical activation (MA). *Via* the 1st route, ceria-alumina support was synthesized by co-precipitation using nitrates of cerium and aluminium as initial salts in the relevant ratio with a solution of K_2CO_3 (10 wt.% and 20 wt.% of alumina were added, the percentage of alumina is shown after the symbol Al). The supports are denoted as CeAl10CP and CeAl20CP. *Via* the 2nd route, mixed CeO_2-Al_2O_3 support was prepared by mechanical mixing of alumina and vacuum dried cerium hydroxide. A mixture of γ-Al_2O_3 (supplied by BASF, $S_{BET} = 231$ m²/g) and freshly prepared cerium hydroxide was subjected to mechano-chemical activation by grinding in a mortar for 30 min. The obtained precursor was calcined at 400°C for 2 h. The content of alumina was again 10 and 20 wt.%. Then, before depositing the gold hydroxide, the mixed oxide support was activated in a disintegrator "Ultrasonic UD-20 automatic" under vigorous stirring for 5 min. The supports are denoted as CeAl10MA and CeAl20MA, respectively.

Gold was loaded by the deposition-precipitation method. Deposition of gold on CeO_2-Al_2O_3 supports,

---

suspended in water, was performed via interaction of $HAuCl_4.3H_2O$ and K_2CO_3 at constant pH = 7.0 and temperature 60°C. After ageing for 1 h, the precipitates were carefully washed, dried in vacuum at 80°C and calcined in air at 400°C for 2 h. The gold loading was 3 wt.%. The syntheses of ceria-alumina and gold catalysts were carried out in a "Contalab" laboratory reactor enabling complete control of the reaction parameters (pH, temperature, stirrer speed, reactant feed flow rate, *etc*.) and high reproducibility.

After deposition of gold, molybdenum was introduced by wet impregnation with $(NH_4)_6Mo_7O_{24}$ solution. The precursors were dried once again under vacuum at 80°C and calcined in air at 400°C for 2 h.

Samples containing only gold or only molybdena were also synthesized. The samples, containing only gold on ceria-alumina were denoted as AuCeAl10CP, AuCeAl20CP, AuCeAl10MA and AuCeAl20MA and the samples, containing only molybdenum – as MoCeAl10CP, MoCeAl20CP, MoCeAl10MA and MoCeAl20MA. The catalysts containing both gold and molybdenum were denoted as AuMoCeAl10CP, AuMoCeAl20CP, AuMoCeAl10MA and AuMoCeAl20MA.

The all used initial salts were of "analytical grade" of purity.

Catalytic activity

The catalytic activity was expressed as a degree of benzene conversion. It was measured using microcatalytic continuous flow fixed-bed reactor at atmospheric pressure, connected to a "Perkin Elmer" gas chromatograph, equipped with a flame ionization detector (2 m column filled with Porapak Q at 65°C). Benzene was fed into the catalytic reactor using air as carrier gas through a benzene saturator, which was kept at an appropriate temperature to maintain the desired benzene concentration. The oxygen to benzene ratio was about 7.5 (the stoichiometric ratio) needed for complete benzene oxidation. The following conditions were chosen: catalyst bed volume 0.5 cm^3 (particle size 0.25−0.50 mm), inlet benzene concentration 4.2 $g·m^{-3}$ in air, space velocity 4000 h^{-1}, temperature range 150−300°C. The catalyst amounts charged into the reactor and the catalysts particles size were selected to be small enough to avoid both bulk and pore diffusion retardation effects. The samples were activated "*in situ*" by purified air at 150°C for 1h. A special experiment with supplementary chromatographic analysis was carried out with a column Carbowax 20M HPDMCS. No byproducts of mild oxidation were registered.

TPR measurements

The TPR measurements were carried out by means of an apparatus described elsewhere [14]. A cooling trap (−40°C) for removing the water formed during reduction was mounted in the gas line prior to the thermal conductivity detector. A hydrogen-argon mixture (10% H_2), dried over a molecular sieve 5A (−40°C), was used to reduce the samples at a flow rate of 24 $ml·min^{-1}$.The temperature was lineally raised at a rate of 15°C·min^{-1}.The sample mass charged was 0.05 g. The amount was selected based on the criterion proposed by Monti and Baiker [15]. In addition, TPR experiments were performed after re-oxidation. The reoxidation with purified air was carried out at two different temperatures. In the first case of high temperature (HT) re-oxidation the H_2-Ar flow was discontinued and air was fed at the temperature immediately after the end of the corresponding TPR peak of the fresh sample. The sample was kept in air at this temperature for 15 min and then the TPR profile was recorded after cooling down to room temperature (RT) in purified argon flow. In the second case after the end of the TPR peak the sample was cooled down in purified argon flow to RT, reoxidized in air for 15 min and then the TPR pattern was registered (RT reoxidation).

Hydrogen consumption (HC) during the reduction processes was calculated using preliminary calibration of the thermal conductivity detector, performed by reducing different amounts of NiO to Ni (NiO "analytical grade" of purity, calcined for 2 h at 800°C to avoid the presence of non-stoichiometric oxygen).

RESULTS

The chemical composition, BET surface area and average size of gold and ceria particles of the gold-containing samples and the initial supports are presented in Table 1. The introduction of gold and alumina causes an increase in the BET specific surface area. The average size of gold particles, determined by XRD measurements, is below 6 nm [10]. In MA samples, the average size of gold is smaller than that in the CP ones. For the ceria particles size the opposite tendency was observed. For the MA samples, the average size of ceria particles was higher than that for the CP catalysts. The addition of alumina led to an increase in the number of oxygen vacancies, estimated by the main line of ceria in Raman spectra [10].

TPR results

The reduction behaviour of the studied samples was evaluated by TPR measurements. The hydrogen

consumption was calculated as well.

Table 1. Chemical composition, BET surface area and average size of Au and CeO_2 particles of the gold-based catalysts and initial supports.

Catalysts	Au content	MoO_3 content	BET surface area	Average size	
				Au	CeO_2
	wt. %	wt. %	$m^2 \cdot g^{-1}$	nm	nm
CeAl10CP	-	-	83	-	5.0
CeAl20CP	-	-	83	-	4.5
CeAl10MA	-	-	89	-	9.5
CeAl20MA	3.0	-	98	-	9.2
AuCeAl10CP	2.9	-	103	4.0	4.0
AuCeAl20CP	3.0	-	140	6.0	3.0
AuCeAl10MA	3.0	-	105	2.9	10.0
AuCeAl20MA	3.0	-	115	3.5	9.7
AuMoCeAl10CP	2.9	4.0	110	4.0	4.0
AuMoCeAl20CP	3.0	4.0	123	6.0	3.0
AuMoCeAl10MA	3.0	4.0	87	2.9	10.0
AuMoCeAl20MA	3.0	4.0	98	3.5	9.7

Figure 1 represents the TPR profiles of gold containing CP catalysts. Only the low temperature (LT) region is represented because only it is of interest for the studied catalytic reaction. The TPR profiles of the initial supports are shown as inset. Two peaks have been registered in the TPR pattern of pure ceria: a high temperature (HT) peak at T_{max} = 855°C, connected with the bulk reduction of ceria and a LT one at T_{max} = 490°C, assigned to the ceria surface layers reduction [16]. In the profiles of both ceria-alumina supports only one peak (T_{max} = 535°C for the CeAl10 sample and T_{max} within the interval 500−550°C for the CeAl20 sample) was registered in the region up to 800°C. For all gold-containing samples a significant lowering of the temperature of ceria surface layers reduction was observed as in a previous study [17].

The TPR patterns of gold-molybdena containing catalysts are shown in Fig. 2, as insets are presented the TPR profiles of samples containing only molybdena. The T_{max} of the peak, assigned to the molybdena and ceria reduction, had the lowest value for the MoCe sample (487°C). The peak with the highest T_{max} (517°C) as well as the highest intensity was observed with the MoCeAl20CP sample. The LT-TPR peaks of gold-molybdena catalysts were located at temperatures about 300° lower than those of the corresponding non-containing gold samples. These peaks are obviously complex due both to ceria surface layers and to MoO_x species reduction. The peak of the AuMoCe sample is a narrow one with a predominant LT part at T_{max} = 120°C and a HT shoulder at about 180°C, assigned to the MoO_x reduction. The peaks of the samples on mixed ceria-alumina supports are broad ones with T_{max} within the interval 120−220°C.
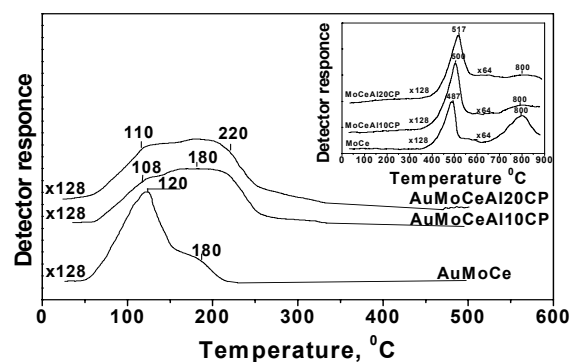
Fig. 2. TPR spectra of gold-molybdena catalysts; inset: molybdena samples.

The TPR patterns of gold-containing samples MA, nonpromoted and promoted by molybdena are represented in Fig. 3, as insets are given the TPR profiles of the initial supports MA.

Fig. 1. TPR spectra of the gold-based catalysts; inset: initial supports.
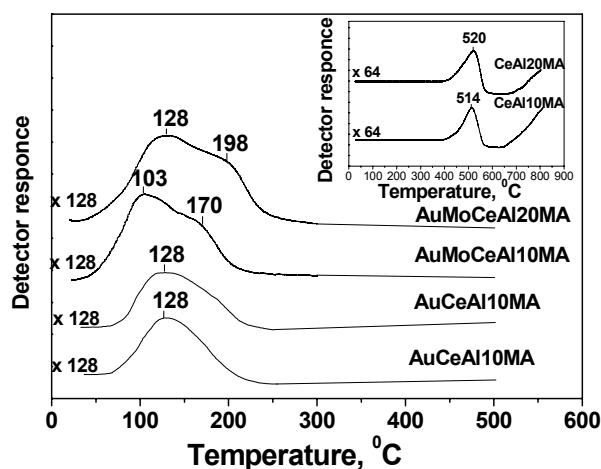
Fig. 3. TPR spectra of the gold-based and gold-molybdena catalysts; inset: initial supports.

For the pure supports, in the region up to 800°C peaks with T_{max} = 514°C for the CeAl10MA, respectively 520°C for the CeAl20MA, were registered, related with the surface layers reduction. The start of the second HT peak is also visible. The addition of gold leads again to a significant shift of the reduction temperature of ceria surface layers to the LT region. For both AuCeAl10MA and AuCeAl20MA samples the reduction peaks are at T_{max} = 128°C and they are very similar, independently of the alumina content. T_{max} in the TPR peaks in the case of MA samples are generally a little bit higher than those of the CP samples.

Additional experiments on reoxidation of the catalysts after the direct TPR were carried out. The reoxidation was accomplished at RT as well as at HT. The TPR profiles of gold-containing CP samples after RT and HT reoxidation are represented in Fig. 4: nonpromoted (Fig. 4A) and promoted by molybdena (Fig. 4B). For gold-molybdena CP catalysts on mixed supports the HC at RT and especially at HT (the temperatures at the end of the TPR peak of the fresh samples, which are practically equal to the reaction temperatures for the highest benzene conversion degree) is very close to that of the initial samples.

(A)

(B)
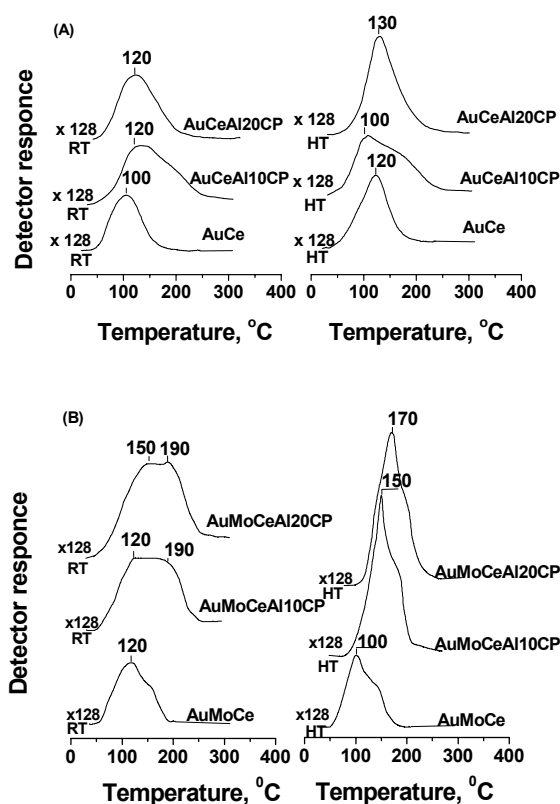
Fig. 4. TPR spectra after RT and HT reoxidation of:
A − gold catalysts and B – gold-molybdena catalysts.

For the gold-containing MA samples the TPR

profiles after reoxidation are given in Fig. 5A and for the gold-molybdena MA catalysts in Fig. 5B. After reoxidation at RT, T_{max} for the ceria-alumina based MA catalysts was shifted to higher temperatures, but after reoxidation at HT, the temperature of the peak maximum was shifted to the LT region – for the AuCeAl10MA sample T_{max} = 80°C and for the AuCeAl20MA – T_{max} = 97°C. The addition of molybdena causes differences in the form and position of the LT TPR peaks. They are complex and are attributed to the reduction of molybdena surface layers as well as of the ceria surface layers. It is interesting to note that after HT reoxidation (the temperature region of the catalytic reaction), the LT shoulder, which we attributed to the reduction of ceria surface layers, was disposed at temperatures higher than those for the samples nonpromoted by molybdena.

(A)

(B)
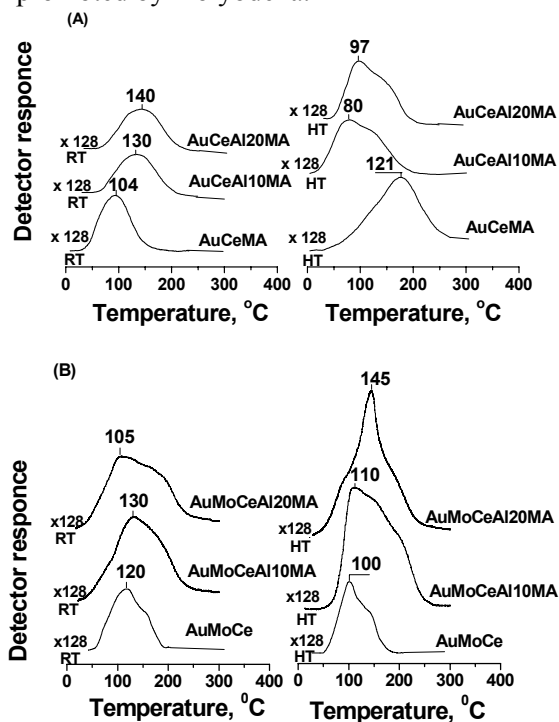
Fig. 5. TPR spectra after RT and HT reoxidation of:
A − gold catalysts and B – gold-molybdena catalysts.

In Table 2 the hydrogen consumption corresponding to the first LT-TPR peak of the studied catalysts is presented. Comparing the initial supports CP and MA, big differences are visible due to the different methods of preparation. It is seen that the hydrogen consumption of the pure supports CP in the presence of alumina is significantly higher compared to that of MA samples and pure ceria. The H_2 consumption of the CeAl20CP sample is the highest. This behaviour could be connected with the enhanced reduction of deeper ceria layers, due to the oxygen vacancies formation in the presence of alumina.

Table 2. Hydrogen consumption to the first TPR peak in the spectrum of the fresh catalysts and after reoxidation at room temperature (RT) and at high temperature (HT).

Sample	HC of direct TPR, $\mu mol \cdot g^{-1}$	HC after RT reoxidation, $\mu mol \cdot g^{-1}$	HC after HT reoxidation, $\mu mol \cdot g^{-1}$
Ce	492	-	-
CeAl10CP	716	-	-
CeAl20CP	1006	-	-
CeAl10MA	299	-	-
CeAl20MA	352	-	-
AuCe	462	240	300
AuCeAl10CP	528	360	360
AuCeAl20CP	572	320	400
AuCeAl10MA	352	216	322
AuCeAl20MA	322	216	334
AuMoCe	550	260	270
AuMoCeAl10CP	570	510	540
AuMoCeAl20CP	730	550	720
AuMoCeAl10MA	422	476	594
AuMoCeAl20MA	458	470	562

After RT or HT reoxidation, the oxygen capacity of the fresh CP catalysts containing gold only cannot be reached. In the case of AuMoCe the oxygen treatment at RT and HT is also not enough to restore the oxygen capacity of the fresh sample. Upon adding molybdena some supplementary amount of hydrogen, corresponding to the reduction of MoO$_x$ species, was consumed. Comparison between gold-molybdena containing catalysts shows that the same tendency is reproduced (higher H$_2$ consumption in the presence of Al^{3+}). In the latter case the peaks are less intensive because they are located at significantly lower temperatures, at which the oxygen mobility is not so high, compared to that of the catalysts without gold. For the MA samples containing only gold, after reoxidation at RT the oxygen capacity did not reach the initial value, but upon reoxidation at HT, the hydrogen consumption of the AuCeAl20MA sample was even higher. On the contrary, the hydrogen consumption was higher with the Au-Mo samples even at RT and the oxygen capacity was fully recovered.

Catalytic activity data

The catalytic activity of the samples was estimated in the reaction of complete oxidation of benzene and the benzene conversion was taken as a measure of it. The results on the temperature dependence of the catalytic activity of the CP samples are represented in Fig. 6. The catalysts containing molybdena show a significantly lower activity in this temperature interval (not shown in the figure). Generally, the catalysts supported on CeAl20CP are more active than the corresponding catalysts on CeAl10CP. In the LT region the activity

is low and there are practically no significant differences.
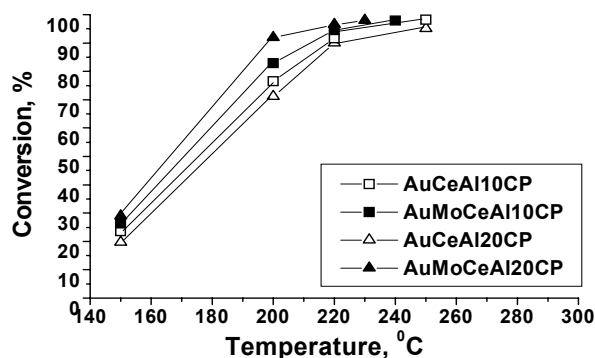
Fig. 6. Temperature dependence of the catalytic activity in CBO of the catalysts studied.

The catalytic behaviour of the MA samples is quite different compared to the CP samples. The catalytic activity data on the corresponding gold samples, supported on CeAl10MA and CeAl20MA, nonpromoted and promoted by molybdena are compared in Fig. 7, A and B.
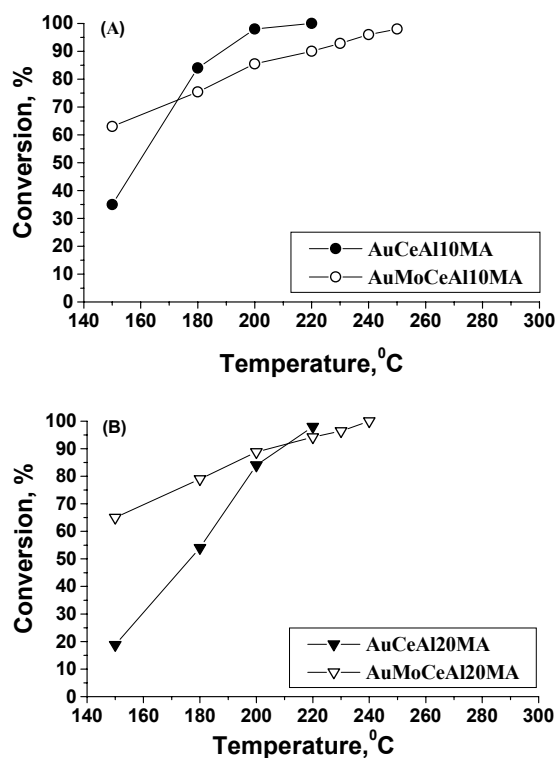
Fig. 7. Temperature dependence of the CBO conversion degree on the catalysts: (A) containing 10 wt. % alumina and (B) containing 20wt. % alumina.

An interesting catalytic behaviour is observed. The gold catalysts promoted by molybdena exhibit a higher activity in comparison to the corresponding nonpromoted ones in the LT interval. At the higher temperatures the opposite behaviour is observed.

Depending on the alumina content, the temperature of the cross-point of the two activity curves is different. This temperature is higher for the sample with higher alumina content. The catalysts containing molybdena showed a significantly lower activity (not shown in Fig.) than that of other catalysts and they will not be an object of further discussion. For the gold MA samples higher activities are exhibited by the AuCeAl10MA sample but at 220°C the activities of gold samples containing 10 and 20% alumina are practically equal (at about 100% conversion). This tendency is reversed for the gold-molybdena samples. The activity in the LT region of the samples containing Au-Mo is higher than that of the samples containing only gold. In the whole temperature range, a slightly higher activity was manifested by the AuMoCeAl20MA catalyst than that of AuMoCeAl10MA.

In Fig. 8 the catalytic activities of the Au-Mo samples, obtained by both preparation methods are compared: for the samples, containing 10 wt.% of alumina (A) and for the samples, containing 20 wt.% of alumina (B). One can see that in the LT region the MA catalysts are more active, while in the HT region the activities are almost equal, a slightly higher being that of the CP ones.
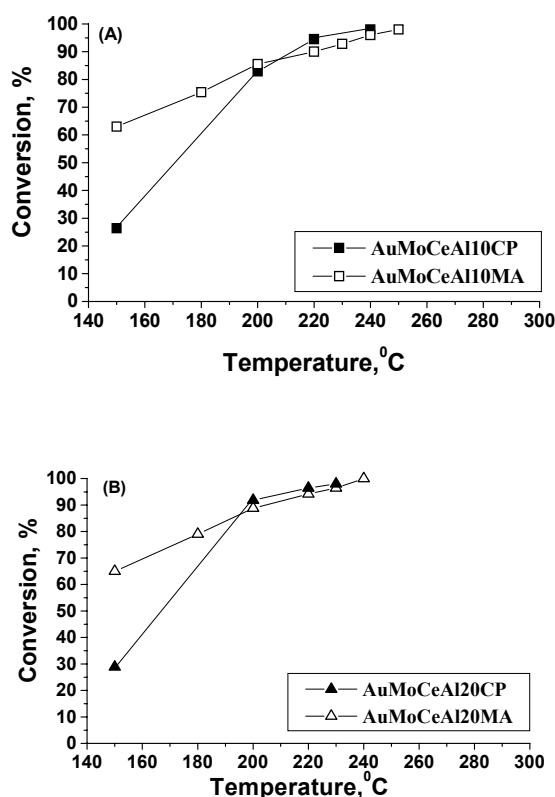
Fig. 8. Temperature dependence of the CBO conversion degree on the gold-molybdena catalysts: (A) containing 10 wt.% alumina and (B) containing 20 wt.% alumina.

DISCUSSION

The obtained catalytic activity data showed different behaviour depending on the applied method of preparation. The MA catalysts containing simultaneously gold and molybdena are more active in the LT interval than the corresponding CP catalysts. In the HT region the opposite behaviour was found out. The MA catalysts, containing only gold were more active in the HT region compared to the gold-molybdena MA samples. The cross-point position depended on the alumina content.

The studied catalytic systems are complicated and more than one factors are of great importance for the higher redox activity. On one hand, this is the oxygen mobility, which is enhanced by the presence of oxygen vacancies. On the other hand is the electron transfer from the hydrocarbon to the oxygen molecule via the catalytic surface by the activation of hydrocarbon on MoO_x species being able to enhance the redox transfer. The activation of hydrocarbons at temperatures below 220°C is possible only in the presence of gold. The electron transfer also proceeds between small gold particles and Ce^{3+} ions via oxygen vacancies and depends strongly on the size of gold particles [10, 18]. The transfer becomes possible due to the strong modification of ceria in the presence of gold [19]. Studying the reaction mechanism by FTIR of CBO on $Au-V_2O_5$ supported on titania it was found out, that the activation of benzene took place on the VO_x species [20]. The MoO_x species should play the same role like that of VO_x in gold-vanadia supported catalysts. The addition of gold to the catalysts in all cases leads to a significant lowering of the reduction temperature of ceria surface layers, which is in accordance with the higher LT redox activity of the gold catalysts.

Concerning Au and Au-Mo MA catalysts, the temperature of the cross-point should be around the point, where the predominant role of the first factor gives away to the role of the second one.

The enhanced oxygen mobility upon adding alumina to ceria is seen very well comparing the HC during TPR of the initial supports prepared by CP. In this case the first peaks in the TPR profiles of the samples are due not only to the ceria surface layers reduction, but also to the reduction of deeper layers. The calculated degree of reduction for CeAl10CP is 27.4% and for CeAl20CP, 43.3% [21]. Sanchez and Gazquez have considered that CeO_2 can be reduced up to 17% without changing the fluorite structure to the hexagonal Ce_2O_3 structure [22]. Laachir and coworkers have observed that when the reduction is limited only to the surface of ceria, this leads to a

20% reduction degree [23]. In view of these observations, the bulk reduction of ceria-alumina samples, leading to structural changes, has to be considered. The bulk ceria reduction is stronger when the amount of alumina is higher. This enhancement of ceria reduction can be connected with increased oxygen mobility in the defective ceria structure generated by the introduction of alumina using the CP method of preparation. In addition, the reduction process is enhanced by the decrease of the size of metal oxide particles. For the CP catalysts the addition of alumina leads to the lowering of the average size of ceria particles (about 2 times) [10]. In the case of MA technique (Table 2), the HC is lower than that of pure ceria. This means that only surface ceria layers are reduced, which could be related to the predominant vacancies formation on the catalysts surface. The increase of alumina amount leads to the higher HC for both preparation methods. However, the differences in the case of CP between 10 and 20% alumina are drastic due to the creation of deep oxygen vacancies at higher concentration.

In all cases the addition of gold leads to a significant lowering of the reduction temperature of ceria surface layers. This effect is related to the hydrogen activation on nanosized gold particles [24] and an increase in number of potential sites for reduction along the border between gold and support. Additionally, the introduction of alumina leads to an enhancement of ceria reduction, connected to the oxygen mobility in the defective ceria structure. After reoxidation at RT and at HT for gold-containing samples, the redox capacity was partially recovered. Comparing the HC of the gold-containing samples in the LT region, it can be seen that the higher HC was registered with the CP samples compared to the MA ones. This is in accordance with the higher concentration of oxygen vacancies, found by Raman spectroscopy [10]. It has to be noted that after reoxidation at HT (the temperature of the catalytic reaction) the oxygen capacity of CP samples cannot be recovered, while in the case of MA catalysts almost the same oxygen capacity as in the fresh samples was restored (Table 2).

In the presence of molybdena as a promoter, a complex TPR peak was registered in the LT region due to the reduction of both ceria surface layers and MoO_x species. Modifying ceria by alumina, a broadening of the LT TPR peaks was additionally found. The TPR results after reoxidation at HT show that for both preparation methods the recovering of the oxygen capacity is complete in the presence of molybdena. After RT reoxidation only for the MA catalysts the HC is even higher than that

of the fresh samples, which is fully in agreement with the higher LT activity of Au-Mo MA samples. This is also in accordance with the higher dispersion of gold in the MA catalysts (2−3 nm compared to the CP ones, 4−6 nm) [10]. Another explanation is the lower surface at.% of Au for the CP catalysts compared to the MA samples, estimated by XPS measurement results (0.30 at.% for AuMoCeAl10CP and 0.16 at.% for AuMoCeAl20CP compared to 0.41 at.% for AuMoCeAl10MA and 0.37 at.% for AuMoCeAl20MA) [10]. In the HT region (200°C and higher) the catalytic activities are almost independent of the preparation methods, the CP catalysts exhibit even a slightly higher activity than the MA ones, most probably due to the higher oxygen mobility. This is valid for the samples with 10 wt.% alumina as well as for those with 20 wt.% (Fig. 8).

CONCLUSIONS

The study of complex catalytic systems based on Au-Mo supported on ceria-alumina showed that more than one factor influenced the CBO activity. In the LT region the effect of electron transfer with the participation of nanosized gold particles has a prevailing effect and this is in agreement with significantly higher activity of Au-Mo MA samples. In the HT region obviously a predominant role is played by the oxygen mobility, related to the presence of oxygen vacancies. It could be concluded that redox activity depends on one hand on the reaction temperature and on the other hand on the method of catalysts preparation.

REFERENCES

1. T. Ono, M. Anpo, Y. Kubokawa, *J. Phys. Chem.*, **90**, 4780 (1986).
2. T. C. Liu, M. Forissier, G. Coudurier, J. C. Vedrine, *J. Chem. Soc. Faraday Trans. I*, **85**, 1607 (1989).
3. N. Giordano, M. Meazzo, A. Castella, J. C. Bart, V. Ragaini, *J. Catal.,* **50**, 342 (1977).
4. M. Banares, H. Hu, I. Wachs, *J. Catal.,* **150**, 407 (1994).
5. G. Mestl, Ch. Linsmeier, R. Gottshall, M. Dieterle, J. Find, D. Herein, J. Jager, Y. Uchida, R. Schlogel, *J. Mol. Catal. A*, **162**, 463 (2000).
6. M. Faraldos, M. Banares, J. A. Anderson, J. L. G. Fierro, *J. Catal.*, **160**, 214 (1996).
7. D. Andreeva, T. Tabakova, L. Ilieva, A. Naydenov, D. Mehanjiev, M. V. Abrashev, *Appl. Catal. A*, **209**, 291 (2001).
8. D. Andreeva, R. Nedyalkova, L. Ilieva, M. Abrashev, *Appl. Catal. A,* **246**, 29 (2003).

9. D. Andreeva, R. Nedyalkova, L. Ilieva, M. Abrashev, *Appl. Catal. B*, **52**, 157 (2004).

10. D. Andreeva, P. Petrova, J. W. Sobczak, L. Ilieva, M. Abrashev, *Appl. Catal. B*, **67**, 237 (2006); **77**, 364 (2008).

11. G. Deo, I. E. Wachs, *J. Catal.,* **146**, 323 (1994).

12. I. E. Wachs, B. M. Weckhuysen, *Appl. Catal. A,* **157**, 67 (1997).

13. R. Nedjalkova, L. Ilieva, M. C. Bernard, A. Hugot–le Goff, D. Andreeva, *Mater. Chem. Phys.* (submitted)

14. N. Kotsev, D. Shopov, *J. Catal.*, **22**, 297 (1971).

15. D. A. M. Monti, A. Baiker, *J. Catal.*, **83**, 323 (1983).

16. B. Harrison, A. F. Diwell, C. Hallett, *Plat. Met. Rev.*, **32**, 73 (1988).

17. D. Andreeva, V. Idakiev, T. Tabakova, L. Ilieva, P. Falaras, A. Bourlinos, A. Travlos, *Catal. Today*, **72**, 51 (2002).

18. D. Andreeva, I. Ivanov, L. Ilieva, J. Sobczak, G. Avdeev, K. Petrov, *Topics Catal.*, **44**, 173 (2007).

19. T. Tabakova, F. Boccuzzi, M. Manzoli, D. Andreeva, *Appl. Catal. A*, **252**, 385 (2003).

20. F. Boccuzzi, A. Chiorino, M. Manzoli, D. Andreeva, T. Tabakova, Heterogeneous Catalysis (Proc. 9th Int. Symp., Varna, 2000), L. Petrov, Ch. Bonev, G. Kadinov (Eds.), Institute of Catalysis, Bulg. Acad. Sci., Sofia, 2000, p.725.

21. L. Ilieva, G. Pantaleo, I. Ivanov, A. M. Venezia, D. Andreeva, *Appl. Catal. B*, **65**, 101 (2006).

22. M. G. Sanchez, J. L. Gazquez, *J. Catal.*, **104**, 120 (1987).

23. A. Laachir, V. Perrichon, A. Bardi, J. Lamotte, E. Catherine, J. C. Lavalley, J. El Faallah, L. Hilaire, F. le Normand, E. Quemere, G. N. Sauvion, O. Touret, *J. Chem. Soc. Faraday Trans.*, **87**, 1601 (1991).

24. F. Boccuzzi, A. Chiorino, M. Manzoli, D. Andreeva, T. Tabakova, *J. Catal.*, **188**, 176 (1999).

РЕДОКС АКТИВНОСТ НА ЗЛАТО-МОЛИБДЕНОВИ КАТАЛИЗАТОРИ: ВЛИЯНИЕ НА МЕТОДИТЕ НА ПОЛУЧАВАНЕ

П. Петрова, Л. Илиева, Д. Андреева*

Институт по катализ, Българска академия на науките, ул. „Акад. Г. Бончев“, бл. 11, 1113 София

(Резюме)

Изучена е редокс активността на злато-молибденови катализатори, нанесени върху цериев диоксид-алуминиев оксид, получени по два различни метода. Окислителната активност на катализаторите е измерена в реакцията на пълно окисление на бензен. Редукционната активност е оценена с помощта на ТПР измервания на свежи катализатори и след реокисление. Дискутирано е влиянието на метода на получаване върху редокс активността. Установено е, че главно два фактора са от съществено значение за високата редокс активност на катализаторите: кислородната мобилност и улеснения пренос на електронна плътност с участието на златото. Двата фактора зависят от степента на формиране на кислородни ваканции след добавката на злато и алуминиев оксид към цериевия диоксид, както и от размера на златните и цериевооксидните частици.

Hydrometallurgical processing of dumped lead paste for lead acid batteries

D. A. Atanasova*

Department of Semiconductors, University of Chemical Technology and Metallurgy,
8 Kliment Ohridski Blvd., 1756 Sofia, Bulgaria

Dedicated to the memory of Prof. N. K. Lyakov and Prof. G. A. Haralampiev

The present work represents an analytical survey of experimental results from conducted investigations, regarding desulphurization of dumped Pb-paste and the possibilities for the realization of the process. The aim is to compare and evaluate the results that we have obtained, with already existing data in the literature of leading technologies. Here are examined the kinetic relationships of the processes that take place and the related problems. The optimal conditions of the desulphurization process, developed by our team, are determined when using the following reagents – Na_2CO_3 and NaOH, depending on the working reactor (reactor with a laboratory stirrer and rotational reactor of drum type). The content of impurities in the solutions of our technology is investigated and compared with others of that type in order to obtain sufficiently clean crystalline Na_2CO_3 for the industry.

Key words: lead paste, Pb-paste desulphurization, lead accumulators processing.

INTRODUCTION

The main aspects regarding chemistry and conduction of the process of desulphurization are targets of many investigations and publications of different authors [1−8]. In the industry there exist installations and technologies for the realization of the process in different hydro-metallurgical schemes [9−13].

Dumped lead acid batteries can be characterized like complicated secondary products because their processing causes many difficulties [14].

Lead acid batteries consist of three basic fractions and electrolyte [1−15]:

- Metalic (combs, poles, lattices and others) with Pb content of 93−95% and Sb content of 0.1−0.3%.

- Oxysulphatic (positive and negative paste), which has 68−76% Pb and 0.1–0.3% Sb.

- Not metallic – organic (boxes made from either ebonite, polypropylene or polyethylene, polyvinyl chloride separators and others).

During the production of the metal fraction lead and antimony or lead and calcium [1, 16] are mainly used, which causes reduction of impurities in the metal.

On the other hand the oxysulphatic fraction is divided into two categories: waste and dumped lead paste [1, 17]. Waste lead paste is obtained during the production of lead acid batteries and it consists of 79−86% Pb, mainly as oxide phase and 0.1−0.3% Sb. Redeemed (positive and negative) paste has 68−76% Pb in the form of $PbSO_4 \sim$ 50–60%, $PbO_2 \sim$ 30–35%, PbO $\sim$ 10–15% and Sb $\sim$0.2–0.7%.

Many authors have investigated the pyrometallurgical processing of the lead pastes [18−21]. During these methods the extraction of lead reaches 98% and it can be conducted at relatively low temperatures 500−600°C under the condition that no lead sulphates are present. The presence of lead sulphate requires increasing of the temperatures of the process above 900°C, which leads to decreasing the degree of lead extraction and causes technological and ecological problems.

The necessity of desulphurization of pastes prior to pyrometallurgical processes of melting and refining is theoretically predicted and experimenttally proved [22].

The preliminary desulphurization of lead paste contributes to the decreasing of the melting temperature, decreasing of the amounts of fluxes and caustic soda, slag and dusts, reduces the content of SO_2 in the gases and the quantity of chemical reagents used in the refining cycle, enhances the degree of lead extraction and so on [5, 11, 22].

The essence of the desulphurization process consists in taking the sulphate ions out of the paste into the solution and generating chemical compound of the lead, which does not cause any difficulties during following pyrometallurgical treatment [22].

Physicochemical and technological investigations of the main aspects of the desulphurization

process of the lead sulphate have been published in the literature [22].

The basic chemical and kinetic principles like: stoichiometry of the reaction and diffusion kinetics, are thoroughly examined by Laidler *et al.* [23].

The most commonly used reagent for desulphurization of dumped lead pastes is the sodium carbonate [1−11, 24−26]. The desulphurization process is accomplished by treating the paste with solutions of sodium carbonate according to the reaction:

$$PbSO_4 + Na_2CO_3 \rightarrow PbCO_3 + Na_2SO_4 \quad (1)$$
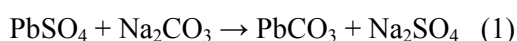
The sulphur goes into the solution in the form of sodium sulphate. The obtained solutions, after separation of the liquid and solid phase, can be subjected to evaporation and centrifuging in order to obtain waterless sodium sulphate [2, 27].

In the presence of electrolyte in the paste - H_2SO_4, a complete neutralization of the acid in the solution of Na_2CO_3 takes place, with molar proportion $Na_2CO_3:H_2SO_4 > 1$, according to the following reaction:

$$Na_2CO_3 + H_2SO_4 \rightarrow Na_2SO_4 + H_2O + CO_2 \quad (2)$$
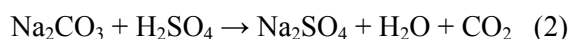
This explains the generation of Na_2CO_3:

$$2Na_2CO_3 + H_2SO_4 \rightarrow Na_2SO_4 + 2NaHCO_3 \quad (3)$$

In view of the conditions during the desulphurization process – concentration of sodium carbonate, ratio of liquid to solid mass, temperature, duration of the process, *etc.*, it is possible to have parallel reactions.

When the consumption of the reagent exceeds the stoichiometrically corresponding to the reaction (1), actually in excess of sodium carbonate, the following reactions take place:

$$PbSO_4 + 4Na_2CO_3 + 2H_2O \rightarrow$$
$$\rightarrow 2PbCO_3.Pb(OH)_2 + 3Na_2SO_4 + 2NaHCO_3 \quad (4)$$

$$3PbCO_3 + Na_2CO_3 + 2H_2O \rightarrow$$
$$\rightarrow 2PbCO_3.Pb(OH)_2 + 2NaHCO_3 \qquad 5)$$
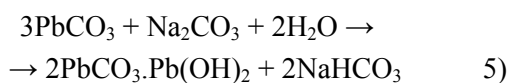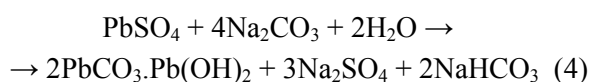
The interaction between the lead sulphate and sodium carbonate has been studied by many authors [1, 2, 8, 28, 29], and according to them reaction (1) describes accurately enough the process of desulphurization. Investigations of the chemistry of the process prove the generation of complex compound of the lead, incorporating in itself sodium and sulphatic ions of the type: $Pb_3(CO_3)_2(OH)_2$, $NaPb_2(CO_3)_2OH$, $Pb_{10}O(CO_3)_6(OH)_6$, $Pb_4(SO_4)(CO_3)_2(OH)_2$ [24, 30].

The nature of the compounds in solid phase depends on several factors, in particular on the pH and on the concentration of sodium carbonate and

sodium sulphate in the solutions [24]. The formation of these compounds causes increase of the reagent consumption and difficulties during further treatment and usage of the ready product.

It is established that during desulphurization of Pb paste with Na_2CO_3, 2−3% of the Sb, contained in the paste, can pass into the solution [22].

Many technologies for processing of dumped lead paste use sodium base for the desulphurization process [7, 9, 10, 30−34].

Also during this method a reaction of neutralization of the H_2SO_4 contained in the paste initially takes place:

$$2NaOH + H_2SO_4 \rightarrow Na_2SO_4 + 2H_2O \quad (6)$$

The transformation of $PbSO_4$ into $Pb(OH)_2$ is typical for the process of desulphurization and it takes place according to the reaction:

$$PbSO_4 + 4NaOH \rightarrow Pb(OH)_2 + Na_2SO_4 \quad (7)$$
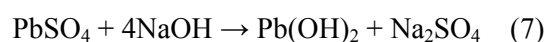
The desulphurization using NaOH can be accomplished at room temperature. Increasing of the temperature may lead to changes in the solid phase of $Pb(OH)_2$ to $3PbO.2H_2O$ (or $PbO.1/3H_2O$), according to the reactions:

$$PbSO_4 + 2NaOH \rightarrow$$
$$\rightarrow PbO.1/3H_2O + Na_2SO_4 + 2/3H_2O \qquad (8)$$

$$PbSO_4 + 2NaOH \rightarrow PbO + Na_2SO_4 + H_2O \quad (9)$$
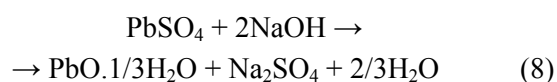
An excess of NaOH ~10−20% of the stoichiometrically needed for the reaction (7) is necessary, for a complete desulphurization process in the technological practice [7, 22].

Part of the lead is transferred into the solution in the form of Na_2PbO_2, according to the reaction:

$$PbSO_4 + 4NaOH \leftrightarrow Na_2PbO_2 + Na_2SO_4 + 2H_2O \quad (10)$$

There is a direct relationship between the concentration of NaOH and the content of Na_2PbO_2 in the solutions. The concentration of Na_2PbO_2 increases at higher excess of NaOH [7, 29].

The solution of Na_2SO_4, obtained after desulphurization process, can be subjected to purifying from the lead using neutralization with H_2SO_4, according to the reaction:

$$Na_2PbO_2 + H_2SO_4 \rightarrow PbSO_4 + Na_2SO_4 + 2H_2O \quad (11)$$

The separated $PbSO_4$ in the form of deposit, again returns into stage for desulphurisation, and the solution of Na_2SO_4 is good for obtaining crystalline Na_2SO_4 which is free of impurities.

Many authors suggest that the regeneration of the Na_2SO_4 is to be conducted using $Ca(OH)_2$ [25, 38−42] and $Ba(OH)_2$ [42].

286

The degree of desulphurization is determined by the content of $PbSO_4$ in the treated paste. The bigger that percentage content in the initial product is, the higher is the consumption of NaOH (the concentration in the solution), which leads to increases in the concentration of Pb in the solutions [7, 29].

During desulphurisation with NaOH almost no Sb passes into the solutions, and no insoluble sodium salts are created [7, 29, 43].

There exists also technology for desulphurization of lead pastes with NaOH, during which the solutions of Na_2SO_4 are subjected to electrolysis for regeneration of NaOH. The ratio of liquid to solid phase, when using this method, is 10−15:1 [33].

In many technologies the desulphurisation of lead pastes with NaOH is followed by treatment with NBF_4 [44−46]. The insoluble remainder is treated with concentrated H_2SO_4. Because of that PbO_2 is transferred in the electrolyte and proceeds as electrolysis with insoluble anode.

Desulphurization of Pb paste can be successfully accomplished with ammonium carbonate, as well [47−52]. The chemical reaction takes place according to the reaction:

$$PbSO_4 + (NH_4)_2CO_3 \rightarrow PbCO_3 + (NH_4)_2SO_4 \quad (12)$$
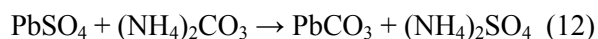
Data in the literature, concerning the usage of ammonium carbonate as a desulphurisation agent, is mainly connected with the investigation of kinetic and technological parameters. According to data by the authors, when the process lasts 30 minutes, the degree of desulphurization reaches 90%. Further increasing of the duration of the process does not affect significantly the degree of desulphurization. Increasing of the temperature in the range of 22−60°C is insignificantly accelerating the process.

Many authors are also investigating the possibility to use K_2CO_3 [2, 53−55] as a desulphurization agent, which reacts with $PbSO_4$ according to the reaction:

$$PbSO_4 + K_2CO_3 \rightarrow PbCO_3 + K_2SO_4 \quad (13)$$

High degree of desulphurization reached ~95%. The process proceeds at temperature ~60°C, ratio of liquid to solid 3:1, excess of K_2CO_3 10−15% and duration of 60 minutes [2].

In the literature there exist data on the influence of the basic factors in the process (degree of desulphurization and utilization of the reagent). The authors have also investigated possible schemes for continuous process, which are followed by evaporation and taking out the salts from the solutions with the aim to obtain crystalline K_2SO_4 [2].

The hydrometallurgical treatment of the lead-containing raw materials can also be done with the use of amines. There also exists a technology for desulphurization of dumped lead pastes using the organic solvent diethylenetriamine (DETA) [1, 8, 56, 57]. The method is based on the formation of metallic complex compound, in which the metal-amine bond is stronger than the metal-water bond.

When the liquid phase is being treated with Na_2CO_3 pure compounds can be obtained: $PbCO_3$ and $PbSO_4$, and when it is treated with H_2SO_4 – pure $PbSO_4$ for the needs of lead acid battery industry. Soft lead can be obtained from the solid phase, when melted at relatively low temperatures, [1, 8].

The chemistry of the process comprises the following reactions:

$$3PbSO_4 + 4DETA \rightarrow [Pb_3(DETA)_4](SO_4)_3 \quad (14)$$

$$[Pb_3(DETA)_4](SO_4)_3 + 3NaCO_3 \rightarrow$$
$$\rightarrow 3PbCO_3 + 3NaSO_4 + 4DETA \quad (15)$$

$$[Pb_3(DETA)_4](SO_4)_3 + 2DETA + 3H_2SO_4 \rightarrow$$
$$\rightarrow 3PbSO_4^- + 2DETA.3H_2SO_4 + 4DETA \quad (16)$$

$$2DETA.3H_2SO_4 + Ca(OH)_2 \rightarrow$$
$$\rightarrow 2DETA + 3(CaSO_4.2H_2O) \quad (17)$$
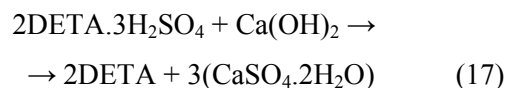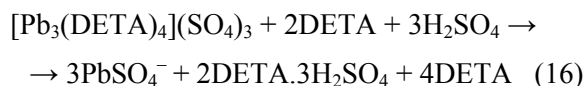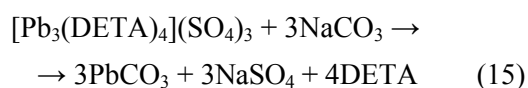
On the basis of the above literature review concerning the methods for desulphurization of dumped lead pastes from lead batteries, the aims of the present investigation are formulated as follows:

- to determine the influence of the basic kinetic factors (concentration of Na_2CO_3 (NaOH) and the ratio of liquid to solid phases as a function of the temperature and duration of the process), that influence the parameters of the process of desulphurization of Pb-pastes − degree of desulphurization and utilization of the reagent;

- to specify the optimal conditions for accomplishing desulphurization of Pb-pastes with Na_2CO_3 or NaOH, depending on the type of the reactors used;

- investigation of the content of impurities in the solutions in order to obtain sufficiently pure crystalline sodium sulphate for further use in the industry;

- the results from the conducted experimental researches on both samples will be compared with each other and with the existing experimental and technological data in the literature.

EXPERIMENTAL

Object of the first part of our investigations [7] is dumped lead paste from lead acid batteries imported from Romania - Sample № 1 given to us by "KCM-Plovdiv", Bulgaria.

The second part of the investigations is done with dumped lead acid battery paste imported from Poland (Sample No. 2) given to us by the same company.

The pastes have the following chemical composition (%):

Sample No. 1: Pb 59.85; Sb 0.73; As 0.042; Cl 0.33; Cu 0.13; Zn 0.10; S_Σ 7.20; $S_{SO_4^{2-}}$ 6.45.

Sample No. 2: Pb 73.05; Sb 0.053; As 0.015; Cl 0.01; Cu 0.007; Zn 0.009; S_Σ 7.15; $S_{SO_4^{2-}}$ 6.38.

It should be pointed out that Sample No. 2 is purer than Sample No. 1 with respect to impurities.

Before subjecting to desulphurization process, the Pb-paste is dried and sifted in a sieve of mesh 5.0 mm.

Sample No. 1: The fraction (< 5.0 mm) is 80% and the fraction (> 5.0 mm) is 20%.

Sample No. 2: The fraction (< 5 mm) is 95%, and the fraction (> 5 mm) is 5%.

Sample № 1 is contaminated, which may be due to ineffective separation technology.

A laboratory stirrer type ER 10 and mass of the paste 200 g are used for the laboratory work and the temperature is maintained constant by thermostat type Ultra NBA. When treating in rotational reactor of drum type VEB Elmo Hartha DDR, the mass of the paste is 400 g. In this case the amount of paste is higher because of the larger working volume of the equipment and the related difficulties. These difficulties concern maintaining constant working temperature in this type of reactor under laboratory conditions, as with increasing the amount of material the rate of cooling under atmospheric air decreases.

The lead paste 200 (400) g is added to solutions of specified Na_2CO_3 (NaOH) concentration and at definite liquid-solid phase ratio (at preset temperature and duration of the desulphurization process).

The analyses are realized using analytical chemical methods. Upon accomplishment of the chemical treatment, the pulp is filtered and the solid phase is washed with water on the filter, dried to constant weight and analyzed for content of SO_4^{2-}. The liquid phases are analyzed for content of Na_2CO_3 (NaOH) and SO_4^{2-}. The determination of SO_4^{2-} in the solid phase is done using weighting method. Initially the sample is decomposed with solution of Na_2CO_3 and after that from the obtained solutions SO_4^{2-} is precipitated using $BaCl_2$ in the form of $BaSO_4$. The analysis of SO_4^{2-} in liquid phase is identical (precipitation with $BaCl_2$). The

data from it in this case can be used for verification of the results from the analysis for SO_4^{2-} in solid phase (balance with respect to sulphur).

The remaining concentration of uncombined Na_2CO_3 and NaOH in the liquid phases (filtrates) is determined by titration with 0.1 M HCl and *Methyl orange* as indicator.

The content of sulphatic sulphur $S_{SO_4^{2-}}$ in the non-desulphurized paste and the chemical composition is determined by phase analysis.

The desulphurization degree α (%) is calculated by the formula:

$$\frac{Ds(\text{initial}) - Ds(\text{final})}{Ds(\text{initial})} \cdot 100 = \alpha,$$

where: $Ds_{(initial)}$ and $Ds_{(final)}$ are initial and residual SO_4^{2-} concentration.

The reagent utilization degree β (%) is calculated by the formula:

$$\frac{C(\text{initial}) - C(\text{final})}{C(\text{initial})} \cdot 100 = \beta,$$

where: $C_{(initial)}$ and $C_{(final)}$ are initial and residual reagent concentrations, $g \cdot L^{-1}$.

RESULTS AND DISCUSSION

Desulphurization of Pb-paste with Na₂CO₃ in a reactor with a laboratory stirrer

For the purposes of the present research, regarding the desulphurization of the paste, an examination regarding the influence of the basic kinetic factors is conducted: initial concentration of Na_2CO_3 (consumption of Na_2CO_3), ratio of liquid to solid phase, duration of the desulphurization process with set temperature interval, which is connected with the properties of the reagent and the products from the reaction.

Based on the conducted preliminary experiments [7, 28, 29] and data from the literature [2] it is determined that the temperature does not affect significantly the parameters of the desulphurization process (degree of desulphurization α, degree of utilization β of the Na_2CO_3), because the work is done in an environment of diffusion control [23]. The coefficients α and β have highest values in the range 30−40°C, above that temperature the solubility of Na_2CO_3 and Na_2SO_4 in water decreases [58−60].

The solubility of Na_2CO_3 and Na_2SO_4 and of the compounds, obtained from them, are directly connected with the indexes of the process – degree

of desulphurization and degree of utilization of the reagent and the stoichiometric realization of the filtration process, as well [5, 6].

Fig. 1 presents the results from the desulphurization of Pb-paste – Sample No. 2 with ratio of liquid to solid phase $m = 2.25$ (m = 2.25:1), temperature 38−40ºC and different initial concentrations of Na_2CO_3:
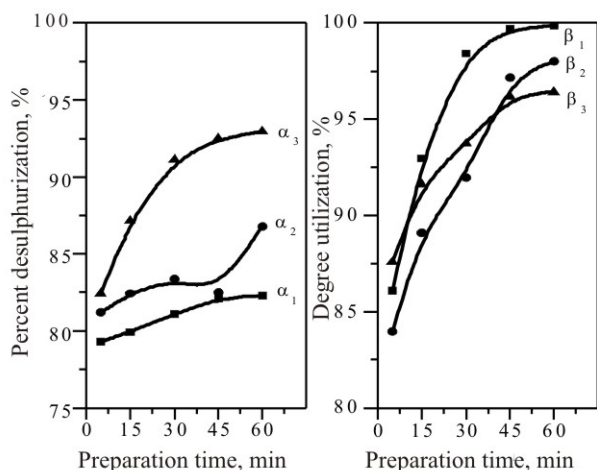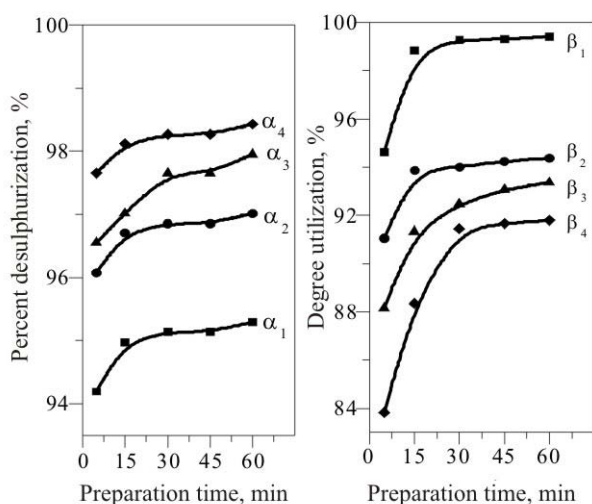

Fig. 1. Dependence of the percentage of desulphurization (α) and Na_2CO_3 utilization degree (β) on the treatment time (τ) when stirring with laboratory agitator (m = 2.25; t = 38−40°C): $C_{initial(1)} = 84.51$ g·L−1 ($α_1$, $β_1$), $C_{initial(2)} = 93.93$ g·L^{-1} ($α_2$,$β_2$) and $C_{initial(3)} = 103.33$ g·L^{-1} ($α_3$, $β_3$); a −$α_1$, $α_2$, and $α_3$; b − $β_1$, $β_2$ and $β_3$.

I experiment – with shortage of 10% with respect to the stoichiometric ratio $C_{initial(1)} = 84.51$ g·L^{-1} Na_2CO_3; II experiment – $C_{initial(2)} = 93.93$ g·L^{-1} Na_2CO_3 (stoichiometric ratio); III experiment – $C_{initial(3)} = 103.33$ g·L^{-1} Na_2CO_3 (10% excess).

A satisfactory degree of desulphurization, corresponding to the technological requirements [10], is achieved after 30 minutes but it is desirable that $τ > 45$, when the degree of desulphurization is $α = 92.48$ % (content of $S_{SO_4^{2-}}$ in the desulphurizated paste 0.48%). With an excess of Na_2CO_3 10% ($C_{initial(3)} = 103.33$ g·L^{-1}) and duration of the process 60 minutes, the degree of desulphurization is $α_3 = 92.95\%$ ($S_{SO_4^{2-}} = 0.45\%$).

The obtained results are in accordance with the data from the literature [2, 7, 22] and are close to those for Sample No. 1. After 15 min treatment of Pb-paste with stoichiometric amount of Na_2CO_3 ($C_{initial(2)} = 94.95$ g·L^{-1}) the degree of desulphurization is $α = 94.11\%$ (0.38% $S_{SO_4^{2-}}$ in the desulphurized paste) [7]. For Sample No. 1, even with 10% shortage of the Na_2CO_3 the degree of desulphurization is $α_1 = 92.09\%$ (0.51% $S_{SO_4^{2-}}$ in

the desulphurized paste) [7].

The high degree of utilization of the Na_2CO_3 is noticeable. This imposed a series of two more experiments with Sample No. 2, to be conducted upon changing the ratio $m = 2.5$, temperature 37−40°C and increasing the initial concentration of Na_2CO_3:

I experiment – with $C_{initial(1)} = 93.00$ g·L^{-1} Na_2CO_3 (10% excess);

II experiment – $C_{initial(2)} = 101.45$ g·L^{-1} Na_2CO_3 (20% excess).

The results are presented in Fig. 2.
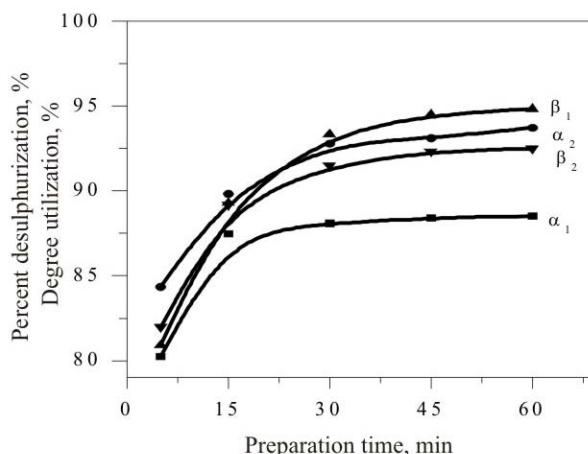
Fig. 2. Dependence of percentage of desulphurization (α) and Na_2CO_3 utilization degree (β) on the treatment time (τ) when stirring with laboratory agitator (m = 2.5; t = 37−40°C): $C_{initial(1)} = 93.00$ g·L^{-1} ($α_1$, $β_1$), $C_{initial(2)} = 101.45$ g·L^{-1} ($α_2$, $β_2$).

Satisfactory for the practice results [10] are obtained after $τ = 30$ min, with initial concentration of Na_2CO_3 with 20% excess ($C_{initial(2)} = 101.45$ g·L^{-1}) – degree of desulphurization $α_2 = 92.79\%$ ($S_{SO_4^{2-}} = 0.46$ % in the desulphurized paste), for 45 min and 60 min respectively 93.10% ($S_{SO_4^{2-}} = 0.44$ %) and 93.73% ($S_{SO_4^{2-}} = 0.40\%$).

These results correspond to existing data in the literature from laboratory experiment, during which the possibility for optimal running of the desulphurization process with excess of Na_2CO_3 − 20% is determined, duration 2 hours, temperature 55°C, <33% solid phase in the pulp and pH 8 [24].

Recommended conditions for desulphurization of Pb-paste – Sample № 1 with Na_2CO_3, when stirred with a laboratory stirrer, were established: excess of the reagent up to 10%; ratio of liquid to solid phase $m = 2.0−2.5$; temperature and duration of the process – t = 35−40ºC and τ = 15−30 min respectively [7].

289

As optimal conditions in regard to degree of desulphurization and utilization of the reagent for Sample No. 2, can be accepted: initial concentration of Na_2CO_3 with 20% excess ($C_{initial(2)} = 101.45$ g·L^{-1}), $m = 2.5$ and duration of the process $\tau = 35-40$ min.

These minor differences in the obtained results for the different Pb-paste samples are due to the differences in their chemical composition.

The condition to work in excess of Na_2CO_3 not higher than 20% was observed during running this group of experiments, in order to avoid the formation of $NaHCO_3$ and the double salt $NaPb_2(CO_3)_2OH$ [24, 30], which increase the consumption of Na_2CO_3.

The results from investigations of the process pointed out by Yanakieva [2] are analogous. For optimal concentration, when working with a laboratory stirrer, the author recommends 20% excess of Na_2CO_3. The same methods of the experiment and the same analytical chemical analysis for determination of the results have been used.

The world leading company in desulphurization of dumped lead acid battery pastes is the Italian company "Engitec Impianti [10]" - installation "CX Compact".

When using the installation "CX Compact", dumped lead paste, after wet transportation on vibration sieve, is transferred into a precipitation device, and after compaction in it, is fed into one of two parallel working mechanical stirrers, where it is treated with solutions based on sodium carbonate or sodium hydroxide. During the process the pulp is heated, where upon the lead sulphate is transformed in either lead carbonate or lead hydroxide, and the sulphur passes into the solution as sodium sulphate. After the desulphurization process the pulp is fed into an automatic filter-press. The filtered solution is then sent for evaporation-crystallization, the solid desulphurizated paste, with humidity below 13% and sulphur content less than 0.8%, is collected in containers for revision.

Based on this technology the following companies are working: Monbat AD - Bulgaria; Asarco; Doerun; GNB - USA; Metallgesellschaft - Germany, STCM - France, Metallum-Switzerland; Enirisorse - Italy, Tonolli - Canada, Brittania - England and others [8].

Desulphurization of Pb-paste with Na_2CO_3 in rotational reactor of drum type

The investigations are conducted in order to avoid the difficulties, which are typical of stirrers: stirring of the materials and emptying the device. The inconvenience when working with rotational reactor is that it is not possible to maintain constant temperature. This disadvantage can be overcome by heating with sharp vapour in the volume of the device.

At temperature $56-28°C$ and $m = 2.25$ two experiments were conducted with Na_2CO_3 and Sample No. 2 (Fig. 3), with changed initial concentration:
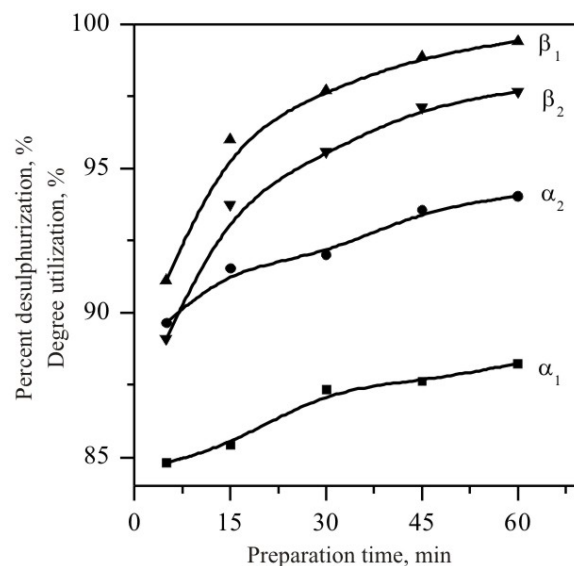
Fig. 3. Dependence of the percentage of desulphurization (α) and the Na_2CO_3 utilization degree (β) on the treatment time (τ) when using rotary reactor at t = $56-28°C$, $m = 2.25$: $C_{initial(1)} = 93.92$ g·L^{-1} (α_1, β_1), $C_{initial(2)} = 103.31$ g·L^{-1} (α_2, β_2).

I experiment – $C_{initial(1)} = 93.92$ g·L^{-1} (stoichiometric ratio);

II experiment – $C_{initial(2)} = 103.31$ g·L^{-1} (10% excess).

Good results, which correspond to the already mentioned technological requirements, were obtained with 10% excess of Na_2CO_3 ($C_{initial} = 103.31$ g·L^{-1}) and duration of the treatment $\tau = 30$ min – degree of desulphurization $\alpha_2 = 92.01\%$ ($S_{SO_4^{2-}} = 0.51\%$); when $\tau = 45$ and 60 min correspondingly 93.57% ($S_{SO_4^{2-}} = 0.41\%$) and 94.04% ($S_{SO_4^{2-}} = 0.38\%$).

The following parameters can be accepted as optimal for the process when working with rotational reactor: initial concentration of Na_2CO_3 with excess of 10% ($C_{initial} = 103.31$ g·L^{-1}), $m = 2.25$ and $\tau = 30-45$ min.

The obtained results supplement the previous data received for Sample № 1. Two experiments were conducted with it using Na_2CO_3, t = $55-28°C$ and changing the ratio m [7], for the following conditions:

I experiment – $C_{initial} = 94.95$ g·L^{-1} (stoichiometry); $m = 2.25$;

II experiment – $C_{initial} = 94.00$ g·L^{-1} (10% ex-

cess); *m* = 2.5.

For *m* = 2.25 and τ = 15 min the obtained degree of desulphurization is 92.40% (in the desulphurized paste $S_{SO_4^{2-}}$ = 0.49%); at τ = 30 min – α = 93.95% ($S_{SO_4^{2-}}$ = 0.39%);

For *m* = 2.5 and τ = 15 min − α = 92.87% ($S_{SO_4^{2-}}$ = 0.46%), when τ = 30 min. − α is 93.64% ($S_{SO_4^{2-}}$ = 0.41%).

The optimal conditions for desulphurization of Sample No. 1 are excess of Na_2CO_3 up to 10%; *m* = 2.25−2.50; t = 40−38ºC; τ = 15−30 min.

The obtained results are close to those obtained when working with an ordinary reactor equipped with a laboratory stirrer [7].

In order to optimize the influence of the initial concentration of Na_2CO_3 and m when using rotational reactor of the drum type, an experiment is conducted with Sample No. 2 (Fig. 4), under the following conditions: *m* = 2.5, t = 58−28°C and initial concentration $C_{initial}$ = 101.44 g·L^{-1} Na_2CO_3 (20% excess).

With 20% excess of Na_2CO_3 the process runs at higher speed. On the 15th minute the degree of desulphurization is 93.57% ($S_{SO_4^{2-}}$ = 0.41%).

As it has already been determined for the same sample (Sample No. 2 in the section above, when using laboratory reactor with a stirrer and initial concentration of Na_2CO_3 with 20% excess ($C_{initial(2)}$ = 101.45 g·L^{-1}), results which are satisfactory for the practice are obtained after τ = 30 min.
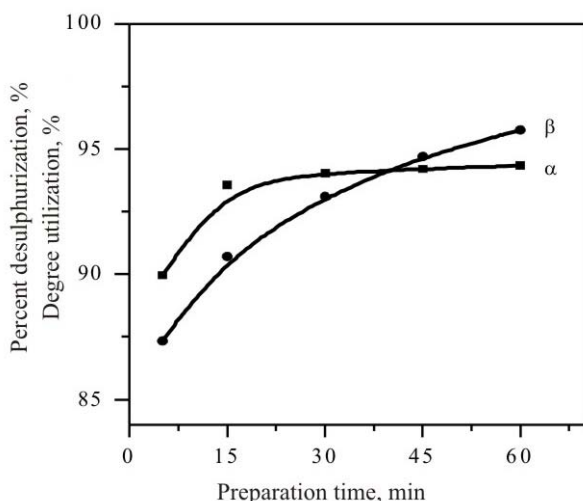
Fig. 4. Dependence of the percent desulphurization (α) and Na_2CO_3 utilization degree (β) on the treatment time (τ) when using rotary reactor at t = 58–28ºC, *m* =2.5, $C_{initial}$ =101.44 g·L^{-1}.

The process of desulphurisation takes place faster in a rotational reactor compared to that in a laboratory stirrer, which is due to improvement of the conditions for better contact with the reagent.

The obtained results clearly show the kinetic correlations described above, that is upon increasing of the concentration of Na_2CO_3 the degree of desulphurization increases but the degree of utilization of the reagent decreases because the process runs with diffusional difficulties [23].

The change in the ratio *m* does not affect significantly the kinetics of the process. The obtained data are in accordance with those mentioned in the literature [7, 22].

The correlations were determined also by Yanakieva [2] by indicating data regarding periodical and continuous process of desulphurization in rotational drum separator in a technological line No. 1 in department "Lead acid battery waste" of the company OCK-LTD in Kurdjali. It is established that when using 20% excess of Na_2CO_3 under industrial conditions, after washing the paste a higher degree of desulphurization is achieved (99%) than under laboratory conditions with a stirrer (95%).

Desulphurization of Pb-paste with NaOH in a reactor with a laboratory stirrer

These investigations were done in order to determine the influence of the initial concentration of NaOH and the ratio of liquid to solid phase at temperature 38−40ºC upon the parameters of the process, as a function of time: degree of desulphurization of the paste and degree of utilization of NaOH.

Here, similarly to the other groups of experiments, it was found out that the temperature above certain value does not affect significantly the parameters of the desulphurization process [7, 28, 29].

Four experiments with Sample No. 2 paste were done at t = 40°C and *m* = 2.25 (Fig. 5a, b) and the following conditions:

I experiment − $C_{initial(1)}$ = 63.80 g·L^{-1} (stoichiometric ratio);

II experiment − $C_{initial(2)}$ = 67.00 g·L^{-1} (5% excess);

III experiment − $C_{initial(3)}$ = 70.20 g·L^{-1} (10% excess);

IV experiment − $C_{initial(4)}$ = 76.56 g·L^{-1} (20 % excess).

On the 5th minute a very high degree of desulphurization is reached, at a stoichiometrical ratio ($C_{initial(2)}$ = 63.80 g·L^{-1}) the degree of desulphuri-

zation is $\alpha_1 = 94.62\%$ ($S_{SO_4^{2-}} = 0.37\%$), and at 5% excess ($C_{initial} = 67.00$ g·L^{-1}) − $\alpha_2 = 96.08\%$ ($S_{SO_4^{2-}} = 0.25\%$).

Fig. 5. Dependence of the percentage of desulphurization (α) and Na$_2$CO$_3$ utilization degree (β) on the treatment time (τ) when stirring with laboratory agitator ($m = 2.5$; $t = 40°C$): $C_{initial(1)} = 63.80$ g·L^{-1} (α_1, β_1), $C_{initial(2)} = 67.00$ g·L^{-1} (α_2, β_2), $C_{initial(3)} = 70.20$ g·L^{-1} (α_3, β_3), $C_{initial(4)} = 76.56$ g·L^{-1} (α_4, β_4), a − α_1, α_2, α_3 and α_4; b − β_1, β_2, β_3 and β_4.

Analogous research works were done with NaOH and change in the ratio m with Sample No. 1 as well [7], at $t = 38−40°C$, $m = 2.0$ and concentration:

I experiment – stoichiometric ratio ($C_{initial} = 80.62$ g·L^{-1});

II experiment – 5% excess ($C_{initial} = 84.65$ g·L^{-1});

III experiment – 10% excess ($C_{initial} = 86.68$ g·L^{-1}).

The indexes of the desulphurization process with NaOH were very good with Sample No. 1, as well [7]. On the 5th minute the degree of desulphurization at stoichiometric ratio is $\alpha = 92.10\%$ (in the desulphurized paste $S_{SO_4^{2-}} = 0.51\%$). After 15 min degrees of desulphurization are achieved $\alpha = 93.64−94.88\%$, depending on the initial concentration of NaOH.

Decrease in the conversion of the reagent (β) is observed with the increase of the initial concentration (excess 5−10%), which is in complete correspondence with the kinetic laws.

When using a bigger excess of NaOH (Sample No. 2) – 10% and 20%, the desulphurization degree is: $\alpha_3 = 96.55\%$ ($S_{SO_4^{2-}} = 0.22\%$) and $\alpha_4 = 97.65\%$ ($S_{SO_4^{2-}} = 0.15\%$).

It is noticeable that the change in the ratio of liquid to solid phase for desulphurization with NaOH in the range m = 2−2.5, does not affect significantly the parameters of the process.

It can be accepted that m = 2.5 is optimal, because bigger ratio will increase the volume of the system and the amount of waste solutions and the consumption of the reagent respectively.

The optimal conditions for desulphurization in relation to α and β are: from 0 to 5% excess of NaOH ($C_{нач} = 63.8−67.00$ g·L^{-1}), m = 2.5, t = 40°C and τ = 5−15 min.

According to data from the technological practice of the desulphurization process, the need of ~10−20% excess of NaOH is determined, and the degree of desulphurization reaches ~95%, and the content of sulphate sulphur in the desulphurized paste does not exceeds 0.6% [22].

Desulphurization with NaOH when working with rotational reactor of the drum type

In order to confirm and summarize the results three experiments were conducted with Sample № 2 (Fig. 6a, b), at t = 48−28°C, m = 2.5 and initial concentration of NaOH:

I experiment − $C_{initial(1)} = 63.80$ g·L^{-1} (stoichiometric ratio);

II experiment − $C_{initial(2)} = 67.00$ g·L^{-1} (5% excess);

III experiment − $C_{initial(3)} = 70.20$ g·L^{-1} (10% excess).
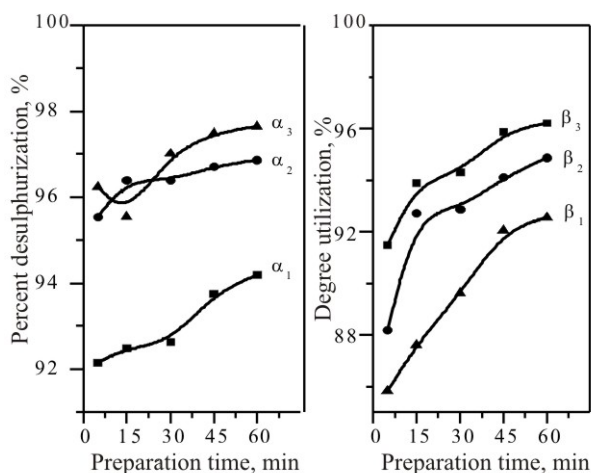
Fig. 6. Dependence of percentage of desulphurization (α) and Na$_2$CO$_3$ utilization degree (β) on the treatment time (τ) when using rotary reactor at t = 48−28°C, $m = 2.5$: $C_{initial(1)} = 63.80$ g·L^{-1} (α_1, β_1), $C_{initial(2)} = 67.00$ g·L^{-1} (α_2, β_2) and $C_{initial(3)} = 70.20$ g·L^{-1} (α_3, β_3); a − α_1, α_2 and α_3; b − β_1, β_2 and β_3.

On the 5th minute and stoichiometric ratio

$C_{initial(1)} = 63.80$ g·L^{-1}: $\alpha_1 = 92.16\%$ ($S_{SO_4^{2-}} = 0.50\%$).

For 5% excess of NaOH ($C_{initial} = 67.00$ g·L^{-1}) we obtained $\alpha_2 = 95.55\%$ ($S_{SO_4^{2-}} = 0.28\%$), and for 10% excess ($C_{initial} = 70.20$ g·L^{-1}) $- \alpha_3 = 96.24\%$ ($S_{SO_4^{2-}} = 0.24\%$).

These data are also confirmed by three experiments conducted with Sample № 1 [7], under the following conditions: $m = 2$, t = 48−28ºC and initial concentration of NaOH: $C_{initial} = 80.62$ g·L^{-1} (stoichiometric content) − I experiment; $C_{initial} = 84.65$ g·L^{-1} (5% excess) – II experiment ; $C_{initial} = 86.68$ g·L^{-1} (10% excess) − III experiment.

These results are similar to those obtained by treating the Pb-paste with NaOH in a reactor with a laboratory stirrer.

During desulphurization in rotational reactor of the drum type increase of the degree of desulphurization is observed after the 15th minute. On the 30th minute values of $\alpha = 95.50-97.36\%$ are reached.

These results exceed significantly the technological requirements [10]. Because of this, the following conditions can be accepted as optimal for both samples: up to 5% excess of NaOH, $m = 2-2.5$, t = 48−42°C and $\tau = 5-15$ min**.**

Data, regarding desulphurization process with NaOH in rotational reactor of the drum type, were not found in the literature.

Behaviour of the impurities during desulphurization of Pb-pastes

Behaviour of the impurities during desulphurization of Pb-pastes with Na$_2$CO$_3$. The results from analysing the liquid phase after desulphurization of the pastes with Na$_2$CO$_3$, using a laboratory stirrer, regarding the concentration of impurities are presented in Table 1.

It is also important to point out the fact that the solutions obtained after treating Sample No. 2 are 10−100 times purer than those from Sample No. 1, regardless of the fact that with it values of the degree of desulphurization above 90% are achieved with stoichiometric amount of Na$_2$CO$_3$ and the process of desulphurization is of shorter duration.

The value of pH of the solutions after desulphurization, is 9.20−9.40 for Sample No. 1 and 8.17−8.63 for Sample No. 2.

The concentration of Sb in the solutions is directly connected with the excess of Na$_2$CO$_3$. For 100% excess of Na$_2$CO$_3$ in the solution one can obtain up to 7% Sb [22]. This causes additional purification of the solutions, including also from Pb, which in the technological practice is done by adding iron salts.

Data by other authors were not found in the literature, concerning investigation of the concentration of impurities under the different conditions of conducting the desulphurization process. There exist only data regarding the content of lead in the crystalline Na$_2$SO$_4$ obtained after desulphurization of the pastes. Yanakieva [2] indicates data received by X-ray-structural (Röntgen-structural) analysis for the percentage content of Pb in the crystalline Na$_2$SO$_4$, which is in the range 0.0129−0.0099%.

Behaviour of the impurities during desulphurization of Pb pastes with NaOH. The results from analyzing the obtained liquid phase after desulphurization of the pastes with NaOH, using a laboratory stirrer and a rotational reactor of the drum type, concerning the concentration of impurities, are presented in Table 2.

In contrast to the solutions obtained after desulphurization of the pastes with Na$_2$CO$_3$, here the lead passes to a greater extent and the antimony to smaller degree.

Table 1. Concentration of impurities in the liquid phase of Na$_2$SO$_4$ when treating the pastes with Na$_2$CO$_3$ and a laboratory stirrer.

No.	Condition of carrying out the process	Inclusion concentrations, mg·L^{-1}							pH
	Sample No. 1	Pb	Sb	Cl$_2$	As	Cu	Zn	Fe	
1	stoichiometric; m = 2; τ = 30 min	4.76	38.40	2160.0	51.00	4.30	0.22	1.5	9.42
2	stoichiometric; m = 2.25; τ = 30 min	2.90	28.44	2140.0	24.20	7.49	2.21	0.04	9.20
3	10% excess Na$_2$CO$_3$; m = 2.25; τ = 15 min	6.80	13.40	1980.0	50.80	2.62	0.54	0.09	9.41
4	10% excess Na$_2$CO$_3$; m = 2.5; τ = 30 min	6.10	15.90	1940.0	42.00	2.39	0.26	0.08	9.27
	Sample No. 2								
1	10% excess Na$_2$CO$_3$; m = 2; τ = 30 min	0.40	32.40	170.0	0.47	0.07	1.16	1.20	8.63
2	10% excess Na$_2$CO$_3$; m = 2.5; τ = 30 min	0.11	29.63	140.0	0.44	0.14	2.20	0.05	8.17
3	20% excess Na$_2$CO$_3$; m = 2.5; τ = 15 min	1.20	15.30	170.0		0.11	0.53	< 0.01	8.48
4	20% excess Na$_2$CO$_3$; m = 2.5; τ = 30 min	1.20	14.70	170.0	0.83	0.05	1.85	< 0.01	8.22

Table 2. Concentration of impurities in liquid phase of Na_2SO_4, when the pastes are treated with NaOH.

No.	Conditions of carrying out the process	Inclusion concentrations, mg·L^{-1}							pH
	Sample No. 1	Pb	Sb	Cl$_2$	As	Cu	Zn	Fe	
A	Common reactor with laboratory agitator								
1	stoichiometric; $m = 2$; $\tau = 30$ min	972.0	< 0.1	1320.0	52.5	< 0.01	13.93	1.8	12.55
2	5% excess of NaOH; $m = 2$; $\tau = 30$ min	1602.6	< 0.1	1640	65.3	< 0.01	6.16	1.8	12.60
3	10% excess of NaOH; $m = 2$; $\tau = 30$ min	2019.2	< 0.1	1560.0	70.3	< 0.01	5.10	1.7	12.60
B	Rotary reactor of drum type								
4	stoichiometric; m = 2; $\tau = 30$ min	874.7	< 0.1	1460.0	48.5	0.60	14.60	1.70	12.50
5	5% excess of NaOH; $m = 2$; $\tau = 30$ min	1097.8	< 0.1	1640.0	60.0	0.90	20.40	1.90	12.53
6	10% excess of NaOH; $m = 2$; $\tau = 30$ min	1496.8	< 0.1	1840.0	68.9	0.80	26.50	2.00	12.55
	Sample No. 2								
A	Common reactor with laboratory agitator								
1	stoichiometric; m = 2.5; $\tau = 30$ min	0.12	< 0.1	54.0	< 0.01	0.05	0.1	< 0.01	10.35
2	5% excess of NaOH; $m = 2.5$; $\tau = 30$ min		< 0.1	40.0	10.8	0.04	4.12	< 0.01	12.46
3	10% excess of NaOH; $m = 2.5$; $\tau = 30$ min	43.84	< 0.1	44.0	4.0	0.07	0.20	< 0.01	12.22
B	Rotary reactor of drum type								
1	stoichiometric; $m = 2.5$; $\tau = 30$ min	76.82	< 0.1	64.0	0.77	< 0.01	1.00	1.2	12.15
2	5% excess of NaOH; $m = 2.5$; $\tau = 30$ min	30.4	< 0.1	60.0	2.40	0.40	0.12	1.2	12.15
3	10% excess of NaOH; $m = 2.5$; $\tau = 30$ min	20.4	< 0.1	46.0	4.70	0.50	0.10	1.30	12.22

The lead passes into the solutions in the form of sodium plumbite (Na_2PbO_2).

Regarding the chlorine and arsenic, the purity of the solutions depends on the purity of the nondesulphurized paste and the presence of other lead-containing impurities or additives (for example lead powder). The latter also holds true to some extent for the arsenic and some of the other impurities in the paste.

The pH value of the solutions after desulphurization is: 12.50−12.60 for Sample No. 1 and 10.30−12.40 for Sample No. 2, respectively.

Based on the analysis of the results received from both paste samples, the increase in concentration of impurities is important when the process is done in rotational reactor of the drum type, which is due to the better conditions of contact between the paste and the reagent.

Data were not found in the literature, concerning investigations on the effect of the concentration of impurities in the solutions after desulphurization with both types of reactors.

CONCLUSIONS

- The process of desulphurization runs at higher speed when using NaOH, than using Na_2CO_3 for both types of reactors;

- The optimal conditions for desulphurization of Pb-paste with Na_2CO_3 in both reactors are: excess of Na_2CO_3 up to 10%, m = 2.0−2.5, t = 55−35ºC and τ = 15−30 min (the degree of desulphurization under

these conditions is 92.4−94.4%, and $S_{SO_4^{2-}}$ = 0.49−0.36%);

- For the two reactors the optimal conditions for desulphurization of Pb-paste with NaOH are: excess of NaOH up to 10%, $m = 2$, t = 55−35ºC and τ = 15−30 min. (the degree of desulphurization under these conditions is 93.64−96.90%, and $S_{SO_4^{2-}}$ = 0.41−0.20%);

- After desulphurization with Na_2CO_3 greater amount of Sb goes into the solutions than of Pb, while when using NaOH into the solutions goes more Pb, and the amount of Sb in them is below 0.1 mg·L^{-1};

- The process of desulphurization of Pb-paste can be realized continuously when using rotational reactor of the drum type, and from the solutions significantly pure crystalline Na_2SO_4 can be obtained, which is suitable for the aims of the industry (Tables 1 and 2).

REFERENCES

1. N. K. Lyakov, PhD Thesis, UCTM, Sofia, 1989.
2. V. P. Yanakieva, PhD Thesis, UCTM, Sofia, 2003.
3. A. G. Morachevskii, *Zh. Prikl. Khim.*, **70**, 3 (1997).
4. Yu. S. Kuznetsova, O. A. Kal'ko, A. G. Morachevskii, E. V. Bakhvalova, *Russ. J. Appl. Chem.*, **81**, 1283 (2008)
5. K. Arai, J. M. Toguri, *Hydrometallurgy*, **12**, 49 (1984).
6. M. S. Kogan, PhD Thesis, St. Petersburg Tekh. Univ., 1994.

7. N. K. Lyakov, D. A. Atanasova, V. S. Vassilev, G. A. Haralampiev, *J. Power Sources*, **171**, 960 (2007).

8. N. K. Lyakov, Secondary Metallurgy of Non-ferrous Metals and Alloys, Martilen, Sofia, 1996 (in Bulgarian).

9. Engitec Impianti, Firm material, System "CX Compakt", 1993.

10. *Eur. Patent* EP 1 619 261 A1, 1 (2006).

11. K. F. Lamm, in: Proc. 1st Int. Congr. Processing of Secondary Raw Materials, Moscow, 1992 (in Russian).

12. R. M. Reynolds, E. K. Hudson, M. Olper, in: The Engitec CX Lead-Acid Battery Recovery Technology, (Proc. 1st Int. Seminar Battery Waste Management, Deerfield Beach, FL, USA, 1989, p. 1.

13. M. Olper, B. Asano, in: Primary and Secondary Lead Processing, Halifax, Nova Scotia, August 1989, M. L. Laeck (Ed.), Pergamon Press, New York, 1989, p. 119.

14. A. G. Morachevskii, *J. Appl. Chem.*, **76,** 1427 (2003).

15. T. T. Chen, J. E. Dutrizac, *Hydrometallurgy*, **40**, 223 (1996).

16. S. Gishin, Accumulators, Tech. Univ., Sofia, 2003 (in Bulgarian??).

17. M. E. Stout, in: Hydrometallurgy: Fundamentals, Technology and Innovations, I. B. Hiskey, G. W. Warren (eds.), Society for Mining, Metallurgy & Exploration, Inc., Colorado, 1993, p. 1185.

18. N. M. Barbin, G. F. Kazantsev, Processing of Secondary Lead Raw Materials in Ion-Salt Melts, Ural Dept. Russ. Acad. Sci., Ekaterinburg, 2002 (in Russian).

19. G. F. Kazantsev, G. K. Monsevich, N. M. Barbin, *Khimiya v interesah ustoichivogo razvitiya*, **2**, 461 (1994).

20. F. M. Loskutov, Metallurgy of Lead, Metallurgia, Moscow, 1965 (in Russian).

21. A. G. Morachevskii, O. A. Kalko, Z. I. Vaisgant, *Zh. Prikl. Khim.*, **68,** 1899 (1995).

22. A. G. Morachevskii, *Zh. Prikl. Khim.*, **71**, 881 (1998).

23. K. J. Laidler, E. T. Denisov, K. H. Homman, T. M. Sugden, *Pure Appl. Chem.*, **53** 753 (1981).

24. Y. Gong, J. E. Dutrizac, T. T. Chen, *Hydrometallurgy*, **28**, 399 (1992).

25. Y. Gong, J. E. Dutrizac, T. T. Chen, *Hydrometallurgy*, **31**, 175 (1992).

26. K. Arai, J. M. Togury, *Hydrometallurgy*, **12**, 49 (1984).

27. V. P. Yanakieva, *Sci. Rep. Union Sci. Techn. Mech. Eng.*, **3**, 236 (2004) (in Bulgarian).

28. D. A. Atanasova, N. K. Lyakov, V. S. Vassilev, G. Angelov, G. A. Haralampiev, in: Proc. 10th Nat. Conf. Metallurgy, A. Avramov (ed.), Varna, 2007.

29. D. A. Atanasova, N. K. Lyakov, V. S. Vassilev, G. Angelov, G. A. Haralampiev, *J. UCTM,* **43,** 267 (2008).

30. P. Taylor, V. J. Lopata, *Canad. J. Chem.*, **62**, 395 (1984).

31. A. G. Morachevskii, *Zh. Prikl. Khim.*, **70**, 167 (1997).

32. D. Blana, *Erzmetall*, B 32, 262 (1979).

33. *RU Patent* 2016104 C1 C22 B7/00, 13/00 (1999).

34. *UK Patent* GB 2309464 A, C22 B 7/00, (1997).

35. R. M. Reynolds, E. K. Hudson, M. Olper, in: Lead-Zinc'90, T. S. Mackey, R. D. Prengaman (eds), TMS, Warrendale, PA, 1990, p. 1001.

36. T. Corsini, in: EPD Congress 93, J. P. Hager (ed.), TMS, 1993, p. 909.

37. M. Olper, M. Maccagni, in: Interbat, M., Feb., 2001.

38. E. V. Javgel, *Zh. Prikl. Khim.*, **8**, 1681 (1978).

39. H. J. Bittrich, E. Leibritz, *J. Prakt. Chem.,* **17**, 92 (1962).

40. E. V. Margulis, P. E. Margulis, V. V. Brigadnova, A. Archinova, *Zh. Prikl. Khim.*, **3**, 558 (1989).

41. A. G. Morachevskii, M. S. Kogan, A. I. Demidov, Z. I. Vaisgant, *Zh. Prikl. Khim.*, **66**, 1871 (1993).

42. A. G. Morachevskii, A. I. Demidov, M. S. Kogan, Z. I. Vaisgant, *Zh. Prikl. Khim.*, **66**, 2101 (1993).

43. A. G. Morachevskii, O. A. Kalko, Z. I. Vaisgant, *Zh. Prikl. Khim.*, **68**, 127 (1995).

44. *US Patent* 4.927.510,5 (1990).

45. *US Patent* 5.039.337,8 (1991).

46. *US Patent* 5.441.609,8 (1995).

47. V. I. Avdyukov, V. T. Tulenkov, L. I. Bezginova, V. V. Studentsov, *Complex Utilization of Mineral Raw Materials*, **3**, 24 (1985).

48. E. R. Cole, A. Y. Lee, D. L. Paulsen, in: Invest. Bur. Mines. Washington: USA Bur. Mines No. 8857, 1984, p. 20.

49. *US Patent* 4220628 (1980).

50. *US Patent* 4.118.219, 10 (1978).

51. *US Patent* 262, 11 (1998).

52. *US Patent* 4.850.278 (1991).

53. M. P. Smirnov, V. S. Sorokina, *Tsvetn. Met.*, **2**, 23 (1999).

54. M. P. Smirnov, V. S. Sorokina, R. A. Gerasimov, *Tsvetn. Met.*, **9**, 13 (1996).

55. V. P. Yanakieva, G. A. Haralampiev, N. K. Lyakov, *J. Power Sources*, **85**, 178 (2000).

56. *BG Patent* 100627 C22B7/00; C22B3/16 (1997).

57. L. A. Kochubei, *Kompleksnoe Izpol'zovanie Mineral'nogo Syr'ia (Almaty)*, **3**, 47 (1990).

58. G. Remi, Course of Inorganic Chemistry, Inostrannaya Literatura, Moscow, 1963, (in Russian?).

59. Handbook of the Chemist, Gostkhimizdat, vol. III, 1962, (in Russian?).

60. Yu. Yu. Lurie, Handbook of Analytical Chemistry, Gostkhimisdat, Moscow, 1962, (in Russian?).

ХИДРОМЕТАЛУРГИЧНО ПРЕРАБОТВАНЕ НА АМОРТИЗИРАНА ОЛОВНА АКУМУЛАТОРНА ПАСТА

Д. А. Атанасова

Химикотехнологичен и металургичен университет, бул. „Климент Охридски" № 8, 1756 София

(Резюме)

Настоящата работа представя анализ на експериментални резултати от извършени изследвания относно десулфатизиране на амортизирана оловна паста и възможностите за осъществяване на процеса. Целта е да се направи сравнителна оценка на получените резултати със съществуващи данни в литературата и водещи технологии. Разгледани са кинетичните зависимости на протичащите процеси и свързаните с това проблеми. Определени са оптималните условия на процеса на десулфатизиране, при използване на реагентите Na_2CO_3 и $NaOH$ в зависимост от типа на работния реактор (обикновен реактор с лабораторна бъркалка и ротационен реактор от барабанен тип). Изследвано е съдържанието на примеси в разтворите с цел получаване на достатъчно чист кристален Na_2SO_4 за промишлеността.

Synthesis and static light scattering studies of hairy rod polymers containing 1,3,4-oxadiazole rings in the repeating units

H. Spasevska[1,]*, A. Andonovski[2], C. Brachkov[3], S. Stoykova[3], R. Kalinova[3], V. Sinigersky[3], I. Schopov[3]

[1] *Faculty of Electrical Engineering and Information Technologies, Sts. Cyril and Methodius University, 1000 Skopje, Republic of Macedonia*

[2] *Faculty of Sciences and Mathematics, Sts. Cyril and Methodius University, 1000 Skopje, Republic of Macedonia*

[3] *Institute of Polymers, Bulgarian Academy of Sciences, Acad. G. Bonchev St., Block 103, 1113 Sofia, Bulgaria*

Three new 'hairy' polymers containing 1,3,4-oxadiazole rings in the repeating units have been prepared and investigated by static light scattering. The two polymers of rod-like structure of the main chain show evidence of the same aggregation phenomena as other well known hairy rod polymers. The dimensions of the aggregates increase with increasing the polarity of the solvent. No aggregation occurs in the solution of the third polymer whose spacers, connecting the conjugated segments, are longer. This probably is determined by the increased flexibility of the polymer backbone. The third polymer, though hairy, has no rod-like structure of the main chain. Obviously, the rod-like structure is the determining factor for the aggregation observed.

Key words*: h*airy rod polymers; 1,3,4-oxadiazole ring; static light scattering.

INTRODUCTION

Hairy rod polymers, unlike the flexible random coil polymers, exhibit unique behaviour due to which nowadays they have often been investigated. These novel materials have good prospects for scientific and technological applications [1, 2]. Wegner and co-workers [3−5] have synthesised poly(*p*-phenylenes) with a large variety of side groups and investigated their properties. One of the major problems in the molecular characterisation of these polymers is their tendency to aggregate in solutions [6].

Most of the hairy rod polymers are substituted poly(*p*-phenylenes). It is well known however that the 1,3,4-oxadiazole ring exhibits the same electronic properties as the benzene ring [7]. Polymers, containing 1,3,4-oxadiazole rings, linked with unsaturated building units exhibit the typical properties of conjugated polymers [8]. Polymers with these rings have the advantage, however, to be more easily prepared than the corresponding polymers containing benzene rings.

The aim of this paper was to prepare a new class of hairy rod polymers containing 1,3,4-oxadiazole rings in the main chain and to investigate the influence of the length of the conjugated segments and their spacers on the aggregation phenomena.

EXPERIMENTAL

General methods

N-methylpyrrolidone (NMP) and N,N-dimethyl-formamide (DMF) (both from Fluka) were dried over phosphorus pentoxide and vacuum distilled. LiCl (Fluka) was dried at 130°C for 3 hrs. Tere-phtaloyl chloride and hydrazine sulphate (both from Fluka) were used without any further purification. 10% solution of phosphorus pentoxide in methane-sulphonic acid (PPMA) was prepared from AR purity reagents (Fluka). All new polymers were characterised by ^{1}H NMR, FT-IR and elemental analysis. The ^{1}H NMR spectra were recorded on a Bruker 250 MHz instrument. Chemical shifts are reported in ppm using tetramethylsilane as an internal standard. The FT-IR spectra were taken as KBr pellets on a Bruker Vector 22 spectrometer. Gel permeation chromatography measurements were performed on a Waters 244 instrument. The number average molecular weight M_n was determined using monodisperse polystyrene standards. Columns of Ultra-Styragel were used with pore sizes of 100 and 500 Å at 45°C, eluent THF.

Static light scattering (SLS)

The refractive index increments (dn/dc) of polymer solutions in DMF were measured by using a Brice-Phoenix Differential Refractometer BP-2000-V.

* To whom all correspondence should be sent:
E-mail: hristina@feit.ukim.edu.mk

Brice-Phoenix Universal Photometer 2000 with light source, high-pressure mercury vapour lamp (λ_0 = 578 nm) was used for the static light scattering experiments. Scattering intensities were measured with photomultiplier over an angular range between 45 and 135º, at three temperatures, 25, 40 and 55ºC.

The same measurements were carried out on a multi-angle laser light scattering detector DAWN DSP Laser Photometer (Wyatt Technology Corp.).

Synthetic procedures

Dihydrazide of hexadecylmalonic acid. To 6.38 g (16.6 mmol) diethylester of hexadecylmalonic acid (obtained acc. [9]), dissolved in 10 ml *n*-butanol, was added slowly a solution of 2.08 g (41.5 mmol) hydrazine hydrate. The mixture was heated under stirring at 100ºC for 4 h. After cooling, the crystals were filtered and recrystallised from ethanol. Yield 4.90 g (83%). M.p. 128−130ºC.

^{1}H NMR ($C_2D_2Cl_4$, ppm): δ = 8.82 (s, 2H, NH); 4.22 (s, 4H, NH$_2$); 2.93 (t, 1H, CH); 1.67 (m, 2H, αCH$_2$); 1.21 (m, 28H, CH$_2$); 0.90 (t, 3H, CH$_3$).

Anal. calc. for $C_{19}H_{40}N_4O_2$ (%): C, 64.00; H, 11.32; N, 15.71; Found: C, 64.11; H, 11.61; N, 15.33.
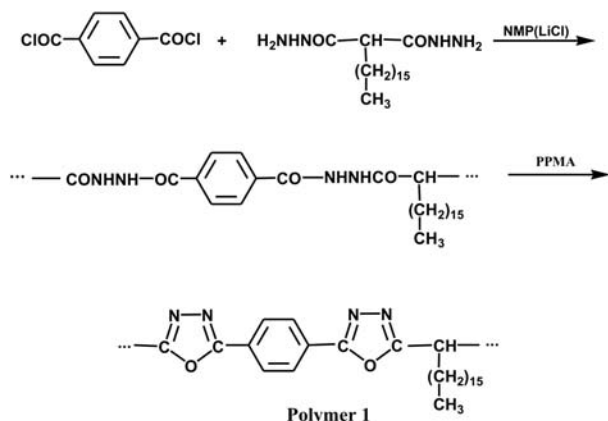
Scheme 1. Synthesis of polymer **1**.

Synthesis of polymer 1. (Scheme1). A mixture of 3 g (8.43 mmol) dihydrazide of hexadecylmalonic acid, 28.1 ml N-methyl-pyrrolidone and 1.45 g LiCl was stirred at room temperature under nitrogen to complete dissolution. The solution was then cooled to 0ºC and 1.71 g (8.43 mmol) terephtaloyl chloride were added in portions. The stirring was continued at this temperature for 1 h and at room temperature for another 6 h. The clear viscous solution was poured slowly in water under stirring. The precipitated polymer was filtered, washed with water and dried. It was dissolved then in 30 ml PPMA and stirred with heating under argon at 90ºC for 3 h. After cooling the reaction mixture was poured in water. The precipitate was filtered,

washed with water and dried. Yield 3.8 g (94%). M_n = 6900, M_w = 9800.

^{1}H NMR ($C_2D_2Cl_4$, ppm): δ = 8.11 (s, 4H, ArH); 2.78 (t, 1H, CH); 2.37 (m, 2H, αCH$_2$); 1.16 (m, 28H, CH$_2$); 0.84 (t, 3H, CH$_3$).

Anal. calc. for $(C_{27}H_{38}N_4O_2)_n$ (%): C, 71.96; H, 8.50; N, 12.43; Found: C, 70.82; H, 8.81; N, 12.09.
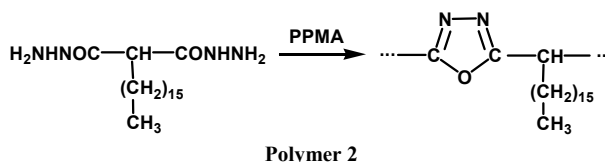
Scheme 2. Synthesis of polymer **2**.

Synthesis of polymer 2. (Scheme 2) 3.00 g (8.43 mmol) dihydrazide of hexadecylmalonic acid and 1.2 g (0.009 mmol) hydrazine sulphate were dissolved in 90 ml. PPMA. The solution was stirred for 30 h at 80ºC, then cooled and poured in water. The polymer was filtered, washed with water and dried. Yield 3.00 g (93%). M_n = 2450, M_w = 3200.

^{1}H NMR ($C_2D_2Cl_4$, ppm): δ = 3.05 (t, 1H, CH); 1.67 (m, 2H, αCH$_2$); 1.22 (m, 28H, CH$_2$); 0.85 (t, 3H, CH$_3$).

Anal. calc. for $(C_{19}H_{34}N_2O)_n$ (%): C, 74.46; H, 11.18; N, 9.14; Found C, 74,11; H, 11.59; N, 8.95.
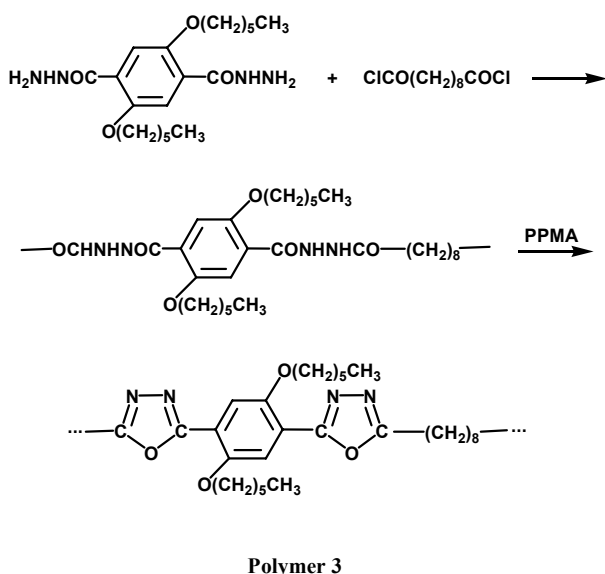
Scheme 3. Synthesis of polymer **3**.

Synthesis of 2,5-dihexyloxyterephthalyc acid diethyl ester. It was prepared by Kossmehl and co-workers [10].

Synthesis of 2,5-dihexyloxyterephthalyc acid dihydrazide. 8.6 g (0.02 mol) 2,5 dihexyloxy-terephthalic acid diethyl ester dissolved in 40 ml ethanol were added dropwise for 2 h, with stirring at 80ºC to 8.7 ml hydrazine hydrate (0.18 mol) dissolved in 65 ml ethanol. Heating was continued

for another 6 h. After cooling a white solid precipitated. It was recrystallised from water- ethanol (1:1) mixture, M.p. 98ºC. Yield 5.8 g (73.6%).

^{1}H-NMR (DMSO-d6, ppm): δ = 9,22 (s,2H, CONH); 7,33 (s,2H, Ar H); 4,577 (s,4H, NH2); 4,05 (t, 4H, OCH2); 1,7 (m, 4H, OCH2CH2);1,32 (m,12H, CH2); 0,87 (t, 6H, CH3).

Anal. calc. for $C_{20}H_{34}N_4O_4$ (%): C, 60.89; H, 8.69; N, 14.20; Found C 60.45; H, 8.67; N, 13.91.

Synthesis of polymer 3 (Sheme 3). 1.86 ml (0.008 mol) sebacoyl chloride were added slowly with stirring to ice-cooled solution of 2.5 g (0.0063 mol) 2,5-dihexyloxyterephthalic acid dihydrazide in 42 ml N-methylpyrrolidone. The mixture was stirred for 6 h and poured in water with stirring. The precipitate was filtered, washed with water and dried. It was dissolved then in 30 ml PPMA and stirred with heating under argon at 75ºC for 24 h. After cooling, the solution was poured in water. The polymer was filtered, washed and dried. Yield 2.72 g (86.8%). M_n = 150 000, M_w = 162 000.

^{1}H-NMR (CDCl3, ppm): δ = 7.67 (s, 2H, ArH); 4.10 (t, 4H, OCH2); 2.90 (t, 4H αCH2); 1.87 (m, 4H, OCH2CH2); 1.34 (m, 24H CH2); 0.89(t, 6H, CH3).

Anal. calc. (%) for $(C_{30}H_{44}N_4O_4)_n$: C, 68.67; H, 8.45; N, 10.68; Found: C, 68.90; H, 8.22; N, 10.33.

RESULTS AND DISCUSSION

Three new polymers (**1**–**3**) with structure designed for our investigations have been prepared. The polymers contain 1,3,4-oxadiazole rings in their repeating units. The conjugated segment in polymer **1** consists of one benzene and two 1,3,4-oxadiazole rings. The segments are connected with very short spacers (CH-group). The conjugated segment in polymer **2** consists of only one 1,3,4-oxadiazole ring. Here the spacer is the same (CH-group). Consequently, the macromolecules of polymer **1** differ from the macromolecules of polymer **2** in the length of the conjugated segment. Due to the very short spacer in polymers **1** and **2** their macromolecules represent typical rigid rods. In order to increase their solubility, side chains are attached to the main polymer chain, therefore, these polymers belong to the class of hairy rod polymers. Polymer **3** contains conjugated segments connected by long flexible spacers with eight methylene groups. This polymer has the same conjugated segments as polymer **1**. In order to get solubility the benzene rings are substituted in this case. We prepared this polymer especially since it is 'hairy', but its main chain has not rod-like structure.

Polymers **1**−**3** were prepared via two different synthetic procedures. For polymers **1** and **3** we applied the two-step method for 1,3,4-oxadiazole ring preparation proposed by Frazer *et al*. [11, 12]. First we prepared polyhydrazides, which were then cyclised to 1,3,4-oxadiazole ring containing polymers. Frazer *et al*. performed the cyclisation in polyphosphoric acid. We used instead a reagent made by dissolving 10% of phosphorus pentoxide in methanesulphonic acid since Ueda *et al*. [13] have shown that it exhibits similar chemical reactivity as polyphosphoric acid but with higher effectiveness. Polymer **2** was prepared according to the direct method of Iwakura *et al*. [14].

The characterisation of polymers **1** and **2** was done in dilute solutions in DMF using static light scattering (SLS) measurements. The results of the SLS measurements were compared to the SLS measurements of the segmented polymer **3** whose repeating unit differs from the repeating units of the other two polymers in the length of the spacers connecting the conjugated segments.

The refractive index increments dn/dc of polymers **1**−**3** in DMF at 578 nm wavelength of the incident light are given in Table 1.

Table 1. Refractive index increment dn/dc (ml·g^{-1}) of polymers **1**–**3** in DMF.

Polymer	1	1^a	2	3
Index	0.1107	0.0745	0.0875	0.1535

a - Refractive index increment of polymer **1** in DMF + 3% LiCl.

Static light scattering was used to determine the weight average molecular weight M_w. Zimm plots were constructed making use of the Rayleigh-Gans-Debye equation [15]:

$$\frac{Kc}{R_\theta} = \frac{1}{M_w}\left(1 + \frac{q^2\left\langle R_g^2\right\rangle}{3}\right) + 2A_2c, \qquad (1)$$

with

$$K = \frac{4\pi^2 n^2}{N_A \lambda_0^4}\left(\frac{dn}{dc}\right)^2, \qquad (2)$$

$$q = \frac{4\pi n}{\lambda_0}\sin\frac{\theta}{2}, \qquad (3)$$

where the Rayleigh ratio R_θ depends on the intensity of scattered light at different scattering angles θ, c is the polymer concentration, q − magnitude of the scattering wave vector, $\left\langle R_g^2\right\rangle$ − the mean square radius of gyration of the particles, A_2 − the second virial coefficient, n − the refractive index of the solvent, λ_0 − the wavelength of incident light in a vacuum, and N_A − the Avogadro constant.

The problem of SLS measurement in coloured solutions was solved by correction of the Rayleigh ratios R_θ of measured intensities of scattered light using the method proposed by Brice and co-workers [16].

One of the ways to analyse the results of the SLS is by using the Zimm plots. With this method, we can obtain the values of $\left\langle R_g^2 \right\rangle^{1/2}$, M_w and A_2 in a single chain. But when the polymer solutions represent complex systems, which, besides unimers, contain aggregates larger than the usual Zimm plot can provide, only the information of the polymer mixture, containing both the unimers and the aggregates could be obtained. Therefore, the appearance of aggregation phenomena in both hairy rod polymers **1** and **2** was studied through the acquired values of M_w and $\left\langle R_g^2 \right\rangle^{1/2}$ of the particles in the system.
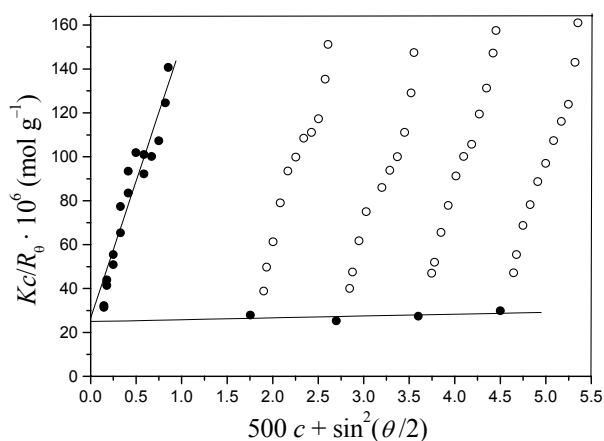
Fig. 1. Zimm plot of polymer 1 in DMF at 25°C.

Figure 1 shows one of the constructed Zimm plots for polymer **1** from which the values for $\left\langle R_g^2 \right\rangle^{1/2}$, M_w and A_2 have been calculated and are given in Table 2 together with the values of these parameters for polymer **2**. The values for M_w and $\left\langle R_g^2 \right\rangle^{1/2}$ for both polymers are high and point to the presence of large aggregates.

Similar results have been obtained from the SLS measurements on poly (*p*-phenylenes) made by Fytas and co-workers [17]. These authors support the idea that rigid rods are aggregated into small units, probably trimers, under these conditions. With the increase of temperature the solvent quality also increases, which can be seen from the values of A_2 for both hairy rod polymers, which suggests that this system becomes more strongly interacting as the temperature is reduced. These interactions in the

300

system enable the dimensions of the aggregates to decrease with the temperature increase, which can be seen from the values for M_w and $\left\langle R_g^2 \right\rangle^{1/2}$.

Table 2. Weight average molecular weights M_w, radius of gyration $\left\langle R_g^2 \right\rangle^{1/2}$ of the particles and second virial coefficient A_2 of polymers **1−3** at different temperatures.

Polymer	T, °C	M_w, kg·mol^{-1}	$\left\langle R_g^2 \right\rangle^{1/2}$, nm	$A_2 \times 10^4$, mol·ml·g^{-2}
1	25	37.8	310.9	2.1
	40	35.5	193.9	2.6
	55	32.9	121.9	11.1
	40	76.3 [a]	83.0 [a]	− 0.1 [a]
2	25	75.2	114.3	5.7
	40	66.4	124.1	10.7
	55	56.2	135.7	11.6
3	25	157.7	140.2	1.9
	40	150.1	150.4	9.7
	55	155.4	151.5	16.8

a - Results of polymer **1** in DMF + 3% LiCl.

Comparing the values for M_w and $\left\langle R_g^2 \right\rangle^{1/2}$ for polymers **1** and **2** it can be concluded that polymer 2 forms larger aggregates in its solutions than the aggregates present in polymer **1** solutions. Most probably this phenomenon is determined by the higher rigidity of its molecular backbone compared with that of polymer **1**. This is also confirmed by the fact that the size of the aggregates in polymer **1** increases with the increase of the polarity of the DMF solvent caused by adding 3% LiCl. Also in this system the second virial coefficient A_2 (Table 2) has a negative value. These results suggest that the solvent quality is not good.
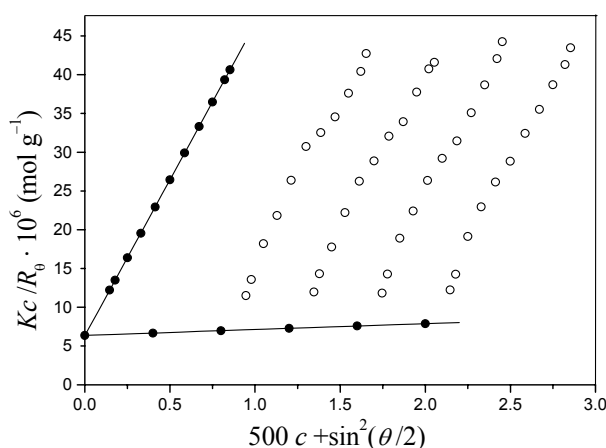
Fig. 2. Zimm plot of polymer 3 in DMF at 25°C.

Unlike polymers **1** and **2**, polymer **3** does not form aggregates in diluted DMF solutions. This can be seen from the shape of the constructed Zimm plots. One of these is shown in Fig. 2. Also, the

acquired values for M_w and $\left\langle R_g^2 \right\rangle^{1/2}$ at all three temperatures in Table 2 correspond to values of a single chain. The values of the second virial coefficient A_2 are positive and show that DMF is a good solvent for this polymer.

In conclusion, apart of the fact that polymer **3** contains the same conjugated segment in the repeating unit as polymer **1**, it does not aggregate. This is obviously due to the longer flexible spacers. In this polymer by bending the flexible spacers enable approaching of the conjugated segments [18]. Here the flexibility of the macromolecule is enhanced also by the higher molecular weight. Polymers **1** and **2,** however, obviously due to the short spacers, have aggregation specific for the hairy rod polymers. The cause for this aggregation is not only the presence of the flexible side chains but the rod-like structure of the polymer backbone.

CONCLUSIONS

Polymers **1** and **2** containing 1,3,4-oxadiazole rings in their repeating units exhibit the same aggregation phenomena as other well known hairy rod polymers [6]. The dimensions of the aggregates increase with increasing the polarity of the solvent. No aggregation occurs in the solution of the third polymer whose spacers, connecting the conjugated segments, are longer. This probably is determined by the increased flexibility of the polymer backbone. The third polymer, though hairy, has not rod-like structure of the main chain. Obviously, the rod-like structure is the determining factor for the aggregation observed.

REFERENCES

1. G. Wegner, K. Mathauer, *Mater Res. Soc. Symp. Proc.*, **247**, 767 (1992).
2. J. S. Miller, *Adv Mater.*, **2,** 601(1990).
3. M. Rehan, A. D. Schlüter, G. Wegner, *Polymer*, **30**, 1060 (1989).
4. A. D. Schlüter, G. Wegner, *Acta Polym.*, **44**, 59 (1993).
5. C. Heldmann, M. Schulze, G. Wegner, *Macromolecules*, **29**, 4686 (1996).
6. T. Liu, R. Rulkens, G. Wegner, B. Chu, *Macromolecules*, **31**, 6119 (1998).
7. J. Sauer, R. Huisgen, H. J. Sturm, *Tetrahedron*, **11**, 241 (1960).
8. I. Schopov, M. Vodenicharova, *Macromol. Chem.*, **179**, 63 (1978).
9. Buu-Hoi, P. Cagniaut, *Bull. Soc. Chim. Fr.*, **10**, 477 (1943).
10. Th. Schleeh, G. Kossmehl, G. Hinrichsen, *Macromol. Chem.*, **191**, 1075 (1990).
11. A. H. Frazer, F. T. Wallenberger, *J. Polymer Sci.*, **2A**, 1147 (1964).
12. A. H. Frazer, W. Sweeny, F. T. Wallenberger, *J. Polymer Sci.*, **2A**, 1157 (1964).
13. M. Ueda, T. Kano, *Macromol. Chem. Rapid Commun.*, **5**, 833 (1985).
14. Y. Iwakura, K. Uno, S. Hara, *Macromol. Chem.*, **94**, 103 (1966).
15. M. B. Huglin, Light Scattering from Polymer Solutions, Academic Press, London and New York, 1972.
16. B. A. Brice, G. C. Nutting, M. Halwer, *J. Am. Chem. Soc.*, **75**, 824 (1953).
17. G. Petekidis, D. Vlassopoulos, G. Fytas, N. Kountourakis, S. Kumar. *Macromolecules*, **30**, 919 (1997).
18. I. Schopov, V. Sinigersky, *Macromol. Symposia*, **121**, 35 (1997).

СИНТЕЗА И ИЗСЛЕДВАНЕ СЪС СТАТИЧНО СВЕТЛОРАЗСЕЙВАНЕ НА ОКОСМЕНИ ПРЪЧКОВИДНИ ПОЛИМЕРИ, СЪДЪРЖАЩИ 1,3,4-ОКСАДИАЗОЛОВИ ПРЪСТЕНИ В ПОВТАРЯЩИТЕ СЕ ЗВЕНА

Хр. Спасевска[1,*], А. Андоновски[2], Хр. Бръчков[3], С. Стойкова[3], Р. Калинова[3],
В. Синигерски[3], Ив. Шопов[3]

[1] *Факултет по електроинженерство и информационни технологии, Университет „Св. Кирил и Методий"*
1000 Скопие, Република Македония
[2] *Факултет по науки и математика, Университет „Св. Кирил и Методий" 1000 Скопие, Република Македония*
[3] *Институт по полимери, Българска академия на науките, ул. „Акад. Г. Бончев" бл. 103, 1113 София*

(Резюме)

Синтезирани са три нови „окосмени" полимери, съдържащи 1,3,4-оксадиазолови пръстени в повтарящите им се звена и са изследвани със статично светлоразсейване. Двата полимера с пръчковидна структура на главната верига показват същото явление на агрегиране както и други добре известни окосмени пръчковидни полимери. Размерите на агрегатите нарастват с увеличаване на полярността на разтворителя. В разтвора на третия полимер, на когото спейсърите, свързващи спрегнатите сегменти са по-дълги, не протича агрегиране. Това вероятно се определя от увеличената гъвкавост на тази полимерна верига. Третият полимер, макар и окосмен, няма пръчковидна структура на главната верига. Очевидно пръчковидната структура е определящия фактор за наблюдаваното агрегиране.

V_2O_5-ZrO_2 catalyst for selective oxidation of *o*-xylene to phthalic anhydride:
I. Catalyst preparation, catalytic activity and selectivity measurements

L. Makedonski*

Medical University, 55 Marin Drinov St., 9002 Varna, Bulgaria

The thermal stability, activity and selectivity of a series of V_2O_5-ZrO_2 catalyst samples towards *o*-xylene oxidation to phthalic anhydride have been investigated. It has been established that the phthalic anhydride content yield reaches about 55 mol.% in samples containing 7 and 10 wt.% V_2O_5. The selectivity of the catalyst with 7 wt.% V_2O_5-ZrO_2 has been compared to that of commercially available V_2O_5-TiO_2 (anatase). The investigations have been performed within two temperature ranges. At low temperatures (below 410°C) the V_2O_5-TiO_2 (anatase) catalyst shows a better selectivity to phthalic anhydride than the V_2O_5-ZrO_2 catalyst does. At high temperatures, the V_2O_5-ZrO_2 catalyst is more selective with respect to the main product of partial oxidation due to the positive effect of the ZrO_2 support. Even when the temperature rises up to 550°C and the time of exploitation becomes 50 h, the selectivity of V_2O_5-ZrO_2 decreases slightly and remains above 50 mol.%, whereas with the V_2O_5-TiO_2 (anatase) sample a significant decrease in selectivity (below 45 mol.%) is observed. The results from experiments on the activity and selectivity of a model mixture of 7 wt.% V_2O_5-ZrO_2 and pure ZrO_2 taken in a ratio of 1:1 show that high catalyst selectivity is achieved when the zirconia surface is completely covered by VO_x-phases. Studies by different physicochemical analysis methods have shown that V_2O_5-ZrO_2 used in a high-temperature regime undergoes no significant phase and structural changes, which is an indication of its good thermal stability. The specific surface area decreases a little, the monoclinic zirconia support exhibits no phase changes and the fine structure of the V_2O_5 active phase displays no substantial alterations.

Key words: V_2O_5-ZrO_2 catalyst, V_2O_5-TiO_2 (anatase) catalyst, partial selective oxidation, *o*-xylene oxidation, phthalic anhydride, maleic anhydride.

INTRODUCTION

Vanadium oxide catalysts are frequently used for the oxidation of aromatic compounds [1, 2]. As the specific surface area and catalytic activity are usually low, the active phase is fixed on a support. The role of the support is not only to increase the surface area and to improve the mechanical strength. It might also modify the active surface due to an interaction of the support and the active phase. Among the multitude processes of partial oxidation of aromatic compounds, the process of oxidation of *o*-xylene is most interesting both in scientific and industrial aspects. Usually such catalysts are supported on TiO_2 in the form of anatase [3] and SiO_2 [2]. In comparison with titanium and silica, much less attention has been paid to zirconium as a support. In our opinion the use of zirkonia is interesting because of its high thermal stability and acid-base character, which is very close to that of TiO_2. Having in mind that the process of partial oxidation is highly exothermic, these properties of the support are of great significance. In the scientific and patent literature there are few communications concerning the use of ZrO_2 as a support of vanadium oxide catalysts for partial oxidation of *o*-xylene. There are no published data regarding the selectivity of V_2O_5-ZrO_2 catalysts to the valuable side product, maleic anhydride, as well as to the undesired substance phthalide.

Supported metal oxides exhibit interesting catalytic properties depending on the kind of the support, the active component content and the preparation method [5−7]. In particular, vanadium oxide catalysts combined with various promoters are widely used for several reactions including oxidation of hydrocarbons [8], ammoxidation of aromatics and methylaromatics [9], olefins [10], ethanol and ethane, ammoxidation of 3-picoline and toluene, oxidation of methanol [11] and selective catalytic reduction of NO_x by NH_3 [12, 13].

All partial oxidation processes are highly exothermic, due to which the support of the V_2O_5 active component should be carefully chosen. Among the mentioned partial oxidation processes and oxidation ammonolysis, the partial oxidation of *o*-xylene to phthalic anhydride is most interesting both from industrial and scientific viewpoint [5, 6, 14]. The V_2O_5-TiO_2 (anatase) system is the basis of modern catalysts for partial oxidation of *o*-xylene to phthalic

* E-mail: lubomir60@yahoo.com

anhydride [5, 14].

It has been established [23, 24] that under the effect of high temperatures and reduction medium the catalyst is sintered, and the anatase is transformed into rutile, part of the V^{4+} ions being incorporated in the rutile lattice [15], which leads to sharply dropping of the catalyst activity. This deactivation is observed mostly in the 'hot spot' zone of the industrial reactor where the temperature exceeds 440°C and where the largest part of the reaction proceeds [16]. These investigations show that it is very important to find supports that would be stable at high temperatures in a reduction medium.

During the past years some patents have reported the use of ZrO_2 as a support of V_2O_5. Systems V_2O_5-ZrO_2 in combination with various promoters are widely used for several reactions including *o*-xylene oxidation [17, 18], ammoxidation of aromatics and methylaromatics, oxidation of toluene [19, 20], decomposition of propan-2-ol [21, 22], oxidative dehydrogenation of propane [23, 24], oxidation of naphthalene, partial oxidation of methanol [25] and selective catalytic reduction of NO_x by C_3H_6 [26]. The utilisation of ZrO_2 is based on the fact that it is stable at very high temperatures [27] and its acid-basic characteristics are very close to those of TiO_2.

Interesting studies [27, 28−33] have reported the use of zirconia as a support of vanadium oxide catalysts. The valuable zirconia properties in this aspect are its high thermal stability and acid-basic characteristics which are close to those of titania (anatase) [28−30].

It is known [34] that vanadia promotes the transition of tetragonal to monoclinic zirconia at high temperatures. The interaction of dispersed vanadium oxide species with a zirconia support leads to the formation of ZrV_2O_7. Antimony tends to stabilise the tetragonal phase of zirconia and its specific area. The simultaneous presence of Sb and V on zirconia at 1 cm coverage leads to a preferential interaction of individual V and Sb oxides on the zirconia surface rather than the formation of a binary Sb-V oxide. However, at high Sb-V coverage, $SbVO_4$ is formed at the expense of surface Sb oxide, while the transition to monoclinic polymorph is minimised. Simultaneously, the excess of antimony forms α-Sb_2O_4.

In previous papers [35, 36], the selectivity of supported V_2O_5-ZrO_2 catalysts for o-xylene oxidation to phthalic anhydride was investigated under conditions close to the industrial ones with conventional supported V_2O_5-TiO_2 (anatase) oxide catalysts. The by-products of this oxidation process were maleic anhydride, phthalide and the combustion products − CO and CO_2. In contrast to conventional V_2O_5-TiO_2 (anatase) catalysts, the V_2O_5-ZrO_2 catalysts exploited at low oxidation temperatures (310−350°C), were found to be very selective to the valuable by-product maleic anhydride, but showed no selectivity to the harmful organic oxidation products. The same catalyst also demonstrated a relatively high selectivity towards the main product of oxidation (phthalic anhydride) and a very low selectivity to the undesired phthalide formed during the oxidation. The data designated brought to assumption [34] that a supported V_2O_5-ZrO_2 catalyst may be used for selective oxidation of o-xylene. This catalyst should be combined with the conventional V_2O_5-TiO_2 (anatase) catalysts and placed in the low-tempe-rature zone of the industrial reactor.

The goal of the present investigation was to prepare a V_2O_5-ZrO_2 catalyst, to study its catalytic activity and selectivity for partial *o*-xylene oxidation towards phthalic anhydride and to compare our results with the conventional V_2O_5-TiO_2 (anatase) catalyst.

EXPERIMENTAL

Synthesis method of the catalyst

Supported V_2O_5-ZrO_2 catalyst samples were obtained by a method based on the preparation of an industrial BASF catalyst: V_2O_5 (specific surface area − 6 m²/g) and NH_4VO_3 (AG-Fluka) were used for V^{5+}-contention; ZrO_2 was taken as a commercial product (AG-Fluka; monoclinic [9], specific surface area − 26 m²/g).

The catalyst samples were prepared by reducing V^{5+} of V_2O_5. The ratio V_2O_5:$H_2C_2O_4$ = 1:(2.5−3.0) in an aqueous solution of oxalic acid at 60−80°C. Zirconia was introduced simultaneously. Surfactants (formamide or diphenylformamide in an aqueous solution at ratios water:formamide = 3.5−5.0:1.0) were used as binding substances. The suspension obtained was subjected to ultrasonic treatment with a view to homogenisation, dispersion and additional activation of the catalyst mass. The active catalyst mass was applied on an inert support (steatite spheres, 6 mm in diameter), by pulverising the suspension on the spheres pre-heated up to 200−250°C. The catalyst samples thus obtained had a coverage layer of the total catalyst mass with 1 mm thickness. They were dried at 110°C and calcined for 2−10 h at 450°C (a temperature corresponding to the calcination temperature of the industrial V_2O_5-TiO_2 (anatase) catalyst in air flow).

Catalytic activity and selectivity measurement

The activity and selectivity of the catalyst

samples for the vapour-phase partial oxidation of *o*-xylene to phthalic anhydride were investigated in a standard flow-type installation functioning at a pressure of 1 atm. The laboratory flow reactor had a length of 450 mm and contained 250 cm^3 catalysts. It was immersed in a salt bath containing KNO_2:$NaNO_3$ (1:1) salt melt, the temperature being maintained with an accuracy of up to 1°C. The temperature of the catalyst grains along the catalyst layer was measured by thermocouples. A minipump achieved the exact dosage of *o*-xylene. Along with the air introduced by a compressor, *o*-xylene came to a mixer with a filling where the temperature of the air-xylene mixture was maintained at 180°C.

Characterisation of catalysts and products of o-xylene oxidation

The analysis of the oxidation products was performed on-line by a gas chromatograph. The contents of phthalic anhydride (FA), phthalide (Ft), benzoic acid (BA), maleic anhydride (MA), CO_x – (CO_2 + CO) were determined. The catalyst samples were activated by air for 48 hours, while the selectivity measurements were done 2 h after fixing the corresponding regime. In all experiments a 100% *o*-xylene conversion was achieved.

The final reaction mixture was subjected to gas-chromatographic analysis in a Perkin Elmer 8500 apparatus (capillary column OV-101, l = 25 m, inner diameter = 0.25 mm, carrier gas H_2, T = 90−120°C, detector PID). The reaction products found were *o*-toluyl aldehyde, benzoic acid, phthalide, maleic anhydride, phthalic anhydride and unreacted *o*-xylene. The products of full oxidation to CO and CO_2 were determined chromatogra-phically in a steel column (l = 4 m, 1/8", GMCS, 60−80 mesh, hot catarometer as a detector).

The catalyst samples were activated in an air flow at the corresponding temperature and volume rate for 48 h. The kinetic measurements were performed two hours after establishing the corresponding regime.

RESULTS AND DISCUSSION

Catalytic activity and selectivity

Catalyst V_2O_5-ZrO_2 samples with 4, 7 and 10% of the active V_2O_5 component content were prepared. In the conventional V_2O_5-TiO_2 (a) catalyst the active component is usually between 2 and 10%. In order to determine the qualities of the synthesised V_2O_5-ZrO_2 catalyst samples, differing in the amount of deposited V_2O_5, we carried out test in the temperature interval 310−410°C, under flow rates of

1500−2500 h^{-1}. These conditions are close to the industrial ones of exploitation of the conventional V_2O_5-TiO_2 (a) catalysts. The experimental results of activity and selectivity and studies of several V_2O_5-ZrO_2 catalyst samples are exposed in Figs. 1−3. It can be seen that the catalytic sample with 7% V_2O_5 content has the best selectivity towards phthalic anhydride exposed at the temperatures 350, 370 and 390°C and space velocity w = 2000 h^{-1}, but in the case of T = 350°C the by-products content (BA and Ft) becomes higher.

The poorest selectivity has been found for the sample with lowest (4%) amount of supported V_2O_5 (Fig. 1). This difference reaches about 15% at temperatures higher than 350°C and is preserved even at the highest temperatures. The fact observed clearly shows the specific promoting effect of ZrO_2. These results are especially interesting having in mind that the highest selectivity to phthalic anhydride is produced by a V_2O_5-ZrO_2 catalyst sample containing 7 wt.% V_2O_5, which contents is much higher than that of a monolayer coverage (about 3 wt.% V_2O_5). On the other hand, it is well known [6] that a V_2O_5-ZrO_2 catalyst having monolayer coverage shows highest selectivity to phthalic anhydride.

As to the selectivity to the valuable side product of oxidation – maleic anhydride (MA), the highest values have been obtained by the sample possessing the highest (10 wt.%) V_2O_5, while the samples of lowest V_2O_5 content show again the lowest selectivity to maleic anhydride (Figs. 1−3). It is worth noting that the highest selectivity (about 6 mol.%) is established not only at low temperature regime 310−350°C, but also at high temperature (450°C) under all flow rates. The promoted industrial V_2O_5-TiO_2 (a) catalyst, depending on the exploitation conditions, shows a lower selectivity to maleic anhydride (in the range of 2–5 mol.%). The high selectivity to maleic anhydride demonstrated by the V_2O_5-ZrO_2 catalyst in all the temperature range is a good basis to optimise the process of partial oxidation of *o*-xylene. For example, a part of the conventional V_2O_5-TiO_2 (a) catalyst operating in the spot zone can be replaced by V_2O_5-ZrO_2 catalyst. It is also of scientific and technological interest the V_2O_5-ZrO_2 catalyst to be promoted in order to raise its total selectivity to phthalic and maleic anhydrides. As can be seen in Figs. 1 and 3, a minimum of the selectivity to maleic anhydride is observed at temperatures about 370°C for the catalyst samples containing 4 and 10 wt.% V_2O_5. We are not able to explain satisfactorily this fact at present, but it is probably due to the specific promoting effect of ZrO_2.
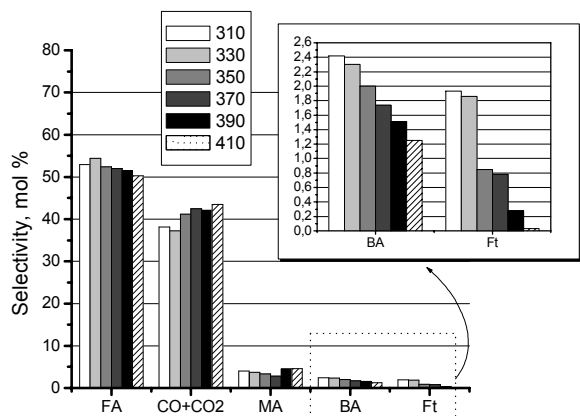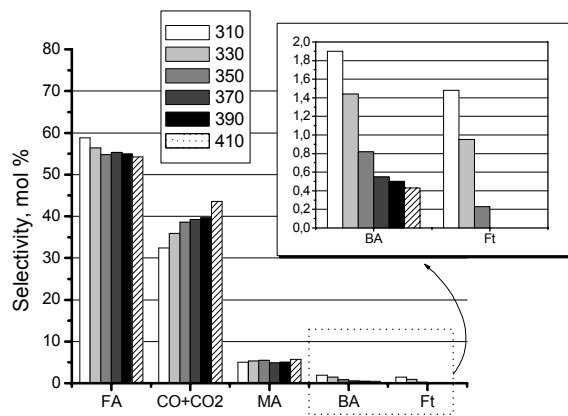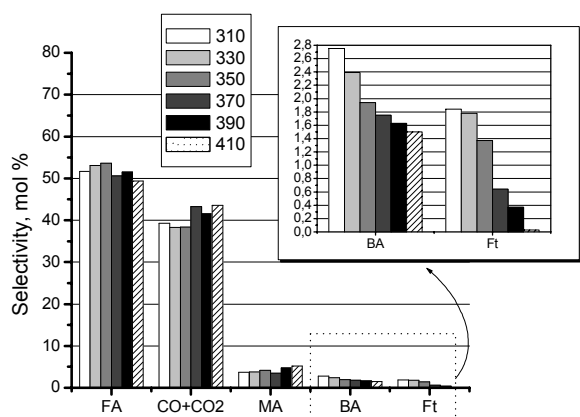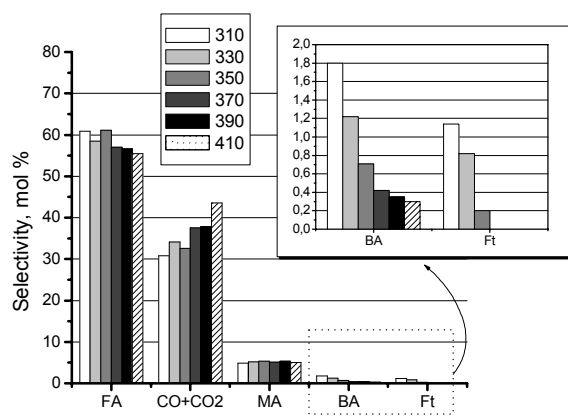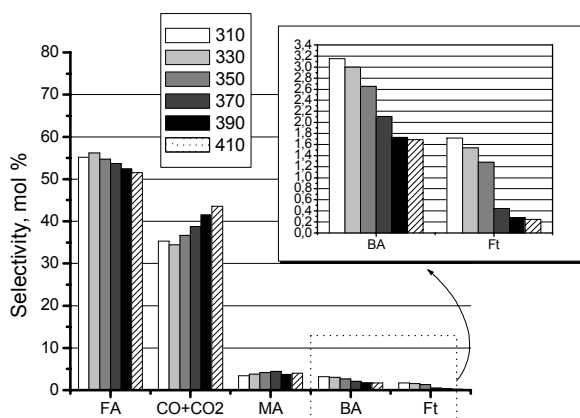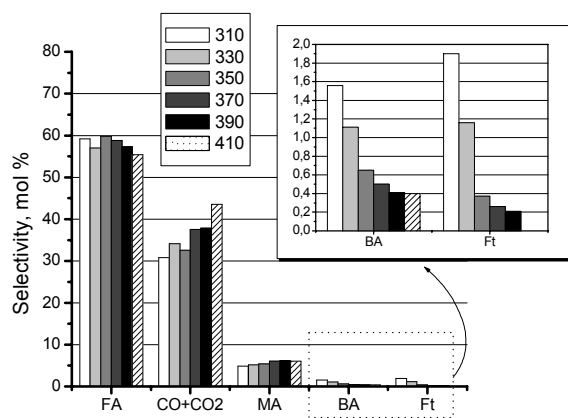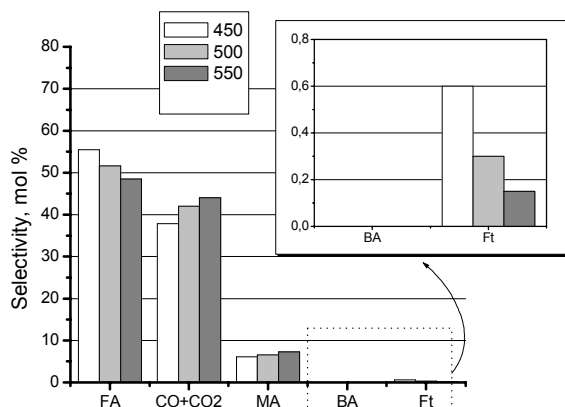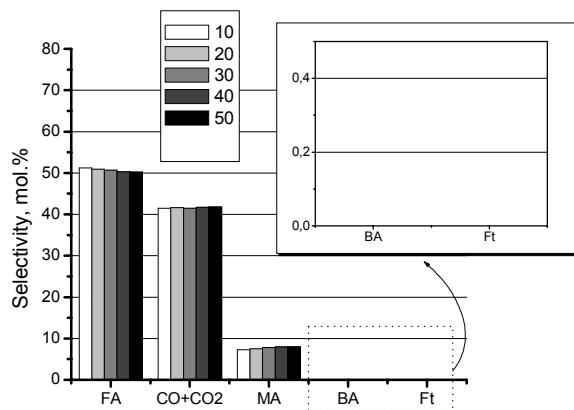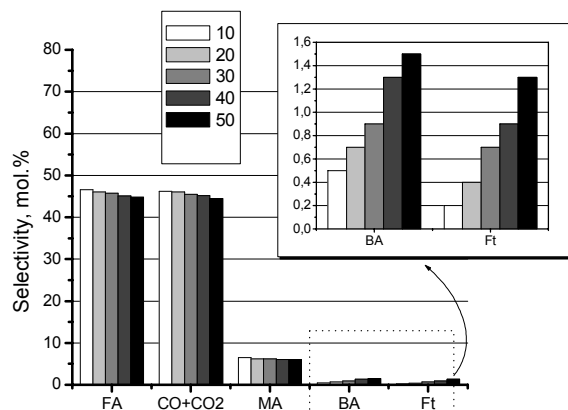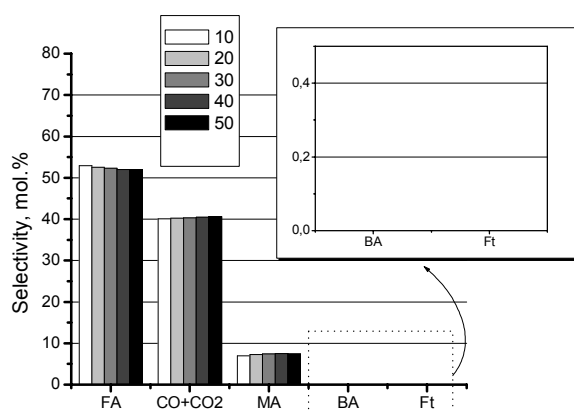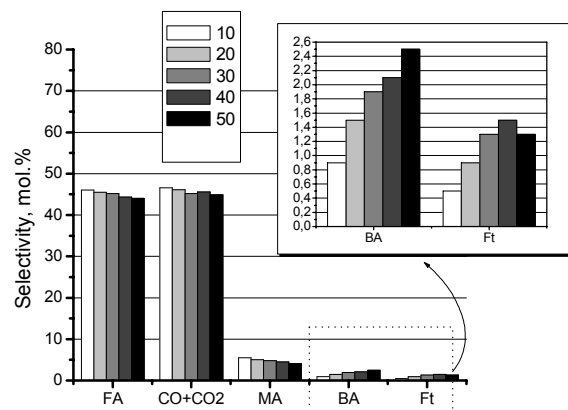
Fig. 1. Oxidation of *o*-xylene over 4% V$_2$O$_5$-ZrO$_2$ catalyst. Product selectivity (S_i) obtained for steady state at different temperatures (T = 310, 330, 350, 370, 390 and 410°C) and different volume rates: a − *w* = 1500 h^{-1}, b − *w* = 2000 h^{-1}, c − *w* = 2500 h^{-1}; initial concentration of *o*-xylene − *C*$_{xylene}$ = 42 g/nm^3.

Fig. 2. Oxidation of *o*-xylene over 7% V$_2$O$_5$-ZrO$_2$ catalyst. Product selectivity (S_i) obtained for steady state at different temperatures (T = 310, 330, 350, 370, 390 and 410°C) and different volume rates: a − *w* = 1500 h^{-1}, b − *w* =2000 h^{-1}, c − *w* = 2500 h^{-1}; initial concentration of *o*-xylene − *C*$_{xylene}$ = 42 g/nm^3.
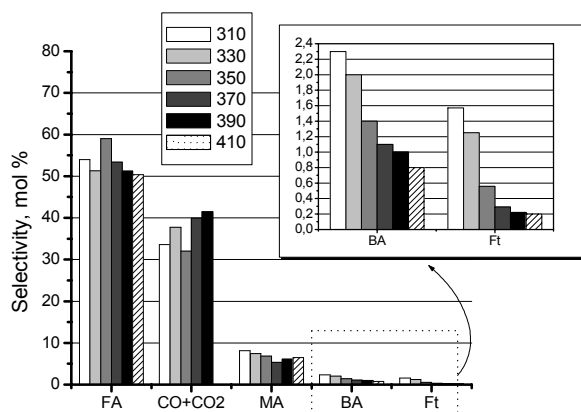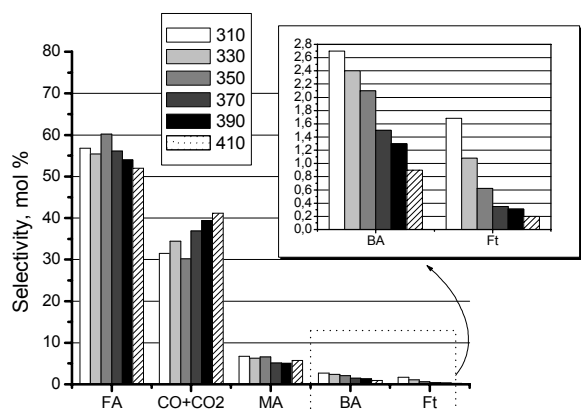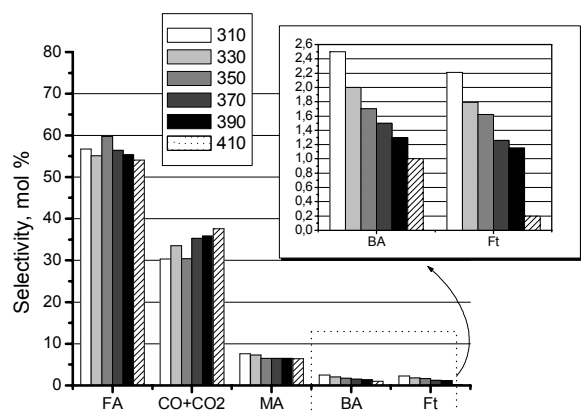
Fig. 3. Oxidation of *o*-xylene over 10% V_2O_5-ZrO_2 catalyst. Product selectivity (S_i) obtained for steady state at different temperatures (T = 310, 330, 350, 370, 390 and 410°C) and different volume rates: a − w = 1500 h^{-1}, b − w = 2000 h^{-1}, c − w = 2500 h^{-1}; initial concentration of *o*-xylene − C_{xylene} = 42 g/nm^3.

As to the selectivity of the undesired intermediate product of partial oxidation phthalide (Ft) and benzoic acid (BA), it is heighten for the samples with 4 and 10 wt.% V_2O_5 and decreases sharply as a function of the temperature for all catalyst samples tested (Figs. 1 and 3). Having in mind that the catalyst V_2O_5-ZrO_2 sample with 7 wt.% V_2O_5 shows highest selectivity (Fig. 2) to phthalic anhydride at

all flow rates and temperatures, it may be concluded that the phthalide is an intermediate oxidation product. It is oxidised to phthalic anhydride like in the presence of V_2O_5-TiO_2 (a) catalyst.
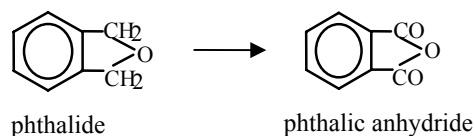
The selectivity to the products of destructive oxidation CO and CO_2 increases significantly (10−15 mol.%) (Figs. 1−3) with temperature for all catalyst compositions and all flow rates. It is remarkable that under highest flow rate (w = 2500 h^{-1}) all catalyst samples show very close selectivity values to CO and CO_2 over the whole temperature range. Taking into account the almost constant catalyst activity to phthalic anhydride at 350°C, one may settle that the increase of the products of destructive oxidation (CO, CO_2) as a function of the temperature can be ascribed to the direct combustion of a part of *o*-xylene, but not of phthalic anhydride.

Comparison between 7% V_2O_5-ZrO_2 and 7% V_2O_5-TiO_2 catalysts

Figure 4 presents the main products of *o*-xylene oxidation - FA, MA, Ft, BA and CO_x, the selectivity of *o*-xylene oxidation towards the different reaction products as a function of temperature (310−410°C) and space velocity (w = 1500−2500 h^{-1}) for a catalyst sample of 7 wt.% V_2O_5-TiO_2 (anatase). This composition exposes the best catalytic properties – a fact, well known from scientific papers.

At a temperature rising from 310 to 370°C, the selectivity increases up to about 10%. The further temperature rising to 390 and 410°C leads to slight decrease in selectivity.

Simultaneously, the undesired product of not complete oxidation (phthalide) decreases signifycantly in amount. The temperature effect on the selectivity towards of over-oxidised products (maleic anhydride, carbon oxide and carbon dioxide) towards oxidation is different. The selectivity to maleic anhydride exhibits a minimum at 350°C under all three volume rates, whereas the selectivity towards oxidation to carbon monoxide and carbon dioxide is constant over the whole temperature range (310−410°C) and is independent of the space velocity. According to the experimental results, the catalytic studies at higher temperatures when the amount of partial oxidation product (phthalide) is small, while the amount of the desired product of *o*-xylene oxidation (phthalic anhydride) increases, are more interesting. However, it is well known [1] that V_2O_5-TiO_2 (anatase) catalysts are strongly deac-

307

tivated at high temperatures (> 440°C). For that reason we also investigated V_2O_5-ZrO_2 catalysts which are expected to have a higher thermal stability and are very close to V_2O_5-TiO_2 (anatase) catalysts with respect to their acid-base characteristics.
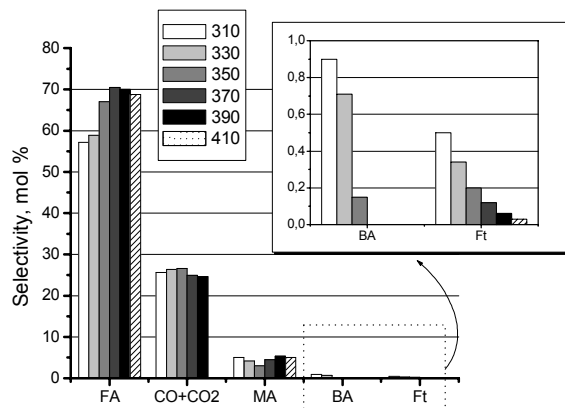
a
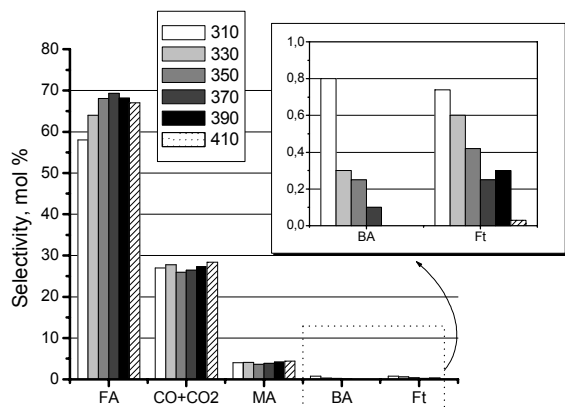
b
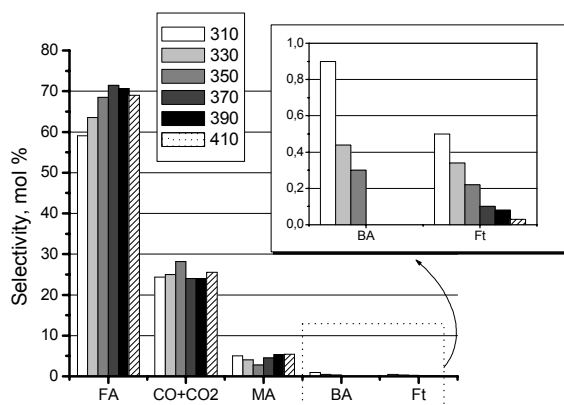
c

Fig. 4. Oxidation of *o*-xylene over 7% V_2O_5-TiO_2 catalyst. Product selectivity (S_i) obtained for steady state at different temperatures (T = 310, 330, 350, 370, 390 and 410°C) and different volume rates: $a - w = 1500$ h^{-1}, $b - w = 2000$ h^{-1}, $c - w = 2500$ h^{-1}; initial concentration of *o*-xylene $- C_{xylene} = 42$ g/nm^3.

It is obvious that the selectivity increases with the reaction temperature although this increase is

smaller than that for the V_2O_5-TiO_2 (anatase) catalyst (Fig. 4). With temperature raising the amount of the partial oxidation product considerably decreases and is practically independent of the space velocity. As to the over-oxidised products (maleic anhydride, carbon monoxide, carbon dioxide), their amount increases with temperature. Comparison with the V_2O_5-TiO_2 (anatase) catalyst shows that 7% V_2O_5-ZrO_2 catalyst samples (Fig. 2) display a 5−15% higher selectivity with respect to carbon monoxide oxidation. These experimental results indicate that at low oxidation temperatures (310−410°C), V_2O_5-TiO_2 (anatase) catalysts have a much higher selectivity towards *o*-xylene oxidation to phthalic anhydride than in the case of the V_2O_5-ZrO_2 catalyst.

The similar catalytic behaviour of the both compared samples was an expected result. The reason is probably in the similar structures of the supports (ZrO_2 and TiO_2) and the active component of V_2O_5.

During industrial catalytic exploitation, the accidental deviation of the normal technology regime is an often case. It is really possible the transcendent temperature rises to act destructively towards the catalyst. In order to check the thermal stability of our catalyst an additional experiment was carried out- to compare the selectivity of both samples in a temperature range of 450−550°C. Those temperatures are much higher over the normal ones for the standard V_2O_5-TiO_2 (anatase) catalysts. The resulting selectivity after 10 h exploitation in overheated regime towards the main products of *o*-xylene oxidation − FA, MA, Ft, BA and CO_x over the V_2O_5-ZrO_2 catalyst are shown in Fig. 5 and over V_2O_5-TiO_2 (anatase) – in Fig. 6. In this case the selectivity towards the main oxidation product FA is comparable (55 mol.%). BA and Ft are not present in V_2O_5-ZrO_2 probes and Ft is about 1.4% Ft in the V_2O_5-TiO_2 (anatase) sample. Probably the high-temperature regime had an influence over the V_2O_5-TiO_2 (anatase) catalyst with resulting structural and morphologic changes and the sintering processes led to catalyst deactivation.

The thermal stability of V_2O_5-ZrO_2 and the conventional V_2O_5-TiO_2 (anatase) sample was investigated after their prolonged (up to 50 h) exploitation at high temperature (500°C). The comperative results are shown in Figs. 7 and 8.

The change in the catalytic selectivity behaviour after their long-time high-temperature treating exposes the main predominance of the V_2O_5-ZrO_2 catalyst. In order to illustrate this one can compare the changes in V_2O_5-TiO_2 (anatase) samples in Figs. 4 and 8 and V_2O_5-ZrO_2 (anatase) samples − in Figs. 2 and 7.
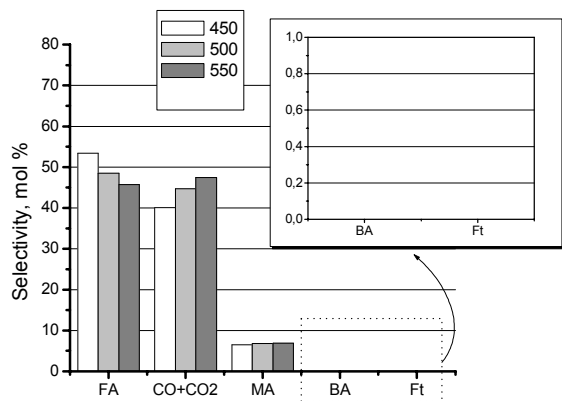
a
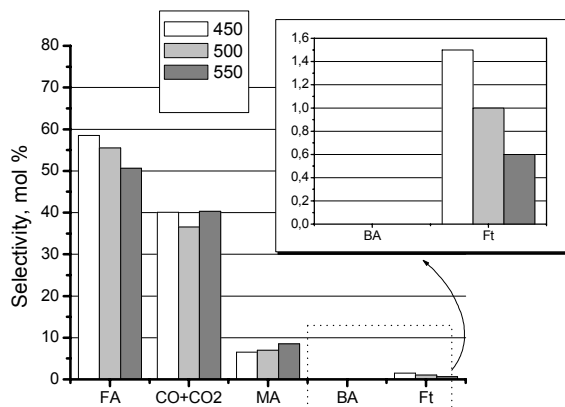
a
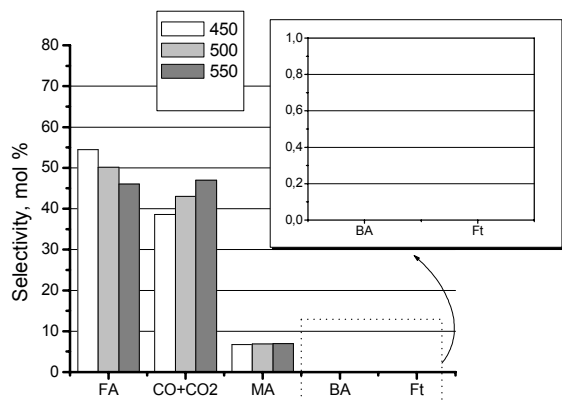
b
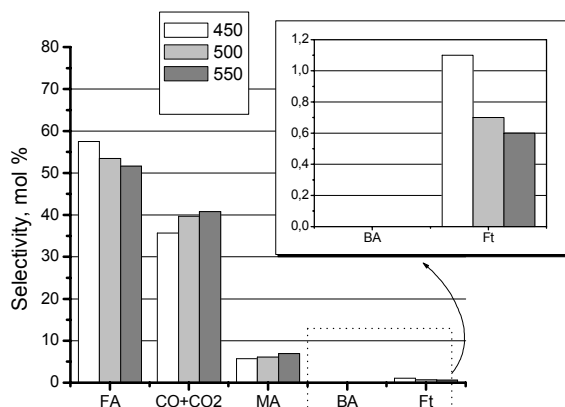
b
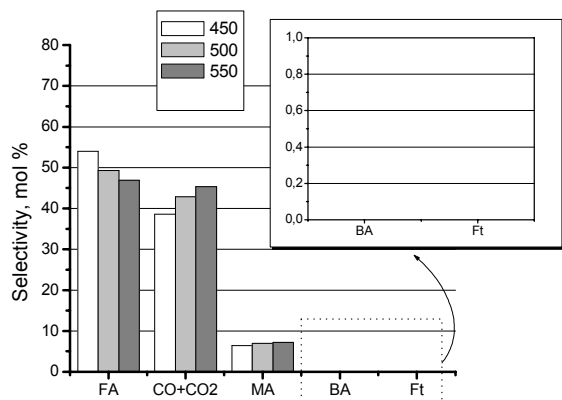
c

c

Fig. 5. Oxidation of *o*-xylene over 7% V_2O_5-ZrO_2 catalyst. Product selectivity (S_i) obtained for steady state at different temperatures (T = 450, 500 and 550°C) and different volume rates: a − *w* = 1500 h⁻¹, b − *w* = 2000 h⁻¹, c − *w* = 2500 h⁻¹; initial concentration of *o*-xylene − C_{xylene} = 42 g/nm³.

Fig. 6. Oxidation of *o*-xylene over 7% V_2O_5-TiO_2 catalyst. Product selectivity (S_i) obtained for steady state at different temperatures (T = 450, 500 and 550°C) and different volume rates: a − *w* = 1500 h⁻¹, b − *w* = 2000 h⁻¹, c − *w* = 2500 h⁻¹; initial concentration of *o*-xylene − C_{xylene} = 42 g/nm³.

a

a

b
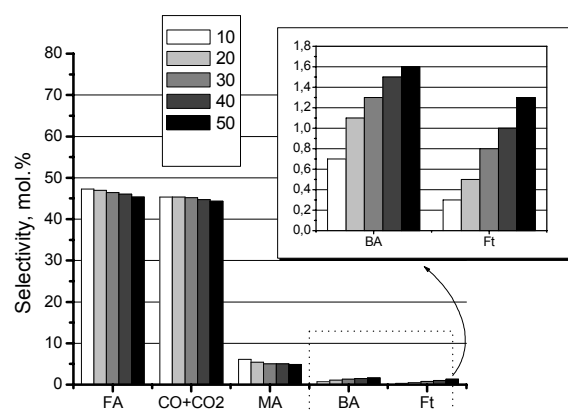
b
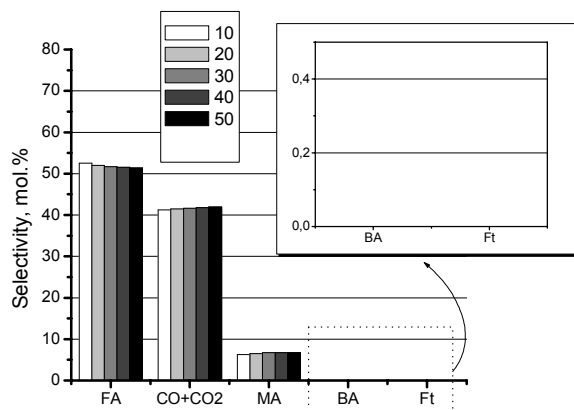
c

c

Fig. 7. Oxidation of *o*-xylene over 7% V_2O_5-ZrO_2 catalyst. Product selectivity (S_i) obtained for steady state (T = 500°C) at different times exploitation (τ = 10, 20, 30, 40 and 50 h) and different volume rates: a − w = 1500 h⁻¹, b − w = 2000 h⁻¹, c − w = 2500 h⁻¹; initial concentration of *o*-xylene − C_{xylene} = 42 g/nm³.

Fig. 8. Oxidation of *o*-xylene over 7% V_2O_5-TiO_2 catalyst. Product selectivity (S_i) obtained for steady state (T = 500°C) at different times exploitation (τ = 10, 20, 30, 40 and 50 h) and different volume rates: a − w = 1500 h⁻¹, b − w =2000 h⁻¹, c − w = 2500 h⁻¹; initial concentration of *o*-xylene − C_{xylene} = 42 g/nm³.

The selectivity of V$_2$O$_5$-TiO$_2$ (anatase) samples to the main product FA drops sharply from 72 mol.% (Fig. 4) to 43 mol.% (Fig. 8). The selectivity to the total oxidation product (CO$_x$) rises twice-from 27 mol.% (Fig. 4) to 45 mol.% (Fig. 8). The maleic anhydride contents stand almost unchanged-able after pre-heating, since the undesirable by-products contents significantly rise: BA content increases from 0.9 mol.% (Fig. 4) to 2.5 mol.% (Fig. 8) and Ft- from 0.01 mol.% (Fig. 4) to 1.3 mol.% (Fig. 8). During the exploitation time the Ft and BA content increase proportionally with pre-heating from 10 to 50 h.

The selectivity of V$_2$O$_5$-ZrO$_2$ samples to the main product FA decrease slightly from 63 mol.% (Fig. 2) to 51 mol.% (Fig. 7). The selectivity to the total oxidation product (CO$_x$) stands almost un-changeable and varies about 40 mol.%. The maleic anhydride contents increase from 5 mol.% (Fig. 2) to 8 mol.% (Fig. 7). The undesirable by-products BA and Ft are not registered at high temperature regime. The experimental results of V$_2$O$_5$-ZrO$_2$ (Fig. 7) and V$_2$O$_5$-TiO$_2$ (Fig. 8) expose a comparable yield of FA in both cases, since there are desirable changes of the by-product content (the rise of MA and total absence of BA and Ft).

An interesting dependence of the selectivity towards maleic anhydride is observed in the case of V$_2$O$_5$-TiO$_2$ (anatase) catalysts. The experimental results in Fig. 7 show the selectivity to drop after 50 h at all space velocities. The selectivity towards *o*-xylene oxidation to CO$_x$ shows a constant value of about 40 mol.% (Figs. 6 and 7). The kinetic tests at high temperatures (> 440°C) show that with respect to its selectivity of *o*-xylene oxidation to phthalic anhydride and phthalide, the V$_2$O$_5$-ZrO$_2$ catalyst has some advantages as compared to conventional V$_2$O$_5$-TiO$_2$ (anatase) catalysts. Nevertheless, it should be noted that the selectivity of V$_2$O$_5$-ZrO$_2$ catalysts in *o*-xylene oxidation to phthalic anhydride, as measured at 410°C, is by about 15% lower than that of conventional V$_2$O$_5$-TiO$_2$ (anatase) catalysts (Figs. 1 and 4).

With rising temperature (up to 450−550°C), a V$_2$O$_5$-TiO$_2$ (anatase) catalyst sample has exhibited a more pronounced decrease of selectivity in partial *o*-xylene oxidation than in the case of V$_2$O$_5$-ZrO$_2$. This decrease amounts to about 7−8 mol.% (Fig. 8), while for V$_2$O$_5$-ZrO$_2$ it is 1−2 mol.% (Fig. 7).

CONCLUSION

A highly active and selective V$_2$O$_5$-ZrO$_2$-based catalyst has been synthesised. In comparison with conventional V$_2$O$_5$-TiO$_2$ (a) catalyst, the V$_2$O$_5$-ZrO$_2$ catalyst has shown a higher selectivity to the valu-able side product maleic anhydride under conditions close to the industrial ones.

At low oxidation temperatures (up to 410°C) this catalyst is inferior to the conventional industrial V$_2$O$_5$-TiO$_2$ (a) catalyst. The kinetic studies per-formed in a high temperature regime (above 440°C) have shown the vanadium-zirconium catalyst to surpass in properties the V$_2$O$_5$-TiO$_2$ (a) catalyst under these conditions. It has been established that a high selectivity in *o*-xylene oxidation is attained when during the preparation of the V$_2$O$_5$-ZrO$_2$ catalyst ZrO$_2$ is completely covered by VO$_x$.

It has been also found that a V$_2$O$_5$-TiO$_2$ (a) catalyst sample containing 7 wt.% V$_2$O$_5$ demon-strates best catalytic activity expressed in highest selectivity to phthalic and maleic anhydrides and lowest selectivity to phthalide, CO and CO$_2$.

In contrast to the conventional V$_2$O$_5$-TiO$_2$ (a) catalyst, the V$_2$O$_5$ contents in V$_2$O$_5$-ZrO$_2$ catalyst is higher than that typical for monolayer coverage.

SYMBOLS

PhA   phthalic anhydride;
Pht   phthalide;
BA   benzoic acid;
MA   maleic anhydride;
w space velocity, h^{-1};
S_i selectivity, mol.%;
C_{xylene} concentration of *o*-xylene, g/nm^3

REFERENCES

1. A. Bielanski, J. Haber, Oxygen in Catalysis, Marcel Dekker, New York, 1991, Ch. 8.
2. C. Saterfield, Heterogeneous Catalysis in Industrial Practice, McGraw-Hill, Inc., 1991, Ch. 8.
3. J. Papachrysanthou, E. Bordes, A. Vejux, P. Cortine, R. Marchand, M. Tournox, *Catal. Today*, **1**, 219 (1987).
4. M. Wainwright, N. Foster, *Catal. Rev.- Sci. Eng.,* **19**, 211 (1979).
5. V. Nikolov, D. Klissurski, A. Anastasov, *Catal. Rev. - Sci. Eng.*, **33**, 319 (1991).
6. L. Makedonski, V. Nikolov, *Bulg. Chem. Commun.*, **28,** 27 (1995).
7. G. Deo, I. Wachs, J. Haber, *Crit. Rev. Surf. Chem.*, **4**, 141 (1994).
8. G. Band, S. Flamers, *Appl. Catal.*, **46**, 89 (1989).
9. F. Cavani, G. Centi, E. Foresti, F. Trifiro, *J. Chem. Soc. Faraday Trans.*, **84**, 237 (1988).
10. V. Escribano, G. Busca, E. V. Lorenz, *J. Phys.Chem.*, **95**, 5541 (1991).
11. G. Deo, I. Wachs, *J. Catal.,* **146**, 323 (1994).
12. N. Y. Topsoe, H. Topsoe, A. Dumesic, *J. Catal.*, **151**, 226 (1995).
13. I. Wachs, G. Deo, B. Weckhuysen, A. Andreini, M.

de Boer Vuurman, M. Amiridis, *J. Catal.*, **161**, 211 (1996).

14. M. Galantowicz, in: 12th Int. Conf. Chem. Proc. Eng., Praha, 1996, Mapret lecture, Prague, 1996.

15. M. Galantowicz, W. Krajewski, S. Karpinski, B. Wielowinska, in: Catalyst Deactivation, (Stud. Surf. Sci. Catal., vol. 88), Elsevier Science B.V., 1994.

16. V. Nikolov , A. Anastasov, *Ind. Eng. Chem. Res.*, **31**, 80 (1992).

17. R. Saleh, I. Wachs, USA Patent 4728744 (1988).

18. C. Val, S. Pieck, M. Grandos, M. Banares, J. Fierro, *Langmuir*, **18**, 2642 (2002).

19. M. Sanati, A. Andersson, L. R. Wallenberg, B. Rebenstorf, *Appl. Catal. A*, **106**, 51 (1993).

20. H. Miyata, T. Ohno, F. Hatayama, *J. Chem. Soc.,-Faraday Trans.,* **91**, 3505 (1995).

21. Y. Toda, T. Ohno, F. Hatayama, H. Miyata, *Appl. Catal. A*, **207**, 273 (2001).

22. Y. Toda, T. Ohno, F. Hatayama, H. Miyata, *Phys. Chem. Chem. Phys.*, **1**, 1615 (1999).

23. A. Adamski, Z. Sojka, K. Dyrek, M. Che, G. Wendt, S. Albrecht, *Langmuir*, **15**, 5733 (1999).

24. A. Khodakov, J. Yang, S. Su, E. Iglesia, A. T. Bell, *J.*

Catal., **177**, 343 (1998).

25. G. Deo, I. E. Wachs, *J. Catal.*, **146**, 323 (1994).

26. T. Ohno, E. Tanaka, F. Hatayama, Y. Toda, H. Miyata, *Catal. Lett.*, **77**, 183 (2001).

27. J. Sohn, S. Cho, Y. Pac, S. Hayashi, *J. Catal.*, **159**, 170 (1996).

28. I. Wang, Y. Cai, I. Wachs, *Langmuir,* **15**, 1233 (1999).

29. B. Olthof, A. Khodakov, A. Bell, *J. Phys. Chem. B.,* **104**, 1516 (2000).

30. E. Reddy, T. Rojas, A. Fernandez, B. Chowdhury, B. Reddy, *Langmuir,* **16**, 4217 (2000).

31. A. Khodakov, B. A. Olthof, *J. Catal.*, **181**, 205 (1999).

32. J. Miller, L. Jhanski, *J. Catal.*, **184**, 183 (1999).

33. X. Gao, J. L. G. Fierro, I. Wachs, *Langmuir*, **15**, 3169 (1999).

34. C. L. Pieck, M. A. Banares, M. A. Vicente, J. L. G. Fierro, *Chem. Mater.*, **13**, 1174 (2001).

35. L. Makedonski, V. Nikolov, N. Nikolov, V. Blaskov, *React. Kinet. Catal. Lett.*, **66**, 237 (1999).

36. V. Nikolov, L. Makedonski, A. Anastasov, *Hung. J. Ind. Chem.*, **28**, 93 (2000).

V₂O₅-ZrO₂ КАТАЛИЗАТОР ЗА СЕЛЕКТИВНО ОКИСЛЕНИЕ НА *о*-КСИЛОЛ ДО ФТАЛОВ АНХИДРИД: I. ПОЛУЧАВАНЕ, КАТАЛИТИЧНА АКТИВНОСТ И СЕЛЕКТИВНОСТ

Л. Македонски

Медицински университет, ул. „Марин Дринов" № 55, 9002 Варна

(Резюме)

Изследвана е термичната устойчивост, каталитичната активност и селективност на серия от V₂O₅-ZrO₂ каталитични образци за парциално окисление на *о*-ксилол до фталов анхидрид. Каталитичната селективност на каталитичния образец със 7% V₂O₅-ZrO₂ е сравнена с конвенционалния промишлен катализатор V₂O₅-TiO₂ (анатаз). Термичната устойчивост е изследвана в два температурни обхвата. При ниски температури (под 410°C) V₂O₅-TiO₂ (анатаз) показва по-ниска селективност спрямо фталов анхидрид в сравнение със синтезирания V₂O₅-ZrO₂ каталитичен образец. При по-високи реакционни температури, дори при 550°C в продължение на 50 часа експлоатационно време, селективността спрямо целевия продукт от фталов анхидрид на V₂O₅-ZrO₂ каталитичен образец намалява незначително.

V_2O_5-ZrO_2 catalyst for selective oxidation of *o*-xylene to phthalic anhydride: II. Physicochemical characterisation of the catalyst

L. Makedonski*

Medical University, 55 Marin Drinov St., 9002 Varna, Bulgaria

Vanadium oxide-zirconia catalysts were prepared by impregnation of ZrO_2 powder with an aqueous solution of NH_4VO_3. The thermal stability, activity and selectivity of a series of V_2O_5-ZrO_2 catalyst samples towards *o*-xylene oxidation to phthalic anhydride have been investigated. It has been established that the phthalic anhydride content reaches about 55 mol% in samples containing 7 and 10 wt% V_2O_5. The physicochemical characterisation of the catalysts prepared was performed using IR spectroscopy, XPS analysis, X-ray spectroscopy, derivatograph analysis, EPR spectroscopy and temperature - programmed reduction.

Key words: V_2O_5-ZrO_2 catalysts, *o*-xylene oxidation, surface characterisation, physicochemical characterization.

INTRODUCTION

Vanadium oxide-based catalysts are well known and extensively employed in industry for hetero-geneous oxidation and ammoxidation of aromatic hydrocarbons [1−7]. Generally these catalysts are supported on oxides such as Al_2O_3, SiO_2 and TiO_2. Supports are often found to modify the physico-chemical properties of vanadia catalysts. The supported oxides do not form three-dimensional crystal phases, but rather a patchy or continuous 'monolayer' covering the support [8, 9]. Recently, ZrO_2-supported catalysts were found to exhibit better catalytic properties than the catalysts supported on other oxides [10].

During the past years some patents have reported the use of ZrO_2 as a support of V_2O_5 [11]. Systems of V_2O_5-ZrO_2 in combination with various promoters are widely used for several reactions including *o*-xylene oxidation [12], ammoxidation of aromatics and methylaromatics [13], oxidation of toluene [14, 15], decomposition of propan-2-ol [16, 17], oxidative dehydrogenation of propane [18, 19], oxidation of naphthalene [21, 23], partial oxidation of methanol and selective catalytic reduction of NO_x by C_3H_6 [20]. The utilisation of ZrO_2 is based on the fact that it is stable at very high temperatures [21] and its acid-basic characteristics are very close to those of TiO_2.

Interesting studies [21−29] have reported the use of zirconia as a support of vanadium oxide catalysts. The valuable zirconia properties in this respect are its high thermal stability and acid-basic character-

istics which are close to those of titania (anatase) [22−25].

The activity of supported vanadia catalysts depends mainly on the method of preparation, the nature of the support and the dispersion of the active component on the support surface. Considerable efforts have been made to develop surface characterisation of the active component in supported catalysts. These include specific surface area, IR spectroscopy, XPS analysis, X-ray spectroscopy, derivatograph analysis, EPR spectroscopy and temperature - programmed reduction.

EXPERIMENTAL

Synthesis of the catalyst

Supported V_2O_5-ZrO_2 catalyst samples were obtained by a method based on the preparation of an industrial BASF catalyst, V^{5+}-V_2O_5 (specific surface area 6 m^2/g), NH_4VO_3 (AG-Fluka) and ZrO_2 (AG-Fluka; monoclinic [6], specific surface area 26 m^2/g) being used.

The catalyst samples were prepared by reducing V^{5+} of V_2O_5 (V_2O_5:$H_2C_2O_4$ = 1:2.5−3.0) in an aqueous solution of oxalic acid at 60-80°C. Zirconia was introduced simultaneously. Surfactants (form-amide or diphenylformamide) in an aqueous solu-tion: surfactants ratio = 3.5−5.0:1.0 were used as binding substances. The suspension obtained was subjected to ultrasonic treatment with a view to homogenisation, dispersion and additional activa-tion of the catalyst mass. The active catalyst mass was applied on an inert support of steatite spheres, 6 mm in diameter, by pulverising the suspension on

---

* E-mail: lubomir60@yahoo.comm

the spheres pre-heated up to 200–250°C. The catalyst samples thus obtained had a coverage thickness of 1 mm of the total catalyst mass. They were dried at 110°C and calcined for 2−10 h at 450°C (a temperature corresponding to the calcination temperature of the industrial catalyst in air flow).

Apparatus for investigating the catalytic activity and selectivity of the samples, under study

The activity and selectivity of the catalyst samples towards the vapour phase partial oxidation of *o*-xylene to phthalic anhydride were investigated with a flow-type installation functioning at a pressure of 1 atm. The laboratory flow reactor had a length of 450 mm and contained 250 cm³ catalysts. It was immersed in a salt bath containing a KNO_2 :$NaNO_2$ (1:1) salt melt, the temperature being maintained with an accuracy of up to 1°C. The temperature of the catalyst grains along the catalyst layer was measured by thermocouples. A minipump achieved the exact dosage of *o*-xylene. Along with the air introduced by a compressor, o-xylene came to a mixer with a filling where the temperature of the air-xylene mixture was maintained at 180°C.

Condensers up took the vapour phase oxidation products and the gas phase was conducted to the gas chromatograph.

Methods and apparatus for characterisation of catalyst samples and products of o-xylene oxidation

The analysis of the oxidation products was performed on-line by a gas chromatograph. The contents of phthalic anhydride (PhA), phthalide (Pht), benzoic acid (BA), maleic anhydride (MA) and CO_2 + CO were determined. The gas chromatograph was connected on-line with the flow installation for *o*-xylene oxidation. The catalyst samples were activated by air for 48 h, while the selectivity measurements were done 2 h after fixing the corresponding regime.

The final reaction mixture was subjected to gas-chromatographic analysis in a Perkin Elmer 850 apparatus (capillary column OV-101, l = 25 m, inner diameter = 0.25 mm, carrier gas = H_2, T = 90−120°C, detector PID). The reaction products found were *o*-toluyl aldehyde, benzoic acid, phthalide, maleic anhydride, phthalic anhydride and unreacted xylene. The products of fragmentary oxidation (CO and CO_2) were determined chromatographically in a steel column (l = 4 m, inner diameter = 0.25 mm, catarometer as a detector).

The catalyst samples were activated in an air flow at the corresponding temperature and volume rate for 48 h. The kinetic measurements were performed two hours after establishing the corresponding regime.

The samples were characterised by a series of physicochemical methods.

The specific surface area was measured with a Klyachko-Gurvich apparatus by the BET method.

The IR spectra were recorded by a Nicolet Avatar 320 FIIR spectrometer using KBr tablets.

The XPS analysis of V_2O_5-ZrO_2 was carried out with an Escalab II electron spectrometer at a pressure of about 10^{-8} Pa. The samples were stored in stainless steel vessels. The photoelectron spectra were excited by MgK_α radiation.

The X-ray spectra were recorded with a DRON-3 apparatus using CuK_α radiation.

The EPR spectra of the samples at room temperature were obtained by an ERS 220/Q electron resonance spectrometer system at 100 kHz modulation of the magnetic field.

Temperature-programmed reduction (TPR) was carried out on a standard laboratory apparatus using a quartz thermometer. The weight of the sample was 0.1 g. The temperature was raised linearly from 30 to 800°C at a constant heating rate of 10°/min. The samples were reduced in a 10% hydrogen + 90% argon mixture (flow-rate of 30 ml/min).

Derivatograph analysis was made with a Paulik Erdey derivatograph apparatus. This permitted simultaneous registration of the temperature curve (T), the enthalpy curve (DTA), the mass change (TG curve) and the DTG curve. The analysis was performed with a TG sensitivity of 200 mg, a sample weight of 0.5 g, a heating rate of 10°C/min, technically pure alumina as an inert substance, turbulence air in the furnace and heating up to 1000°C.

RESULTS AND DISCUSSION

In order to elucidate the behaviour of the zirconium cations in the catalyst samples, we performed the following experiment. The catalytic activity and selectivity of a 7% V_2O_5-ZrO_2 sample, 1:1 mechanic (physical) mixture of the same catalyst sample with pure ZrO_2, and a sample of pure zirconia were investigated and compared.

The experimental results in Fig. 1 show that pure zirconia oxide has very low catalytic selectivity in vapour phase oxidation of *o*-xylene to phthalic anhydride. The coordinatively unsaturated cations initiate processes of complete oxidation. On this basis it can be expected that the pure zirconia surface would lead to complete *o*-xylene oxidation. At first sight the relatively low activity of pure zirconia seems to be an indication of its inertness

towards the complete *o*-xylene oxidation to phthalic anhydride. From the scientific literature it is known that coordinatively unsaturated titanium cations also have a low activity with respect to the oxidation of *o*-xylene oxidation to phthalic anhydride. However, they favour the complete oxidation of the intermediate products of partial oxidation.
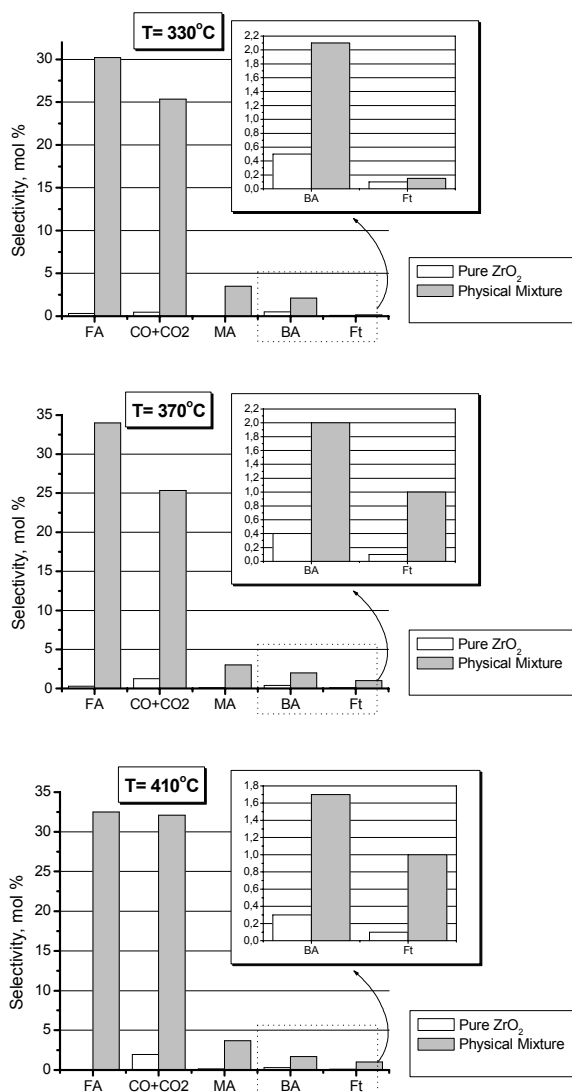
Fig. 1. Selectivity of pure ZrO_2 and a physical mixture of pure ZrO_2 and catalyst sample 7% V_2O_5-93% ZiO_2 (1:1) at a different temperature oxidation of *o*-xylene. $C_{o-xylene} = 42$ g/nm^3, w = 1500 h^{-1}, time of exploitation $\tau = 10$ h.

Let us study the behavior of the zirconium species. If they are completely inert, a drop in catalyst activity should be observed due to the lower (50%) relative content of the active V_2O_5 phase.

The experimental results (Fig. 1) obtained at different (330, 370 and 410°C) temperatures reveal a significant drop (by about 10%) in activity of the 7% V_2O_5-ZrO_2 sample when it is mixed mechanically with pure zirconia in a 1:1 ratio. Simulta-

neously, the amount of CO_x in the products increases. The content of *o*-toluyl anhydride and phthalide in the oxidation products increases several times. This is also an indication of a reaction proceeding towards complete oxidation.

The experimental results permit the important, with respect to the catalyst structure, conclusion that high catalyst selectivity towards the oxidation reaction can be achieved when the zirconia surface is completely covered by VO_x. It should also be noted that the amount of the VO_x surface phase needed for monolayer coverage would not necessarily ensure the absence of a bare zirconia surface. It is known that in many cases the VO_x surface phase forms the so-called islands. A suitable method is needed for the synthesis of surface phase VO_x coverage.

Determination of specific surface

The specific surface areas are: 26 m^2/g for the initial monoclinic ZrO_2, 28 m^2/g for the obtained fresh catalyst of 7% V_2O_5-ZrO_2, 22 m^2/g for the catalyst 10 h at 450°C, and 7 m^2/g for the heated in air at 800°C for 3 h (Table 1). These data show that during the exploitation of the 7% V_2O_5-ZrO_2 catalyst at 450°C no intense sintering proceeds since the specific surface area does not change substantially. The sintering occurring at 800°C leads to a strong decrease of the specific surface area.

It should be noted that according to [30] the conventional V_2O_5-TiO_2 (anatase) catalyst is strongly sintered (deactivated) at this temperature. However, considerable sintering of the 7% V_2O_5-ZrO_2 catalyst resulting in a specific surface area drop has been observed at 800°C.

Derivatograph analysis (DTA, DTG, TG)

The DTA curve of the synthesised catalyst sample (7% V_2O_5-93% ZrO_2) exhibits a double exothermic effect beginning above 100°C and showing a maximum at about 260°C, then a second maximum at 365°C. The latter is visible within the same temperature range on the TG curve (Fig. 2) and is produced by a two-stage decomposition process. According to our opinion this may be due to further decomposition of the vanadium-oxalate complex used as a precursor in preparation of catalysts samples. The supposition is confirmed by IR and X-ray phase analyses of the catalyst samples. The total weight drop of the sample indicates about 93% of undecomposed oxalate complex.

The DTA curve (Fig. 3) of the same catalyst sample (7% V_2O_5-93% ZrO_2) after 100 h exploitation in *o*-xylene oxidation to phthalic anhydride at 450°C displays one barely visible exothermic effect at 230−290°C with a maximum at 260°C. It is

probably a result of additional decomposition, which is indicated by the DTG and TG curves within the same temperature range.

XP spectroscopy

The XPS studies of the catalyst samples have registered Ti $2p^{3/2}$ and Zr $3d^{3/2}$ lines. On the surface there are only ZrO_2 and TiO_2 in the 4^+ oxidation state. This is evident from Figs. 4 and 5 presenting the XPS spectra of Ti2p and Zr3d. The chemical shift of the above lines is characteristic of TiO_2 and ZrO_2. In both substrates (Figs. 4 and 5) vanadium is in the same oxidation state as V_2O_5, which is proved by the shift of the V $2p^{3/2}$ lines.
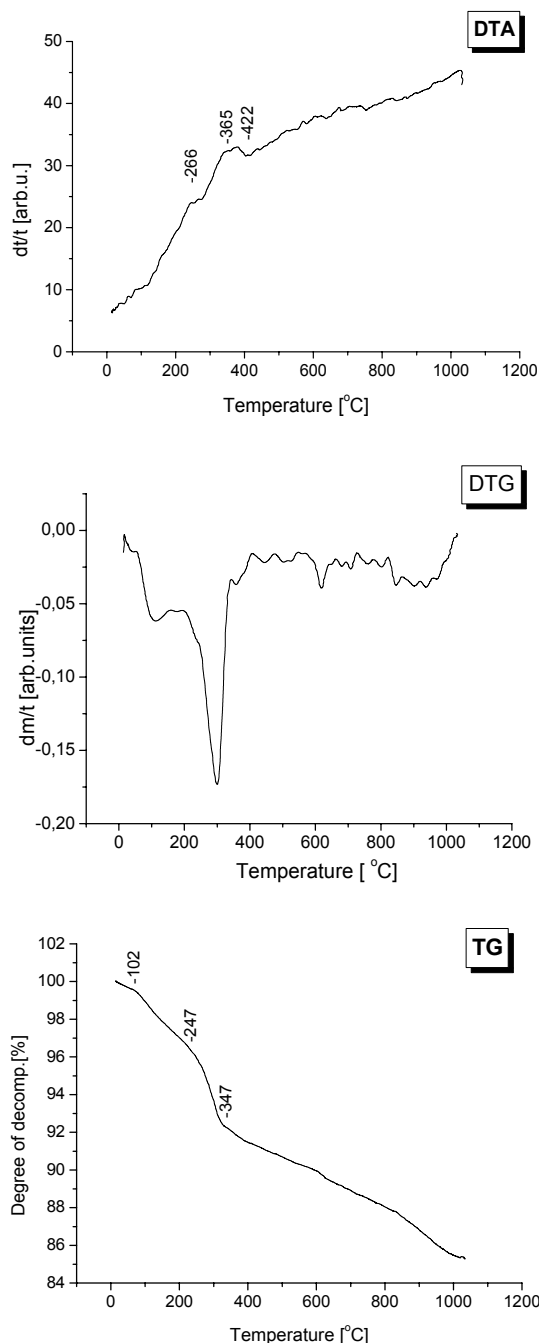
Fig.2. Derivatograph analysis (DTA, DTG, TG) of fresh 7% V₂O₅-93% ZiO₂ catalyst sample.
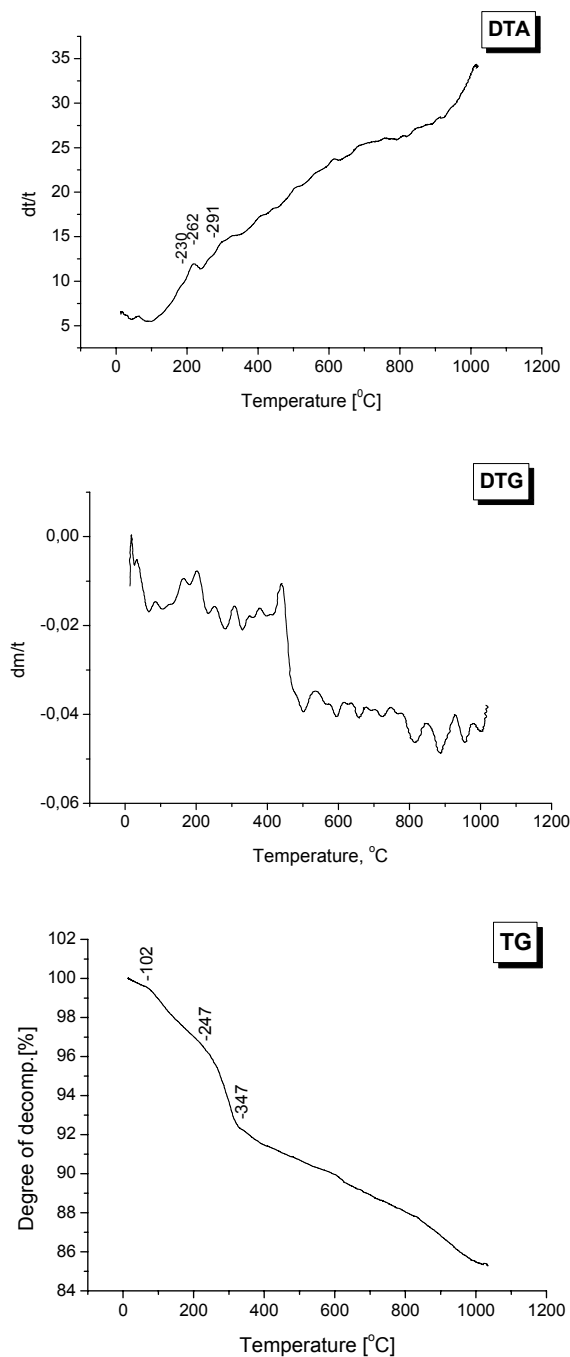
Fig. 3. Derivatograph analysis (DTA, DTG, TG) of catalysts samples 7% V₂O₅-93% ZiO₂ tested in *o*-xylene oxidation, T=370°C, C$_{o-xylene}$= 42 g/nm³, w = 1500 h⁻¹, time of exploitation τ = 10 h.
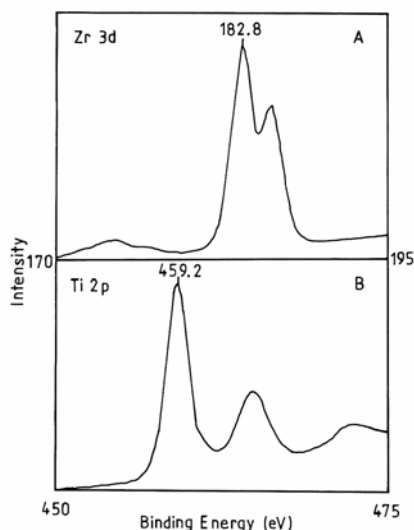
Fig. 4. Photoelectron spectra of pure ZrO_2 (curve A) and pure TiO_2 (anatase) (curve B).

The Ti:V:O or Zr:V:O concentration ratio (at.%) calculated on the basis of XPS experiments (Table 1) is, after correcting the free path of photoemitted electrons, in a very good agreement with the above considerations.
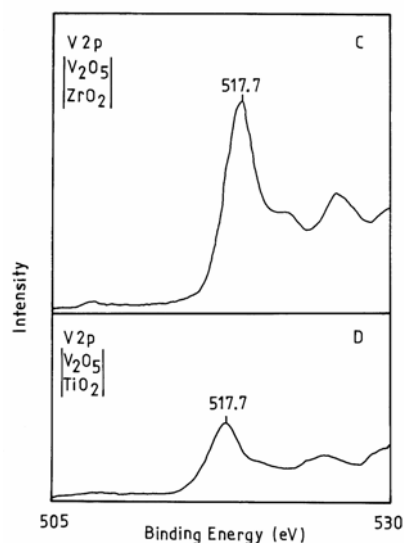
Fig. 5. Photoelectron spectra of catalyst sample 7% V_2O_5-93% ZiO_2 (curve C) and catalyst sample 7% V_2O_5-93% TiO_2 (anatase) (curve D), tested in *o*-xylene oxidation (curve B), T = 370°C, $C_{o\text{-xylene}}$ = 42 g/nm^3, w = 1500 h^{-1}, time of exploitation τ = 10 h.

Thermoprogrammed reduction

The catalyst samples were subjected to temperature programmed reduction. Figures 6 and 7 present results from TPR of fresh V_2O_5-ZrO_2 samples containing different V_2O_5 concentrations (from 4 to about 10%). The peaks observed up to 300°C with samples a, b and c are probably due to desorption of water from the samples. Two more

groups of peaks are observed: low-temperature peaks at 340−360°C and high-temperature ones at 460−480°C. According to literature [49, 50], the low-temperature peaks are characteristic of the reduction of V_2O_5 crystals, while the high-temperature ones are produced by reduction of surface vanadium. The areas of the low-temperature peaks (a-c) show an obvious trend to increase with the V_2O_5 content. The same trend, although much less pronounced, is observed with the areas of the high-temperature peaks.
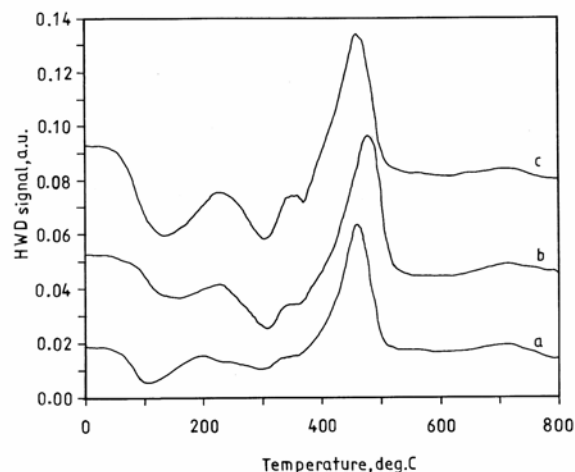
Fig. 6. Temperature-programmed reduction of fresh catalysts systems V_2O_5-ZiO_2 at different contents of V_2O_5 (wt.%): a. catalyst sample 4% V_2O_5-96% ZiO_2; b. catalyst sample 7% V_2O_5-93% ZiO_2; c. catalyst sample 10% V_2O_5-90% ZiO_2.
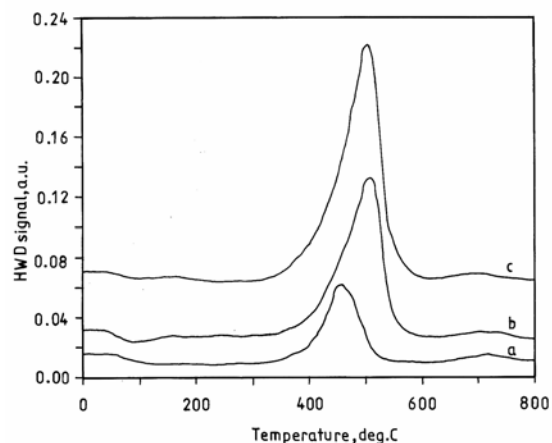
Fig. 7. Temperature-programmed reduction of tested in *o*-xylene oxidation catalysts systems V_2O_5-ZiO_2, T = 450°C, $C_{o\text{-xylene}}$ = 42 g/nm^3, w = 1500 h^{-1}, time of exploitation τ = 10 h at different contents of V_2O_5 (wt.%): a. catalyst sample 4% V_2O_5-96% ZiO_2; b. catalyst sample 7% V_2O_5-93% ZiO_2; c. catalyst sample 10% V_2O_5-90% ZiO_2.

Comparison of the data from TPR of a conventional V_2O_5-TiO_2 (anatase) catalyst [31, 32] with those on V_2O_5-ZrO_2 shows a low-temperature peak

317

much smaller than the high-temperature one in the first case. This is attributed to the fact that the V_2O_5-TiO_2 (anatase) catalyst samples contain a much larger amount of surface vanadium. On the zirconia substrate, vanadium is coordinated much more easily and is more difficult to remove than in the case of the titania (anatase) support. Taking into account that V_2O_5 is the active phase, the V_2O_5-ZrO_2 catalyst should have a good catalytic activity.

The spectra of used in process of oxidation of *o*-xylene V_2O_5-ZrO_2 catalyst samples (Fig.7) show a single peak at $450-510°C$, which is probably due to the reduction of surface vanadium. With increasing V_2O_5 amount in samples a-c, the peak areas increase. The ratio between the areas of the peaks for fresh and used samples also increases with the active phase (V_2O_5) concentration in the direction a-c.
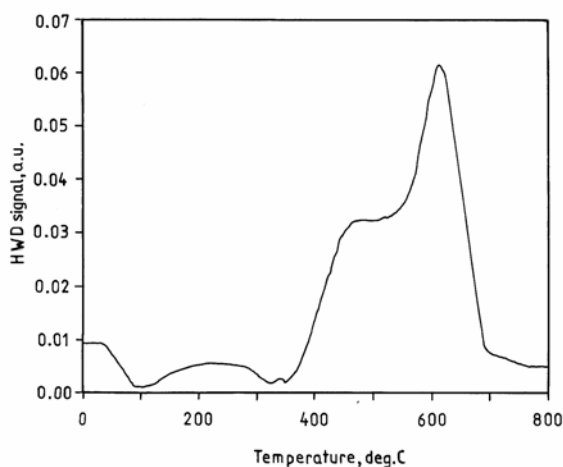
Fig. 8. Temperature-programmed reduction of tested in *o*-xylene oxidation catalysts sample 7% V_2O_5-93% TiO_2 (anatase), $T = 450°C$, $C_{o\text{-}xylene} = 42$ g/nm^3, $w = 1500$ h^{-1}, time of exploitation $\tau = 10$ h.

For the sake of comparison, a 7% V_2O_5-TiO_2 (anatase) sample was also subjected to TPR. Figure 8 shows the spectrum, which is very close to that of the conventional V_2O_5-TiO_2 (anatase), described in literature [30]. The low-temperature peak is observed at about $460°C$. It is due to reduction of surface vanadium. A high-temperature peak, much more intense than the low-temperature one, is observed at $600°C$. No such peak has been established with V_2O_5-ZrO_2 samples. According to Wachs *et al.* [30], this peak is due to the partial reduction of V_2O_5 probably to V_2O_4 during the catalytic reaction. A low-intensity peak is observed at $340-350°C$. Its presence indicates that not completely reduced crystallites of V_2O_5 have remained in the used catalyst sample.

Previous studies on the catalytic activity of the V_2O_5-ZrO_2 system [33] have shown values commensurable with those for the system V_2O_5-

318

TiO_2. Taking into account this and the experimental results of TPR one may draw some conclusions on the role of the V_2O_5 active phase with respect to the catalytic properties of the samples.

The relatively high catalytic activity of samples of the V_2O_5-ZrO_2 system may be due to distribution of the active sites on the surface of the vanadium support. This assumption is based on the fact that the peak area of 7% V_2O_5-ZrO_2 – used in oxidation of *o*-xylene (Fig. 7) is much larger that the area of the low-temperature peak in the spectrum of using V_2O_5-TiO_2 (anatase) sample (Fig. 8).

The high catalytic activity of the catalyst sample from the V_2O_5-TiO_2 (anatase) system shows that the partial reduction of V_2O_5 to V_2O_4 is also of importance for the catalytic reaction.

EPR spectroscopy

Figure 9 shows the EPR spectra of fresh V_2O_5-ZrO_2 catalyst samples as well as of samples used in *o*-xylene oxidation to phthalic anhydride.
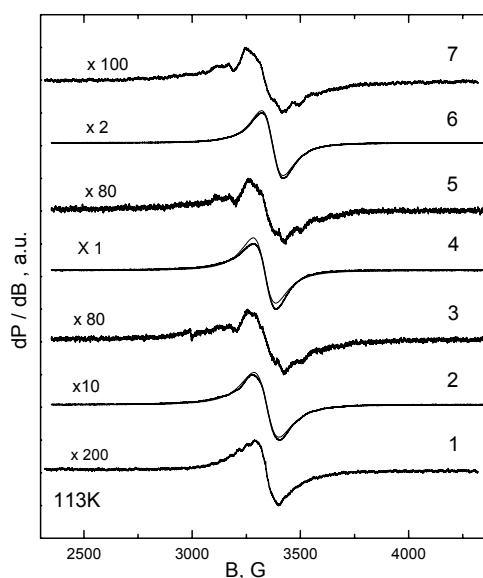
Fig. 9. EPR spectra of the catalyst system V_2O_5-ZiO_2: 1. pure V_2O_5; 2. fresh catalyst sample 4% V_2O_5-96% ZiO_2; 3. tested in *o*-xylene oxidation catalyst 4% V_2O_5-96% ZiO_2, $T = 450°C$, $C_{o\text{-}xylene} = 42$ g/nm^3, $w = 1500$ h^{-1}, time of exploitation $\tau = 10$ h; 4. fresh catalyst sample 7% V_2O_5-93% ZiO_2; 5. tested in *o*-xylene oxidation catalyst 7% V_2O_5-93% ZiO_2, $T = 450°C$, $C_{o\text{-}xylene} = 42$ g/nm^3, $w = 1500$ h^{-1}, time of exploitation $\tau = 10$ h; 6. fresh catalyst sample 10% V_2O_5-90% ZiO_2; 7. tested in *o*-xylene oxidation catalyst 10% V_2O_5-90% ZiO_2, $T = 450°C$, $C_{o\text{-}xylene} = 42$ g/nm^3, $w = 1500$ h^{-1}, time of exploitation $\tau = 10$ h.

In the same figure a comparison with the EPR spectrum of a sample of V_2O_5 is made. Evidently, the EPR spectrum of V_2O_5 (curve 1) consists of a single line on which an unresolved fine structure is

visible. According to the data from literature [34, 35], this signal may be ascribed to exchange-associated VO^{2+} complexes. The spectra (2, 4 and 6) of fresh catalyst samples exhibit a single line with a Lorentzian shape whose width slightly decreases with increasing the amount of supported V_2O_5 (from curve 2 to curve 6): curve 2: 4% V_2O_5-96% ZrO_2 – ΔH_{pp} = 115 ± 1G; curve 4: 7% V_2O_5-93% ZrO_2 – ΔH_{pp} = 104 ± 1G; curve 6: 10% V_2O_5-90% ZrO_2 – ΔH_{pp} = 100 ± 1G.

The model V_2O_5 used as a standard has about 200 times lower intensity as compared to the EPR signal of the sample where V_2O_5 is the active phase.

With the catalyst samples used in *o*-xylene oxidation to phthalic anhydride (Fig.9, curves 3, 5 and 7), the intensity of the EPR signal sharply drops and the EPR spectra (Fig. 9, curves 3, 5 and 7) contain an asymmetric signal of isolated VO^{2+} complex group.

In these catalyst samples the amount of exchange-associated VO^{2+} groups decreases. The appearance of isolated VO^{2+} groups (having not changed during the catalytic reaction) can be attributed to that part of the active V_2O_5 phase, which has partly interacted with zirconia support.

The period of exploitation of catalyst depends significantly on their thermal stability. The EPR spectra of a fresh 7% V_2O_5-ZrO_2 catalyst and catalysts samples calcined at 450°C and 800°C for 10 h are show in Fig. 10.

The EPR spectrum of a fresh 7% V_2O_5-ZrO_2 catalyst (Fig. 10, curves 1a–1c) shows two signals: a singlet signal being 11 mT wide (curve 1a) and an octet signal, which is not well solved (curve 1b). The combination of both signals (curve 1a and 1b) leads to the registration of a total signal presented in Fig. 5 by a thick line (curve 1c). According to the authors [34, 36], these two signals are due to clustering V^{4+} (with respect to the singlet signal) and to a VO^{2+} complex (for the octet signal).

The form and the view of EPR spectrum of a catalyst sample calcined at 450°C for 10 h (curve 2a–2b) do not differ practically from that of a fresh catalyst (Fig. 10, curves 1a–1c). This means that there is no significant change of the fine structure of the active phase (V_2O_5) of the catalyst calcined at 450°C. The thermal treating of the catalyst under this temperature has practically no influence on its thermal stability. On the contrary, a V_2O_5-TiO_2 (anatase) catalyst undergoes consider-able structural changes under such conditions of calcination.

An appreciable variation of the shape of the EPR spectrum of a sample calcined at 800°C for 10 h is observed (Fig. 10, curve 3). The singlet signal (clustering V^{4+}) disappears and is completely

compensated by the octet signal due to the VO^{2+} complex. The last one is presented in Fig.10 by a thick line (curve 3).
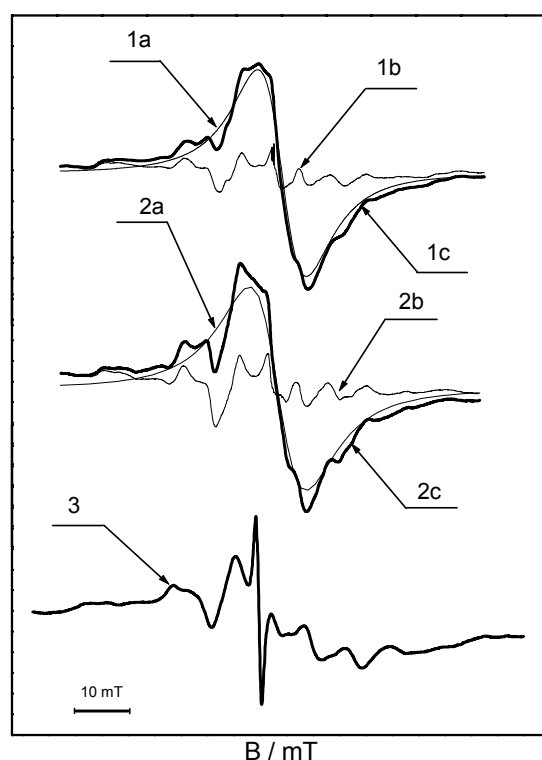
Fig. 10. EPR spectra of 7% V_2O_5-93% ZiO_2 catalyst sample. curves 1a-1c – fresh catalyst; curves 2a-2c – catalyst calcined at 450°C for 10h; curves 3a-3c – catalyst calcined at 800°C for 10h

X-ray phase analysis

The X-ray phase analysis of catalyst samples used in the *o*-xylene oxidation to phthalic anhydride shows the presence of a crystalline phase of mono-clinic zirconia with all catalysis samples (Fig. 11). Peaks of the supported V_2O_5 phase are not visible, which indicates that at the working temperature of the catalyst samples (450°C) it is amorphous or clusters of V_2O_5 particles have been formed. Well shaped V_2O_5 crystals have not been observed.

The intensity of the zirconia peaks decreases with the increase in V_2O_5 concentration (from 3 to 1 in Fig. 11). The mean thickness of the V_2O_5 coverage in the whole bulk surface of the zirconia support was estimated from the decrease in integral intensities of the zirconia peaks due to absorption of the X-rays by the catalyst layer.

The calculations were performed according to the formula [37]:

$$I = I_0 e^{\frac{-\mu}{\rho}} \rho \frac{2t}{\sin \theta}$$

$$\frac{\mu}{\rho} = \frac{1}{M} \sum \left(\frac{\mu}{\rho}\right)_i m_i$$

$$t = -\frac{1}{2} \ln \frac{I}{I_0} \sin \frac{\Theta}{\mu},$$

where I denotes the integral intensity of the of 7% V_2O_5-93% ZrO_2 sample, I_0 − the integral intensity of the peak of zirconia, μ − absorption coefficient, ρ − the density (g·cm3), t − the density of the coverage and θ is the angle for which the intensities I and I_0 are calculated. According to the calculations, the mean thickness of the V_2O_5 coverage in the whole bulk surface of the zirconia support of the 7% V_2O_5-93% ZrO_2 catalyst is 375 nm.
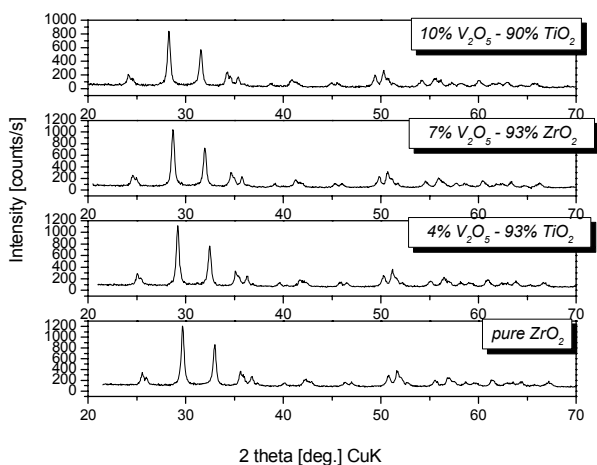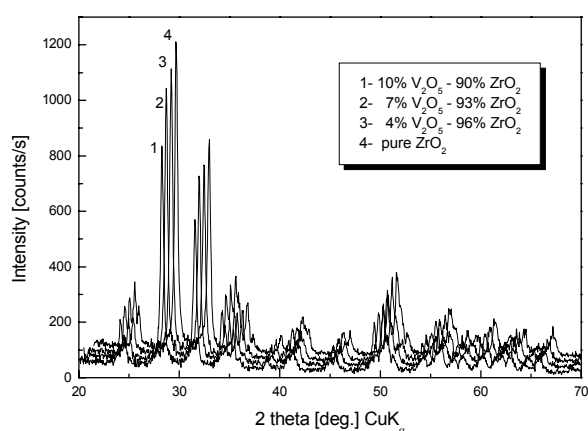
Fig. 11. X-ray spectra of the catalyst system V_2O_5-ZiO_2: 1. tested in *o*-xylene oxidation catalyst 10% V_2O_5-90% ZiO_2, T = 450°C, $C_{o\text{-xylene}}$ = 42 g/nm³, w = 1500 h⁻¹, time of exploitation τ = 10 h; 2. tested in *o*-xylene oxidation catalyst 7% V_2O_5-93% ZiO_2, T = 450°C, $C_{o\text{-xylene}}$ = 42 g/nm³, w = 1500 h⁻¹, time of exploitation τ = 10 h; 3. tested in *o*-xylene oxidation catalyst 4% V_2O_5-96% ZiO_2, T = 450°C, $C_{o\text{-xylene}}$ = 42 g/nm³, w = 1500 h⁻¹, time of exploitation τ = 10 h; 4. pure ZrO_2.

IR Spectroscopy

Figure 12 shows the IR spectra of the fresh

synthesised sample (with 4 and 7% V_2O_5) and catalysts samples tested in *o*-xylene oxidation.
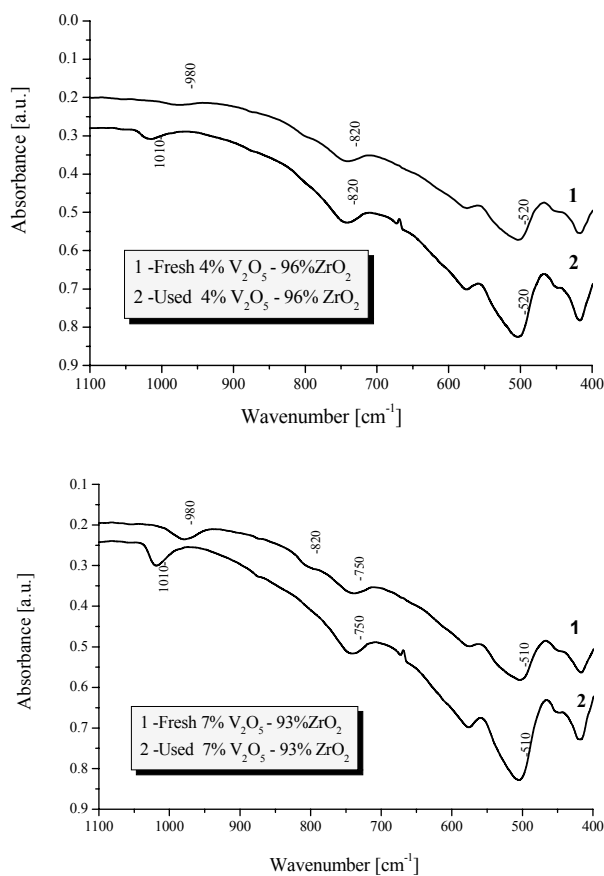
Fig. 12. IR spectra of catalysts samples 4% V_2O_5-96% ZiO_2 and 7% V_2O_5-93% ZiO_2: 1 - fresh catalysts samples; 2 - tested in *o*-xylene oxidation catalysts samples, T = 450°C, $C_{o\text{-xylene}}$ = 42 g/nm³, w = 1500 h⁻¹, time of exploitation τ = 10 h.

The IR spectra of use catalyst samples contain absorption bands at 1010, 820 and 520 cm⁻¹, which are characteristic of pure V_2O_5. The high-frequency band at 1010 cm⁻¹ is assigned to vibration of isolated V=O non-bridge bonds in the [VO_5] trigonal bipyramids [38, 39]. The broad absorption band at 810 cm⁻¹ is due to stretching modes of V–O–V chains, while the bands at 500 and 430 cm⁻¹ are associated with bending modes of the V_2O_5 network consisting of [VO_5]. The intensity of these absorption bands is higher than that of the band of fresh catalyst samples. This may be a result of crystallisation processes initiated by the temperature of *o*-xylene oxidation.

A characteristic feature of the IR spectra of fresh catalyst samples is the shift of the absorption lines of [VO_5] groups to lower frequencies, which is probably due to lengthening of the V–O bonds.

The IR spectra of 7% V_2O_5-93% ZrO_2 system treated at 450 and 800°C (normalised with respect to the most intensive peak at 501 cm⁻¹) are presented

in Fig. 13. The spectra of both samples (curve 1 - 450°C and curve 2 - 800°C) in the region of 1100−400 cm^{-1} do not show significant variations in the structure of the active phase. The reason for such a statement is the fact that the positions of the peaks (characteristic for the system V_2O_5-ZrO_2) of the absorption band coincide. On the other side, it can be seen that the intensity of the peak at 1020 cm^{-1} for the catalyst sample calcined under 800°C (curve 2) increases significantly. Most probably this is due to crystallisation processes taking place at this high temperature. In our point of view, they lead to an intensive sintering of the catalyst sample and as a result the adsorption characteristics of the support decline and the thermal stability of the catalyst being worsened, respectively. This is in accordance with the specific surface data (Table 1). It is worth noting that in the interval 450−800°C a separation of the water occurs and the peak observed at 1633 cm^{-1} for a sample calcined at 450°C (curve 1) disappears (curve 2) (deformation fluctuation of the water). The peaks observed in the spectrogram 1 at 1384 and 1458 cm^{-1} are very likely due to the thermal decomposition of the binding agent that is used in the synthesis of the catalyst.
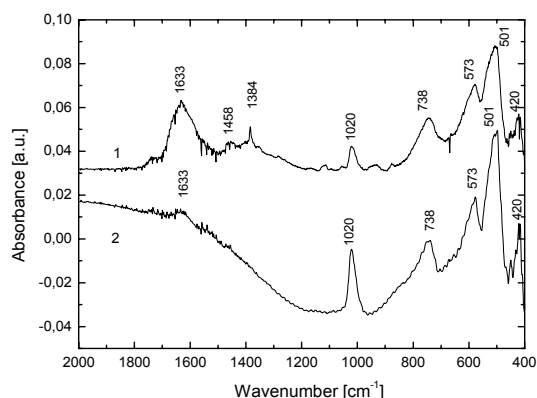
Fig. 13. IR spectra of 7% V_2O_5-93% ZiO_2 catalyst sample: 1 - catalyst samples calcined at 450°C for 10 h; 2 - catalyst samples calcined at 800°C for 10 h.

CONCLUSIONS

The physicochemical characterisation of prepared V_2O_5-ZrO_2 catalyst samples was performed using IR spectroscopy, XPS analysis, X-ray spectroscopy, derivatograph analysis, EPR spectroscopy and temperature-programmed reduction.

A high catalyst selectivity towards the oxidation reaction can be achieved when the zirconia surface is completely covered by VO_x. The amount of the VO_x surface phase needed for monolayer coverage would not necessarily ensure the absence of a bare zirconia surface.

In the synthesised V_2O_5-ZrO_2 and V_2O_5-TiO_2 catalyst samples vanadium is in the same oxidation state as V_2O_5, which is proved by the shift of the V $2p^{3/2}$ lines.

The relatively high catalytic activity of samples of the V_2O_5-ZrO_2 system may be due to distribution of the active sites on the surface of the vanadium support. The high catalytic activity of the catalyst sample on the base of V_2O_5-TiO_2 (anatase) system shows that the partial reduction of V_2O_5 to V_2O_4 is also of importance for the catalytic reaction.

The EPR analyses of fresh V_2O_5-ZrO_2 catalyst samples expose the presence of exchange-associated VO^{2+}complexes and isolated VO^{2+}complex groups. The appearance of isolated VO^{2+} groups (having not changed during the catalytic reaction) can be attributed to that part of the active V_2O_5 phase which has partly interacted with zirconia support.

The thermal treating of the catalyst has practically no influence on its thermal stability. On the contrary, a V_2O_5-TiO_2 (anatase) catalyst undergoes considerable structural changes under such conditions of calcinations.

REFERENCES

1. L. Makedonski, V. Nikolov, *Bulg. Chem. Commun.*, **28**, 27 (1995).
2. G. Deo, I. Wachs, J. Haber, *Crit. Rev. Surf. Chem.*, **4**, 141 (1994).
3. V. Escribano, G. Busca, V. Lorenzelli, *J. Phys. Chem.*, **95**, 5541 (1991).
4. G. Deo, I. Wachs, *J. Catal.*, **146**, 323 (1994).
5. N. Y. Topsoe, H. Topsoe, A. Dumesic, *J. Catal.,* **151**, 226 (1995).
6. I. Wachs, G. Deo, B. Weckhuysen, A. Andreini, M. Vuurman, M. de Boer, M. Amiridis*, J. Catal.*, **161**, 211 (1996).
7. M. Galantowicz, in: 12th Int. Conf. Chem. Proc. Eng., Praha, 1996, Mapret lecture, Prague, 1996.
8. G. Bergeret, K. V. Chary, B. Rama Rao, V. S. Subrahmanyam, N. K. Nag, *Appl. Catal.*, **40**, 191 (1988).
9. K. V. Chaty, K. Narsimha, K. S. Rama Rao, P. Kanta Rao, *J. Mol. Catal.*, **58**, 13 (1990).
10. T. Ono, H. Miyata, Y. Kubokawa, *J. Chem. Soc., Faraday Trans. I.*, **83**, 1761 (1987).
11. R. Saleh, I. Wachs, *USA Patent* 4728744 (1988).
12. C. L. Pieck, S. Del Val, M. L. Grandos, M. A. Banares, J. L. G. Fierro, *Langmuir*, **18**, 2642 (2002).
13. R. Y. Saleh, I. E. Wachs, *Eur. Patent* 21325-A (1987).
14. M. Sanati, A. Andersson, L. R. Wallenberg, B. Rebenstorf, *Appl. Catal. A.*, **106**, 51 (1993).
15. H. Miyata, T. Ohno, F. Hatayama, *J. Chem. Soc.-Faraday Trans.*, **91**, 3505 (1995).
16. Y. Toda, T. Ohno, F. Hatayama, H. Miyata, *Appl. Catal. A.*, **207**, 273 (2001).

17. Y. Toda, T. Ohno, F. Hatayama, H. Miyata, *Phys. Chem. Chem. Phys.*, **1**, 1615 (1999).
18. A. Adamski, Z. Sojka, K. Dyrek, M. Che, G. Wendt, S. Albrecht, *Langmuir.*, **15**, 5733 (1999).
19. A. Khodakov, J. Yang, S. Su, E. Iglesia, A. T. Bell, *J. Catal.*, **177**, 343 (1998).
20. T. Ohno, E. Tanaka, F. Hatayama, Y. Toda, H. Miyata, *Catal. Lett.*, **77**, 183 (2001).
21. J. Sohn, S. Cho, Y. Pac, S. Hayashi, *J. Catal.*, **159**, 170 (1996).
22. I. Wang, Y. Cai, I. Wachs, *Langmuir,* **15**, 1233 (1999).
23. B. Olthof, A. Khodakov, A. Bell, *J. Phys. Chem. B.,* **104**, 1516 (2000).
24. S. Su, A. Bell, *Phys. Chem. B.*, **102**, 7000 (1998).
25. E. Reddy, T. Rojas, A. Fernandez, B. Chowdhury, B. Reddy, *Langmuir*, **16**, 4217 (2000).
26. I. Wachs, G. Deo, B. Weckhuysen, *J. Catal.*, **170**, 75 (1997).
27. A. Khodakov, B. Olthof, *J. Catal.*, **181**, 205 (1999).
28. J. Miller, L. Jhanski Lakshmi, *J. Catal.*, **184**, 183 (1999).
29. X. Gao, J. L. Fierro, I. Wachs, *Langmuir,* **15**, 3169 (1999).
30. M. Galantowicz, W. Krajewski, S. Karpinski, B. Wielowinska, in: Catalyst Deactivation, (Stud. Surf. Sci. Catal., vol. 88), Elsevier Science B.V., 1994.
31. C. G. Bond, S. Flamerz, *Appl. Catal.*, **46**, 89 (1989).
32. H. Bosch, B. Kip, J. Vanommen, P. Gellings, *J. Chem. Soc. Faraday Trans. I.,* **80**, 2479 (1984).
33. V. Nikolov, L. Makedonski, A. Anastasov, *Hung. J. Ind. Chem.*, **28**, 93 (2000).
34. S. Masters, A. Chrissanthopouls, K. Eriksen, S. Boghosian, R. Fermann, *J. Catal.,* **166**, 16 (1997).
35. K. Dyrek, A. Adamski, Z. Sojka, *Spectrochim. Acta*, Part A.*,* **54**, 2337 (1998).
36. K. Eriksen, D. Karydis, S. Boghosian, R. Fehrman, *J. Catal.*, **155**, 32 (1995).
37. International Tables for X-ray Crystalography, vol. III, Kynoch Press, Birmingham, 1968, p.157.
38. J. Sohn, S. Cho, Y. Pae, S. Hayashi, *J. Catal.*, **159**, 170 (1996).
39. C. Pieck, M. Banares, M. Vicente, J. Fierro, *Chem. Mater.,* **13**, 1174 (2001).

V₂O₅-ZrO₂ КАТАЛИЗАТОР ЗА СЕЛЕКТИВНО ОКИСЛЕНИЕ НА *о*-КСИЛОЛ ДО ФТАЛОВ АНХИДРИД: II. ФИЗИКОХИМИЧНО ОХАРАКТЕРИЗИРАНЕ

Л. Македонски

Медицински университет, ул. „Марин Дринов" № 55, 9002 Варна

(Резюме)

V₂O₅-ZrO₂ катализатор е синтезиран чрез нанасяне на прах от ZrO₂ с воден разтвор NH₄VO₃. Изследвана е термичната устойчивост, каталитичната активност и селективност на серия от V₂O₅-ZrO₂ катализаторни образци спрямо окислението на *о*-ксилол до фталов анхидрид. Установена е селективност около 55 мол.% за образци съдържащи 7 и 10% V₂O₅. Направена е физикохимична характеристика на катализаторните образци с помощта на инфрачервена спектроскопия, рентгенофазов анализ, ЕПР анализ, деритографски анализ и термопрограмирана редукция.

Modeling of enzymatic esterification kinetics with respect to the substrates ratio

K. Tonova[1,*], Z. Lazarova[2]

[1] Institute of Chemical Engineering, Bulgarian Academy of Sciences, Acad. G. Bonchev St., Block 103, 1113 Sofia, Bulgaria

[2] Austrian Research Centres GmbH-ARC, Biogenetics-Natural Resources-Water, 2444 Seibersdorf, Austria

Enzymatic esterification in reversed micelle system is presented. The initial reaction rate has its local maximum at equimolar initial ratio of alcohol to acid for each one of the studied acid concentrations. Modelling of this phenomenon is made based on Michaelis-Menten equation for Ping-Pong Bi-Bi mechanism. One variable in this equation changes with the initial acid concentration while the other is set to alter with the ratio of alcohol to acid and its deviation from the determined optimal value of 1. The observed inhibition by the acid is considered. The effect of acid dilution when the initial water concentration in the reversed micelle system is increased is also taken into account. The kinetic parameters are determined graphically. The modelled rate dependences on the substrates ratio are compared to the measured data. Suggestions for further model development are made.

Key words: enzymatic esterification, Ping-Pong Bi-Bi kinetic model, substrate inhibition, *Candida rugosa* lipase, reversed micelles.

INTRODUCTION

The kinetics of many fatty ester syntheses catalysed by fungal lipases (free or immobilised) has been shown to follow Ping-Pong Bi-Bi mechanism [1]. This mechanism was postulated for reactions in biphasic organic-aqueous systems with solvent [2, 3], in solvent-free systems [4] or in reversed micelle solvents [5−7]. Regarding microemulsion reaction network, some elaborated theoretical models were proposed which took into account the partitioning of the substrates between the phases [5, 8]. For biphasic systems, the effect of the organic solvents polarity was mathematically described through dissociation constants for the substrates [2] or by their thermodynamic activities [4]. However, substrate inhibition was included only in the latter case taking into account a competitive inhibition by the alcohol solely.

The enzymatic esterification that proceeds in the fastest way at one and the same ratio (despite the change in both substrates concentrations) was previously studied by us [9]. Although such phenomenon has not been directly stated anywhere in literature, similar relationship can be revealed if some data are carefully examined. Thus in *n*-heptane Novozyme 435 catalyses best the ethyl acetate synthesis at an ethanol molar excess of *ca.* 4.5 [10], and *i*-amyl oleate at about an equimolar ratio of the substrates [3].

In the present article, we propose an approach to modelling the enzymatic synthesis, which proceeds with optimal rates at a constant initial ratio of alcohol to acid in spite of the change in their concentrations.

EXPERIMENTAL

Materials and methods

The studied reversed micelle system (RMS) consisted of substrates, oleic acid and *i*-amyl alcohol dissolved in *i*-octane, all p.a. (Merck or Sigma-Aldrich). The enzyme, CRL (*Candida rugosa* lipase, TypeVII, Sigma), was incorporated inside the reversed micelles formed by the quaternary ammonium salt, cetyl pyridinium chloride, CPC (Sigma) under injection of a known amount of an aqueous buffer solution.

The effects of substrates and water concentrations on the initial esterification rate were examined in kinetic series following titrimetrically (alcoholic 0.1 mol·dm^{-3} KOH/*phenolphthalein*) the consumption of the free oleic acid [11]. Some esterifications were performed in duplicate, the rates determined deviated from each other by a relative error of 1%. CRL was used as received and the initial rates were referred to g {solid}. The protein content in the solid CRL preparation was assayed according to Sigma Diagnostics, Procedure No. 690 and it was found to be $\approx$ 14%. In the same origin CRL preparation, $\approx$8% protein was measured by *Zaidi et al.* [12].

In the studies (if otherwise stated) the following RMS parameters were held constant: CRL − 3 g {solid}·dm^{-3}; CPC − 0.115 mol·dm^{-3}; aqueous buffer type - K$_2$H/KH$_2$ phosphate − 0.05 mol·dm^{-3}; pH 6.88−7.09; temperature − 35°C; stirring rate − ~ 70 rpm.

Experimental base of the model

In Fig. 1, the effects of the initial concentration of the acid and of the initial ratio R = mol [alcohol]$_0$/mol [acid]$_0$ (Fig. 1a) and of the water, *i.e.* the aqueous buffer (Fig. 1b) on the initial reaction rate (V_0) are shown. For [oleic acid]$_0$ = 0.1 mol·dm^{-3} at R = 0.5 and R = 0.75 (Fig. 1a), the initial CPC concentration was reduced 3-fold (to 0.0383 mol·dm^{-3}) in order to establish a stable RMS of W$_0$ = 30 (W$_0$ = mol H$_2$O/mol CPC). In Fig. 1a it is well seen that for each acid concentration the rate has its local maximum at R = 1. The aim of this work is to consider this phenomenon 'optimal rates at a constant substrates ratio' into well known kinetic model for Ping-Pong Bi-Bi mechanism (Eqn. (1)):

$$\frac{1}{V_0} = \frac{1}{V_{max}} + \frac{K_{mB}}{V_{max}} \times \frac{1}{B} + \frac{K_{mA}}{V_{max}} \times \frac{1}{A} \quad (1).$$

For the purpose, we propose a modification of the variable for the alcohol concentration *A*, in the model equation (1).

Moreover, from the data represented in Fig. 1b, it is seen that the initial water concentration in the RMS-volume, [H$_2$O]$_0$, affects significantly the reaction rate. For highest [oleic acid]$_0$ = 0.4 mol·dm^{-3} and W$_0$ = 30 ([H$_2$O]$_0$ = 3.45 mol·dm^{-3}) the rates decreased (Fig. 1a), obviously due to the inhibition caused by the acid. However, increasing the water concentration the rates increased substantially (Fig. 1b). At [H$_2$O]$_0$ = 4.60 mol·dm^{-3} (W$_0$ = 40) the rates approached the highest values gained at [oleic acid]$_0$ = 0.3 mol·dm^{-3}. The effect of substrates dilution by water is evident and it diminishes the inhibition effect. It can be concluded that both substrates influence the reaction rate through their concentrations with respect to the dispersed aqueous phase of the reversed micelles where the enzyme molecule is incorporated and where the reaction proceeds. In eq. 1, the variables for the substrates concentrations *A* and *B* should be transformed taking into account the dilution effect of the water initially present in the RMS.

Model development

Transformation of the variables A and B in order to consider the effect of the initial water. The first transformation consists in normalisation of both

initial substrates concentrations, *A* and *B*, to the initial water concentration in the RMS-volume.

initial W$_0$=30

a

[oleic acid]$_0$ = 0.4 mol dm^{-3}

b
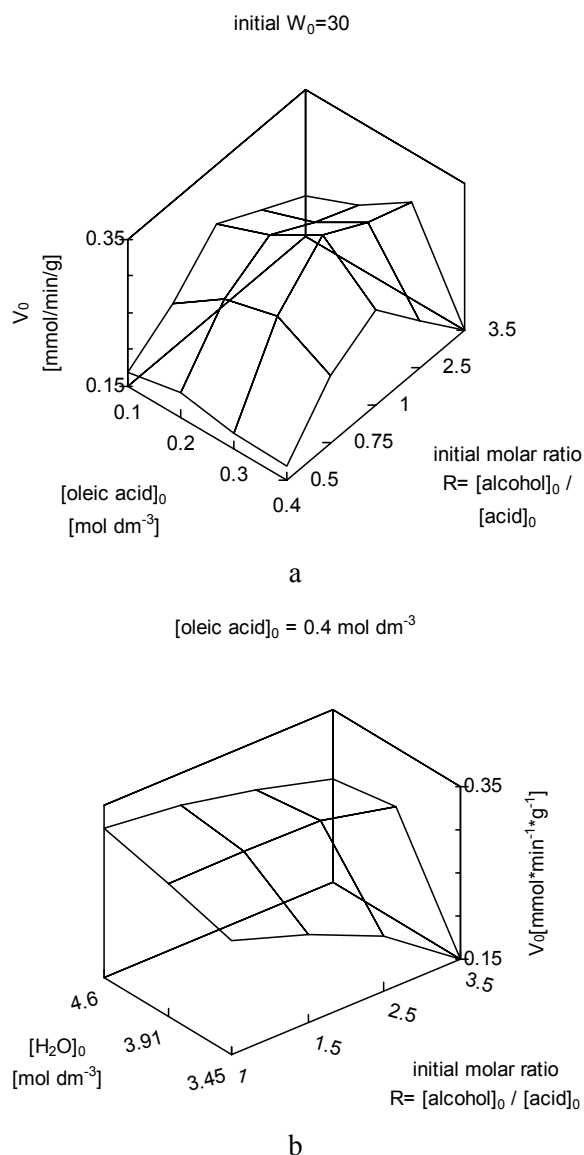
Fig. 1. Effect of the initial concentrations of the substrates (a) and of the water (b) on the initial reaction rate, V_0. CPC and CRL concentrations were as mentioned in Experimental, except for [oleic acid]$_0$ = 0.1 mol·dm^{-3} at R = 0.5 and R = 0.75 where CPC-concentrations were 0.0383 mol·dm^{-3} and CRL, 1 g·dm^{-3}. [Oleic acid]$_0$ = 0.4 mol·dm^{-3}, R = 3.5 and [H$_2$O]$_0$ = 3.45 mol·dm^{-3} was not measured.

The reason is, that the substrates concentrations with respect to the dispersed aqueous phase of the RMS can not be initially settled and known as they are consequent upon the spontaneous processes of micelle formation and mass exchange between the reversed micelles and the continuous hydrocarbon phase where the substrates are dissolved. The variables *B* and *A* in Eqn. (1) are transformed into B^* and A^* and the following expressions (2) and (3) are assigned:

$$B^* = \frac{[\,oleic\;acid\,]_0}{[\,H_2O\,]_0} \qquad (2),$$

i.e. B^* is the initial molar ratio of the oleic acid to the water in the RMS-volume. B^* is dimensionless variable. As it can be calculated from the data in Fig. 1, the effect of B^* is studied for five B^*_i-values: 0.0299, 0.0614, 0.0899, 0.1053, and 0.1189;

$$A^* = \frac{[\,i-amyl\;alcohol\,]_0}{[\,H_2O\,]_0} \qquad (3),$$

i.e. A^* is the respective dimensionless variable for the initial molar ratio of the *i*-amyl alcohol to the water in the RMS-volume.

Further transformation of the variable A^* in order to consider the effect of the initial substrates ratio. As already discussed, for each one experimental B^*_i, the highest initial rate, $V_{0,ij}$, was measured when $A^*_j = B^*_i$, *i.e.* always at R = 1. In Fig. 1 two areas can be distinguished. In the series $B^*_I = A^*_j > A^*_{j-1} > A^*_{j-2} > ...$ (R decreases from 1 to 0.5), $V_{0,ij} > V_{0,ij-1} > V_{0,ij-2} >$ as a result of the reduction in the initial alcohol concentration. In the series $B^*_I = A^*_j < A^*_{j+1} < A^*_{j+2} <...$ (R increases from 1 to 3.5), $V_{0,ij} > V_{0,ij+1} > V_{0,ij+2} >...$ due to the inhibition by the alcohol.

On this experimental base, further transformation of the variable A^* is made in order to consider the described effect of the initial substrates ratio. Instead of A^* in the model Eqn. (1) we propose a new variable A_R which represents a relationship between the two substrates according to the following expression:

$$A_R = e^{-\frac{|A^*-B^*|}{A^*}} \qquad (4).$$

Each one value $A_{R,ij}$ can be directly calculated from the known initial concentrations in the RMS, [oleic acid]$_0$, [*i*-amyl alcohol]$_0$, and [H$_2$O]$_0$ using expressions (2) and (3). The power on the right side of Eqn. (4), $\frac{|A^*-B^*|}{A^*}$, is involved in the following two equalities:

- for each $A^* < B^*$, $\dfrac{|A^*-B^*|}{A^*} = \dfrac{B^*}{A^*} - 1$ (4');

- for each $A^* > B^*$, $\dfrac{|A^*-B^*|}{A^*} = 1 - \dfrac{B^*}{A^*}$ (4'').

In both cases the power represents a measure of how much A^* deviates from B^*, *i.e.* how much the substrates molar ratio deviates from its optimum value of 1. Otherwise, the new variable can be represented as follows:

$$A_R = e^{-\frac{|A^*-B^*|}{A^*}} = e^{-\left|1-\frac{1}{R}\right|} = e^{-\frac{|R-1|}{R}} \qquad (4''').$$

The present exponential form is chosen to limit up the A_R-value when $A^* = B^*$ (R = 1). A_R can be maximally equal to 1 only if $A^* = B^*$ (R = 1).

Using the new variable A_R, Eqn. (1) is transformed into Eqn. (5):

$$\frac{1}{V_0} = \frac{1}{V_{max}} + \frac{K_{mB^*}}{V_{max}} \times \frac{1}{B^*} + \frac{K_{mA_R}}{V_{max}} \times \frac{1}{A_R} \qquad (5),$$

where the variable B^* is defined according to Eqn. (2), and the variable A_R, − according to Eqn. (4).

Our arguments that the variable A_R can introduce correctly the observed effect of the initial substrates ratio on V_0 (Fig. 1a) are pointed as follows:

- A_R is maximal (= 1) for each pair $A^*_j = B^*_i$ (each R = 1) and according to Eqn. (5) the initial rate, V_0, will have its local maximum depending only on B^*_i-value.

- In the series $B^*_I = A^*_j > A^*_{j-1} > A^*_{j-2} >$ (R decreases from 1 to 0), A_R diminishes and tends to 0 at $A^*_j << B^*_i$. In this way the decrease in V_0 with the alcohol reduction is described.

- In the series $B^*_I = A^*_j < A^*_{j+1} < A^*_{j+2}...$ (R increases above 1), A_R diminishes. Thus the decrease in V_0 caused by inhibition by the alcohol can be described. It has to be mentioned that the values $A^*_j >> B^*_i$ are not allowed due to system restrictions. It is known that large amounts of the alcohol (co-surfactant) cause an increase in the interface curvature and reversed micelles too small in size do not suit the enzyme [13, 14].

The dependence of the measured V_0 on the new variable A_R is illustrated in Fig. 2 for two of the studied B^*_i-values: 0.0614 and 0.1189. The values $V_{0,i}$ raise from 0 to $V_{max,i}$ with A_R altered from 0 to 1. A_R tends to 0 when R tends to 0 (4'''), which means no alcohol in the system, so it is logical to have no reaction rate. On the other hand, due to the discussed system restrictions, it is not advisable to raise the alcohol concentration very much; R is recommended to be below 9 [15]. It can be calculated that for R up to 9 A_R has great sensibility to the change in R. Thus, by means of the variable A_R the effect of the alcohol concentration can be considered, including its inhibition effect.

The dependences like those shown in Fig. 2 can be further transformed into the known linear forms of the Michaelis-Menten equation, and the kinetic parameters in Eqn. (5), Michaelis-Menten constants

$K_{mB}*$ and K_{mA_R}, and V_{max} can be graphically determined.
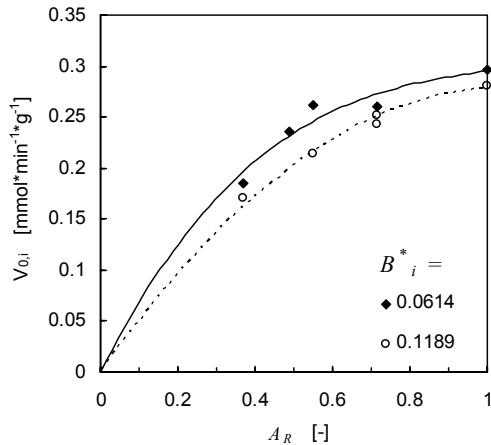
Fig. 2. Dependence of the measured rates on the new variable A_R (Eqn. (4)).

Kinetic parameters determination. Lineweaver-Burk transformations $\frac{1}{V_{0,i}} \propto \frac{1}{A_R}$ ($B*_I$ = const) based on experimental data (Fig. 1a and 1b) are represented in Fig. 3.
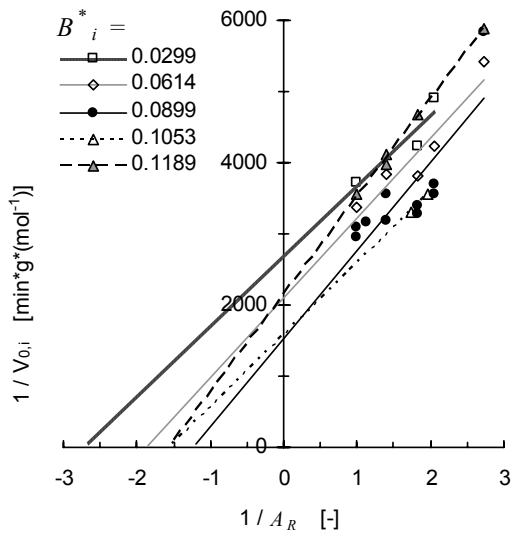
Fig. 3. Lineweaver-Burk linearisation $\frac{1}{V_{0,i}} \propto \frac{1}{A_R}$ for different fixed $B*_i$.

The slopes, intercepts and correlation coefficients of the lines obtained are listed in Table 1.

Table 1. Characterisation of the lines obtained from Lineweaver-Burk transformations $\frac{1}{V_{0,i}} \propto \frac{1}{A_R}$ in Fig. 3.

$B*_i$	Slope, min·g·mol^{-1}	Intercept, min·g·mol^{-1}	Correlation coefficient, R^2
0.0299	996.16	2676.6	0.8511
0.0614	1128.6	2105.9	0.8974
0.0899	1238.4	1544.0	0.6833
0.1053	1003.2	1576.7	1
0.1189	1372.2	2153.9	0.9789

It is seen that the slope is not constant but it rises with $B*$. This is due to the competitive inhibition effect caused by the acid. The linear dependence of slopes on $B*$ is shown in Fig. 4a and the following equation 6 is drawn:

$$\frac{K_{mA_R}}{V_{max}} \times \left(1 + \frac{B*}{K_{iB*}}\right) = \frac{K_{mA_R}}{V_{max}} + \frac{K_{mA_R}}{V_{max}} \times \frac{B*}{K_{iB*}} =$$
$$= 926.2 + 2732 \times B* \qquad (6),$$

where K_{iB*} is inhibition constant of the acid under the form of the variable $B*$.

a

b
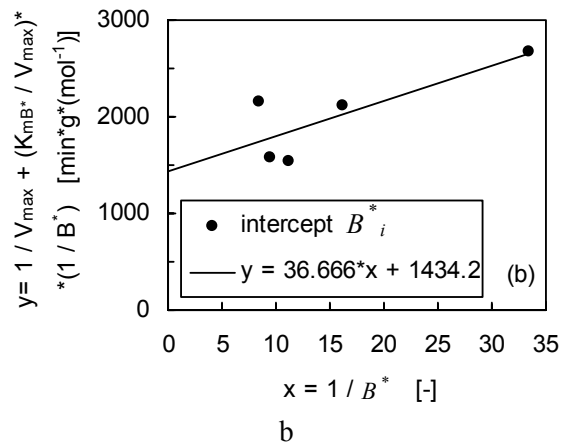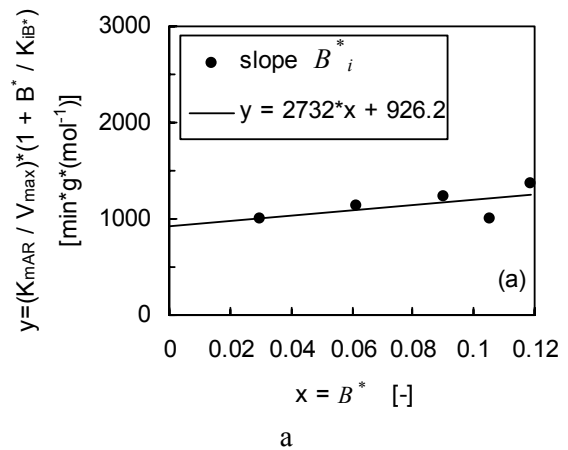
Fig. 4. Replot of slopes (a) and intercepts (b) of the lines in Fig. 3.

The intercepts are proportional to $1/B*$ as shown in Fig. 4b and the following linear equation is drawn:

$$\frac{1}{V_{max}} + \frac{K_{mB*}}{V_{max}} \times \frac{1}{B*} = 1434.2 + 36.666 \times \frac{1}{B*} \qquad (7).$$

Including the inhibition observed, Ping-Pong Bi-Bi model for the studied reaction (Eqn. (5)) is transformed in the final form:

$$\frac{1}{V_0} = \frac{1}{V_{max}} + \frac{K_{mB*}}{V_{max}} \times \frac{1}{B*} + \frac{K_{mA_R}}{V_{max}} \times \left(1 + \frac{B*}{K_{iB*}}\right) \times \frac{1}{A_R} \qquad (8).$$

326

From equations (6) and (7) the kinetic parameters for the studied reaction are determined and listed in Table 2. As in parameters determination are involved experiments of $[H_2O]_0$ = 3.45−4.6 mol·dm^{-3}, according to Eqn. (2) $K_{mB}*$ corresponds to [oleic acid]$_0$ = 0.0882−0.1176 mol·dm^{-3}. According to Eqn. (4'''), K_{mA_R} corresponds to R = 0.696. Taking into account the protein content of the lipase preparation used, ≈14%, the determined value of V_{max} can be recalculated to be 0.30 mol·h^{-1}·g^{-1} {protein}, which is comparable to published data for oleate esters produced by nylon-immobilised *Candida rugosa* lipase [12]. Thus, for butyl oleate enzymatic syntesis, V_{max} was determined to be 0.19 mol·h^{-1}·g^{-1} {protein}, and the ratio $K_{m(alcohol)}/K_{m(acid)}$ corresponded to R = 0.5.

Table 2. Kinetic parameters in Ping-Pong Bi-Bi model with inhibition (Eqn. (8)) for the studied esterification reaction in RMS [a].

$V_{max,}$ mmol·min^{-1}·g^{-1}	K_{mB*}	K_{iB*}	K_{mA_R}	R corresponding to K_{mA_R} (Eqn. (4'''))
0.6973	0.0256	0.3390	0.6458	0.696

a - RMS consisted of CPC − 0.115 mol·dm^{-3}; CRL − 3 g·dm^{-3}; $[H_2O]_0$ = 3.45−4.6 mol·dm^{-3}.

Comparison between experimental and model data. Suggestions for further model development. Comparison between experimental and model values of the initial reaction rate is shown in Fig. 5a–d. The model data describe well the trend of rate dependence on R, which is the goal of the proposed modelling approach. However, the model Eqn. (8) describes poorly the rate decrease at [oleic acid]$_0$ =

0.4 mol·dm^{-3} (Fig. 5c). It is due to the fact that inhibition effect on $1/V_{max}$ has not been introduced. As seen in Fig. 3 at B* = 0.1189 the rate decreases (intercept in Fig. 4b is increased). Dependence on B*, $\frac{1}{V_{max}} \times [1 + f(B^*)]$, has to be involved when experiments at B* > 0.1189 are carried out.

Experimental and predicted values for some esterifications, which have not been used in the parameters determination procedure, are com-pared in Table 3. The model proposed is sensitive to the increase in $[H_2O]_0$ through the variable B^* (Eqn. (2)). This means that the model is sensitive to the acid dilution by the dispersed aqueous phase. However, the second variable, A_R (Eqn. (4''')), does not depend on water. The model is not sensitive to the dilution of the alcohol-substrate, which needs further resolution. As it has been discussed, some esterifications in Fig. 1a required a special condition, lower CPC-concentration, 0.0383 mol·dm^{-3} and subsequently lower water concentration, $[H_2O]_0$ = 1.15 mol·dm^{-3}, in order to keep W_0 = 30. These data can be also modeled using the kinetic parameters in Table 2 if the variables are recalculated for $[H_2O]_0$ = 3.45 mol·dm^{-3} where the parameters are valid. The recalculated variables $(B^*)'$ and $(A^*)'$ should keep the following ratio constant:

$$\frac{(B^*)'}{B^*} = \frac{(A^*)'}{A^*} = \frac{([H_2O]_0)' = 3.45 \ mol \cdot dm^{-3}}{[H_2O]_0 \quad = 1.15 \ mol \cdot dm^{-3}} \quad (9).$$

The recalculated variables, experimental and predicted (in Eqn. (8)) rates are shown in Table 4. The comparison shows good approximation of modeled to measured rates.

Table 3. Experimental and predicted values of the initial reaction rate[a].

Initial concentrations in RMS, mol·dm^{-3}			Variables in Eqn. (8)		V_0, mmol·min^{-1}·g^{-1}	
[oleic acid]$_0$	[alcohol]$_0$	$[H_2O]_0$	B^*	A_R	experimental	predicted
0.3083	0.3	3.45	0.0894	0.9727	0.3391	0.3281
0.3015	0.3	4.60	0.0655	0.9951	0.3088	0.3221
0.4126	0.4	4.60	0.0897	0.9689	0.3232	0.3277
0.4115	0.4	5.175	0.0795	0.9717	0.3162	0.3255

a - Predicted values are calculated upon model Eqn. (8) and parameters in Table 2.

Table 4. Experimental and predicted values of the initial reaction rate[a].

initial concentrations in RMS, mol·dm^{-3}			variables in Eqn. (8)		V_0, mmol·min^{-1}·g^{-1}	
[oleic acid]$_0$	[alcohol]$_0$	$[H_2O]_0$	$(B^*)'$	$(A_R)' = A_R$	experimental	predicted
0.1113	0.050	1.15	0.2904	0.2932	0.1682	0.1347
0.1043	0.075	1.15	0.2721	0.6764	0.2115	0.2477
0.1043	0.150	1.15	0.2721	0.7375	0.2659	0.2609

a - Predicted values are calculated upon model Eqn. (8) and parameters in Table 2.

a

b

c

d
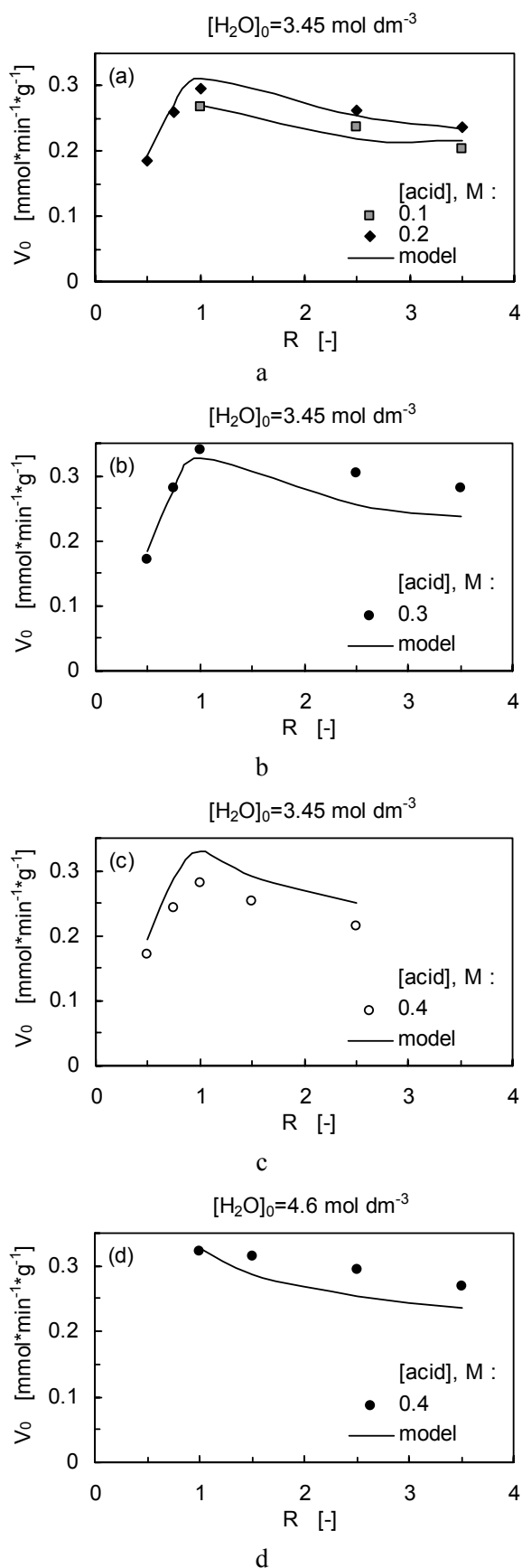
Fig. 5. Comparison between experimental and model values of reaction rate for different initial concentrations of acid, alcohol, and water in RMS (a)–(d).

CONCLUSIONS

Esterification reaction in RMS, characterised by optimal rates achieved when keeping constant the initial molar ratio of alcohol to acid, is modeled. The modeling is based on the Michaelis-Menten equation for Ping-Pong Bi-Bi mechanism. One variable in this equation is conventional and changes with the concentration of the acid while the other alters with the ratio of alcohol to acid and its deviation from the optimal value is experimentally determined. By this transformation, the effect of the alcohol concentration including its inhibition effect, which causes the rate decrease above the optimal ratio, is considered together in one variable. This simplifies the model equation. The approach could be applied to other reaction systems of similar catalytic behavior, i.e. the highest rates at constant substrates ratio.

In the studied reaction inhibition by the acid is observed and considered in the model equation. The effect of acid dilution when the initial water concentration in RMS is increased is also taken into account. The modeled rate dependences on the substrates ratio correspond well to the measured data. The model needs further evolution with respect to dilution effect on the alcohol-substrate. The inhibition effect of the acid-substrate also needs future experimental research and model refinement.

REFERENCES

1. N. N. Gandhi, N. S. Patil, S. B. Sawant, J. B. Joshi, P. P. Wangikar, D. Mukesh, *Catal. Rev.- Sci. Eng.,* **42**, 439 (2000).
2. M. S. Shintre, R. S. Ghadge, S. B. Sawant,. *J. Chem. Technol. Biotechnol.,* **77**, 1114 (2002).
3. N. Nemestóthy, L. Gubicza, E. Fehér, K. Bélafi-Bakó, *Food Technol. Biotechnol.*, **46**, 44 (2008).
4. G. Sandoval, J. S. Condoret, P. Monsan, A. Marty, *Biotechnol. Bioeng.*, **78**, 313 (2002).
5. H. Stamatis, A. Xenakis, U. Menge, F. Kolisis, *Biotechnol. Bioeng.*, **42**, 931 (1993).
6. K. Nagayama, S. Matsu-ura, T. Doi, M. Imai, *J. Mol. Catal. B, Enzym.*, **4**, 25 (1998).
7. K. Naoe, T. Ohsa, M. Kawagoe, M. Imai, *Biochem. Eng. J.*, **9**, 67 (2001).
8. R. Verhaert, R. Hilhorst, M. Vermüe, T. J. Schaafsma, C. Veeger, *Eur. J. Biochem.*, **187**, 59 (1990).
9. K. Tonova, Z. Lazarova, N. Nemestóthy, L. Gubicza, K. Bélafi-Bakó, *CI&CEQ*, **12**, 175 (2006). Available

via http://www.ache.org.rs/CICEQ/CI&CEQ.html Accessed 10 July 2008.

10. K. Bélafi-Bakó, A. Kabiri Badr, N. Nemestóthy, U. Ehrenstein, L. Gubicza, *Chem. Pap*., **57**, 277 (2003).

11. K. Bélafi-Bakó, Á. Dombi, L. Szabó, E. Nagy , *Biotechnol. Tech*., **9**, 59 (1995).

12. A. Zaidi, J. L. Gainer, G. Carta, A. Mrani, T. Kadiri, Y. Belarbi, A. Mir, *J. Biotechnol*., **93**, 209 (2002).

13. R. Hilhorst, M. Sergeeva, D. Heering, P. Rietveld, P. Fijneman, R. B. G. Wolbert, M. Dekker, B. H. Bijsterbosch, *Biotechnol. Bioeng*., **46**, 375 (1995).

14. F. Lopez, G. Palazzo, G. Colafemmina, G. Cineli, L. Ambrosone, A. Ceglie, *Prog. Colloid. Polym. Sci*., **123**, 174 (2004).

15. K. Naoe, C. Takeuchi, M. Kawagoe, K. Nagayama, M. Imai, *J. Chromatogr. B,* **850**, 277 (2007).

МОДЕЛИРАНЕ НА КИНЕТИКАТА НА ЕНЗИМНА ЕСТЕРИФИКАЦИЯ ПО ОТНОШЕНИЕ НА СЪОТНОШЕНИЕТО НА СУБСТРАТИТЕ

К. Тонова[1,*], Здр. Лазарова[2]

[1] *Институт по инженерна химия, Българска академия на науките, ул. „Акад. Г. Бончев“, Блок 103, 1113 София*
[2] *Австрийски изследователски център, Биогенетика и природни ресурси - Вода, 2444 Зайберсдорф, Австрия*

(Резюме)

Изследвана е реакция на ензимна естерификация в система с обърнати мицели. За всяка една от изследваните концентрации на киселината е установен локален максимум в профила на началната скорост на реакцията, съответстващ на еквимоларното начално съотношение на алкохола към киселината. Предложено е моделиране на това явление. Моделното описание се основава на трансформиране на уравнението на Михаелис-Ментен за реакции, протичащи по „Пинг-понг“ механизъм. Едната от променливите в модифици-раното уравнение е свързана с началната концентрация на киселината, докато другата променлива отразява съотношението на алкохола към киселината и се явява количествена мярка за това, с колко то се различава от експерименталната оптимална стойност 1. Отчетен е наблюдаваният ефект на субстратно инхибиране от киселината. Под внимание е взет ефектът на разреждане на киселината при повишаване на концентрацията на водата в системата с обърнати мицели. Кинетичните параметри в моделното описание на изследваната ензимна естерификация са определени графично. Експерименталните и моделните зависимости на началната скорост на реакцията от началното молно съотношение на субстратите са сравнени. Направени са предложения за допъл-нително подобряване на моделното описание.

Potentiodynamic and galvanostatic investigations of copper deposition from sulphate electrolytes containing large amount of zinc

G. A. Hodjaoglu, A. T. Hrussanova, I. S. Ivanov*

Institute of Physical Chemistry, Bulgarian Academy of Sciences, Acad. G. Bonchev St., Block 11, 1113 Sofia, Bulgaria

The electroextraction of copper was studied on platinum cathode from sulphate electrolytes containing large amount of zinc. It was established that in electrolytes, containing 50 $g \cdot dm^{-3}$ Zn^{2+} and 1 or 5 $g \cdot dm^{-3}$ Cu^{2+} at potentials more negative than −1.6 V *vs*. SSE both copper and zinc deposition takes place. At concentration higher than 5 $g \cdot dm^{-3}$ Cu^{2+} and in the presence of 130 $g \cdot dm^{-3}$ H_2SO_4 (independently of Cu^{2+} concentration) only copper is deposited. The addition of H_2SO_4 to the electrolyte leads to abrupt increase in cathodic current but it decreases the current efficiency of both copper and zinc deposition, which means that the current increase is a result of enhanced hydrogen evolution. The additive hydroxyethylated-2-butyne-l,4-diol (Ferasine) decreases the areas of Cu and Zn dissolution peaks, showing that the deposition process is inhibited. Dense, smooth and bright coatings of pure copper are deposited at current densities 0.5–2 $A \cdot dm^{-2}$ in electrolytes with Cu^{2+} concentration higher than 5 $g \cdot dm^{-3}$ in the presence of Ferasine. Non-adherent, dark-red slime of copper is obtained at lower Cu^{2+} concentrations.

Key words: copper, cyclic voltammograms, deposition, electroextraction, zinc.

INTRODUCTION

Metallurgy is a branch of the industry that affects very strongly the environment. After a number of pyro- or hydrometallurgical ores treating processes, large amount of wastes with high metal content remain. For example, the waste product known as "blue powder" that results by condensing furnace gases during the thermometallurgical processing of non-ferrous ores contains: Zn (25−41%), Pb (20−25%), Fe (3−5%), Cu (0.5−1%), Cd (0.5−1%), *etc*. [1, 2]. The purification of the electrolytes for Zn electrowinning by cementation is another process that produces wastes containing large amount of different metals such as: copper cake(containing 36−54% Cu, 5−10% Zn and 0.08−0.16% Cd), copper-cadmium cake (containing 10% Cu, 30% Zn, 12% Cd), collective cake (containing 5.8% Cu, 35.9% Zn, 7.2% Cd), copper-nickel cake (containing 25% Cu, 20% Zn, 3% Cd, 0.75% Co, 0.05% Ni). [3]. Cementates of the zinc industry, obtained during the hydrometallurgical zinc winning process, where the sulphate leach liquor is treated with arsenic trioxide and zinc powder for the removal of Cu, Ni, Co, Cd and other impurities before electrowinning, contain: Cu (28.6%), Zn (22.4%), Cd (6.7%), Co (1.32) and Ni (0.16%) [4]. Flue dusts in a secondary copper smelter treated in the electrowinning zinc plant contain: Zn (40−65%), Cu (1−6%), (Pb 6−20%), Cd (0.5−0.8%), Ni (0.1−1%), Sn (1−2%), *etc*. [5]. Muresan *et al*. [2, 6] studied the process of Cu electrowinning from sulphate acidic electrolytes and observed that the addition of small amounts of Zn^{2+} had no effect on the composition of the Cu deposits, but it increased their microscopic roughness. The effect of horse-chestnut extract (HCE) and IT-85, representing a mixture of triethyl-benzyl-ammonium chloride (TEBA) and hydroxy-ethylated-2-butyne-l,4-diol (Ferasine) upon the morphology and structure of Cu deposits was studied. The cathodic polarization was also investigated and compared to the effect exerted by thiourea and animal glue. The additive IT-85 was found to be an efficient inhibitor of the Cu electrocrystallization process, leading to levelled, fine-grained cathodic deposits. The effect of HCE was similar to the effect exerted by animal glue, leading to deposits consisting of rounded nodules, reflecting a smaller levelling effect. Varvara *et al*. [7−10] studied the influence of TEBA, Ferasine and IT-85 on the kinetics of Cu electrodeposition from such electrolytes and on the morphology and structure of Cu deposits. TEBA acts as an inhibitor of the electrodeposition process only as a blocking agent competing with cuprous ions for the adsorption sites of the cathodic surface. Due to its adsorption on the electrode surface, Ferasine inhibits the charge transfer and thus affects the electrocrystallization step, impeding the crystal growth process and promoting the nucleation of Cu. In spite of their different chemical nature, both additives were found

* To whom all correspondence should be sent:
E-mail: isivanov@ipc.bas.bg

to be efficient as levelling agents, leading to fine-grained cathodic deposits. Comparison of the inhibiting effects exerted by IT-85 and its components on the electrodeposition process pointed out to the existence of a beneficial complementarity of TEBA and Ferasine when they are used in mixture.

The aim of this paper was to study the influence of Zn^{2+} ions, Ferasine and some experimental conditions on the process of Cu electroextraction from sulphuric acid electrolytes.

EXPERIMENTAL

The experiments were carried out in a thermostated ($37 \pm 1°C$), three-electrode glass cell without stirring of the electrolyte.

The cathode (2.0 cm^2) and both anodes (4.0 cm^2 total area), used in the potentiodinamic studies, were Pt plates. The reference electrode was a mercury/mercurous sulphate electrode in 0.5 M H_2SO_4 (SSE), its potential *vs.* NHE being $+0.720$ V. The studies were carried out using a cyclic potentiodynamic technique. The potential scanning at a rate of 30 mV·sec^{-1} in the potential range from $+1.000$ to -1.800 V *vs* SSE was performed by means of computerized PAR 263A potentiostat/galvanostat using Soft Corr II software. The current efficiency of deposition process was obtained by integration of cathodic part and anodic peaks on the cyclic voltammograms (CV curves). The potential range and scanning rate were chosen experimentally as the most suitable.

Galvanostatic deposition was carried out using copper cathodes (4.0 cm^2) and two Pt anodes (4.0 cm^2 total area) at current densities in the range of $0.5-2$ A·dm^{-2}.

All electrodes were degreased in an ultrasound bath and then only Cu cathodes were etched in HNO$_3$ ($1:1$).

Cu^{2+} ions (1, 5 or 10 g·dm^{-3}) were added to electrolytes, containing from 14 to 50 g·dm^{-3} Zn^{2+} ions (as ZnSO$_4$.5H$_2$O) and from 0 to 130 g·dm^{-3} H$_2$SO$_4$. The organic additive was 30% solution of hydroxy-ethylated-butyne-2-diol-1,4 (Ferasine).

RESULTS AND DISCUSSION

Potentiodinamic studies

Influence of the vertex potential on CV curves. Figure 1 shows CV curves obtained in an electrolyte, containing 50 g·dm^{-3} Zn^{2+} and 1 g·dm^{-3} Cu^{2+}. The potential scan direction is changed at cathodic potentials (vertex potentials) -0.8, -1.2 or -1.6 V. When the change of scan direction is made

at -0.8 or -1.2 V (curves 1 and 2) one little cathodic peak at -0.265 V and one higher cathodic peak at -0.455 V due to Cu deposition on the Pt surface are observed on the cathodic part of the curves. At more negative potentials simultaneous Cu deposition and hydrogen evolution is occuring. On the anodic part of each CV curve one high peak at -0.275 V (curve 1) and at -0.250 V (curve 2), due to the dissolution of the larger amount of the deposited Cu, and much lower one at 0.035 V (curve 1) and 0.130 V (curve 2), due to the dissolution of the Cu layer deposited on the Pt surface, are observed. When the vertex potential is -1.6 V (curve 3) on the cathodic part of the CV curve the two peaks due to Cu deposition are followed by sharp rise of the current due to codeposition of Cu and Zn as well as to hydrogen evolution. On the anodic part of the curve at -1.260 V peak of Zn dissolution appears, followed by the peaks of Cu dissolution at -0.210 V and 0.135 V, respectively. CV curves obtained in the presence of 1 cm^3·dm^{-3} of the organic additive Ferasine in the electrolyte are similar.
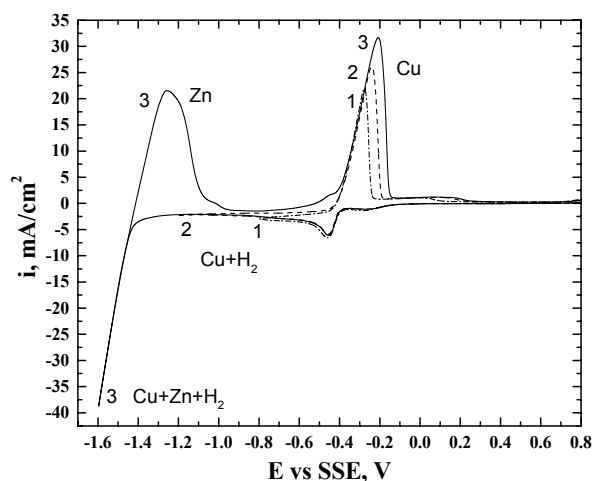
Fig. 1. Cyclic voltammograms, obtained on Pt cathode in an electrolyte, containing 50 g·dm^{-3} Zn^{2+} and 1 g·dm^{-3} Cu^{2+}. Vertex potentials *vs.* SSE (V): 1) -0.8; 2) -1.2; 3) -1.6. Scan rate 30 mV·sec^{-1}.

Figure 2 shows the CV curves obtained in an electrolyte, containing 50 g·dm^{-3} Zn^{2+}, 1 g·dm^{-3} Cu^{2+} and 130 g·dm^{-3} H$_2$SO$_4$. The change of the scan direction is made at the same potentials as in the absence of acid. The peaks of Cu deposition are similar to those shown in Fig. 1. When the vertex potential is -1.6 V or more negative on the anodic part of the curves only peaks of Cu dissolution are observed. This shows that in the presence of H$_2$SO$_4$ Zn is not deposited. The addition of 1 cm^3·dm^{-3} Ferasine to the electrolyte does not change the CV curves.
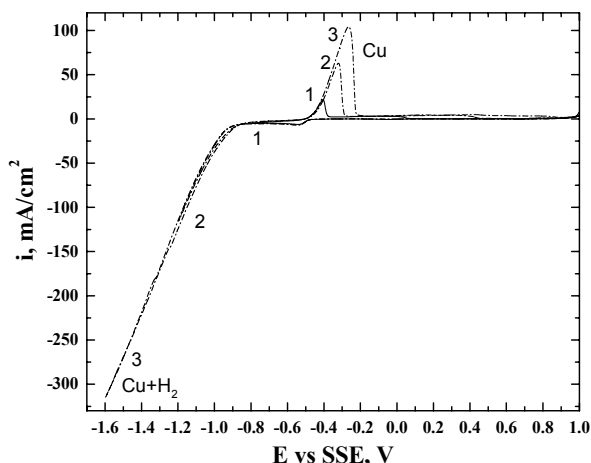
Fig. 2. Cyclic voltammograms, obtained on Pt cathode in an electrolyte, containing 50 g·dm^{-3} Zn^{2+}, 1 g·dm^{-3} Cu^{2+} and 130 g·dm^{-3} H$_2$SO$_4$. Vertex potentials *vs.* SSE (V): 1) −0.8; 2) −1.2; 3) −1.6. Scan rate 30 mV·sec^{-1}.

CV curves obtained in an electrolyte, containing 50 g·dm^{-3} Zn^{2+} and 10 g·dm^{-3} Cu^{2+} are shown in Fig. 3. The change of the scan direction is made at the same potentials as in Figures 1 and 2. The cathodic part of the curves is similar to those obtained in the electrolyte, containing 1 g·dm^{-3} Cu^{2+}. The peaks of Cu deposition are higher, as it could be expected. Only peaks of Cu dissolution are observed on the anodic part of the curves showing that Zn deposition does not take place. The CV curves, obtained in the presence of Ferasine, H$_2$SO$_4$ or both H$_2$SO$_4$ and Ferasine are similar. In all cases Zn deposition does not take place, even if the vertex potential is −1.8 V.

Zn deposition. Integration of the cathodic part of CV curves as well as of the anodic peaks of Zn and Cu dissolution is used to determine the current efficiency of Zn and Cu deposition according to the following formulae:

$$CE_{Zn} [\%] = q^{anode}_{Zn}/q^{cathode}.100$$

$$CE_{Cu} [\%] = q^{anode}_{Cu}/q^{cathode}.100$$

Figure 4 shows the dependence of the current efficiency of Cu and Zn deposition on the vertex potential in electrolytes, containing 50 g·dm^{-3} Zn^{2+} and 1, 5 or 10 g·dm^{-3} Cu^{2+}, respectively. It can be seen that in the electrolyte, containing 1 g·dm^{-3} Cu^{2+}, when the change of scan direction is made at −1.4 V, the current efficiency of Cu deposition is 70−72% and it decreases to about 20 %, when the vertex potential is −1.8 V (curve 1a). In the same electrolyte the current efficiency of Zn deposition rises from 0% at vertex potential −1.4 V to about 75% at vertex potential −1.8 V (curve 1b). At Cu^{2+} concentration 5 g·dm^{-3} the current efficiency of Cu deposition is higher than 85% when the vertex potential is −1.6 V and it decreases to 75% at vertex potential −1.8 V (curve 2a). In the same electrolyte the current efficiency of Zn deposition rises from 0% at vertex potential −1.6 V to 15% at vertex potential −1.8 V (curve 2b). At Cu^{2+} concentration 10 g·dm^{-3} the current efficiency of Cu is in the range 80−95% at all vertex potentials (curve 3). In this case, Zn is not deposited at all. The results obtained in electrolytes, containing Zn^{2+} 50 g·dm^{-3}, Cu^{2+} (1, 5 or 10 g·dm^{-3}) and 1 cm^3·dm^{-3} Ferasine are similar.

Fig. 3. Cyclic voltammograms, obtained on Pt cathode in an electrolyte, containing 50 g·dm^{-3} Zn^{2+} and 10 g·dm^{-3} Cu^{2+}. Vertex potentials *vs.* SSE (V): 1) −0.8; 2) −1.2; 3) −1.6. Scan rate 30 mV sec^{-1}.

Influence of the Cu^{2+} concentration and the vertex potential on the current efficiency of Cu and
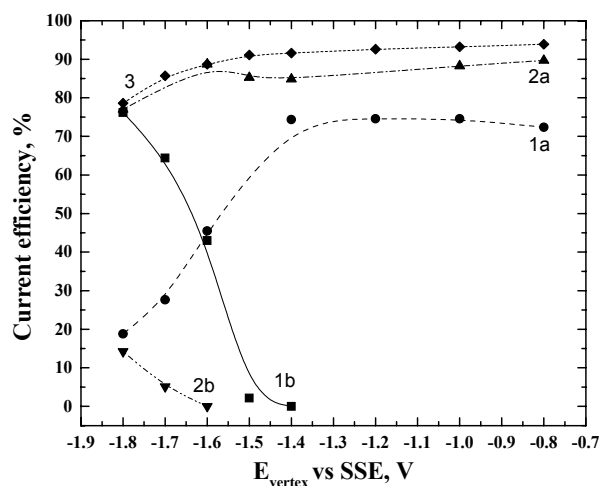
Fig. 4. Current efficiency (CE) of Cu and Zn deposition on Pt cathode *vs.* vertex potential (E$_{vertex}$). Electrolyte, containing 50 g·dm^{-3} Zn^{2+} and 1 g·dm^{-3} Cu^{2+}; 1a) CE of Cu; 1b) CE of Zn. Electrolyte, containing 50 g·dm^{-3} Zn^{2+} and 5 g·dm^{-3} Cu^{2+}: 2a) CE of Cu; 2b) CE of Zn. Electrolyte, containing 50 g·dm^{-3} Zn^{2+} and 10 g·dm^{-3} Cu^{2+}: 3) CE of Cu.

In Figure 5 the dependence of current efficiency on vertex potential in electrolytes, containing 50 g·dm^{-3} Zn^{2+}, 130 g·dm^{-3} H$_2$SO$_4$ and 1, 5 or 10 g·dm^{-3} Cu^{2+}, respectively, is represented. The current efficiency of Cu decreases with the shift of vertex potential in negative direction, which is an indication of enhanced hydrogen evolution. As it could be expected, the increase in Cu^{2+} concentration leads to increase in the current efficiency. CV curves show that in the presence of H$_2$SO$_4$ at all Cu^{2+} concentrations Zn is not deposited. The addition of 1 cm^3·dm^{-3} Ferasine in these electrolytes does not lead to any significant changes in the CV curves.

Fig. 6. Current efficiency (CE) of Cu and Zn deposition on Pt cathode versus vertex potential (E$_{vertex}$). Electrolyte, containing 50 g·dm^{-3} Zn^{2+} and 1 g·dm^{-3} Cu^{2+}: 1a) CE of Cu; 1b) CE of Zn. Electrolyte, containing 50 g·dm^{-3} Zn^{2+}, 1 g·dm^{-3} Cu^{2+} and 130 g·dm^{-3} H$_2$SO$_4$: 2) CE of Cu. Electrolyte, containing 50 g·dm^{-3} Zn^{2+} and 10 g·dm^{-3} Cu^{2+}: 3) CE of Cu. Electrolyte, containing 50 g·dm^{-3} Zn^{2+}, 10 g·dm^{-3} Cu^{2+} and 130 g·dm^{-3} H$_2$SO$_4$: 4) CE of Cu.

Fig. 5. Current efficiency (CE) of Cu deposition on Pt cathode *vs.* vertex potential (E$_{vertex}$). Electrolytes, containing 50 g·dm^{-3} Zn^{2+}, 130 g·dm^{-3} H$_2$SO$_4$ and: 1) 1 g·dm^{-3} Cu^{2+}; 2) 5 g·dm^{-3} Cu^{2+}; 3) 10 g·dm^{-3} Cu^{2+}.

Influence of H$_2$SO$_4$ and the organic additive Ferasine on the current efficiency of Cu and Zn deposition. Figure 6 shows the influence of the vertex potential on the current efficiency of Cu in electrolytes, containing 50 g·dm^{-3} Zn^{2+} and 1 or 10 g·dm^{-3} Cu^{2+} in presence or in absence of 130 g·dm^{-3} H$_2$SO$_4$. The current efficiency of Cu decreases in the presence of H$_2$SO$_4$, (curves 2 and 4) compared to the current efficiency in absence of H$_2$SO$_4$ (curves 1a and 3). Zn is deposited in electrolytes containing 50 g·dm^{-3} Zn^{2+} and only 1 g·dm^{-3} Cu^{2+} (curve 1b).

The CV curves show that Ferasine decreases the cathodic current and the anodic peaks of metal deposition, which means that the organic additive inhibits the process. The influence of Ferasine is more pronounced in electrolytes without H$_2$SO$_4$. The additive decreases the current efficiency of both metals, especially the current efficiency of Cu. In the presence of H$_2$SO$_4$ in the electrolyte Zn is not deposited at all vertex potentials.

Galvanostatic studies

The effects of current density and electrolyte composition on the surface morphology and composition of galvanostatically deposited coatings on Cu substrates were also studied. In all cases only copper is detected by microprobe analysis.

It has been established that dense and smooth Cu coatings are deposited when the Cu^{2+} concentration is higher than 5 g·dm^{-3} and the current density is in the range 0.5 ÷ 2 A·dm^{-2}. At density of 1 A·dm^{-2} the deposition potential is −0.500 ÷ −0.600 V. In all cases the current efficiency of Cu deposition is higher than 95%. Figure 7 shows SEM micrograph of Cu coatings obtained after 3 h deposition at density of 1 A·dm^{-2} in an electrolyte, containing 50 g·dm^{-3} Zn^{2+}, 10 g·dm^{-3} Cu^{2+} and 130 g·dm^{-3} H$_2$SO$_4$. The coating is light-red, smooth and semi-bright. The addition of Ferasine (1 cm^3·dm^{-3}) leads to more fine-grained surface morphology of the coatings (Fig. 8). The additive effect is more strongly expressed at Ferasine concentration 5 cm^3·dm^{-3}. In the presence of Ferasine the coatings are light-red, smooth and bright. Coatings obtained in electrolytes containing 20 g·dm^{-3} Cu^{2+} and, respectively 50 and 100 g·dm^{-3} Zn^{2+} are more coarse-grained but in the first case they are bright, while in the second – dark-red and rough.

The grain size of all coatings is presented in Table 1.

Table 1. Grain size of Cu coatings obtained in different electrolytes (in μm).

Electrolyte	Grain size, μm
50 g·dm^{-3} Zn^{2+} + 10 g·dm^{-3} Cu^{2+}	25−30
50 g·dm^{-3} Zn^{2+} + 10 g·dm^{-3} Cu^{2+} + 1 ml·dm^{-3} Ferasine	15−18
50 g·dm^{-3} Zn^{2+} + 10 g·dm^{-3} Cu^{2+} + 130 g·dm^{-3} H$_2$SO$_4$	12−18
50 g·dm^{-3} Zn^{2+} + 10 g·dm^{-3} Cu^{2+} + 130 g·dm^{-3} H$_2$SO$_4$ + 1 cm^3·dm^{-3} Ferasine	10−12
50 g·dm^{-3} Zn^{2+} + 10 g·dm^{-3} Cu^{2+} + 130 g·dm^{-3} H$_2$SO$_4$ + 5 cm^3·dm^{-3} Ferasine	< 3
50 g·dm^{-3} Zn^{2+} + 20 g·dm^{-3} Cu^{2+} + 130 g·dm^{-3} H$_2$SO$_4$ + 5 cm^3·dm^{-3} Ferasine	9−12
100 g·dm^{-3} Zn^{2+} + 20 g·dm^{-3} Cu^{2+} + 130 g·dm^{-3} H$_2$SO$_4$ + 5 cm^3·dm^{-3} Ferasine	15−20
50 g·dm^{-3} Zn^{2+} + 5 g·dm^{-3} Cu^{2+} + 130 g·dm^{-3} H$_2$SO$_4$ + 5 cm^3·dm^{-3} Ferasine	< 6
14 g·dm^{-3} Zn^{2+} + 1.25 g·dm^{-3} Cu^{2+} + 16.5 g·dm^{-3} H$_2$SO$_4$ + 0.6 cm^3·dm^{-3} Ferasine	< 1−2
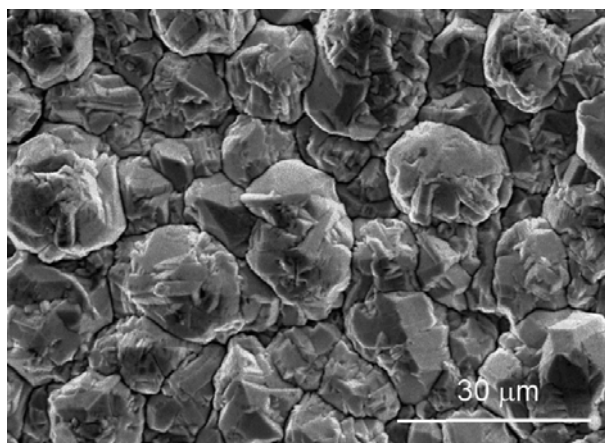
Fig. 7. SEM micrograph of Cu coating, obtained after 3 h deposition at density 1 A·dm^{-2} in an electrolyte, containing 50 g·dm^{-3} Zn^{2+}, 10 g·dm^{-3} Cu^{2+} and 130 g·dm^{-3} H$_2$SO$_4$. Magnification ×1000.
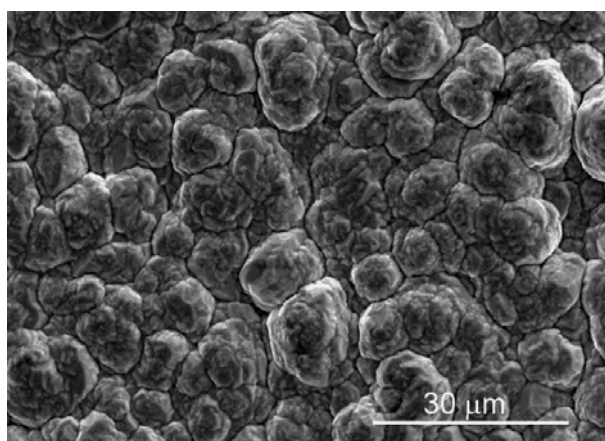
Fig. 8. SEM micrograph of Cu coating, obtained after 2 h deposition at density 1 A·dm^{-2} in an electrolyte, containing 50 g·dm^{-3} Zn^{2+}, 10 g·dm^{-3} Cu^{2+}, 130 g·dm^{-3} H$_2$SO$_4$ and 1 cm^3·dm^{-3} Ferasine. Magnification ×1000.

It was established that non-adherent, dark-red Cu slime is deposited on Cu substrate at Cu^{2+} concentration lower than 5 g·dm^{-3}. In the case of low Cu^{2+} concentration the deposition potential is more negative (between −1.000 and −1.100 V) due to the concentration polarization. Figure 9 shows the morphology of Cu slime obtained after 30 min

deposition at density 0.5 A·dm^{-2} and potential −1.05 V in an electrolyte, containing 1.25 g·dm^{-3} Cu^{2+}, 14 g·dm^{-3} Zn^{2+}, 16.5 g·dm^{-3} H$_2$SO$_4$ and 0.6 cm^3·dm^{-3} Ferasine. In this case the current efficiency is less than 75%.
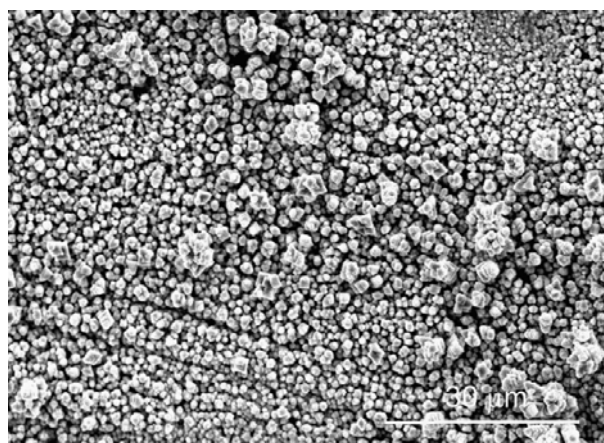
Fig. 9. SEM micrograph of Cu coating, obtained after 30 min deposition at density 0.5 A·dm^{-2} in an electrolyte, containing 14 g·dm^{-3} Zn^{2+}, 1.25 g·dm^{-3} Cu^{2+}, 16.5 g·dm^{-3} H$_2$SO$_4$ and 0.6 cm^3·dm^{-3} Ferasine. Magnification ×1000.

CONCLUSIONS

In electrolytes, containing 50 g·dm^{-3} Zn^{2+} and 1 or 5 g·dm^{-3} Cu^{2+} at potentials more negative than −1.6 V *vs*. SSE simultaneous deposition of Cu and Zn on Pt cathode is taking place. With the increase in Cu^{2+} concentration, the anodic peaks of Zn dissolution decrease. At Cu^{2+} concentration 10 g·dm^{-3} only Cu deposition takes place. In electrolytes, containing 50 g·dm^{-3} Zn^{2+} and 130 g·dm^{-3} H$_2$SO$_4$ at all studied Cu^{2+} concentrations and vertex potentials only Cu deposition takes place.

In electrolytes, containing 50 g·dm^{-3} Zn^{2+} current efficiency of Cu deposition at vertex potentials more negative than −1.6 V *vs*. SSE decreases from 70% to 20% (at Cu^{2+} concentration 1 g·dm^{-3}) and from 85−90% to 75–80% (at Cu^{2+} concentration 5 or 10 g·dm^{-3}). As it is expected current efficiency of Cu increases with the increase in Cu^{2+} concentration. Current efficiency of Zn deposition increases at

vertex potentials more negative than –1.6 V *vs*. SSE from 0 to 75% and 15% (at Cu^{2+} concentrations of 1 and 5 $g \cdot dm^{-3}$, respectively). At Cu^{2+} concentration of 10 $g \cdot dm^{-3}$ Zn deposition does not take place.

In electrolytes containing 50 $g \cdot dm^{-3}$ Zn^{2+} and 130 $g \cdot dm^{-3}$ H_2SO_4 the current efficiency of Cu deposition increases with the increase in Cu^{2+} concentration and decreases with the increase in the vertex potential. In all cases Zn deposition does not take place. The current efficiency of Cu deposition in the presence of 130 $g \cdot dm^{-3}$ H_2SO_4 is lower than the current efficiency in its absence.

Dense and smooth copper coatings on Cu cathode with current efficiency higher than 95% are deposited when Cu^{2+} concentration is higher than 5 $g \cdot dm^{-3}$ and the current density is in the range 0.5−2 $A \cdot dm^{-2}$. More fine-grained coatings are obtained in the presence of H_2SO_4 and the organic additive hydroxyethylated-2-butyne-l,4-diol (Ferasine). At lower Cu^{2+} concentration, non-adherent dark-red slime of copper is deposited with current efficiency less than 75%.

REFERENCES

1. L. Muresan, A. Nicoara, S. Varvara, G. Maurin, *J. Appl. Electrochem*., **29,** 719 (1999).
2. L. Muresan, S. Varvara, G. Maurin, S. Dorneanu, *Hydrometallurgy*, **54,** 161 (2000).
3. V. D. Karoleva, Metallurgy of Heavy Non-ferrous Metals, Part II, c/o Jusautor, Sofia, 1986.
4. D. Melzner, J. Tilkowski, A. Mohrmann, W. Poppe, W. Halwachs, K. Schogerl, *Hydrometallurgy,* **13,** 105 (1984).
5. R. Kammel, M. Goktepe, H. Oelmann, *Hydrometallurgy*, **19,** 11 (1987).
6. L. Muresan, A. Nicoara, S. Varvara, G. Maurin, *J. Appl. Electrochem*., **29,** 719 (1999).
7. S. Varvara, L. Muresan, I. C. Popescu, G. Maurin, *J. Appl. Electrochem*., **33,** 685 (2003).
8. S. Varvara, L. Muresan, I. C. Popescu, G. Maurin, *Hydrometallurgy*, **75**, 147 (2004).
9. S. Varvara, L. Muresan, A. Nicoara, G. Maurin, I. C. Popescu, *Mater. Chem. Phys.* **72,** 332 (2001).
10. S. Varvara, L. Muresan, I. C. Popescu, G. Maurin, *J. Appl. Electrochem*. **35,** 69 (2005).

ПОТЕНЦИОДИНАМИЧНИ И ГАЛВАНОСТАТИЧНИ ИЗСЛЕДВАНИЯ НА ОТЛАГАНЕ НА МЕД ОТ СУЛФАТНИ ЕЛЕКТРОЛИТИ СЪДЪРЖАЩИ ГОЛЕМИ КОЛИЧЕСТВА ЦИНК

Г. А. Ходжаоглу, А. Т. Хрусанова, И. С. Иванов*

Институт по физикохимия, Българска академия на науките, ул. „Акад. Г. Бончев“, бл. 11, 1113 София

(Резюме)

Изследвана е електроекстракцията на мед върху платинов катод от сулфатни електролити, съдържащи големи количества цинк. Установено е, че в електролити, съдържащи 50 $g \cdot dm^{-3}$ Zn^{2+} и 1 или 5 $g \cdot dm^{-3}$ Cu^{2+}, при потенциали по-отрицателни от −1.6 V *vs*. SSE се отлагат едновременно мед и цинк. При концентрация на Cu^{2+} по-висока от 5 $g \cdot dm^{-3}$ и в присъствие на 130 $g \cdot dm^{-3}$ H_2SO_4 (независимо от концентрацията на Cu^{2+}) се отлага само мед. Прибавянето към електролита на H_2SO_4 води до рязко нарастване на катодния ток, но същевременно понижава добива по ток, както на отлагането на мед, така и на цинк, което означава, че нарастването на тока е резултат от засиленото отделяне на водород. Добавката хидроксиетилиран-2-бутин-1,4-диол (Ферасин) намалява площта на медните и цинкови пикове на разтваряне, което показва, че процесът на отлагане е инхибиран. Плътни, гладки и блестящи покрития от чиста мед се отлагат при плътности на тока 0.5−2 $A \cdot dm^{-2}$ в електролити с концентрации на Cu^{2+} по-високи от 5 $g \cdot dm^{-3}$ в присъствие на Ферасин. Тъмночервен и със слаба адхезия към катода меден шлам се получава при по-ниски концентрации на Cu^{2+}.

CONTENTS

СЪДЪРЖАНИЕ